Swansea University
Prifysgol Abertawe

Cronfa
Setting Research Free

Swansea University E-Theses

Laser ultrasonic testing for on-line inspection of laser metal deposition.

Garner, Simon

How to cite:

Garner, Simon (2015) *Laser ultrasonic testing for on-line inspection of laser metal deposition..* thesis, Swansea University.
http://cronfa.swan.ac.uk/Record/cronfa42997

Use policy:

This item is brought to you by Swansea University. Any person downloading material is agreeing to abide by the terms of the repository licence: copies of full text items may be used or reproduced in any format or medium, without prior permission for personal research or study, educational or non-commercial purposes only. The copyright for any work remains with the original author unless otherwise specified. The full-text must not be sold in any format or medium without the formal permission of the copyright holder. Permission for multiple reproductions should be obtained from the original author.

Authors are personally responsible for adhering to copyright and publisher restrictions when uploading content to the repository.

Please link to the metadata record in the Swansea University repository, Cronfa (link given in the citation reference above.)

http://www.swansea.ac.uk/library/researchsupport/ris-support/

SWANSEA UNIVERSITY
1300141145

Prifysgol Abertawe
Swansea University

Laser Ultrasonic Testing for On-line Inspection of Laser Metal Deposition

Simon Garner

Doctor of Philosophy

2015

ProQuest Number: 10821387

All rights reserved

INFORMATION TO ALL USERS
The quality of this reproduction is dependent upon the quality of the copy submitted.

In the unlikely event that the author did not send a complete manuscript
and there are missing pages, these will be noted. Also, if material had to be removed,
a note will indicate the deletion.

ProQuest 10821387

Published by ProQuest LLC (2018). Copyright of the Dissertation is held by the Author.

All rights reserved.
This work is protected against unauthorized copying under Title 17, United States Code
Microform Edition © ProQuest LLC.

ProQuest LLC.
789 East Eisenhower Parkway
P.O. Box 1346
Ann Arbor, MI 48106 – 1346

Abstract

Laser ultrasonic testing is a non-destructive testing technique which is seeing increased interest and application in recent years. Its non-contact nature and small footprint allow laser ultrasonic testing to be deployed on structures with small and/or limited access surfaces and in environments with raised temperatures. Laser metal deposition is an additive manufacturing method often used in the creation of aerospace components with complex geometries which are costly or difficult to produce using traditional methods of manufacture. The formation of intra-layer flaws in deposited layer structures is well researched, although current inspection methods involve testing a structure after manufacture and improving the deposition process through iteration. In-situ non-destructive testing would bring the possibility of re-working structures during deposition as flaws are detected, further saving on material usage and costs. In this work, the capabilities of laser ultrasonic testing are investigated within the context of detecting sub-surface flaws. Ultrasonic wave interactions are studied using finite element modelling and data analysis techniques developed. Following this, off-line laboratory-based trials are carried out on test pieces manufactured to contain near-surface flaws representative of those seen in deposited structures, so that detection limitations can be established. Finally, laser ultrasonic testing equipment is integrated into a working laser metal deposition system to explore the practicality of producing an on-line inspection system.

DECLARATION

This work has not previously been accepted in substance for any degree and is not being concurrently submitted in candidature for any degree.

Signed ..... (candidate)

Date 16/06/2016

STATEMENT 1

This thesis is the result of my own investigations, except where otherwise stated. Where correction services have been used, the extent and nature of the correction is clearly marked in a footnote(s).

Other sources are acknowledged by footnotes giving explicit references. A bibliography is appended.

Signed .... (candidate)

Date 16/06/2016

STATEMENT 2

I hereby give consent for my thesis, if accepted, to be available for photocopying and for inter-library loan, and for the title and summary to be made available to outside organisations.

Signed ..... (candidate)

Date 16/06/2016

Declarations and Statements

DECLARATION

This work has not previously been accepted in substance for any degree and is not being concurrently submitted in candidature for any degree.

Signed ..... (candidate)

Date .....

STATEMENT 1

This thesis is the result of my own investigations, except where otherwise stated. Where correction services have been used, the extent and nature of the correction is clearly marked in a footnote(s).

Other sources are acknowledged by footnotes giving explicit references. A bibliography is appended.

Signed ..... (candidate)

Date .....

STATEMENT 2

I hereby give consent for my thesis, if accepted, to be available for photocopying and for inter-library loan, and for the title and summary to be made available to outside organisations.

Signed ..... (candidate)

Date .....

Table of Contents

List of Figures

List of Tables

Definitions and Abbreviations

a	Amplitude
A	Area
B_{mod}	Bulk modulus of elasticity
c	Speed of light in a vacuum = 2.9979×10^8 m s^{-1}
C	Specific heat capacity
$[C]$	Heat matrix (FEM)
d_{opt}	Light propagation distance
D	Collimated beam diameter
D_{ii}	Force dipole strength
E	Energy
E_{mod}	Modulus of elasticity
h	Planck's constant = 6.626×10^{-34} J s
f	Ultrasonic frequency
f_{rep}	Pulse repetition frequency
F	Focal length
$\{F_{ext}\}$	External force vector (FEM)
k	Wavenumber
$[K]$	Conductivity matrices (FEM)
I	Intensity
l_e	Finite element length
L	Latent heat
$[M]$	Mass matrix (FEM)
P	Power
P_{peak}	Peak power
P_{avg}	Average power
Q	Surface heat flux
$\{q\}$	Heat source vector (FEM)
r	Radius
R	Reflectivity
R_a	Surface roughness (arithmetic average of profile deviations from the mean)
R_{coeff}	Reflection coefficient

$[S]$	Stiffness matrix (FEM)
t	Time
T	Temperature
$\{T\}$	Temperature vector (FEM)
u	Displacement
$\{U\}$	Displacement vector (FEM)
v	Velocity
v_L	Longitudinal wave velocity
v_T	Transverse wave velocity
v_R	Rayleigh wave velocity
V	Volume
Z	Acoustic impedance
w	Laser beam radius
α	Coefficient of linear thermal expansion
β	Heat per unit volume per unit time
γ	Absorption coefficient
Γ	Phase difference
ε_{ii}	Elastic strain component
E	Electric field
Θ	Half-angle of divergence
κ	Thermal diffusivity
λ	Elastic wavelength
λ_{opt}	Optical wavelength
μ_r	Relative permeability
μ_0	Permeability of free space = $4\pi \times 10^{-7}$ H m^{-1}
ν	Poisson's ratio
ξ	Rate of material removal
ρ	Density
σ	Electrical conductivity
σ_{ii}	Elastic stress component
τ	Pulse duration
φ	Phase
Φ	Scalar potential

Ψ	Vector potential
ω	Electromagnetic frequency
cos	Cosine function
d	Derivative operator
exp	Natural exponential function
i	Imaginary number = $\sqrt{-1}$
ierfc	Integral error function
sin	Sine function
δ	Infinitesimal quantity
Δ	Finite change in quantity
∂	Partial derivative operator
∇	Vector derivative operator
Al	Aluminium
ALM	Additive Layer Manufacturing
BRU	Basic Resolution Unit
CAD	Computer Aided Design
CFPI	Confocal Fabry-Perot Interferometer
CLS	Constant Laser Separation
CW	Continuous-Wave
DMD	Direct Metal Deposition
DOF	Depth Of Focus
EMF	Electromotive Force
FEA	Finite Element Analysis
FEM	Finite Element Method
FFT	Fast Fourier Transform
FWHM	Full Width Half Maximum
GTAW	Gas Tungsten Arc Welding
LASER	Light Amplification by Stimulated Emission of Radiation
LENS	Laser Engineered Net Shaping
LMD	Laser Metal Deposition
NA	Numerical Aperture

Nd	Neodymium
NDT	Non-Destructive Testing
PREP	Plasma rotating electrode process
SLD	Scanning Laser Detection
SLM	Selective Laser Melting
SNR	Signal-to-Noise Ratio
SSL	Sub-Surface Longitudinal
TEM	Transverse Electromagnetic Mode
Ti	Titanium
TWM	Two-Wave Mixing
YAG	Yttrium Aluminium Garnet

Chapter 1: Introduction

1.1. Research Rationale

Additive Layer Manufacturing (ALM) refers to various material processes by which solid metal parts are deposited layer-by-layer onto a substrate, compared to traditional manufacturing which relies on subtractive machining. ALM has seen interest in the aerospace industry as it allows for the manufacture of complex structures and has the potential to reduce material wastage. Of particular interest in this research is an ALM process called Laser Metal Deposition (LMD), in which structures a built-up by the addition of powdered material onto localised melted areas facilitated by a laser beam.

Quality assurance is an important aspect of aerospace manufacturing – parts must satisfy high quality standards in order to meet the requirements of the intended use. A fully dense structure is essential in aerospace components which experience high temperatures and stress so that premature failure can be avoided. Non-Destructive Testing (NDT) refers to a range of techniques for examining a structure in a non-damaging manner in order to detect and characterise flaws which might compromise its performance or safety. In-process inspection enables monitoring of quality as a part is built so that corrective actions can be taken if a flaw is detected; furthermore, there is the potential to identify the cause of structural flaws and improve the manufacturing process.

There are currently no commercially available NDT techniques for the in-process validation of LMD structures; most traditional inspection methods are either only useful after a part has been manufactured, or otherwise not physically suited to installation into a working LMD system. For example, X-ray Computed Tomography has been used in the characterisation of volumetric defects in deposited structures [1] [2], but requires access to both sides of the structure under evaluation and has inherent radiation hazards; furthermore, post-processing is required to resolve acquired data so the method is not suitable for real-time monitoring. Piezo-electric probes can produce high frequency ultrasound but require contact with the surface of a test sample via a contact medium such as gel. The footprint of such probes is also much larger than that required in this project and an inherent dead zone prevents inspection directly beneath a surface. Eddy current testing is non-contact and capable of real-time inspection but has proven limited to the detection of flaws with volume no smaller than 1 mm^3 [3].

Laser ultrasonic testing has been identified as the most appropriate NDT technology for the evaluation of deposited structures and integration into an LMD platform. Its advantages specific to this project can be summarised as follows:

Table 1.1. Reasons for selecting laser ultrasonic testing as an inspection method.

Property of Laser Ultrasonic Testing	**Advantage for On-line Inspection of LMD**
Non-contact – remote generation and detection of ultrasound.	Deployment on high temperature and moving surfaces is possible.
Small footprint – typically less than 1 mm^2 area on the test surface.	Inspection of thin structures and deployment on small surfaces areas is possible.
Generated ultrasound is high frequency and covers a broad spectrum.	Small features and microstructural flaws can be detected.
Surface ultrasonic waves are produced and propagate along boundaries.	Surface and near-surface inspection is possible.

1.2. Work Objectives

The aims of the work reported in this thesis are to investigate capabilities of laser ultrasonic testing for the identification and characterisation of discontinuities, and to carry out a trial of the integration of the aforementioned inspection method in a working LMD manufacturing environment. In all the work carried out, Inconel 718 alloy will be the choice of material as a medium for investigation. This particular super-alloy has seen widespread use in aero-engines due to its ability to withstand corrosion and deformation and generally maintain its material properties under conditions of high temperature and pressure. A review of literature will be presented in order to understand the formation processes and likelihood of occurrence of microstructural flaws in parts manufactured by LMD, and to summarise the typical properties of such flaws. The following objectives have been set in order to achieve the aims of this work:

i. The creation of two-dimensional and three-dimensional numerical models to facilitate the simulation of ultrasound generation and propagation via a coupled thermal-

mechanical interaction. Geometries will be selected to correspond to typical microstructural LMD flaws as identified through literature review.

ii. To analyse simulated ultrasound propagation and interaction with flaw geometries in order to identify wave signals revealing quantitative information about location and size.

iii. To select and set-up off-the-shelf laser equipment for the purpose of generating ultrasound and receiving ultrasonic surface displacements, and computer equipment for recording received data, suitable for use in laboratory and industrial environments.

iv. To select and manufacture test pieces with artificial flaws inserted corresponding as closely as physically possible to typical microstructural LMD flaws.

v. To conduct laboratory-based off-line sensitivity tests and calibration on the test pieces, applying laser ultrasonic testing techniques as already identified and analysing the capabilities of flaw identification and sizing techniques.

vi. To carry out a trial integration of laser ultrasonic testing and data acquisition equipment into a working LMD system in order to carry out on-line transmission and reception of ultrasound on a relevant LMD part.

vii. To provide analysis of the limitations met and provide recommendations for future work.

1.3. Thesis Structure

This thesis presents the theoretical, finite element and experimental analysis of the capabilities of laser ultrasonic testing in the detection and characterisation of sub-surface voids in order to assess the feasibility of applying the technology to on-line quality control in the LMD manufacturing process. The practicalities of installing and operating the necessary equipment in a working LMD system are also considered.

Chapter 2 presents a fundamental review of the theory and application of laser ultrasonic testing. Several theoretical aspects are covered including laser devices and propagation, ultrasonic wave generation by the irradiation of a solid material by pulsed laser light, propagation of ultrasonic waves through solid media, and measurement of ultrasonic surface displacements by interferometry. This is followed by a literature review of the use of laser ultrasonic testing for the detection of material flaws, with a focus on ultrasonic surface waves.

Chapter 3 provides an introduction to the development and advantages of ALM followed by a more detailed summary of the LMD process. A detailed literature review, in the context of quality assurance of LMD manufacturing, provides a qualitative and quantitative overview of reported microstructural flaws in deposited structures and the current state of research into on-line testing of LMD components.

Chapter 4 details work carried out using Finite Element Analysis (FEA), starting with relevant Finite Element theory linked with knowledge of laser beam thermal-mechanical interaction with solid materials in order to provide a basis for model set-up and input parameters. Ultrasonic wave propagation is observed in 2D using geometries matching the real test pieces to simulate interaction with artificial flaws, and extended to 3D to consider wave interaction with realistic flaws as detailed in literature. The output surface displacements are analysed in the time domain to determine indications of flaw location and wave signal features which vary with geometry.

Chapter 5 details laboratory experiments of laser ultrasonic testing on manufactured test pieces with sub-surface voids of varying depth and diameter in order to validate FEA results and evaluate the effect of real conditions on identified indication signals. The equipment specifications, laboratory set-up, and test methods are explained with capabilities defined in terms of established theory. Results are analysed in the time and frequency domains to determine indications of flaw presence and size which could be useful in the context of on-line inspection.

Chapter 6 reports on a trial integration of a laser ultrasonic testing system into a working LMD environment. Consideration is given to safety requirements and space limitations in the installation of necessary equipment. Limitations in the efficacy of the applied inspection technique are assessed and recommendations given for further development.

Chapter 2: Review of the Fundamental Theory and Application of Laser Ultrasonic Testing

2.1. Introduction

NDT methods are of great importance across all sectors of engineering and infrastructure – in its many forms, it facilitates the inspection of whole parts and can be applied during or immediately after manufacture and also whilst a part is in service. The purpose of NDT is to reveal information about the internal or external structure of a part under investigation so that potential flaws in the material can be identified and actions taken to mitigate their impact on performance by repair or replacement. Ultrasonic testing is a widely used NDT technique in which an ultrasonic acoustic wave is transmitted into a test-piece via one or more surfaces, propagates through its volume whilst interacting with material features and discontinuities, and is then received at one or more surfaces to be displayed and/or recorded. The resulting ultrasonic wave signals may be analysed by a skilled operator in order to identify flaw indications. Many technologies exist to facilitate the transmission and reception of ultrasonic waves, taking advantage of mechanical, electrical, and magnetic interactions in target materials.

Since their invention and rapid development in the 1960s [4], lasers have found use in a wide range of applications in science and engineering. Laser-based ultrasonic testing has been developed over several decades and has seen a lot of research into its effectiveness as an NDT technique due to its many advantages compared to established technologies as listed in Section 1.1. Examples of the application of laser ultrasonic testing are numerous, illuminating the scope of academic and industrial interest, and include: the inspection of complex-shaped composite structures on an in-service military aircraft to measure thickness variation in panel sections and joints [5]; dynamic inspection of rails and train wheels to find defects usually missed by existing techniques and on sections with limited accessibility for contact methods [6]; and long-distance generation of ultrasonic waves in wind turbine blades for damage visualisation and development of automated, remote inspection at operational wind farms [7].

The generation of ultrasound is facilitated by a laser beam which irradiates the surface of a test sample in a short pulse, producing both surface and bulk ultrasonic waves in a thermal-mechanical interaction (see Section 2.5). One type of ultrasonic wave of particular interest in this research is the Rayleigh wave, which travels along the surface of the test sample and

penetrates the material to a depth approximately equal to its wavelength (see Section 2.4.1). This wave type is therefore potentially useful in detecting defects which exist at or within the depth of a single powder-LMD layer, typically 200 to 750 μm (see Section 3.2.1). The following sections will cover the scientific theory necessary to describe the physical processes and technical operation of hardware relevant to work reported in later Chapters.

2.2. Laser Basics

2.2.1. Light Amplification by Stimulated Emission of Radiation

L.A.S.E.R. is an acronym for Light Amplification by Stimulated Emission of Radiation and describes a device which produces a monochromatic beam of photons with a wavelength between the infrared and ultraviolet parts of the electromagnetic spectrum – in general usage, the word 'laser' describes this kind of device. Light is a form of electromagnetic radiation which behaves as a wave but can also be described as being composed of discrete packets of energy called photons – this phenomenon is referred to as wave-particle duality and is one aspect of quantum theory.

Atoms, made up of one or more electrons orbiting a central nucleus of protons and neutrons, are also described in terms of discrete energy levels. This knowledge is essential for understanding the basic principles of laser operation. An atom can exist in a series of excitation states, each characterised by a discrete electron energy level. The lowest energy level is the ground state, and an electron may undergo a transition to a higher energy level by the absorption of electromagnetic energy, bringing the atom to a higher excitation state. The absorption of a photon with energy equal to the difference between two excitation states will cause such a transition. The reverse of this process is emission, whereby an atom will emit a photon of corresponding energy as an electron transitions from a higher to a lower energy level. The energy of an absorbed photon is given by the equation [8]:

$$h\omega = E_x - E_0 \tag{2.1}$$

where h is Planck's constant, ω is frequency of the electromagnetic field, E_x is the energy level of the high excitation state, and E_0 is the energy level of the ground excitation state. An atom in normal conditions with a well-populated ground state has a high probability of absorption. The introduction of an electromagnetic field causes the transition of an atom to a higher excitation state, such that a higher energy level becomes populated with electrons. This process is known as pumping. Population inversion occurs as a higher energy level

becomes more populated with electrons than a lower, intermediate level. In these conditions, the incidence of electromagnetic radiation causes the emission of photons as electrons transition to a lower energy level. This process is known as stimulated emission (Figure 2.1) and produces laser light at a frequency determined by Equation (2.1), with the frequency of the pumping photons being necessarily higher than that of the emitted photons.

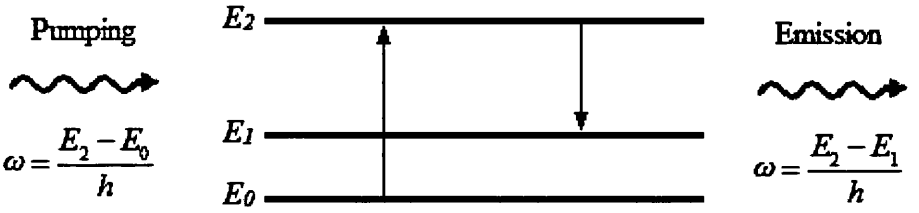

Figure 2.1. Illustration of the process of stimulated emission. Electron transitions are represented by vertical arrows.

The atomic structure and sequence of transitions in a lasing medium can be more complex than described above, although the principle of stimulated emission remains unchanged. Emitted photons have the same energy and wavelength, and are in phase. Therefore laser light is formed of monochromatic, coherent electromagnetic radiation and propagates in a singular directional beam. In order to produce laser light of sufficient intensity, defined by energy flux per unit area and time, the emitted photons must be kept in a feedback system before release. This is achieved by placing a mirror at each end of the length of the lasing medium such that electromagnetic radiation oscillates due to reflection. On each pass through the medium, further emission is stimulated and intensity increases as long as optical pumping continues. This configuration is called a resonator cavity. Release of laser light is enabled by the manufacture of a transmitting aperture in one of the mirrors [8].

2.2.2. Solid State Lasers

A solid state laser consists of a cylindrical prism-shaped solid crystalline lasing medium acting as a host lattice. Optically active ions, consisting of atoms with fewer electrons than protons and thus net positive electric charge, are dissolved in the host lattice by replacing a chemically similar element. The concentration of replacement, or dopant, ions only needs to be a few per cent in order to achieve a higher density of excited atoms than in the gain medium of a gas laser [9]. A common example of a replaceable host element is yttrium. Rare-earth metal ions form a group of elements which are used a replacement for yttrium in the host lattice. One type of solid state laser uses a neodymium (Nd^{3+}) ion dissolved within an

yttrium aluminium garnet ($Y_3Al_5O_{12}$) host lattice to form an Nd:YAG laser. Here, the numbered superscript notation for the ion represents net charge. This arrangement forms a four-level energy system which facilitates optical emission (Figure 2.2). Optical pumping excites electrons from the $^4I_{9/2}$ level to the $^4F_{5/2}$ level, which quickly transition to the lower $^4F_{3/2}$ level. Since the $^4I_{11/2}$ level is also de-excited quickly, a population inversion takes place. High electron population builds up in the $^4F_{3/2}$ level, followed by slower transition to the $^4I_{11/2}$ level and thus optical emission at a wavelength of 1064 nm [9]. The energy level labels refer to standard electron configuration notation used in chemistry.

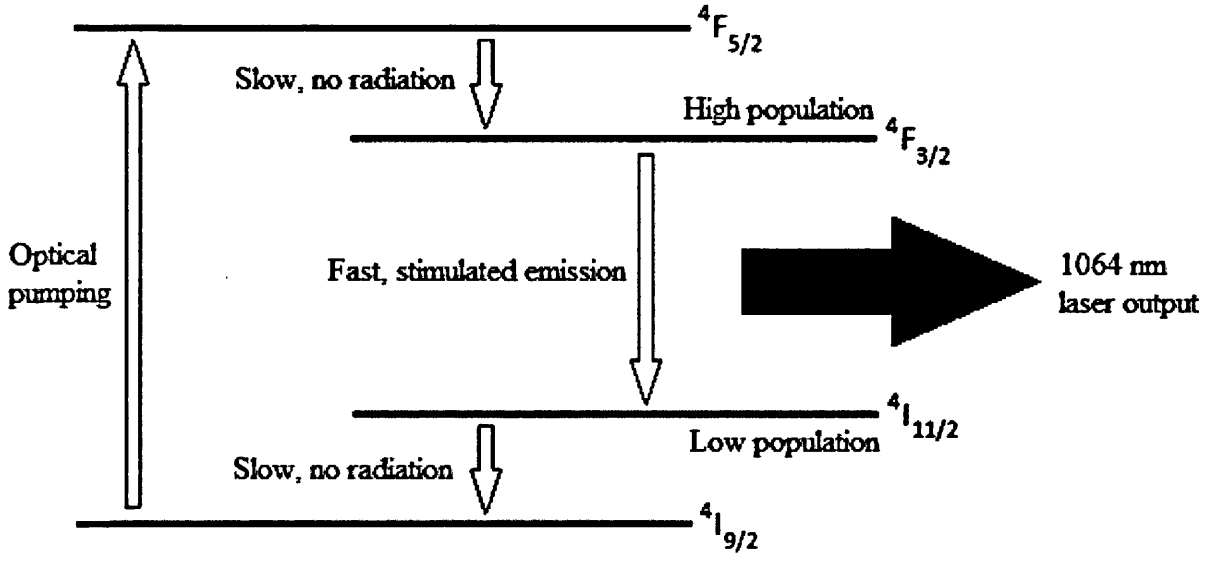

Figure 2.2. Four-level electron energy system of a solid state Nd:YAG laser. Electron transitions are represented by vertical arrows.

A common source of pumping used in solid state lasers is a flash-lamp, which consists of a gas-filled sealed glass tube containing electrodes at each end. A capacitor stores electrical energy to supply to the electrodes, generating electromagnetic energy. In Nd:YAG lasers, the flash-lamp is commonly placed parallel to the lasing medium with matching length to achieve uniform pumping. These components may also be contained inside a chamber with reflective sides to direct maximum electromagnetic energy to the lasing medium [10].

2.2.3. Laser Pulsing

Continuous laser output is appropriate for many industrial applications such as cutting and welding. In laser ultrasonic testing, it is advantageous to be able to output a short pulse of electromagnetic energy, on the order of nanoseconds, as this enables the generation of high frequency ultrasonic waves without too high a build-up of heat at the irradiated surface of a

test piece. This is explained further in Section 2.5. In a laser device, electron population inversion is built up by optical pumping until a threshold is reached in the lasing medium and stimulated emission begins. The system then returns to its equilibrium state in the absence of pumping. In a neodymium laser, the damping in photon emission occurs fast enough that the laser output power follows the pumping de-activation [9].

Q-switching is a method of producing a pulsed laser output and utilises a property of the resonator cavity called the Q-factor, which is a dimensionless measure of the energy loss as light propagates through the length of the cavity. The Q-factor value is inversely proportional to energy loss. A Q-switch device consists of a variable attenuator which is positioned within the resonator cavity and provides a means to control the Q-factor. The process of generating a pulsed laser output begins by decreasing the Q-factor, and therefore increasing attenuation, thus preventing stimulated emission whilst the lasing medium is continually pumped. Population inversion continues and energy is stored up to a saturation or gain limit of the medium. A sudden increase in the Q-factor allows stimulated emission to commence and the stored energy is quickly released in a pulse of electromagnetic energy.

2.2.4. Laser Beam Propagation

Light can be considered to be an electromagnetic wave composed of an electric field and a magnetic field, which propagate perpendicular to each other in a direction k and at 90 degrees out of phase (equal to one quarter of a wavelength) [11]. In a stable resonator cavity, light is concentrated around the axis of propagation and resonates in one of a series of Transverse Electromagnetic Modes (TEM) determined by the radius of curvature and separation of the opposite mirrors [12]. These modes are characterised by the distribution of output beam intensity along the two transverse axes of the beam cross-section, which can be approximated to a corresponding Hermite-Gaussian distribution in space. Distribution is equal along each axis, resulting in an axially symmetric beam. Each mode is described as TEM_{mn}, where the indices n and m refer to the number of intensity minima in the direction of electric and magnetic field oscillation, respectively.

The fundamental TEM_{00} mode produces an intensity of approximately Gaussian spatial distribution which is ideal for many applications as this provides the greatest power density within a single area at the location of laser irradiation. The maximum intensity I_0 exists at the centre of a Gaussian beam and is related to the total power $P(\infty)$ by [12]:

$$I_0 = P(\infty)\left(\frac{2}{\pi w^2}\right) \tag{2.2}$$

where w is the beam radius, along both transverse axes, where intensity falls to $1/e^2$ (approximately 13.5 %) of its peak [13]. The wave-front of an output beam increases in two dimensions as it propagates: in its radius and in the curvature of its wave-front. According to diffraction theory, if a Gaussian beam with an initially flat wave-front propagates along an axis z, it would expand as follows [12]:

$$R(z) = z\left(1+\frac{\pi w_0^2}{\lambda_{\text{opt}} z}\right)^2 \tag{2.3}$$

$$w^2(z) = w_0^2\left(1+\frac{\lambda_{\text{opt}} z}{\pi w_0^2}\right) \tag{2.4}$$

where $R(z)$ is the radius of curvature of the wave-front, z is the position along the axis of propagation, λ_{opt} is the wavelength of light, $w(z)$ is the beam radius, and w_0 is the minimum beam radius at $z = 0$, also known as the beam waist. For a large value of z, known as the far-field, Equations (2.3) and (2.4) approach the following values:

$$R(z) = z \tag{2.5}$$

$$w(z) = \frac{\lambda_{\text{opt}} z}{\pi w} \tag{2.6}$$

Simultaneously, the beam radius approaches an asymptotic cone originating from $z = 0$ with angular radius:

$$\theta_{\text{far}} = \frac{w(z)}{z} = \frac{\lambda_{\text{opt}}}{\pi w} \tag{2.7}$$

where θ_{far} is the angular radius in the far-field and is equal to the half-angle of beam divergence. Thus in the far-field, divergence can be considered a fixed value. For a real laser, the beam quality might be affected by misalignments in the output apparatus causing higher modes to appear [14]. Such imperfections in the beam are quantified by a dimensionless value M^2 which is defined as [15]:

$$M^2 = \frac{\theta_{\text{far}} w_0 \pi}{\lambda_{\text{opt}}} \tag{2.8}$$

Thus Equation (2.7) must be multiplied by M^2 to take into account beam quality. In the near-field, immediately adjacent to the beam waist position along the z axis, the divergence angle increases by a factor of $\sqrt{2}$ up to a value of z given by a combination of Equations (2.3) and (2.4) [12]:

$$z_R = \frac{\pi w_0^2}{\lambda_{opt}} \tag{2.9}$$

where z_R is the Rayleigh range.

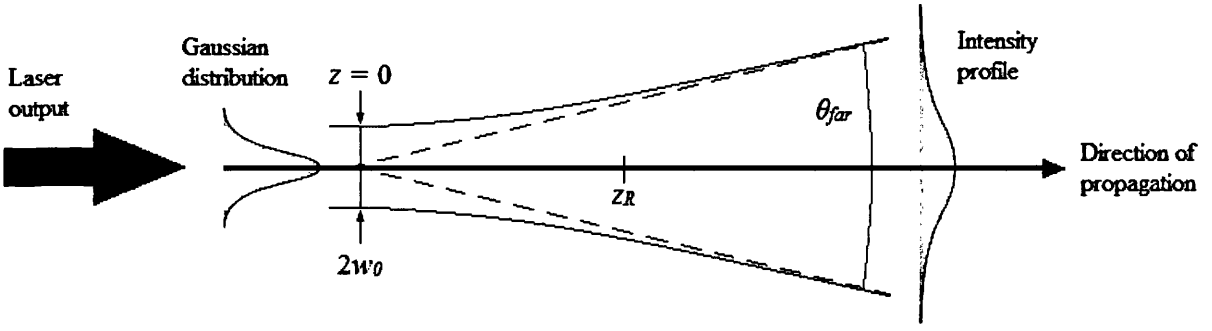

Figure 2.3. Propagation and distribution of a Gaussian beam from laser output to the far-field.

Polarisation is a property of laser light which refers to the path followed by the electric field vector as it propagates in time and space. In the context of the hardware to be used in this work, it is useful to consider first the linearly polarised state of laser light, in which the electric field oscillates about the axis of propagation in a single plane:

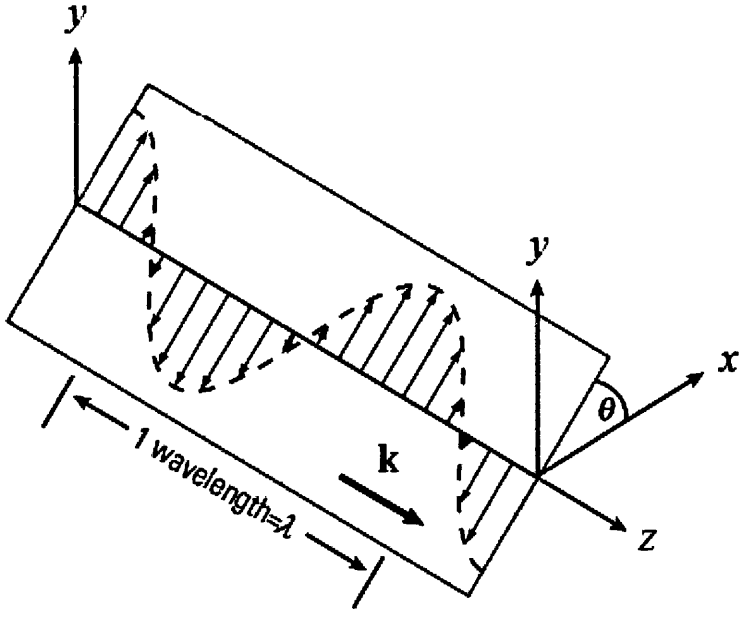

Figure 2.4. Illustration of electric field propagation using a Cartesian co-ordinate system [16].

In a Cartesian co-ordinate system, if the propagation direction is parallel to the z-axis, the two orthogonal components E_x and E_y are parallel to the x and y axes respectively. The electric field can be described mathematically in terms of these components [11]:

$$E = E_x \cos(\omega t - k \cdot z) + E_y \cos(\omega t - k \cdot z) \tag{2.10}$$

where ω is angular frequency (equal to $2\pi c/\lambda_{opt}$ where c is the speed of light), t is time, and k is wavenumber (equal to $2\pi/\lambda_{opt}$). The magnitudes of the two components of the electric field are given in terms of the angle θ of the oscillation plane with respect to one reference axis, also referred to as the polarisation angle (Figure 2.4):

$$|E_x| = |E| \cos\theta \tag{2.11}$$

$$|E_y| = |E| \sin\theta \tag{2.12}$$

Thus for a linearly polarised laser beam, these components are in phase, meaning that concurrent cycles of both E_x and E_y are synchronised in time. Circular polarisation describes the movement of the electric field vector in time in the case that the x and y components are equal in magnitude, i.e. two linear waves oscillating on separate planes orthogonal relative to each other, and out of phase by 90 degrees such that one component reaches maximum magnitude when the other is at zero. The electric field vector thus follows a circular path in space, forming a helix shape as time advances. The electric field for a circularly polarised wave is given by [11]:

$$E = E_x \cos(\omega t) + E_y \sin(\omega t) \tag{2.13}$$

2.3. Optical Elements

The experimental setup described in Chapters 5 and 6 make use of a range of optical elements which are necessary for manipulating and delivering laser beams for their intended purpose. This section provides an overview of the relevant components and the associated light theory.

2.3.1. Wave Plate

The polarisation state of a laser beam can be altered by propagation through a birefringent crystal which, due to the arrangement of atoms in the crystal structure, contains an axis with a smaller refractive index than the other two axes. This is referred to as the optical axis. A phase delay is introduced between the two components of an incident beam depending on the orientation of its linear polarisation relative to the optical axis of the crystal: the extra-

ordinary component E_e is characterised by a refractive index n_e and travels with speed c/n_e, and the ordinary component E_o is characterised by a refractive index n_o and travels with speed c/n_o. After propagation through the crystal, the beam will exhibit a phase difference between its respective components given by [11]:

$$\Gamma = \frac{2\pi}{\lambda_{opt}}(n_e - n_o)d_{opt} \tag{2.14}$$

where d_{opt} is the length of the propagation path of the light within the crystal. An optical element constructed from a birefringent crystal is called a wave plate. From Equation (2.14), it can be seen that the thickness of a wave plate, equal to d_{opt}, is proportional to the induced phase delay. A half-wave plate is an element with thickness chosen to produce π radians (180 degrees) of phase difference. This configuration has the effect of inverting the polarisation angle of a linearly polarised beam relative to the optical axis [11]:

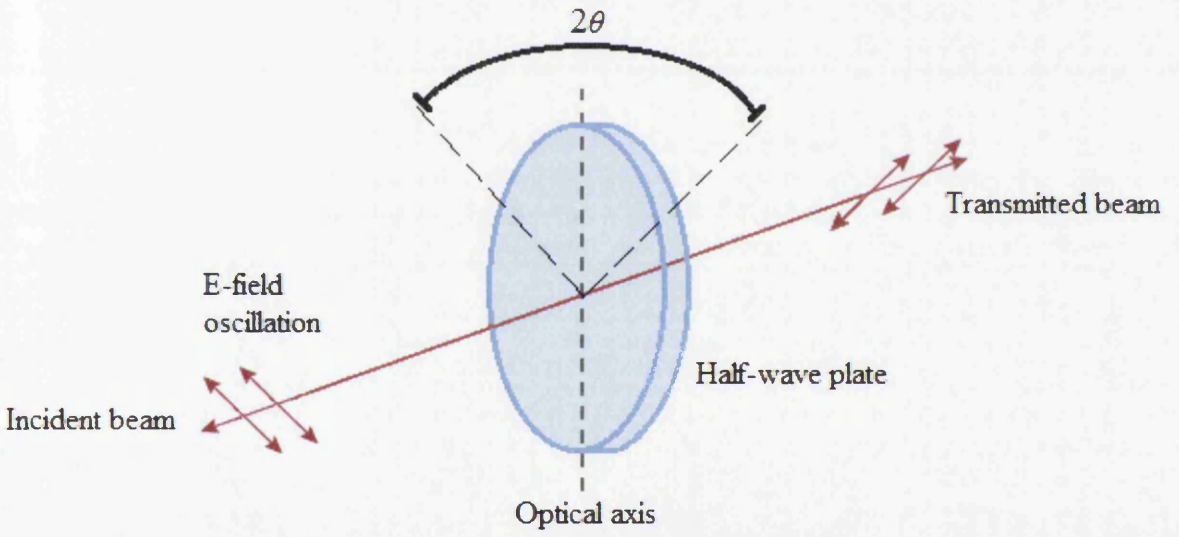

Figure 2.5. Propagation of a linearly polarised laser beam through a half-wave plate, displaying change in beam orientation due to rotation of the wave plate by an angle of θ.

2.3.2. Beam-Splitter

A beam-splitter is an optical element which splits a single incident laser beam into two separate beams with a variable ratio of intensity. A common type of beam-splitter is a cube consisting of two right angled glass prisms adhered along the hypotenuse sides using transparent cement. In order to create a polarising beam-splitter, this interface can be coated with a dielectric material which serves to simultaneously reflect and transmit an incident linearly polarised beam in a ratio depending on the orientation of wave oscillation relative to

the plane of incidence (Figure 2.6). It is common to refer to the incident beam as *p*-polarised if its oscillation is oriented parallel to the plane of incidence or *s*-polarised if its oscillation is oriented perpendicular. The former is transmitted while the latter is reflected, with a variable split for intermediate beam orientations.

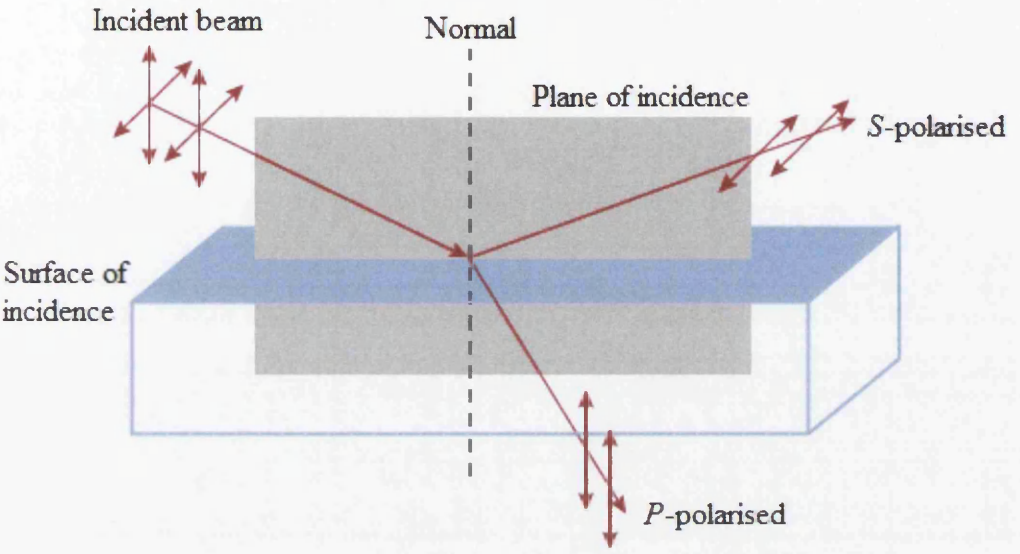

Figure 2.6. Schematic diagram of beam-splitting due to a dielectric coated surface and notation of incident beam polarisation.

Variable power split can be achieved using a combination of the optical elements described above. For a linearly polarised laser beam propagating through a half-wave plate and then a beam-splitter cube, rotating the wave plate about its optical axis will correspondingly rotate the oscillation plane of the beam incident on the cube and in turn alter the power split ratio of the reflected and transmitted beams.

2.3.3. Fibre Cable

Laser beams propagate in free-space in the direction in which emission takes place. A beam can be guided as desired by the use of mirrors or an optical fibre; the latter consists of a thin cylinder of glass or plastic surrounded by a cladding material with a lower refractive index than that of the core material. The refractive index for a particular medium, denoted by n, is a ratio of the speed of light in a vacuum to the speed of light in that medium. The behaviour of a beam of light propagating through the interface between two regions of dissimilar refractive index can be described using Snell's Law [17]:

$$n_1 \sin\theta_i = n_2 \sin\theta_2 \tag{2.15}$$

where n_1 is the refractive index in medium 1, n_2 is the refractive index in medium 2, θ_1 is the angle of incidence, and θ_2 is the angle of refraction. In the following example, a beam of light is incident on an interface and originates from medium 1, which has a higher refractive index than medium 2. In Figure 2.7.a, the incident beam has an angle less than a critical value θ_c as measured from the normal for which Snell's Law predicts a 90 degree angle of refraction, also measured from the normal. In this case, the beam is partially reflected and partially refracted. In Figure 2.7.b, the angle of incidence is increased to θ_c and Equation (2.15) can thus be evaluated:

$$n_1 \sin\theta_1 = n_1 \sin\theta_c = n_2 \sin 90$$

$$\theta_c = \sin^{-1}\left(\frac{n_2}{n_1}\right) \tag{2.16}$$

In this case, the beam is partially reflected and the previously refracted part propagates along the interface. In Figure 2.7.a, the angle of incidence is greater than the critical angle, leading to total internal reflection of the beam.

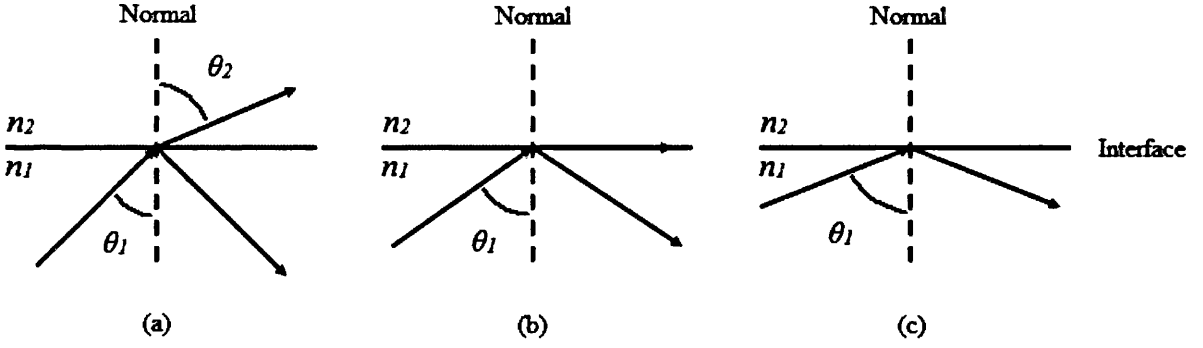

Figure 2.7. Schematic diagrams of reflection and refraction of light at an interface between dissimilar materials with varying angle of incidence: (a) $\theta_1 < \theta_c$, (b) $\theta_1 = \theta_c$, (c) $\theta_1 > \theta_c$.

Light travels through the central core of a fibre cable by the principle of total internal reflection. For a beam entering the aperture at one end of a fibre cable (Figure 2.8), the largest incident angle relative to the aperture normal for which total internal reflection can occur is referred to as the acceptance angle, Θ, also the half-angle of divergence.

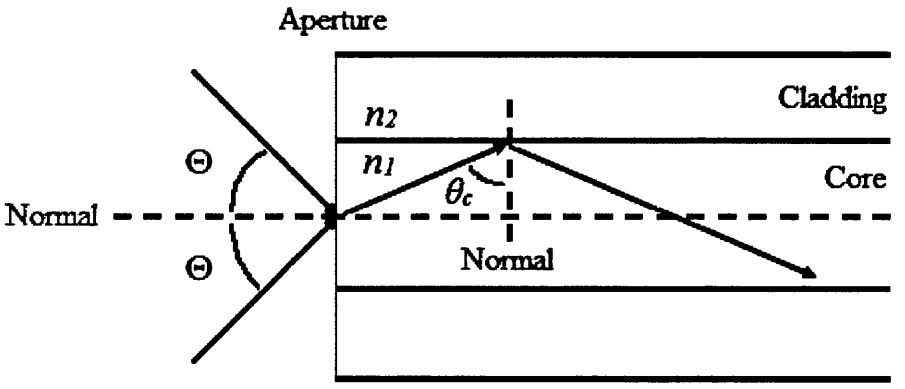

Figure 2.8. Schematic diagram of a laser beam entering and propagating through a fibre cable.

The Numerical Aperture (NA) of a fibre cable can be calculated as [18]:

$$\mathrm{NA} = \sin\Theta = \sqrt{n_1^2 - n_2^2} \tag{2.17}$$

The value of NA for any particular fibre cable is fixed; therefore a guided laser beam exits the aperture at the other end of the cable with the same angle Θ. Such a beam would be divergent, meaning that the diameter of the beam expands as it propagates through space.

2.3.4. Lens

For the applications considered within this work, it is essential that laser beams are collimated (of a constant diameter) and thus do not diverge within the short distances over which the beams are to be delivered and collected. Light propagating through a lens undergoes refraction at either or both of the two surfaces of the lens if the direction of propagation is not normal relative to the surface; thus for a curved surface the angle of refraction varies.

A plano-convex lens consists of a piece of a circular glass element with one spherical face and one flat face. The focal length F represents the distance, measured from the centre of the lens thickness, at which a beam entering the flat face of the lens is refracted such that it converges to a point. Collimation of a divergent beam is achieved through the reverse of this process. With a known beam divergence, a plano-convex lens with the correct diameter, radius of curvature, refractive index, and thickness can be chosen in order to collimate the beam. In the case of collimating a ray of light diverging from a source (Figure 2.9), the radius of the fibre core represents the height of the source y_1 and the half-angle θ_1 of the incident beam is equal to α.

Using these values, the radius y_2 and divergence θ_2 of the collimated ray can be calculated [19]:

$$y_2 = \theta_1 F \tag{2.18}$$

$$\theta_2 = \frac{y_1}{F} \tag{2.19}$$

Thus a beam shaped in the manner described above would not be truly collimated, but rather would have a relatively small divergence which may be negligible depending on the intended application.

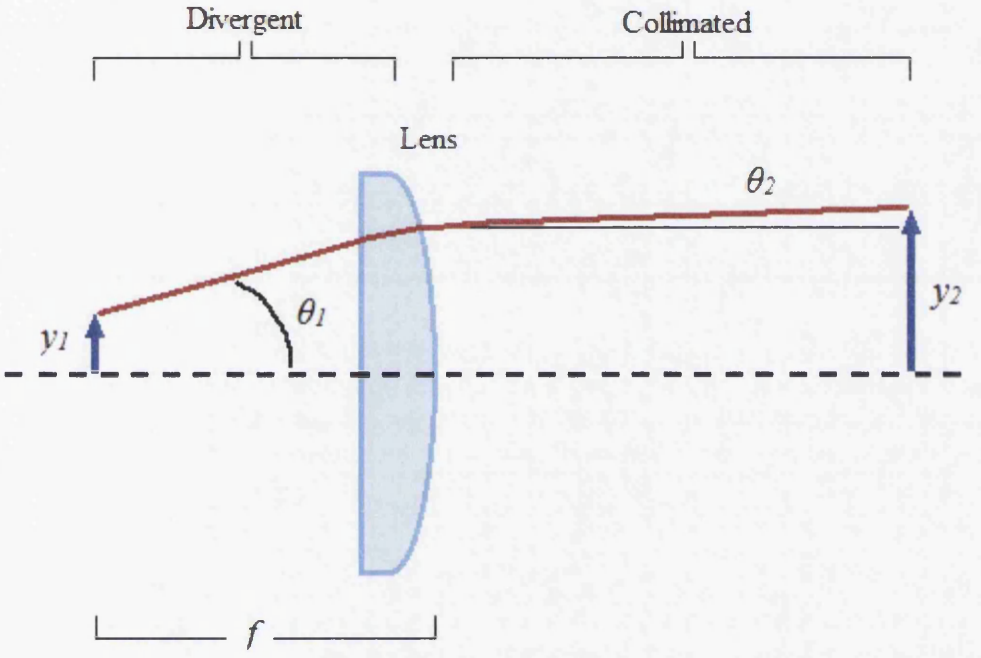

Figure 2.9. Schematic diagram of the collimation of a divergent light ray using a plano-convex lens (also applicable to focusing a collimated beam).

The addition of a plano-convex lens in the propagation path of the collimated ray of light, flipped horizontally, would have the effect of focusing the beam to a point of finite radius. It can be deduced from Equations (2.18) and (2.19) that there is a fundamental limit to the minimum spot size when evaluated using ray optics due to diffraction. For a Gaussian beam, the focused spot size w_F and depth of focus (DOF) are calculated in terms of the collimated beam and focusing lens parameters [20]:

$$w_F = \left(\frac{4\lambda_{opt}}{\pi}\right)\left(\frac{F}{D}\right) \tag{2.20}$$

$$DOF = \left(\frac{8\lambda_{opt}}{\pi}\right)\left(\frac{F}{D}\right)^2 \quad (2.21)$$

where D is the diameter of the collimated beam. DOF is defined as the length contained on either side of the focal point where $w > \sqrt{2}w_F$ and is analogous to the Rayleigh range defined in Equation (2.9).

2.4. Ultrasound and Ultrasonic Testing Basics

2.4.1. Ultrasonic Wave Propagation in Elastic Solids

Sound is a form of mechanical energy that propagates in waves through a medium, formed by the oscillation of constituent particle about a fixed position. Propagation is supported by the transfer of kinetic energy between adjacent particles. Ultrasound refers to sound with a frequency above 20 kHz, where frequency is a measure of the number of oscillations per second. One period is the time taken for one particle to complete a single oscillation. One wavelength is the distance between successive maxima of a wave. Isotropic elastic solids are able to support the propagation of longitudinal and transverse ultrasonic wave types in their bulk, and surface ultrasonic waves along boundaries.

In longitudinal mode, particles oscillate parallel to the direction of wave propagation in a series of compressions and rarefactions (Figure 2.10). In transverse mode, particles oscillate perpendicular to the direction of wave propagation in a sinusoidal pattern (Figure 2.11). Both of these are referred to as bulk waves as their propagation is supported within the volume of a solid. Transverse waves can only exist in elastic solids due to their rigid particle structure [21].

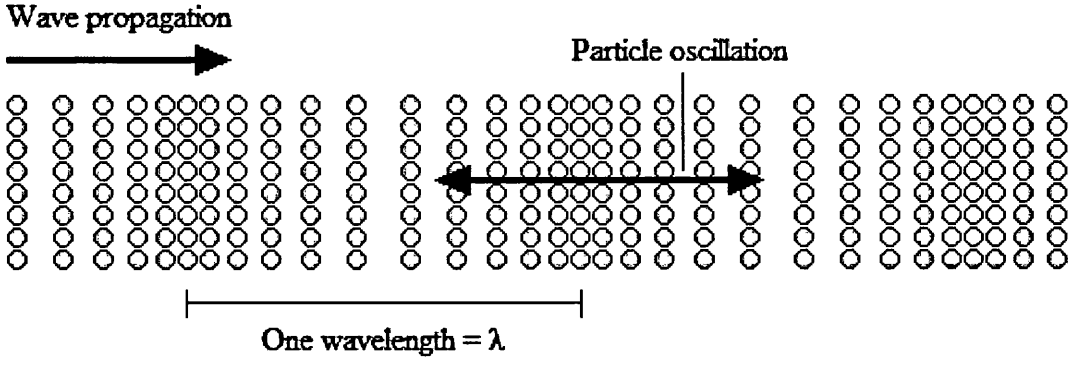

Figure 2.10. Illustration of particles oscillating in longitudinal wave motion.

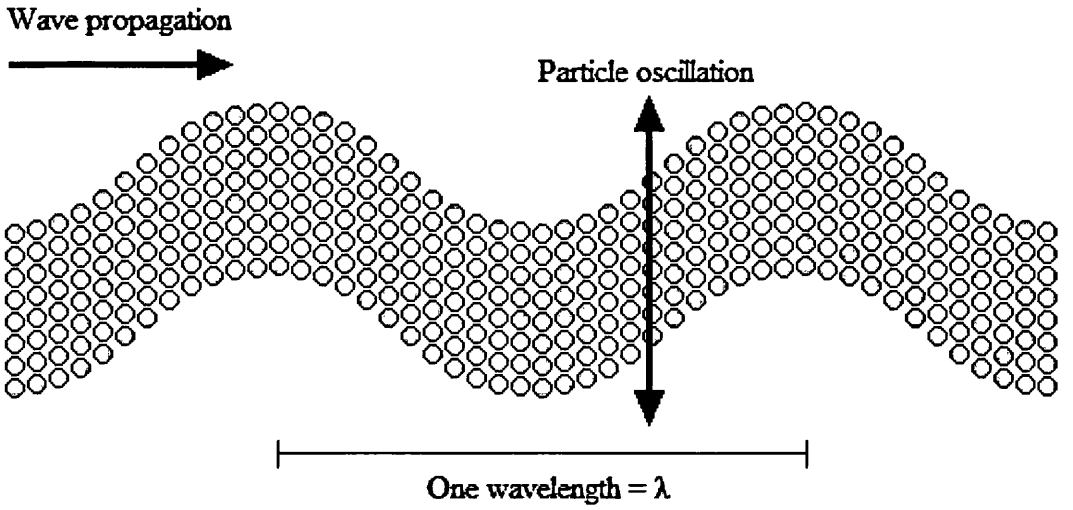

Figure 2.11. Illustration of particles oscillating in transverse wave motion.

Particle displacement in an elastic solid medium can be represented in terms of a scalar potential Φ and a vector potential Ψ [21]:

$$\mathrm{u} = \nabla \cdot \Phi + \nabla \times \Psi \tag{2.22}$$

where u is displacement. These potentials satisfy the following wave equations [21]:

$$\nabla^2 \mathrm{u} - \frac{1}{\mathrm{v}_\mathrm{L}^2} \frac{\partial^2 \mathrm{u}}{\partial t^2} = 0, \quad \text{with } \mathrm{u} = \nabla \Phi \tag{2.23}$$

$$\nabla^2 \Psi - \frac{1}{\mathrm{v}_\mathrm{L}^2} \frac{\partial^2 \Psi}{\partial t^2} = 0, \quad \text{with } \mathrm{u} = \nabla \times \Psi \text{ and } \nabla \cdot \Psi = 0 \tag{2.24}$$

where $\mathrm{v_L}$ is the longitudinal wave velocity and $\mathrm{v_T}$ is the transverse wave velocity. The solutions to these wave equations are given by the following expressions with real and imaginary parts [21]:

$$\mathrm{u} = a_1 \exp\left[-\zeta_\mathrm{L} x\right] * \exp\left[i\left\{k_\mathrm{L} x - ft\right\}\right] \tag{2.25}$$

$$\mathrm{u} = a_2 \exp\left[-\zeta_\mathrm{T} x\right] * \exp\left[i\left\{k_\mathrm{T} x - ft\right\}\right] \tag{2.26}$$

where a_1 and a_2 are arbitrary amplitudes, and ζ represents wave attenuation or energy loss as a function of distance x.

Velocities for longitudinal and transverse waves in isotropic elastic solids are given by [21]:

$$v_L = \sqrt{\frac{E_{mod}(1-\upsilon)}{\rho(1+\upsilon)(1-2\upsilon)}} \tag{2.27}$$

$$v_S = \sqrt{\frac{E_{mod}}{2\rho(1+\upsilon)}} \tag{2.28}$$

where E_{mod} is the elastic modulus, ρ is density, and v is Poisson's ratio. The velocity of a plane wave is related to its frequency and wavelength as follows:

$$v = f\lambda \tag{2.29}$$

Where v is phase velocity, f is frequency, and λ is wavelength. In solid objects, the volume is finite and boundaries exist on all sides of the solid. When a bulk wave is incident on a boundary, there is a reflection at the same angle and part of the wave energy can be refracted following Snell's Law given in Equation (2.15). The proportion of reflected energy for an acoustic wave is given as the reflection coefficient R_{coeff} [22]:

$$R_{coeff} = \frac{(Z_2 - Z_1)^2}{(Z_2 + Z_1)^2} \tag{2.30}$$

$$Z = \rho v \tag{2.31}$$

where Z is the acoustic impedance and medium 1 is the origin medium of the incident wave. At the boundary between a typical metal and air, the difference in acoustic impedance is such that the transmitted energy is negligible.

Along a free boundary, the propagation of surface waves is supported. One type is the Rayleigh wave, in which particles oscillate in two elliptical paths each with a major axis normal to the surface and displacement approximately 1.5 times larger than in the minor axis (Figure 2.12). Closer to the surface, the elliptical motion is retro-grade, such that particle motion at the upper part of the ellipse is opposite to the direction of the wave. Deeper below the surface, the elliptical motion is pro-grade with respect to the direction of wave propagation. The magnitude of particle displacements associated with a Rayleigh wave decay exponentially with depth into the bulk and significant displacements penetrate to a depth approximately equal to one wavelength [8].

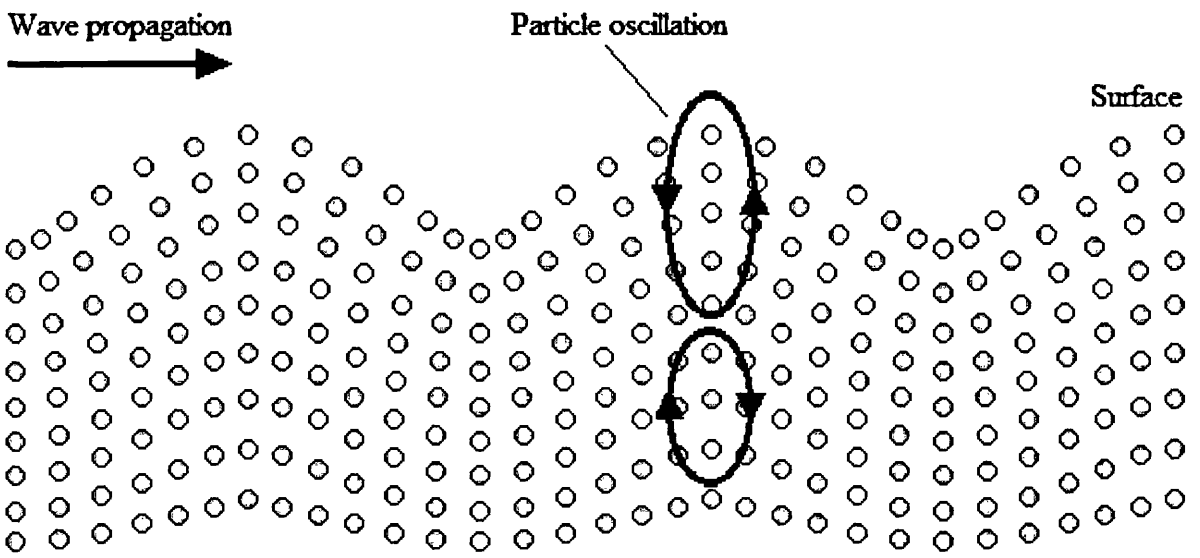

Figure 2.12. Illustration of particles oscillating in Rayleigh wave motion.

The velocity of Rayleigh wave propagation along the surface is given as v_R, which is the root of the following equation [8]:

$$\left(2-\frac{v_R^2}{v_T^2}\right)^2-4\left(1-\frac{v_R^2}{v_L^2}\right)^{1/2}\left(1-\frac{v_R^2}{v_T^2}\right)^{1/2}=0 \tag{2.32}$$

To avoid solving this equation numerically, the following expression gives an approximate value for Rayleigh wave velocity [8]:

$$v_R=\frac{v_T}{1.14418-0.25771\nu+0.12661\nu^2} \tag{2.33}$$

2.4.2. Ultrasonic Testing Basics

In ultrasonic testing, periodic pulses of mechanical energy are transferred into the bulk of a test piece via the surface where the energy propagates in the form of ultrasonic waves. The permanent structure and dimensions of the test object remain unchanged. This is achieved by applying mechanical stresses at a magnitude below that of the test object's elastic limit so that Hooke's Law is obeyed, whereby the ratio of stress to strain is constant. Elastic waves interact at boundaries, such as an edge or a discontinuity. The time of travel and amplitude of the ultrasonic waves after propagation through a test piece can be measured by receiving associated displacements at a surface. Measured displacements are converted to electrical signals to be processed by a computer and displayed for further analysis, where voltage is proportional to pressure in the ultrasonic medium [22]. A wave-form of received voltage as a

function of time is called an A-scan. During a single test, several A-scans can be recorded either continuously or in individual instances as the transmission and/or reception positions are re-located so that two-dimensional sections of a test piece are examined. In this way, multiple A-scans can be displayed in a B-scan or waterfall plot with position as a function of time and amplitude represented virtually in the z-axis by a colour-scale (Figure 2.13).

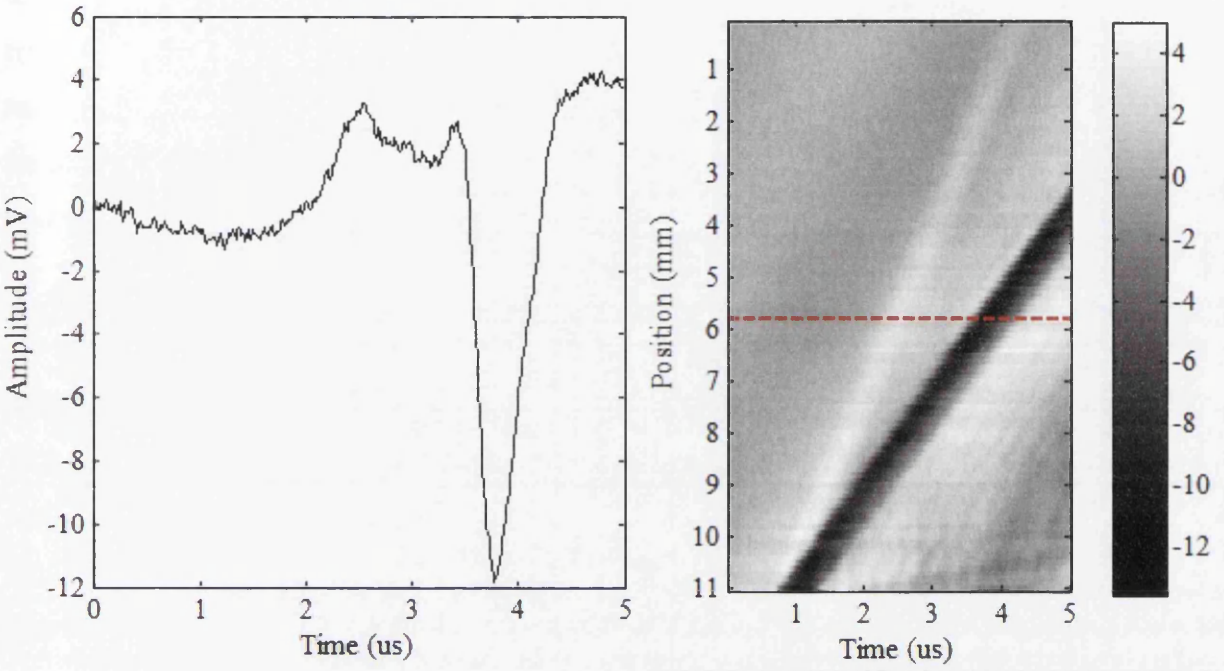

(a) (b)

Figure 2.13. Example of received surface displacement data in the form of (a) an A-scan, and (b) a B-scan with a horizontal line displaying the position of the A-scan (grey-scale in mV).

Information in the received signal can provide indications of ultrasonic wave reflections and changes in amplitude, allowing an operator to evaluate many properties of the test piece including thickness, grain size, elastic modulus, and the location and dimensions of discontinuities due to flaws in the material [22]. Such flaws are the subject of investigation in NDT and there exist several technologies for the purpose of transmitting and receiving ultrasound in solid objects.

The most widely used method of ultrasound generation is by the use of a piezo-electric transducer. A piezo-electric material produces a rapid release of mechanical energy if a potential difference is applied across it. A piezo-electric element contracts and expands in orthogonal directions according to the electric field applied. Conversely, the same element becomes electrostatically charged if pressure is applied to it. This phenomenon allows a piezo-electric element to be used as both an ultrasound transmitter and receiver, and common

transducers function at relatively narrow-band frequencies in the range 0.5-20 MHz [22]. Ultrasonic waves are generated in a test piece via a piezo-electric transducer in contact with the surface as an electric field is applied across the piezo-electric element. Upon the incidence of returning ultrasonic waves, pressure experienced on the face of the transducer is converted to electrical signals. Transmission of ultrasound between the transducer and the test object requires a coupling medium with a refractive index in between that of the transducer material and the test piece material in order to minimise energy loss during transmission. The coupling medium can be a liquid, gel or adhesive and prevents gaps forming between the coupled surfaces, to avoid variations in the amplitude of the transmitted and received ultrasonic wave-field.

2.5. Laser-based Generation of Ultrasonic Waves

2.5.1. Absorption of Electromagnetic Radiation

When a laser beam is incident on a solid surface, most of the electromagnetic energy is reflected and scattered, while a small amount is absorbed into the material [8] to cause localised heating, leading to the generation of elastic waves. At higher energy density, the laser power can damage the material by ablation and melting.

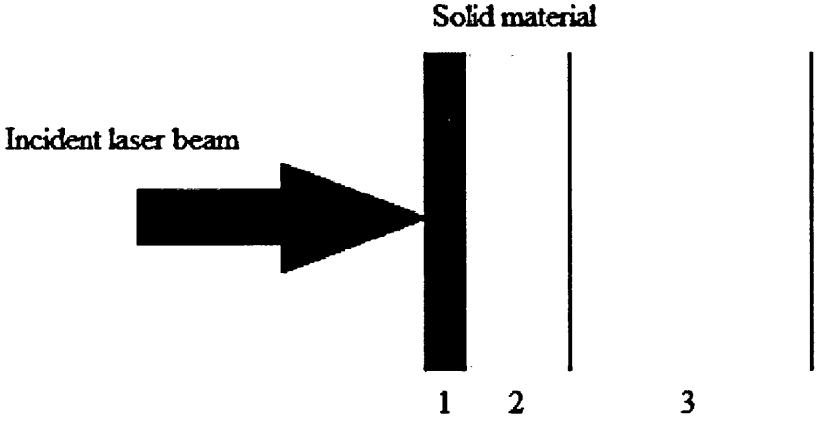

Figure 2.14. Illustration of regions in which different physical processes take place due to the absorption of laser light in solid material: (1) absorption of electromagnetic radiation; (2) absorption of heat through thermal conduction; (3) propagation of ultrasonic waves generated by thermal expansion and subsequent elastic stresses.

In a conducting material, the electrons at the surface interact to shield the interior structure by interaction with the incident electromagnetic energy, ensuring that all absorption and reflection takes place within a finite layer called the skin depth, δ. Within this distance, the

electromagnetic wave amplitude falls to $1/e$ of its initial value. Absorbed electromagnetic energy causes a temperature rise at the surface local to the irradiated area and heat is gradually conducted along the surface and into the bulk of the material. The absorption of electromagnetic radiation occurs fast enough to produce a thermal shock excitation at skin depth, causing a mechanical vibration in the solid lattice structure. Damage by surface ablation or melting can result if there is a high enough power density at the irradiated area. For a continuous laser, power delivered to the surface is constant and follows the relationship:

$$P = \frac{E}{t} \tag{2.34}$$

where P is power, E is energy, and t is time. Pulsed lasers provide a solution to generating mechanical stresses in a solid material. High power can be delivered to the surface intermittently in short and regularly repeating pulses (Figure 2.15). The peak power P_{peak} in each individual pulse is given by:

$$P_{peak} = \frac{E}{\tau} \tag{2.35}$$

where τ is the pulse duration, measured at the Full Width Half Maximum (FWHM) of a pulse with a Gaussian temporal profile. The average power P_{avg} over many pulses is given by:

$$P_{avg} = \frac{P_{peak}\tau}{t} \tag{2.36}$$

Thus the average power delivered to the surface is less than the peak power, allowing heat to conduct into the bulk of the material between each pulse before surface damage can occur.

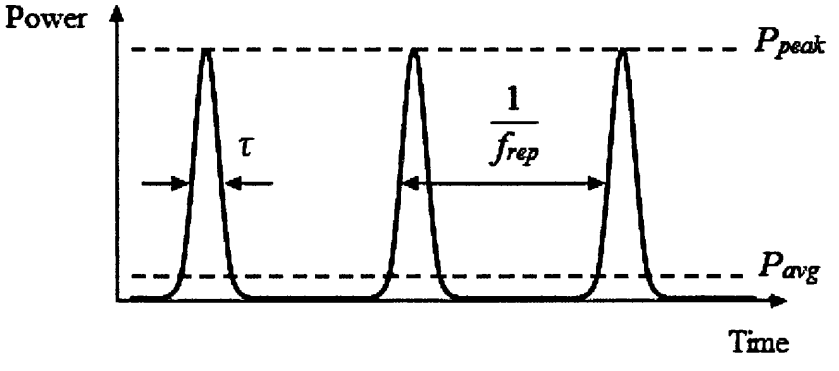

Figure 2.15. Power as a function of time for a pulsed laser output, with relevant quantities labelled.

2.5.2. Surface Temperature Distribution

For a metal sample with a laser pulse incident on its surface, the case can be considered where incident power is low enough such that the only effect it has is to increase temperature at the surface, and that the pulse is short enough that thermal conductivity and absorption of energy takes place uniformly within the skin depth. The cross-sectional energy distribution of a laser beam can be uniform or Gaussian and is equivalent to the power density at an irradiated surface (Figure 2.16) which creates a localised increase in temperature.

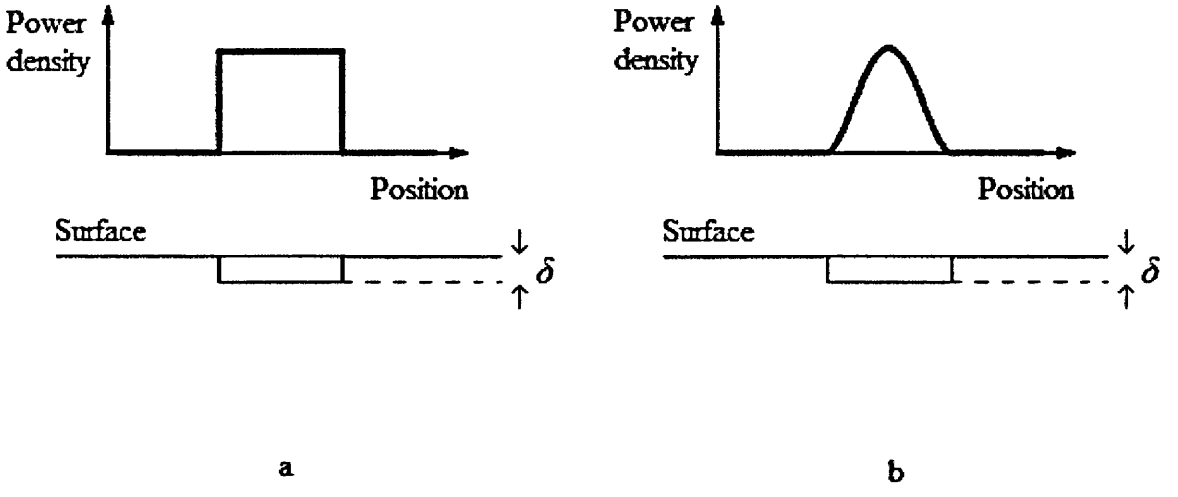

Figure 2.16. Power density at a surface irradiated by a laser beam with a Gaussian spatial distribution.

For uniform irradiation the rise in temperature T within the skin depth is given by [8]:

$$\Delta T = \frac{\Delta E}{C\rho \mathrm{A}\delta} \tag{2.37}$$

where ΔT is temperature rise, ΔE is absorbed energy, and C is specific heat capacity of the material. Thus temperature rise is proportional to absorbed energy density. For a non-uniform surface irradiation, the energy absorbed within an element of area dx is given by [8]:

$$(1-R)\int_t I(x,t)\mathrm{d}x\mathrm{d}t = C\rho \mathrm{d}x\delta\Delta T(x) \tag{2.38}$$

where I(x,t) is incident power density as a function of time and distance over the circular area of irradiation with x = 0 at the centre, and similarly T(x) is temperature as a function of distance. Rearranging Equation (2.38) gives the following expression:

$$\Delta T(x) = \frac{1-R}{C\rho\delta}\int_t I(x,t)\,\mathrm{d}t \tag{2.39}$$

Thus the distribution of temperature within the irradiated surface area is identical to the spatial distribution of energy over a cross-section of the incident laser beam. This is an important consideration for the FEA work reported in Chapter 4; simulation of incident laser irradiation can be achieved via an equivalent surface heat input.

For a realistic calculation of absolute temperature increase due to a pulse of laser irradiation, thermal conductivity must be taken into account – heat from the incident laser penetrates further into the sample than the skin depth. The depth of the thermal absorption layer is represented in Figure 2.14 as the boundary between the second and third labelled absorption regions. Temperature at the surface rises for a length of time slightly longer than the duration of the laser pulse as energy is absorbed and then gradually falls over a longer period on the order of microseconds as heat conducts into the bulk of the sample. It is assumed that energy loss due to surface radiation is negligible. The equation for heat flow for a solid material represented in a three-dimensional half-space with infinite depth is given by [8]:

$$\nabla^2 T(x,y,z,t) - \frac{1}{\kappa}\frac{\Delta T(x,y,z,t)}{\Delta t} = -\frac{\beta(x,y,z,t)}{K} \tag{2.40}$$

where κ is thermal diffusivity, β is heat produced per unit volume per unit time, and K is thermal conductivity. Here, depth of the half-space increases in the z-direction and boundary conditions are applied such that heat flux takes place at the plane where $z = 0$, $T(x,y,z,0) = 0$, and $T \to 0$ as $z \to \infty$. Typically, the depth of maximum heat conduction is much smaller than the width of the irradiated area [8], so it is appropriate to give Equation (2.40) in one-dimensional form:

$$\frac{\partial^2 T(z,t)}{\partial z^2} - \frac{1}{\kappa}\frac{\partial T(z,t)}{\partial t} = -\frac{\beta(z,t)}{K} \tag{2.41}$$

In the case of irradiation by a pulsed laser beam with a square temporal profile and uniform power density, and assuming the start of the pulse to coincide with $t = 0$, the solution to Equation (2.41) is [24]:

$$T(z,t) = \frac{2I_0\sqrt{\kappa t}}{K}\,\mathrm{ierfc}\left(\frac{z}{2\sqrt{\kappa t}}\right) \tag{2.42}$$

where I_0 is the absorbed laser power flux density, and ierfc is the integral error function which is defined as:

$$\text{ierfc}(x)=\frac{1}{\sqrt{\pi}}\exp\left[-x^2\right]-\frac{2x}{\sqrt{\pi}}\int_x^{\infty}\exp\left[-x^2\right]\mathrm{d}x \tag{2.43}$$

At the surface where $z = 0$, Equation (2.43) becomes:

$$T(0,t)=\frac{2I_0\sqrt{\kappa t}}{\sqrt{\pi}K} \tag{2.44}$$

If a square laser pulse starts at time $t = 0$ and ends at time $t = t_0$, Equation (2.42) is modified to include a second term to represent temperature change after the pulse ends:

$$T(z,t)=\frac{2I_0\sqrt{\kappa t}}{K}\text{ierfc}\left(\frac{z}{2\sqrt{\kappa t}}\right)-\frac{2I_0\sqrt{\kappa(t-t_0)}}{K}\text{ierfc}\left(\frac{z}{2\sqrt{\kappa(t-t_0)}}\right) \tag{2.45}$$

A laser pulse with a Gaussian temporal profile (Figure 2.17) has a non-instantaneous rise and fall in power density and is of the form:

$$I(t)=I_1\exp\left[\frac{-xt^2}{\tau^2}\right] \tag{2.46}$$

where I_1 is the maximum power density at the peak of the pulse. In order to obtain temperature as a function of time in the case of a Gaussian pulse, Duhamel's theorem is applied to obtain [25]:

$$T(z,t)=\int_z^{\infty}\int_0^{t}\frac{I(t')}{I_0}\frac{\partial}{\partial t}\left(\frac{\partial}{\partial z}\left[T'(z',t-t')\right]\right)\mathrm{d}z'\mathrm{d}t' \tag{2.47}$$

where $T'(z,t)$ is a solution to heat flow with a multiple stepped increase in absorbed power flux density to form a Gaussian distribution. This is substituted into Equation (2.42) to give:

$$T(z,t)=\frac{\sqrt{\kappa}}{K\sqrt{\pi}}\int_0^{t}\frac{I(t-t')\exp\left[\frac{-z^2}{4\kappa t'}\right]}{\sqrt{t'}}\mathrm{d}t' \tag{2.48}$$

From Equation (2.48) the characteristic rise and fall in surface temperature (Figure 2.17) is obtained and applies over the entire area of irradiation for a laser beam with uniform spatial distribution of power density. These analytical equations will form the basis for verifying the interactions calculated due to simulated thermal input in the FEA model.

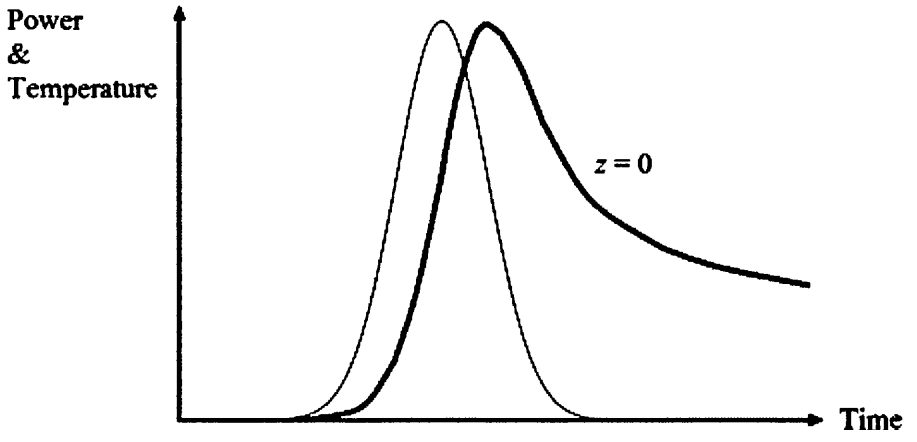

Figure 2.17. Representation of the relationship between laser power (black) and surface temperature (red), as a function of time and normalised, due to the irradiance of a metal by a pulsed laser beam with Gaussian temporal profile and uniform spatial profile.

This temperature profile is also correct at the centre of the area of irradiation for a beam with Gaussian spatial distribution, which is of the form:

$$I(r) = I_1 \exp\left[\frac{-r^2}{d^2}\right] \tag{2.49}$$

where r is the radius of power flux and therefore also of the area of surface heat flux, I_1 is the maximum flex density, and d is linear distance from the centre of the irradiated area. In the FEA model, this will be input directly as the spatial distribution of heat input over a finite area.

2.5.3. Thermal-mechanical Stress

A low power laser incident on the surface of a metal will cause a localised rise in temperature and consequently thermal expansion of the material which generates thermo-elastic stresses and strains. This process can be considered in a three-dimensional model, taking into account components of stress and strain which are parallel to the surface of the metal sample. This provides a mechanism for generating transverse and longitudinal elastic waves in solid material. The source can be considered as an expansion within the bulk of the material, centred on and contained within an infinitesimal volume δV. The following local strains and stress field are produced [8]:

$$\varepsilon_{11} = \varepsilon_{22} = \varepsilon_{33} = \frac{1}{3}\frac{\delta V}{V} = \alpha \Delta T \tag{2.50}$$

$$\sigma_{11} = \sigma_{22} = \sigma_{33} = B_{\text{mod}} \frac{\delta \text{V}}{\text{V}} \tag{2.51}$$

where ε_{ii} is a strain component, α is the coefficient of linear thermal expansion, σ_{ii} is a stress component, and B_{mod} is the bulk modulus of elasticity (equal to $\lambda + 2/3\mu$). Here the subscript labels 1, 2, and 3 refer to the orthogonal directions x, y, and z, respectively. This is equivalent to an expansion within the same volume and can be described as three orthogonal dipoles, or pairs of opposing forces (Figure 2.18), each with strength equal to the product of stress and volume:

$$D_{11} = D_{22} = D_{33} = B_{\text{mod}} \delta \text{V} \tag{2.52}$$

where D_{ii} is dipole strength. The source of thermo-elastic stress is a heat flux at the surface; if the heat source is assumed to be flat, there is no net stress component perpendicular to the surface. Thus in this plane, $\sigma_{33} = \sigma_{31} = \sigma_{32} = D_{33} = 0$ and only the force dipoles D_{11} and D_{22} have non-zero magnitude, with the remaining stresses acting parallel to the surface. If the thermo-elastic source has a small thickness and is free to expand in a direction normal to the surface (Figure 2.18), a non-zero strain will exist at the surface [8]:

$$\varepsilon_{33}(z=0) = \frac{3B_{\text{mod}} \alpha \Delta T}{\lambda + 2\mu} \tag{2.53}$$

This leads to a displacement at the surface given by:

$$\text{u} = \frac{3B_{\text{mod}} \alpha \Delta T \Delta z}{\lambda + 2\mu} \tag{2.54}$$

where Δz is equal to the maximum depth of the associated temperature rise.

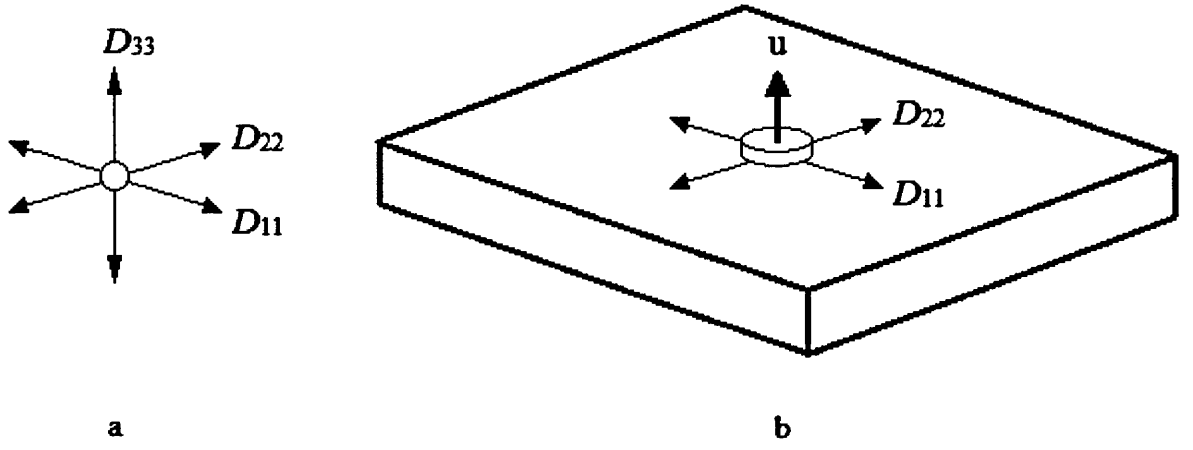

Figure 2.18. Orthogonal force dipoles generated by the expansion of an infinitesimal volume in a solid material (a) inside the bulk, and (b) at the surface and with finite thickness.

Stress induced by surface heating is redistributed through the bulk of the material in the form of an elastic stress wave field, or ultrasonic waves. The dipole model predicts directionality patterns for laser-generated longitudinal and transverse waves (Figure 2.19) which represent the variation of amplitude at different angles from the surface normal as directed into the bulk [8].

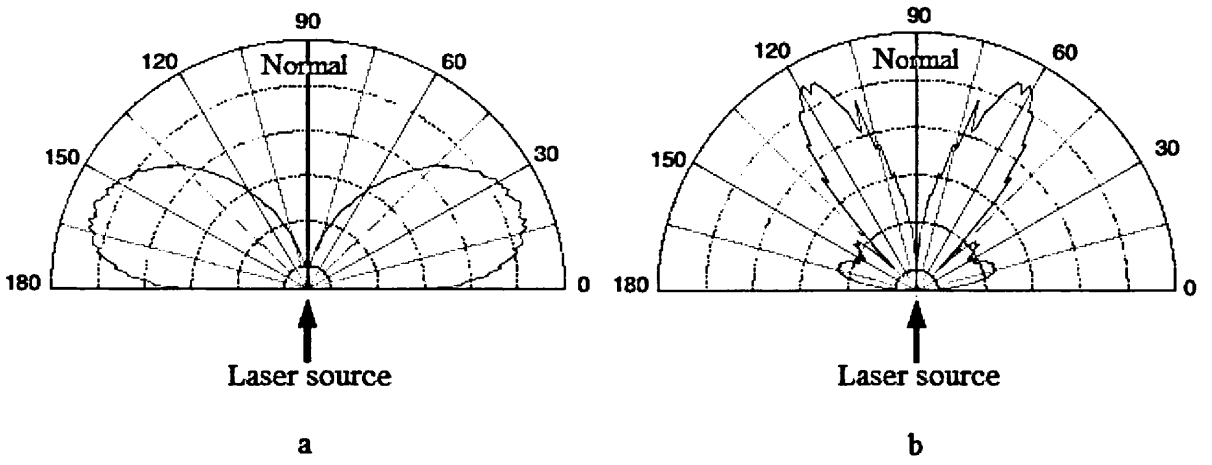

Figure 2.19. Theoretical directionality patterns for (a) longitudinal waves, and (b) transverse waves generated in the thermo-elastic regime [26].

A Rayleigh wave is also produced, propagating along the surface in directions depending on the shape of the focused laser beam. For example, a circular area of irradiation produces a wave-front which propagates radially outwards from the source in all directions. The Rayleigh wave generated from a thermoelastic heat source as detected and displayed in an A-scan is characterised by a large negative amplitude peak, such as that visible in Figure 2.13.a.

2.5.4. Surface Ablation

Damage to the surface of a metal by ablation occurs if the power density of an incident pulsed laser is high enough to heat the material to its vaporisation temperature. The power density depends on pulse energy, pulse duration, and beam diameter at the point of incidence. Vaporised material is removed and leads to the formation of plasma above the irradiated surface in a complex process [25]. Ablation can continue if the pulse repetition frequency is too high for heat to be conducted into the bulk at a sufficient rate between successive pulses, and the surface damage caused can amount to micrometres or tens of micrometres depth of material removal. Ablation of material from the surface produces a reaction force directed into the bulk and perpendicular to the surface (Figure 2.20), in opposition to the direction and momentum of ablated material.

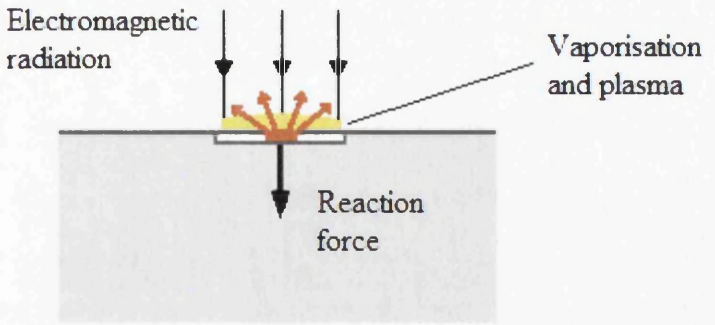

Figure 2.20. Schematic representation of surface material vaporisation and plasma formation with the resulting net reaction force.

2.6. Laser-based Detection of Ultrasonic Waves

2.6.1. Interferometry

Optical interferometers make use of laser beams for measuring displacements with high sensitivity, and can therefore be applied to the non-contact detection of ultrasonic waves at the surface of a solid material. Laser interferometry offers several other advantages over traditional piezo-electric receivers: the measurement position can be easily altered by scanning the laser beam relative to the test surface; the measurement can be localised to a relatively small area; and the receiving equipment can have a good response over a broad range of frequencies [8]. The ability to encode information about surface displacements or velocities into a light medium is the basis of interferometry for use in NDT, and this is achieved through the interaction of a laser beam reflecting, at normal incidence, from the surface of an opaque material experiencing ultrasonic motion. The electric field of a laser beam can be expressed in terms of its optical properties as [26]:

$$E = a\exp\left[\mathrm{i}\left(\omega t - \varphi\right)\right] \tag{2.55}$$

where a is amplitude, ω is optical frequency, and φ is optical phase. The normal displacement at the point of laser irradiation, given as a function of time by $\mathrm{u}(t)$, causes a change in the path length of the beam which is equal to $2\mathrm{u}(t)$ taking into account propagation before incidence and after reflection. This alters the phase of the light wave and the electric field is then expressed as:

$$E = a\exp\left[\mathrm{i}\left\{\omega t - 2k_{opt}\mathrm{u}\left(t\right) - \varphi\right\}\right] \tag{2.56}$$

where k_{opt} is optical wavenumber. Here the original optical phase in the absence of surface displacements is represented. The interaction at the surface can also be described as an instantaneous Doppler shift in the optical frequency, considering that surface velocity v(t) is equal to the derivative of displacement du/dt, as follows [26]:

$$\omega t = \int_0^t \omega \left\{ 1 - \frac{2\mathrm{v}}{c} \right\} \mathrm{d}t \tag{2.57}$$

where c is the speed of light in the relevant medium. It is not possible to directly measure the phase because optical frequency is too high for current photo-detectors [26]; however, the beam can be demodulated to extract information about surface displacements or velocities associated with local propagation of ultrasonic waves in the material. There are different types of interferometer designed for this purpose.

2.6.2. Two-Wave Mixing

Two-Wave Mixing (TWM) interferometry is so named because it requires that two laser beams, split into separate optical paths from the same source, interfere in a precisely controlled manner after one of the beams has reflected from the surface under investigation. The signal beam is reflected from the surface of the test piece to collect surface displacement information, and the reference beam remains unaltered by external influences. The optical arrangement can be exposed when used in a laboratory environment, but commercially available interferometers enclose as much of the optical equipment and laser beams as is practical in order to provide protection and safety in operation. A beam-splitter module forms an essential part of the optical arrangement, with the purpose of splitting a single incident laser beam into two or more coherent output beams.

A photorefractive crystal forms the basis of a TWM interferometer; this is used to compensate for distortions or a phase shift in the reference beam. The photorefractive effect refers to the non-linear response of a photorefractive crystal to the incidence of electromagnetic radiation with non-uniform intensity, whereby the refractive index of the crystal is altered [27]. TWM makes use of this phenomenon; the signal beam and reference beam are directed to propagate, at an angle to each other, through a photorefractive crystal such that the beams cross paths and interfere (Figure 2.21). Additionally, both beams are refracted. A dynamic holographic element records the interference pattern and adapts the wave-front of the reference beam to match that of the reference beam which experiences a phase change due to interaction with ultrasonic displacements on the surface of the test piece.

The hologram combines the transmitted signal beam with the refracted reference beam such that they are coherent, i.e. propagate with a constant phase difference. This combined beam irradiates a photo-detector which measures intensity variation, which is proportional to the phase shift and therefore surface displacement [28].

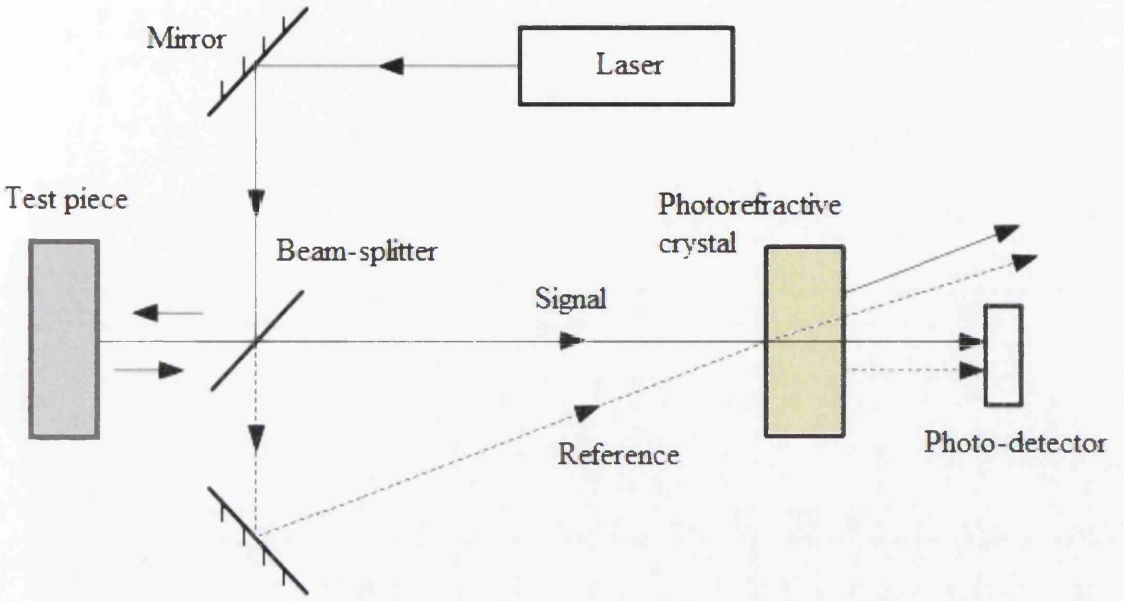

Figure 2.21. Schematic of the optical arrangement of a TWM interferometer.

In the context of applying laser-based reception of ultrasound to an active manufacturing environment, an advantage of a TWM interferometer is that the surface under inspection does not have to be polished to provide sufficient reflection of the detection beam [29], and as such it is better suited to rougher, unfinished surfaces.

2.6.3. Fabry-Pérot

Fabry-Pérot interferometers detect a signal proportional to velocity and are therefore have excellent immunity to ambient vibrations such as those expected in manufacturing environments [30]. This type of interferometer consists of a cavity with a partially reflecting mirror at each end. Light from the vibrating surface enters the cavity generating multiple reflections (Figure 2.22). In a Confocal Fabry-Pérot Interferometer (CFPI), the mirrors are spherical with a radius of curvature equal to their separation distance. The inner surface of each of these mirrors is partially reflecting.

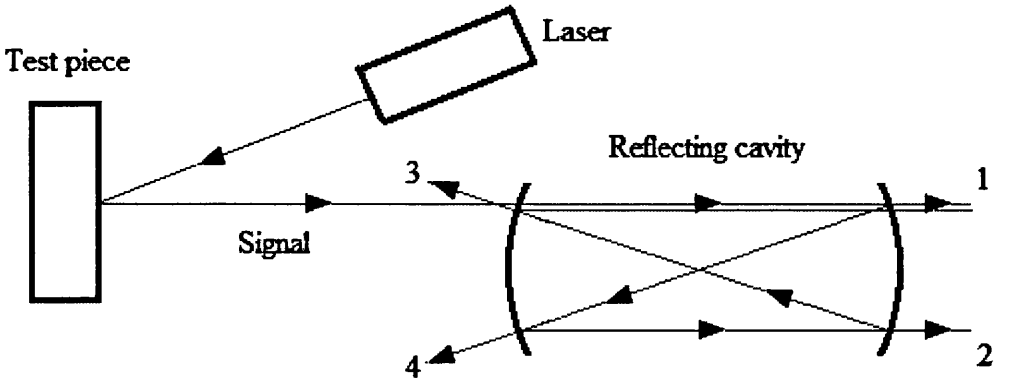

Figure 2.22. Simplified schematic of the optical arrangement of a CFPI interferometer.

Light reflected from the surface under investigation enters the interferometer at point 3 by passing through one of the partially transmitting mirrors. This light then reflects within the cavity following the path as shown, resulting in two transmitted parallel rays from position 1 and position 2 as well as two transmitted diverging rays from position 3 and position 4. The transmitted beams have a phase difference due to the difference in path length propagated within the reflecting cavity. Similarly, for each of the transmission positions 1-4, there is a phase difference between the initial ray and each successive ray which has undergone intra-cavity reflections.

In practice, the rays forming each pair of transmitted beams are simultaneously detected by their respective photo-detectors and for each pair an intensity transmission coefficient is measured. These coefficients include terms for the phase and can change periodically due to a change in the optical frequency of the incoming light. Laser light scattered from the surface of a test-piece, where ultrasonic motion is taking place, has its frequency shifted due to the Doppler effect; therefore the velocity of the surface can be measured [31]. This can be associated with particular wave types by taking into account the test-piece geometry and position of signals on the time-base.

A Fabry-Pérot type interferometer was not available for the practical work carried out as described in later Chapters; a TWM interferometer was selected based on the performance advantages offered by the technology and installation flexibility offered by the delivery of laser beams by fibre cable.

2.6.4. Detection and Characterisation of Defects

The following is a literature review of research into the detection and characterisation (including positioning, sizing, and determination of defect type) of both real and induced flaws in metal structures. This review is focused particularly on examples of surface and near-surface flaws under evaluation using laser-generated surface ultrasonic waves.

Aindow et al. [32] applied laser ultrasonic testing to the detection and characterisation of artificial sub-surface flaws in the form of flat-bottomed holes, drilled into aluminium blocks from the surface opposite to that of the irradiated surface. The holes had diameter 6.35 mm and depths ranging from 1.22 mm to 4.80 mm. With the transmission and detection lasers scanned across the position of a flaw in a co-incident arrangement, the authors were able to accurately calculate the depth of a flaw by evaluating the propagation of the longitudinal ultrasonic wave. In another configuration, the laser beams were set a fixed distance apart and scanned such that each beam passed either side of the flaw. Significant distortion in the Rayleigh wave signal was observed due to the presence of a flat-bottomed hole, at all depths, although the authors did not link the wave behaviour to a quantitative measure of any flaw. They noted that it was necessary to polish the metal surface in order to receive sufficient reflected laser light to obtain a good signal, due to the low sensitivity of the Michelson interferometer used in experiments.

Cooper et al. [33] studied the interaction of surface ultrasonic waves with artificial surface-breaking flaws. A linear slot of width 100 μm, and depth ranging from 1 mm to 100 μm, was cut into a thick aluminium block, and the same surface was irradiated by a transmission and a detection laser beam. The beams were focused at separate positions several millimetres apart on the same side of the slot and then on opposite sides of the slot, such that an axis joining the two positions would intersect the slot perpendicularly. This set-up allowed the researchers to analyse and compare the incident Rayleigh wave signal to the same wave which reflected from the slot, and also that which transmitted through the slot. The results show a broadening of the transmitted Rayleigh wave, in the time domain, compared to the incident wave. In addition, the reflected Rayleigh wave signal displayed two distinct peaks, with a temporal separation which increased linearly with slot depth. In the frequency domain, it was observed that frequency components below 2 MHz were reduced in amplitude in the reflected wave compared to the incident wave, with this frequency corresponding to a Rayleigh wavelength approximately equal to twice the depth of the slot. This is attributed to shorter wavelengths,

and therefore higher frequencies, being reflected by the slot whilst longer wavelengths transmit through the slot. This result is confirmed in a comparison of the frequency spectra of the incident and transmitted ultrasonic wave signals – higher frequency components are significantly reduced in amplitude.

Dixon et al. [29] studied the enhancement of ultrasonic surface waves due to the presence of surface-breaking cracks. Several phenomena were observed through measurement of surface displacements when the pulsed laser source was positioned above a crack. It is stated that the pulsed laser beam was kept at low enough energy density to produce a thermo-elastic source. Aluminium samples were used for testing, containing an artificial slot of width 700 μm and depth 900 μm as well as a real surface-breaking crack. Several experiments were conducted; in each case, the position of the detection laser beam was constant and the results were analysed in the frequency domain. In their first experiment, the transmission laser beam was scanned towards the edge of the block such that the source became truncated, with the centre of the focal spot directly over the edge. In another experiment, the laser source was scanned towards the edge of the machined slot. Finally, the test method was repeated with the laser source approaching the surface-breaking crack. Similar behaviour is observed in all results: as the ultrasound source approaches a discontinuity, there is an increase in both the peak frequency and the arbitrary spectral amplitude of the peak frequency. The authors note that the higher frequency components of the Rayleigh wave display larger relative increases in magnitude and suggest that a detection system would be more useful if it was sensitive to these higher frequencies.

Dutton et al. [34] further progressed research on the interactions of ultrasonic waves with surface-breaking flaws oriented at angles other than 90 degrees to the surface. As in previous works, experiments were performed on an aluminium block with wedge-shaped slots machined into the surface, tapering to a point at the greatest depth. The slots had width 500 μm at the surface, with depth ranging from 0.5 mm to 4.8 mm and angle from the surface plane ranging from 30 to 150 degrees. The transmission laser beam was focused to a fixed position on the surface, in a line shape to produce a straight wave-front parallel to the length of the slot. It is stated that a TWM interferometer was chosen for detection due to its performance on non-polished surfaces, an advantage in testing industrial samples. During the experiment, the detection laser beam was focused at two points on the surface, on either side of the slot; this set-up facilitated measurement of the Rayleigh wave after reflection from the slot and also after transmission through the slot. A-scans were recorded stationary and with

64 averages in order to minimise noise in the signal. The results were displayed in terms of reflection and transmission coefficients, calculated as the ratio of the reflected and transmitted wave magnitudes, respectively, to that of the undisturbed incident Rayleigh wave, in both the time and frequency domains. Variation of these coefficients with slot angle was observed, although the authors note that the measured values can be affected by the presence of mode-converted ultrasonic waves formed due to interaction with the surface flaw. The extra wave-modes were analysed separately and found to be useful in gaging the angle of slots. Concluding remarks claim that discrimination of different real crack defect types might be possible simply by knowing whether a surface-breaking crack is angled or not.

In a continuation of the above work, Hernandez-Valle et al. [35] carried out laser ultrasonic testing on similar aluminium blocks with angled slots as previous and also branched slots which consisted of a vertical slot of depth 2 mm, with a branching section of various lengths angled at 45 degrees and starting either at the surface or half-way to the maximum depth of the vertical section. Experiments were performed with the transmission laser beam stationary and the detection beam scanned from the same side and over the slot opening, and then vice-versa. For the simple angled defects, it was found that for both scanning methods employed, there was an increase in the peak-to-peak signal amplitude of the measured Rayleigh wave when either laser beam approached close to the slot edge. This enhancement was found to increase inversely proportional to slot angle relative to the surface, and the dependence on slot angle was several times greater when the detection beam was being scanned. This behaviour is attributed to surface waves propagating as Lamb waves near the slot opening, with an A0 wave contributing to the measured out-of-plane surface displacements. Results of similar scans over the branching slots reveal further dependence on flaw geometry; the same signal enhancement is reduced when the branch begins half-way down the slot, although in this case increases in proportion to the length of the branched slot section.

Santospirito et al. [36] applied two non-contact NDT techniques for the detection of artificial flaws representing sub-surface voids which can occur in structures manufactured by the LMD powder process. One of the techniques considered was laser ultrasonic testing; both surface and bulk ultrasonic waves were relied on to detect and characterise a set of sub-surface holes drilled through the width of deposited wall structures. The holes ranged in diameter from 500 μm to 120 μm and in depth from 280 μm to 13 μm. The transmission and detection laser beams were scanned along the top surface of the wall samples at a fixed distance apart in steps of 0.1 mm, i.e. in a non-continuous motion. Their results displayed an attenuation and

temporal delay in the surface wave whilst the sub-surface holes were in-between the laser beam positions, although this effect was only significant for the holes which had either the largest diameter or were closest to the surface. It was found that deeper holes did not produce this effect but did display a hyperbola shape in B-scans due to reflection of bulk waves. An algorithm was developed to automatically match a hyperbolic line to the wave data, with flaw diameter proportional to the spacing between the two arms of the line, and flaw depth proportional to the time between the arrivals of the surface wave and the apex of the hyperbola. It is noted that human input is required for setting up the hyperbola in each case and that further development might allow for automation via image processing.

2.6.5. On-line Inspection

The following are examples of laser ultrasonic testing used for the on-line inspection of manufacturing and welding processes. These works take the form of field trials in industrial conditions and thus take into account laser safety requirements and installation of laser equipment without disturbing the active process and machinery.

Jeskey et al. [37] installed a laser ultrasonic testing system after the final stage of a seamless Steel tube manufacturing system. The transmission and reception laser beams were delivered by optical fibre cable to an inspection head positioned above the manufactured tube (Figure 2.23), with the tube under continuous motion during inspection. A Fabry-Pérot type interferometer was used for this industrial installation. The laser generating equipment and interferometer were stored in a cabin separate from the production line, and laser safety was provided by a light shield encircling the manufactured tube such that only a negligible amount of scattered laser light could escape the enclosure. Transmission and reception of ultrasound was done on the outer surface of each tube. In one application, the arrival time of a bulk ultrasonic wave, reflected from the inside surface of the tube, was used to measure wall thickness over the length of a tube by taking into account a known wave velocity in the material. Eccentricities in tube wall thickness were detected and successfully corrected in subsequent productions (Figure 2.24). In another application, real-time grain size measurements were carried out by correlating on-line ultrasound attenuation to experimentally obtained attenuation curves and grain size data. The authors cite reduced production costs as a result of being able to inspect each produced specimen immediately after manufacture, with time savings and reduced scrap.

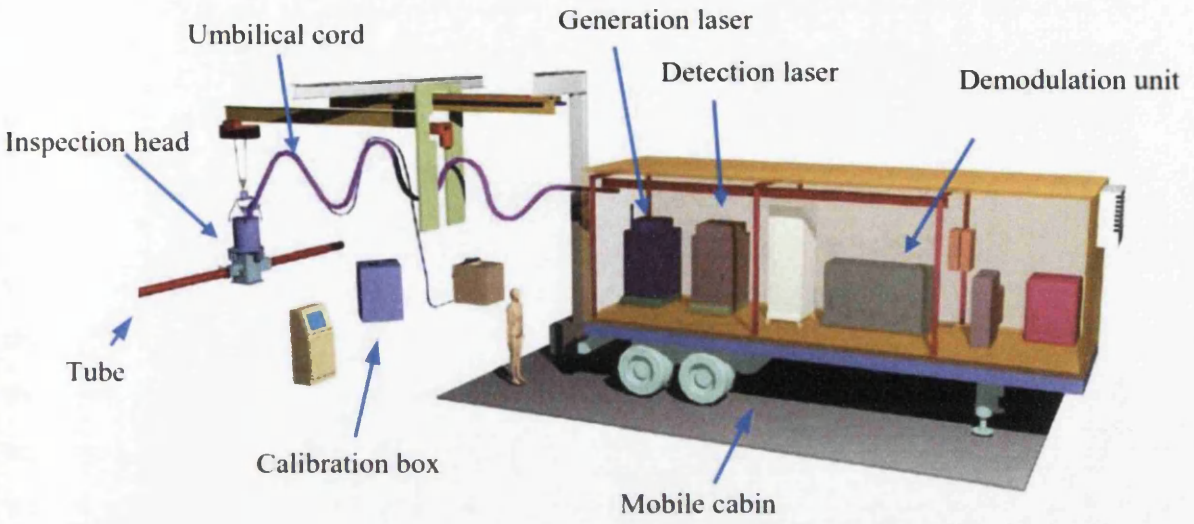

Figure 2.23. Overview of the laser ultrasonic system used by Jeskey et al. [37] for on-line inspection of Steel tubes.

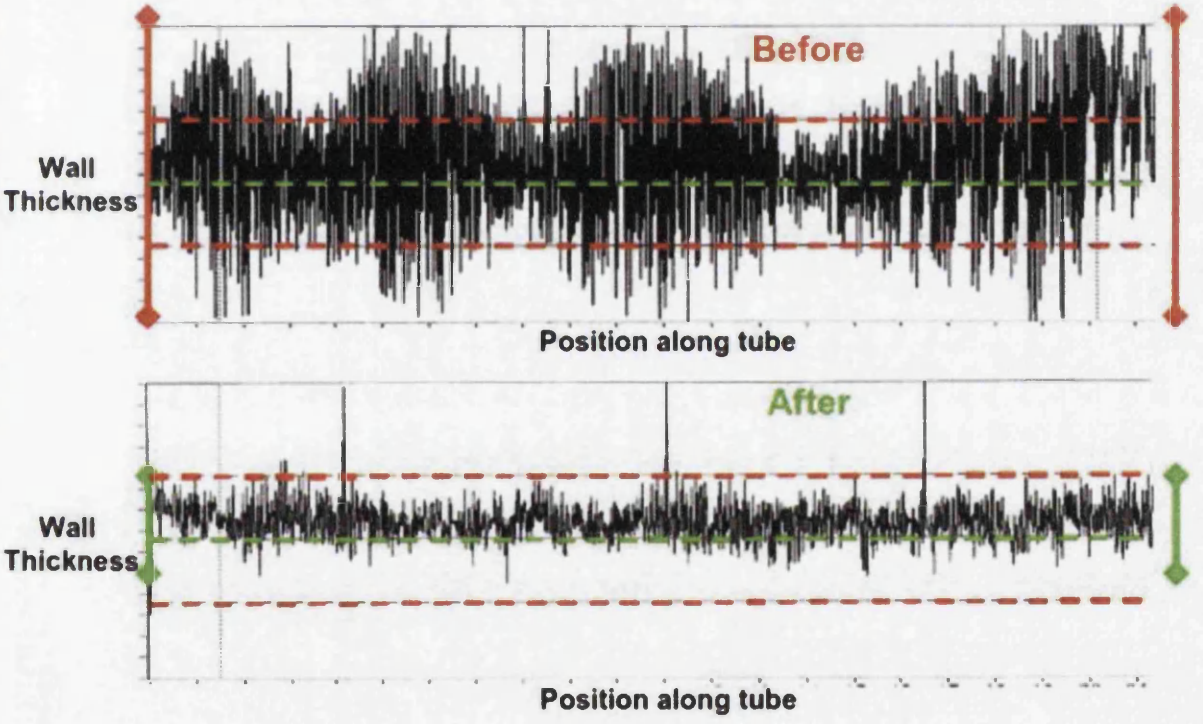

Figure 2.24. Example of wall thickness measured over the length of a Steel tube by Jeskey et al. [37], showing deviation from specification (dashed red lines) before and after alterations to manufacturing parameters.

Another example of the integration of laser ultrasonic testing into a working manufacturing environment is 'SignaStir', a European collaborative project lead by TWI [38]. The manufacturing process under evaluation was Friction Stir Welding (FSW), in which two

separate metal plates, in contact at their edges, are welded together by the action of a rotating tool which is pressed onto and translated along the interface between the plates. The friction of the tool causes heating sufficient to soften the plate metal such that it is stirred into a consolidated weld. The purpose of the project was to develop in-process quality assurance of welds to reduce waste by identifying regions of a weld to be re-worked. Flaws in friction stir welds can manifest as sub-surface voids in the welded region (Figure 2.25.a) – in SignaStir, the method of flaw detection used laser-generated bulk waves transmitted from one side of the welded plate, reflecting from the opposite surface after propagating through the welded region. It is claimed that common voids were successfully detected in laboratory testing of welds, while results from on-line trials did not provide real-time correlation with lab results. However, it is claimed that the installation provided useful information with regards to the practical aspects of integrating laser ultrasonic testing equipment into an FSW system, and that further improvements have been identified for future development. An enclosed optical head was attached to the FSW tool-head such that the transmission and reception of ultrasonic waves, taking place on either side of the weld, would follow directly behind the welding tool along the entire length of a linear weld (Figure 2.25.b). Both laser beams were delivered by optical fibre cable and safety was provided by a telescopic beam guard which extended close to the weld surface, blocking direct reflected laser light.

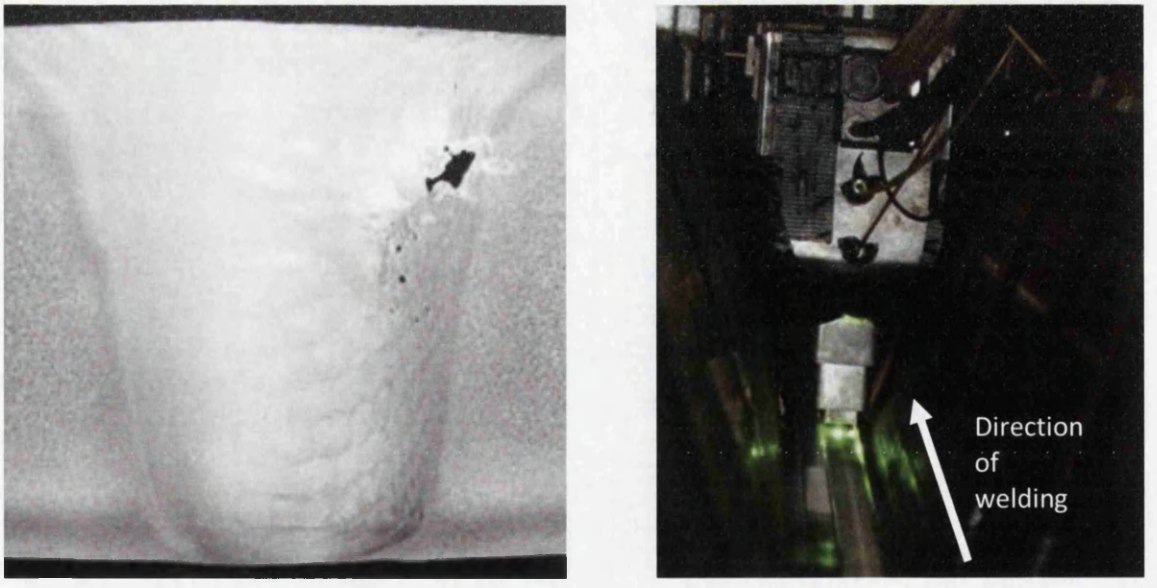

(a) (b)

Figure 2.25. (a) Vertical cross-section of a friction stir weld showing a typical void-type flaw, and (b) laser ultrasonic testing integrated into an FSW system for on-line inspection as part of the SignaStir project [38].

Chapter 3: Review of Laser Metal Deposition for Aerospace Manufacturing and Repair

3.1. Introduction

There are many well-established methods of metal manufacturing of parts, including machining, forging, casting, rolling and extrusion. Aerospace manufacturing companies have made use of machining for the manufacture of aero engine turbine blades for decades [39]. Machining is a subtractive manufacturing technique which involves cutting away volumes of material from a starting block such that the final component is constructed of a single, solid piece of material. For aerospace components made of high-grade materials for use in extreme conditions, machining can result in the wastage of over 90% of the starting block of material and the process can take a significant amount of time. There is interest in the aerospace manufacturing industry to reduce production costs in light of increasing raw material prices, and there is pressure from governments to reduce environmental damage and carbon emissions; as a consequence, there is on-going investment from aerospace manufacturing companies in ALM as an alternative to traditional manufacturing techniques [40].

ALM is a computer-controlled method of component manufacture by which material is added in layers, by heat input and fusion, to a substrate in order to build up a shape as stored in a computer aided design (CAD) data file. The geometry in the CAD file is sliced into a finite number of layers based on the capabilities of the target ALM process. ALM systems in general consist of four main components: a substrate of solid material, a heat source, a material feed (wire or powder) and motion control of either the substrate or deposition apparatus. The advantages of ALM over machining include the ability to produce more complex shapes (without the need for cutting tool access), reduced energy usage, reduced production time and increased usage of input material [41]. Re-use of un-fused material is also possible [42], further reducing waste. There are several different ALM processes, of which a few examples will be summarised to provide an overview.

Gas tungsten arc welding (GTAW) is a well-established welding technique which has been adapted for ALM; the method of heat input is an arc between a Tungsten electrode and the substrate material and additional material is fed as a continuous wire. Its use in the manufacture of high-quality aerospace components is the subject of contemporary research [43]. In Selective Laser Melting (SLM), a layer of additive material, in powder form, is

spread over a substrate by a wiping blade mechanism in order to form a uniform layer of powder. A focused laser beam is scanned over the powder bed in order to provide a heat input and fuse precise areas into a common layer. This process repeats to build up a part. The final quality of SLM components can be sufficient for use in extreme conditions, such as the J-2X rocket engine, manufactured and operated by the National Aeronautics and Space Administration (NASA) [44].

LMD makes use of either wire or powder as a material feed and heat input is provided by a laser beam. The additive material is fed selectively onto the molten region in the vicinity of the laser beam focus, facilitating precise control over the amount of material used. The LMD process is known by several acronyms including direct metal deposition (DMD), Laser Engineered Net Shaping (LENS), and laser cladding.

LMD has seen increasing interest from manufacturers in recent years; there are many examples of parts created for demonstrating the capability of LMD in the manufacture of aerospace components. TWI, in collaboration with helicopter engine manufacturer Turbomeca, has developed the LMD process to produce a combustor casing in a single, continuous deposition track. The final part required only 1.2 kg of material to be passed through the deposition nozzle, with 70 % fused into the deposited structure. A major claimed advantage is the reduction in build time, reduced from 8 weeks to less than 8 hours compared to the current manufacturing method [45]. In collaboration with aero engine manufacturer Rolls-Royce PLC, a boss manufactured using LMD was demonstrated. A reduction in wasted material from 1500 kg to 240 kg was claimed compared to the conventional manufacturing method, with associated cost savings [46]. In both cases, material density in the finished part was reported as being over 99.5%. Other aerospace components available from a manufacturer and produced by LMD include casings and parts for landing gear, as well as forged structures with bosses and flanges added directly by LMD [47].

Apart from component manufacturing, LMD is also utilised for the repair of pre-made, in-service components. For example, turbine blades have been re-manufactured to high accuracy and with good material qualities, with a demonstrated reduction in energy and material use compared to producing a new blade [48].The use of LMD as a repair technology has also been tested on components such as aircraft brackets and aluminium wheels [49].

In this work, Inconel 718, a nickel-based alloy commonly used in the manufacture of high-grade aerospace components was selected for test specimens and simulations. It holds

material strength at temperatures of hundreds of degrees Celsius and has good resistance to corrosion and oxidisation. As such, Inconel 718 is ideal for applications where a structure experiences high temperatures and pressures, such as gas turbine engines for commercial and military aircraft [50]. Inconel 718 is reported to have good microstructural stability and resistance to cracking which can occur during post-weld heat treatment. This makes the alloy a good choice for welding processes such as LMD [51]. The work in this thesis will refer in particular to the LMD-powder process due to its increasing importance in the ALM and aerospace industries. Thus all further references to 'LMD' should be understood to concern the LMD-powder process.

3.2. Laser Metal Deposition Basics

3.2.1. LMD-powder Process

In LMD, a track of additive material is formed using metal powder which is fed, through a nozzle, on to a melt-pool created by the irradiance of a focused, high-power, continuous laser beam on a metal substrate. The integration and angle of the powder stream can vary (Figure 3.1); a co-axial solution built into the nozzle allows for more flexibility in movement and therefore higher geometric complexity in deposited parts compared to a side-mounted, off-axis solution.

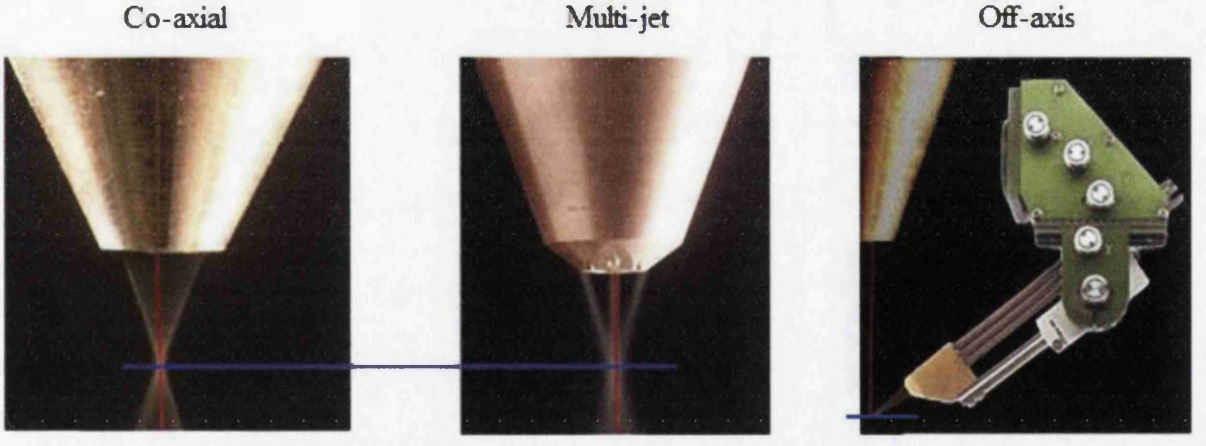

Figure 3.1. LMD nozzles with different methods of additive powder stream integration (photograph from Fraunhofer ILT – used with permission). The blue line represents the working plane of deposition.

In this work, the LMD system available for on-line trials is of the co-axial type (Figure 3.2). The powder stream and laser beam are both focused to the same distance (the working plane)

so that powder is deposited only in the region of the melt pool. A stream of inert gas surrounds the powder stream and melt-pool in order to prevent oxidisation of the deposited material. As the deposition nozzle is traversed relative to the substrate, or vice-versa, the weld track forms a layer of new material in a shape defined by the deposition path. In a multi-axis system, the deposition nozzle or work-piece can be tilted so that protruding sections of the desired geometry can be realised – the laser beam axis remains normal to the plane of deposition. A multi-layer, 3D structure is built up by successive passes of material deposition, with the previous layer acting as the substrate on each pass. The deposition path is generated in software and the motion of the LMD nozzle and parameters such as powder feed rate, laser beam power and rate of motion are controlled by computer, providing automated manufacturing.

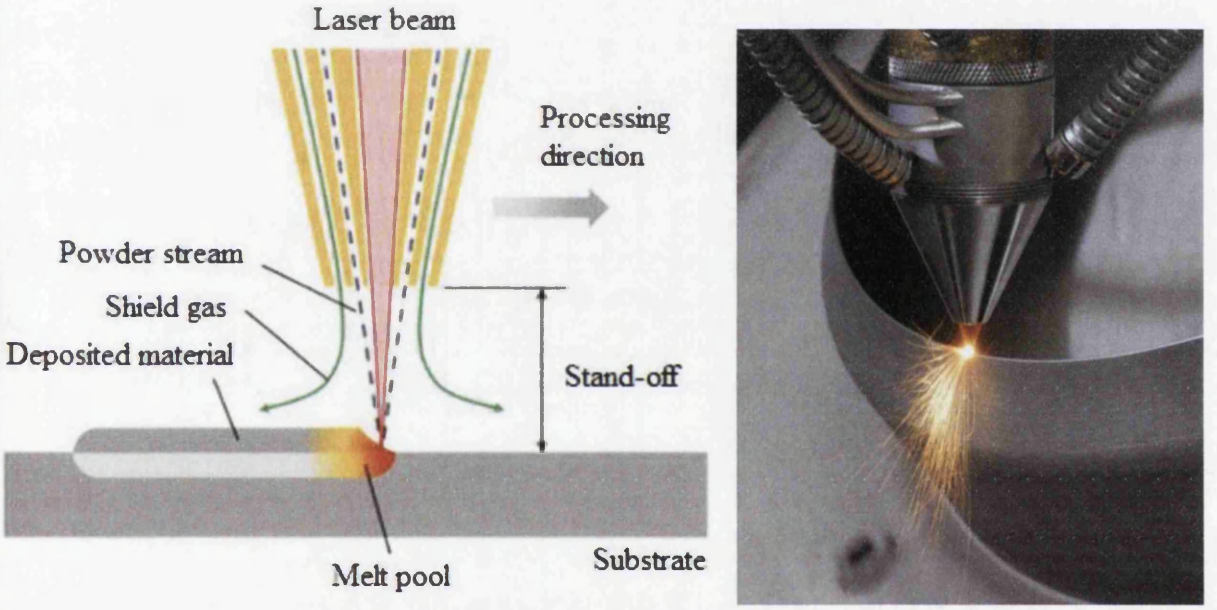

(a) (b)

Figure 3.2. (a) Schematic of the Laser Metal Deposition process using a co-axial powder spray for material addition and (b) powder-based deposition of a cylindrical, thin walled structure (photograph from TWI – used with permission).

Materials commonly used in LMD include nickel alloys [46, 52], stainless steel [48, 53], and titanium alloys [2, 54]. The rate of material deposition/addition varies by process parameters – examples of reported deposition rates are 0.9 kg/h [45] and 3.5 kg/h [55], thus allowing the rapid manufacture of complete structures. Powder usage efficiency is measured as the proportion of powder blown from the nozzle which is successfully fused into the deposited structure and can depend on the nozzle design, orientation relative to the target geometry and

other deposition parameters. Experiments by Carroll et al. [42] have demonstrated that un-fused powder can be recovered and re-used for deposition several times without introducing contaminants or changes in microstructure, although surface roughness was found to increase. LMD systems can also include integrated monitoring devices for better control of the deposition process. One example is a pyrometer which measures melt pool temperature to provide data feedback to software so that laser power can be continuously adjusted in order to maintain optimum deposition conditions [56].

3.2.2. Geometric Properties of Deposited Material Structures

Parts created by LMD usually have a rough surface finish and require post-process machining to improve the surface quality for the intended application [57]. The surface roughness can arise from the ridges between adjacent layers on either vertical or lateral surfaces, powder particles sticking to surfaces near to the powder spray, or from sputtering of material outwards from the melt pool during deposition. In a recent application, the manufacture of a helicopter engine combustor casing in a single deposition pass is reported to have produced a surface roughness of 15 μm (R_a) [45]. There have been attempts to improve surface finish in LMD parts without introducing additional equipment or processes. Mahamood & Akinlabi [57] were able to reduce surface roughness in the deposition pass by increasing laser power in a controlled manner. Rombouts et al. [58] were able to improve surface finish by re-melting the surfaces of a deposited structure – the reported roughness was reduced from between 10 μm and 30 μm down to less than 5 μm (R_a). Average roughness, R_a, is a commonly quoted and standardised parameter measured as the root mean square value of the positive and negative vertical deviations from the mean surface level from a linear surface profile within a set sampling length [59].

Layer height and width depend on properties of the material powder and process parameters used in deposition. For example, layer height and width both have a dependence on laser power – the melt pool can increase in area if more energy is absorbed by the substrate or previous layer due to laser irradiance, thus allowing the deposited material to spread out more and lose height before it cools and solidifies [60]. Typical layer geometry (height, width, melt height) is given by Thivillon et al. [61] using the Trumpf DMD 505 system. A list of specifications gives a possible layer height range of 0.2 – 1.2 mm. Their results show that layer geometry varies with traverse speed of the deposition nozzle, powder feed rate and laser power.

Table 3.1. Reported LMD layer height for various materials and deposition geometries

Researchers	Material	Reported Layer Height (μm)	Deposit Type
Mahamood et al. [60]	Ti-6AL-4V	170 – 450	Single track
Kobryn et al. [54]	Ti-6Al-4V	200 – 550	Block
Susan et al. [53]	304L & 17-4PH Stainless Steel	250 (thin wall) 750 (block)	Thin wall & block
Wang et al. [1]	316L Stainless Steel	380	Block
Kamara et al. [62]	Inconel 718	558 *	Thin wall
Rombouts et al. [58]	316L Stainless Steel	450	Block
Wang & Felicelli [63]	410 Stainless Steel	500 *	Thin wall

* Parameter used in Finite Element model of deposited layers; based on expected or experimentally measured layer height

3.3. Quality Control in LMD Manufactured Parts

3.3.1. Quality Requirements and Defect Types

The quality of a part manufactured by LMD, like in other manufacturing processes, is determined by several factors including the accuracy and reliability of part dimensions, surface roughness and consistency, microstructural material properties, and microstructural defects. It is of high importance that the presence and size of defects is minimised to be within acceptable standards as their existence can result in sub-optimal material properties and bring about structural failure sooner than expected [2, 52].

There are two main void-type microstructural defects encountered in LMD-manufactured parts which have been widely reported and studied in terms of measured extent and causes of occurrence. Inter-layer or lack of fusion porosity is caused by insufficient/incomplete melting along layer boundaries and is generally irregularly shaped and elongated in the plane of the deposit. It can occur when there is not enough energy input during deposition to melt the substrate or previous layer [1]. Intra-layer or gas porosity can be caused by a number of factors such as variations of powder mass flow at the nozzle and inclusion of gas pores in process powder before deposition. This type of porosity can exist within the volume of a deposited layer and individual pores are spherical or near-spherical in shape. Both inter-layer and intra-layer porosity are types of defects which are unique to ALM structures due to the

fashion in which they form during manufacture. Crack generation and expansion is also a concern due to high thermal stress and large temperature gradients with rapid rate of temperature change [64].

It is desirable to reduce the frequency and maximum size of such defects in all parts of a deposited structure – near the substrate, in between layers, within layers, and at the surfaces. Ideally, defects would be completely eliminated, but it is more practicable to improve the parameters of the manufacturing process such that the probability of producing a defect of a certain size is sufficiently reduced. In assessing the quality of a part, it is common for defects to be graded according to the size of one measured dimension – this was done for parts manufactured and assessed as part of the FP7 project 'FANTASIA' (Flexible and Near-net-Shape Generative Manufacturing Chains and Repair Techniques for Complex-shaped Aero-engine Parts) using the Trumpf DMD 505 system at TWI Technology Centre (Yorkshire). The overall objective of this project was to develop new manufacturing and repair techniques using LMD. In published work, the researchers detailed the defect size grading system used in the evaluation of defects observed in deposited Inconel 718 structures [46]:

Table 3.2. Grading of several defect types previously used for parts produced with the Trumpf 505 DMD system at TWI

Grade	Gas Porosity: Pore diameter, d (μm)	Lack-of-fusion: Gap length, l (μm)	Cracking: Crack length, l (μm)
1	0 < d <= 50	0 < l <= 50	None
2	50 < d <= 200	50 < l <= 500	10 < l <= 200
3	d > 200	l > 500	l > 200

These grades were defined in consultation with Rolls-Royce plc and are based partly on sizes given as part of a British Standard on imperfections in welded joints [65]. The strictest 'Grade 1' represents the requirement for a part to be deemed of acceptable quality and therefore resulting in adequate performance in real use, while the following two grades were chosen arbitrarily in order to quantify the increase in porosity when depositing a part with decreased heat input. This provides an indication of the size of defects for which it is desirable to be able to detect using on-line laser UT, although the target sensitivity in any given case should depend on the material and quality requirements of the intended application.

The following sections comprise a review of studies, both experimental and using simulations validated by experimental data, on the causes and characteristics of porosity in LMD structures and methods of reducing defect occurrence. In addition, a summary of measured features of LMD structures from these studies is provided for the purpose of setting a realistic range of parameters for the defects simulated in this work, both in FEA and laboratory trials.

3.3.2. Typical Porosity Characteristics

There has been extensive research into the quantification of porosity defect occurrence in structures created using the LMD process, taking into account the causes, locations, frequency, and sizes of both intra-layer (gas) pores and inter-layer (lack-of-fusion) pores. The main motivations of much of this research have been the increase in quality of LMD manufactured parts and cost-efficiency of utilising the LMD process for manufacturing. A quantitative review of reported porosities facilitates the establishment of a range of defect properties to use as input in evaluating the capabilities of laser ultrasonic testing for defect detection in LMD structures.

Wang et al. [1] investigated the origin of porosity in steel bar deposits, taking into account both inter-layer and intra-layer porosity whilst varying process parameters including powder mass flow rate/stability and laser power. They calculated a sphericity coefficient in order to quantify the resemblance of each measured pore to a perfect sphere, with most having a coefficient in the range 0.7 to 0.9 and an average not lower than 0.8. It was concluded that intra-layer porosity could be moderated with better control of powder flow stability. Observation of inter-layer porosity revealed that its formation was more favourable in a deposition environment that allows for higher oxidisation and the presence of un-melted powder.

Ahsan et al. [2] carried out a study into the formation of porosity and minimisation by selection of processing parameters. They found that deposition using powder prepared by gas-atomisation produces more gas porosity than powder prepared using the plasma rotating electrode process (PREP). They also observed a correlation between powder porosity and deposition porosity, although with different volume percentage from powder to deposit. Further minimisation of gas porosity was achieved with a combination of laser power, powder mass flow rate, and deposition speed settings. The authors discuss the complex relationship between laser processing parameters and porosity formation. They also explain that optical microscopy is unlikely to give an accurate measurement of porosity since it only

records planes and not a volume as with 3D X-ray CT, and that the CT method of porosity characterisation is indicatively more reliable. It was reported that inter-layer porosity mainly occurs at the deposition-substrate interface.

Kobryn et al. [54] investigated the effect of deposition process parameter selection, namely traverse speed and laser power, on structural and microstructural properties as well as extent of porosity in deposited block structures. They observed near-spherical shaped intra-layer porosity, originating from existing gas pores in the process powder or entrapment of powder feed shielding gas. It was found more likely to occur in thick-substrate deposits and both types of porosity were minimised by increasing laser power and traverse speed. Inter-layer porosity was found to occur more in thin-substrate deposits and mostly between the substrate and the first deposited layer, caused by incomplete melting along layer boundaries.

Susan et al. [53] investigated the effect of the specification of starting powders and selection of process parameters on the occurrence and severity of porosity in both thin-walled (shell) and thick (block) deposit geometries. They measured the diameters and frequency of porosity from planar microscope photos and applied a correction in order to convert the data to a measure of volumetric diameter. They noted that in general, their histograms of porosity frequency as a function of diameter were not significantly altered in distribution, following an approximately log-normal shape. Their investigation compared the amount of gas porosity in deposited material to the porosity content in different types of process powder, and in general the two quantities were positively correlated. It was also demonstrated that gas porosity can be reduced by re-melting a deposited layer. Inter-layer porosity was attributed to insufficient layer build height, since the deposited surface could be too far vertically from the focal point of the process laser beam.

Carrol et al. [42] measured the effect of process powder recycling on microstructural and material properties of thin-walled deposits. They observed no flaws between the substrate and first deposited layer or between subsequent deposited layers. Intra-layer porosity was ascribed to a likely combination of pre-existing pores in gas-atomised powder and selection of process parameters. No quantification of measured porosity was provided apart from an optical microscope image showing a cross-section of a layer deposited using recycled powder, with visible intra-layer porosity.

Ng et al. [52] investigated the causes of both types of porosity in laser deposited structures and quantified the dependency of the severity of porosity on deposition parameters and melt-

pool dynamics. They attribute different factors to the formation of each type of porosity: intra-layer porosity formation was affected by process parameters, namely laser power, powder feed-rate and shielding gas flow-rate – for example, shielding gas can become trapped by the powder stream and remain in the deposited material. A detailed analysis was provided to explain the tendency of gas pores to be retained in the deposit due to melt pool dynamics, rather than simply rising to the surface. It was noted that the amount of intra-layer porosity in deposited material can be greater than the gas porosity measured in the starting powder, with increased pore diameter due to coalescence. The volume percentage of inter-layer porosity was found to be affected most significantly by deposition powder feed rate, nozzle traverse speed and the extent of overlap of adjacent deposition tracks in the building of block structures, with the latter being relatively less significant. Laser power and shielding gas flow rate are regarded as having a non-significant effect on inter-layer porosity.

Zhang et al. [51] evaluated the macrostructure and microstructure of laser-powder deposited Inconel 718 and compared the deposits before and after heat treatment, measuring improvements in microstructure and material properties after heat treatment was applied. Their analysis included microscope photography of defects including gas porosity, lack of fusion due to un-melted powder and inter-layer micro-cracks. It is noted that during deposition, gas caught in the deposited layer may only escape via the top surface and can become permanently entrapped if not rising to the surface before solidification.

Kong et al. [46] optimised the process of LMD of Inconel 718 powder using the Trumpf DMD 505 system in order to produce high quality parts whilst minimising energy usage and depositing on thin substrates without causing distortion. Their demonstrator parts were created using relatively low laser power and high deposition rate and were found to contain only small amounts of porosity and cracking regarded as acceptable within the provided defect grading system.

Foroozmehr et al. [66] investigated the application of in-process vibration to improve the quality of deposited structures, following on from previous research where the quality of metal castings and welds have been improved using controlled in-process vibration. The effects of applied vibrations, over a range of frequencies and amplitudes, on both defect content and microstructural properties were quantified; it was concluded that vibratory conditions can decrease porosity and improve the yield strength and uniformity of hardness distribution in deposited structures. Furthermore, vibration transverse to the deposition path

was found to be more effective in reducing porosity percentage and maximum diameter. As in other research, it was noted that inter-layer porosity occurred more frequently in the first few layers. This phenomenon is attributed to an increased solidification rate due to heat conduction into the substrate.

Mahamood et al. [60] investigated the effect of varying process laser power on the efficiency of powder utilisation and geometric properties of deposited layers, keeping other deposition parameters constant throughout their experiments. It was found that both layer width and layer height increased with process laser power, and that the latter eventually decreases. They reported only one instance of lack-of-fusion porosity between a substrate and the first deposited layer.

Lewis & Schlienger [67] reviewed the capabilities of the LMD process and the quality of produced parts. Looking specifically at porosity, it was noted that residual gas content in the metal powder can develop into inter-layer and intra-layer pores during solidification of the deposited material.

Table 3.3 summarises the reported intra-layer porosity in terms of percentage (area or volume, as provided) and maximum/minimum diameters (tabular, graphical or visual data) in the reviewed literature. Similarly, Table 3.4 summarises the reported inter-layer porosity in terms of percentage and maximum dimensions. The reported data ranges include measurements from both un-optimised and optimised deposition conditions, where applicable. It should be noted that there is variation in the methods and accuracy of quantification for these data – for example, porosity sizes measured by visual inspection of randomly selected 2D cross-sections may be over-estimated or under-estimated. Nonetheless, a qualitative summary is formed from these results. Following the data tables are typical microscopy images of microstructural flaws from a range of test samples as described in the literature.

Table 3.3. Reported intra-layer porosity volume percentage and sizes for various materials and deposition geometries

Researchers	Material	Reported Porosity (%)	Reported Pore Diameters (μm)	Quantification Method
Kobryn et al. [54]	Ti-6Al-4V	< 0.05 (area)	N/A	Optical Microscopy
Susan et al. [53]	304L Stainless Steel	2.1 (volume, thin wall) *	Min. 4 Max. 98	Optical Microscopy
	17-4PH Stainless Steel	0.1 – 0.3 (volume, thin wall & block) *	Min. 1 Max. 90	
Lewis & Schlienger [67]	Ti-20V/oNb	N/A	Min. < 10 ** Max. 200 **	Optical Microscopy
Ahsan et al. [2]	Ti-6Al-4V (GA)	0.006 – 0.027 (GA)	Min. 20-40 Max. 185	X-ray Computed Tomography
	Ti-6Al-4V (PREP)	0.003 – 0.0024 (volume, thin wall)	Min. 20-40 Max. 230	
Wang et al. [1]	316L Stainless Steel	0.005 – 0.022 (volume)	Min. 20 Max. 180	X-ray Computed Tomography
Zhang et al. [51]	Inconel 718	N/A	Min. < 30 Max. 360	Optical Microscopy
Ng et al. [52]	Inconel 718	0.037 – 0.7 (area)	Min. < 10 Max. 130	Optical Microscopy
Carrol et al. [42]	Waspaloy	N/A	Min. < 10 ** Max. 20 **	Optical Microscopy
Kong et al. [46]	Inconel 718	N/A	Max. < 50	Optical Microscopy
Foroozmehr et al. [66]	AISI H13	N/A	Min. 30 Max. 116	Optical Microscopy

* Calculated from indirect data provided in graphical form

** Approximate values measured from provided microscope photos of deposit cross-sections

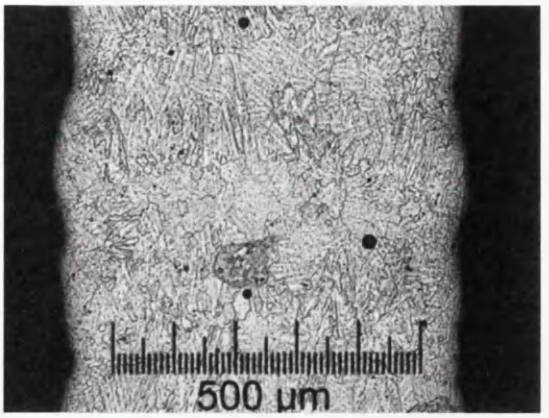

(a)

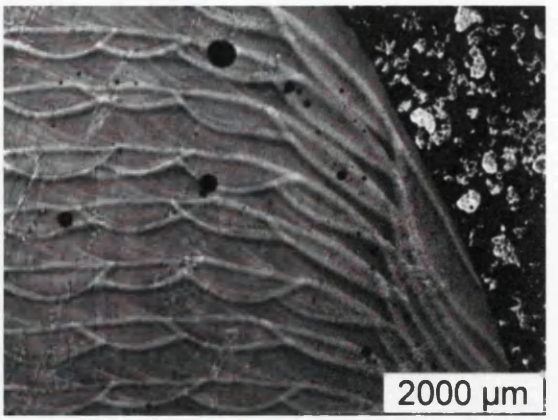

(b)

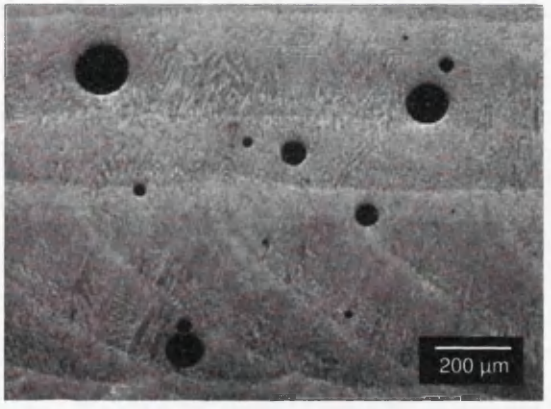

(c)

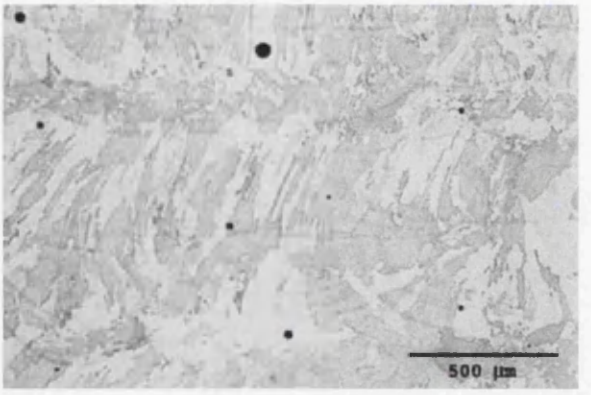

(d)

Figure 3.3. Examples of microscopic images of intra-layer porosity from cross-sections of deposited metal structures: (a) Waspaloy by Carroll et al. [42], (b) Inconel 718 by Zhang et al. [51], (c) Inconel 718 by Ng et al. [52], and (d) 304L/17-4PH Steel by Susan et al. [53].

Table 3.4. Reported inter-layer porosity volume percentage and sizes for various materials and deposition geometries

Researchers	Material	Reported Porosity (%)	Dimensions of largest example (μm) **			Quantification Method
			Height	Length	Ratio	
Kobryn et al. [54]	Ti-6Al-4V	0.02 – 1.2 (area)	170	50	3.5 : 1	Optical Microscopy
Susan et al. [53]	304L & 17-4PH Stainless Steel	N/A	80	60	1.3 : 1	Optical Microscopy
Lewis & Schlienger [67]	Ti-20V/oNb	N/A	350	100	3.5 : 1	Optical Microscopy
Ahsan et al. [2]	Ti-6Al-4V	N/A	150	30	5 : 1	X-ray Computed Tomography
Wang et al. [1]	316L Stainless Steel	N/A	90	60	1.5 : 1	X-ray Computed Tomography
Ng et al. [52]	Inconel 718	0.02 – 0.6 (area)	N/A	N/A	N/A	Optical Microscopy
Foroozmehr et al. [66]	AISI H13	0.2 – 0.96 (area) *	N/A	N/A	N/A	Optical Microscopy

* Includes intra-layer porosity

** Approximate values measured from provided microscope photos of layer cross-sections

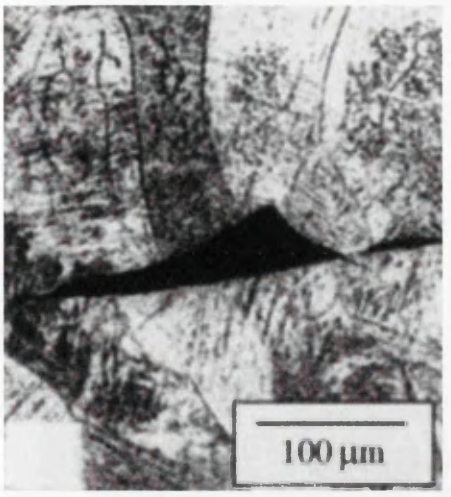

(a)

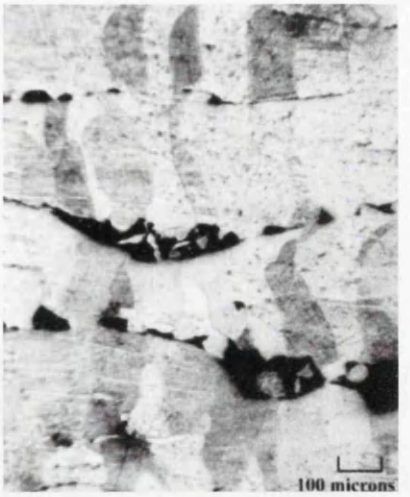

(b)

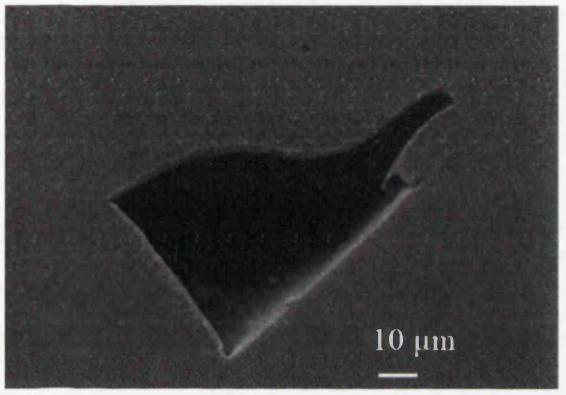

(c)

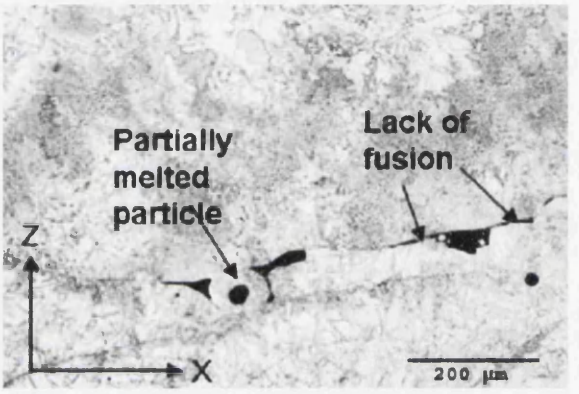

(d)

Figure 3.4. Examples of microscopic images of inter-layer porosity from vertical cross-sections of deposited metal structures: (a) Ti-6Al-4V by Kobryn et al. [54], (b) Ti-20V by Lewis & Schlienger [67], (c) 316L Steel by Wang et al. [1], and (d) 304L/17-4PH Steel by Susan et al. [53].

3.3.3. On-line Quality Control in LMD

There is interest from aerospace companies and organisations in creating solutions for on-line inspection solutions to continuously monitor the quality of deposited structures. This can include quality in terms of physical dimensions and also microstructure and microstructural defects as reviewed in the previous section.

Yang et al. [68] describe the use of a high resolution 3D laser scanning system to inspect the external dimensions of an LMD structure. Each layer was profiled and the deposited structure continuously compared to the intended dimensions stored in a 3D CAD model to ensure sufficient quality before machining to create the final part. Any missing or poor-shaped

volume could be re-deposited before completion of the structure. According to the authors, the system is fast and accurate enough for deployment in a working LMD system.

Wang et al. [64] developed a novel method of recording the formation and propagation of stress-related cracks in the laser cladding process by detecting acoustic emissions from the region where cracks formed. Acoustic emission sensors were attached to the sides of the substrate and protected from heat conduction with integrated water-cooling. The detected cracks were validated using optical microscopy after deposition. Using Finite Element analysis of the temperature field during and after deposition, as well as time and position data of crack formation, it was possible to identify the cause of each crack as hot-cracking or cold-cracking. A parametric study identified the conditions with a higher likelihood of crack formation, demonstrating that the deposition process can be optimised for improved quality using results from continuous on-line inspection.

Clark et al. [69] investigated the capabilities of laser ultrasonic testing for on-line inspection of deposited structures in order to increase efficiency in the LMD manufacturing process by enabling immediate correction to undesired features. Their work made use of high frequency (82 MHz) surface ultrasonic waves, generating and detecting on polished surfaces for optimum optical reflection properties. The SRAS (spatially resolved acoustic spectroscopy) method was used, which relies on a grating of laser lines spaced by one wavelength of the surface ultrasonic wave for transmission and allows for measurement of wave velocity, which can vary with material microstructure [70]. The authors were able to resolve grain boundaries in deposited Nickel alloys, noting that surface wave attenuation is dependent on direction of wave propagation relative to grain orientation. Variations in surface wave amplitude were also measured, enabling the detection of cracks in deposits where crack growth was encouraged by selecting process parameters. These results are reported as a proof-of-concept, with potential for the technique to be further developed for on-line integration.

Klein et al. [71] have successfully published a patent in the U.S.A. for the detection of the scattering of surface ultrasonic waves by sub-surface defects using laser-based transmission and reception on the surface of a deposited layer. The method is intended for on-line inspection of laser cladding and similar metal deposition processes. The detection method describes recording both the initial surface ultrasonic wave arriving directly from a pulsed laser source and any further waves scattered from a defect beneath the surface. For the identification of defect indications, post-processing methods described include calculating the

Mean Square Error between a reference wave-form in a raster scan and all other wave-forms in the raster scan normalised to this reference, as well as performing a wavelet transform on the acquired wave-forms to reveal typical scattered wave characteristics. Examples of experiments performed included titanium and steel plates with defects simulated by drilled holes of diameter 1.0 to 1.5 mm and depth below the surface of 0.4 mm, successfully detected and positioned. No published work has been identified to demonstrate that the described technique has been applied for on-line inspection of laser-based deposition manufacturing.

3.4. Restatement of Work Objectives

The remaining chapters will describe the work carried out in simulated, laboratory and industrial environments towards fulfilment of the following objectives as set out at the beginning of this thesis:

i. The creation of two-dimensional and three-dimensional numerical models to facilitate the simulation of ultrasound generation and propagation via a coupled thermal-mechanical interaction. Geometries will be selected to correspond to typical microstructural LMD flaws as identified through literature review.

ii. To analyse simulated ultrasound propagation and interaction with flaw geometries in order to identify wave signals revealing quantitative information about location and size.

iii. To select and set-up off-the-shelf laser equipment for the purpose of generating ultrasound and receiving ultrasonic surface displacements, and computer equipment for recording received data, suitable for use in laboratory and industrial environments.

iv. To select and manufacture test pieces with artificial flaws inserted corresponding as closely as physically possible to typical microstructural LMD flaws.

v. To conduct laboratory-based off-line sensitivity tests and calibration on the test pieces, applying laser ultrasonic testing techniques as already identified and analysing the capabilities of flaw identification and sizing techniques.

vi. To carry out a trial integration of laser ultrasonic testing and data acquisition equipment into a working LMD system in order to carry out on-line transmission and reception of ultrasound on a relevant LMD part.

To provide analysis of the limitations met and provide recommendations for future work.

Chapter 4: Finite Element Analysis of Ultrasonic Wave Interaction with Common Defect Geometries

4.1. Introduction

Finite Element Method (FEM) is a numerical method for simulating multi-physics interactions (e.g. dynamic, thermal, electrical, etc.) and is commonly applied to engineering problems. In FEM, any particular domain under analysis is discretised into many sub-domains, or finite elements, and partial differential equations are solved with boundary conditions applied. The application of FEM in software for simulating engineering problems is known as Finite Element Analysis. In FEA code, each simulated finite element contains one or more nodes which act as integration points. Boundary conditions, initial conditions and material properties are input by the user. The interaction under investigation is applied as required (e.g. force, heat flux, etc.) and the FEA code calculates stresses, strains and displacements at each node in a succession of time steps, using the results at each step as input for the subsequent step of the simulation.

FEA provides a method of simulating ultrasound generation and propagation in 2D and 3D geometries. This allows for detailed analysis of ultrasonic wave interactions with user-defined geometries and the flexibility to simulate microstructural flaws which can be difficult to produce reliably in real samples. Another advantage of FEA is that it provides for a simulated environment free of noise and varying surface conditions, providing stable and reliable data to validate real NDT. Abaqus FEA is a commercially available software package chosen for the simulation of laser ultrasonic testing in this work. This task is achieved via a three stage process: pre-processing involves geometry creation and input of variables (material properties, surface load, boundary conditions, etc.) via a graphical user interface; in the analysis step the model as input is simulated and user-selected data is recorded; in post-processing the results can be exported as tabular data and/or visual field representations for external analysis and reporting.

4.2. Finite Element Theory

Approximate solutions to systems defined by partial differential equations or integral equations can be found by FEM, whereby a system is discretised into a collection of finite length elements and sufficiently small time increments are chosen to simulate a continuous dynamical system. Each step in the calculation uses values from the previous step, and

therefore initial conditions and boundary conditions are required at the start of a calculation. Since laser-based generation of an elastic stress field relies on heat transfer into a solid material, the thermal conduction equation must first be considered [72]:

$$[K]\{T\}+[C]\{\dot{T}\}=\{q\} \tag{4.1}$$

where [*K*] represents conductivity matrices, $\{T\}$ is the temperature vector, [*C*] is the heat matrix, and $\{q\}$ is the heat source vector. The equation of motion which governs the propagation of waves in an elastic medium is [72]:

$$[M]\{\ddot{U}\}+[S]\{U\}=\{F_{ext}\} \tag{4.2}$$

where [*M*] is the mass matrix, [*S*] is the stiffness matrix, $\{U\}$ is the displacement vector, and $\{F_{ext}\}$ is the external force vector. The above formulation uses an implicit integration rule, which is better suited to 'slow' problems where longer time increments are appropriate. For elastic wave propagation problems, the explicit integration rule is more efficient since the interactions strictly require small element sizes and short time intervals due to the high velocities and frequencies of the waves [73]. A dynamic analysis using explicit integration uses short time intervals because it is only stable if mechanical or thermal information does not propagate further than the length of one element per time step. The use of short time intervals and small elements in a numerical simulation increases the number of calculations required, and therefore increases computational costs.

In an explicit analysis, discrete displacements calculated for each successive time increment only require information about displacements and their time derivatives from the end of the previous time increment; thus the mass and stiffness matrices are not required, providing increased efficiency compared to an equivalent implicit analysis. Since laser-based generation of ultrasound involves an elastic response due to heating, a coupled thermal-stress analysis is required. An explicit analysis uses diagonal element mass matrices, where the equation of motion at a time increment *n* is given by [72]:

$$[M]\{\ddot{U}\}_n+[C]\{\dot{U}\}_n+[K]\{U\}_n=\{F_{ext}\}_n \tag{4.3}$$

The displacement vector in the next time increment is calculated as:

$$\{U\}_{n+1}=f\left(\{U\}_n,\{\dot{U}\}_n,\{\ddot{U}\}_n,\{U\}_{n-1},\{\dot{U}\}_{n-1},\ldots\right) \tag{4.4}$$

The equation of motion given in Equation (4.3) is solved using central-difference integration:

$$\{\dot{U}\}_n = \frac{1}{2\Delta t}\left(\{U\}_{n+1} - \{U\}_{n-1}\right) \tag{4.5}$$

$$\{\ddot{U}\}_n = \frac{1}{\Delta t^2}\left(\{U\}_{n+1} - 2\{U\}_n + \{U\}_{n-1}\right) \tag{4.6}$$

Substituting these solutions into the equation of motion yields:

$$\begin{aligned}&\left[\frac{1}{\Delta t^2}M + \frac{1}{2\Delta t}C\right]\{U\}_{n+1} \\ &= \{F_{ext}\} - [K]\{U\}_n + \frac{1}{\Delta t^2}[M]\left(2C\{U\}_n - \{U\}_{n-1}\right) + \frac{1}{2\Delta t}[C]\{U\}_{n-1}\end{aligned} \tag{4.7}$$

Placing the mass of a particle at the node(s) of each element means that the total mass of an element is equal to the sum of those masses. This is represented by a 'lumped' mass matrix which is diagonal, allowing Equation (4.7) to become uncoupled since the heat matrix is also diagonal [72]. A global stiffness matrix isn't necessary in an explicit analysis because the internal force vector $[K]\{U\}_n$ can be calculated by the summation of element contributions. In order to integrate the thermal conduction equation given in Equation (4.1), forward-difference time integration is applied:

$$\{T_{n+1}\} = \{T\}_n + \Delta t_{n+1}\{\dot{T}\}_n \tag{4.8}$$

This integration is also explicit if a lumped capacitance matrix is used, and therefore both the thermal and mechanical components can be solved simultaneously using a coupled analysis [72]. Abaqus/Explicit uses an explicit finite element solver as described above.

4.3. Finite Element Model Inputs and Parameters

4.3.1. Surface Heat Flux

The finite element model was set up to produce interactions and results as close to the real case as possible. Temperature dependent elements were chosen to allow for the simulation of a surface heat source in a coupled thermal-mechanical analysis. A surface heat flux represents the heat input which in reality would result from the irradiation of a laser beam. This is appropriate since the spatial and temporal properties of a pulsed laser beam are transferred to the resulting surface heat flux. The surface heat flux resulting from a pulsed laser beam with Gaussian spatial and temporal power density profile is given by:

$$Q(x,t) = \frac{(1-R)E}{w} f(x) g(t) \tag{4.9}$$

$$f(x) = \exp\left[-\frac{x^2}{w^2}\right] \tag{4.10}$$

$$g(t) = \frac{t}{\tau^2} \exp\left[-\frac{t}{\tau}\right] \tag{4.11}$$

where Q is surface heat flux and the functions $f(x)$ and $g(t)$ represent the spatial and temporal profiles of the surface heat flux, respectively. The resulting curve for $g(t)$ (Figure 4.2) is normalised such that the maximum value is equal to 1 and values of $g(t)$ and t saved in separate columns in a text file to input as the surface heat flux amplitude variation over time.

(a) (b)

Figure 4.1. (a) Sketch of the function given in Equation (4.10) and (b) cross-sectional spatial light intensity profile of a Quantel Ultra 50 laser output, measured by Lamba Photometrics Ltd. (both axes and colour map displaying intensity with arbitrary units).

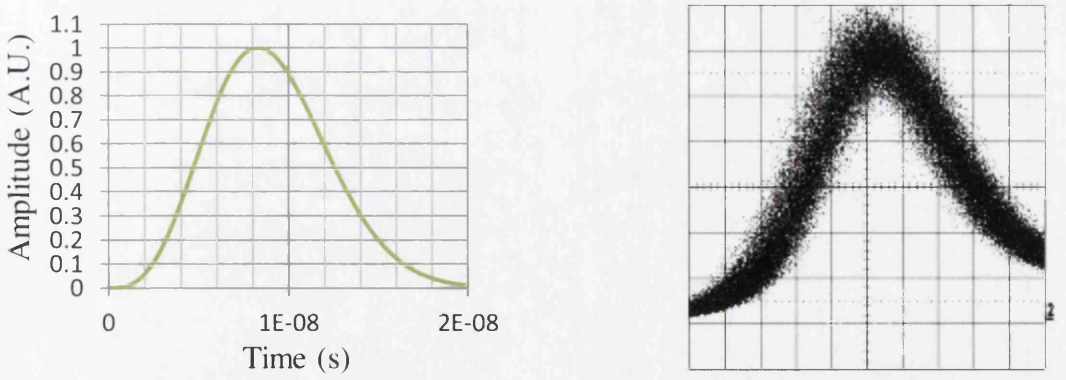

(a) (b)

Figure 4.2. Temporal profile for (a) surface heat flux magnitude with FWHM = 8 ns, plotted according to the function given in Equation (4.11), and (b) real output from a Q-switched Quantel Ultra 50 laser (plotted over many pulses to display timing jitter) [74].

Spatial profile $f(x)$ is applied over the surface heat flux area taking the central point to be x = 0, with a radius of 200 μm. To calculate the magnitude of the surface heat flux to be input, the case should be considered when heat flux is maximised but not high enough to cause melting, thus representing heat input within the thermo-elastic regime. The maximum surface heat flux magnitude is calculated as [73]:

$$Q_{\max} = \frac{T_m \sqrt{\pi} K}{2\sqrt{\kappa \tau}} \tag{4.12}$$

where T_m is the melting temperature of the material. This gives a value of 8.64×10^{10} W m^{-2} at a temperature of 294 K using the material properties of Inconel 718 (Table 4.1) and pulse duration of 8 ns. A uniform temperature field with magnitude 294 K was applied as an initial condition to all geometry in the model to simulate room temperature material before the surface heat flux is activated. Temperature dependent material properties for Inconel 718 were input to ensure thermal and mechanical behaviour close to that of real test samples. To minimise complexity, only isotropic material was considered in this work. In anisotropic material, elastic properties and thus ultrasonic wave speeds vary with direction.

Table 4.1. Typical material properties of Inconel 718 at a temperature of 294K [50] [75] [76].

Symbol	Property Name	Quantity and Units
ρ	Mass density	8193 kg m^{-3}
E	Young's modulus	2 x 10^{11} kg m^{-1} s^{-2}
ν	Poisson's ratio	0.294
α	Expansion coefficient	1.28 x 10^{-5} K^{-1}
C	Specific heat	430 J kg^{-1} K^{-1}
K	Thermal conductivity	11.4 W m^{-1} K^{-1}
κ	Thermal diffusivity	3.24 x 10^{-6} m^2 s^{-1}

4.3.2. Temporal and Spatial Resolution

For Inconel 718 at a temperature of 294 K, the Rayleigh wave velocity can be calculated from the material properties to be 2880 m s^{-1}. It is this wave-type which shall be utilised in

the interrogation of sub-surface discontinuities. For the minimum the defect diameter explored the target Rayleigh wavelength will be no more than twice the minimum diameter of a discontinuity – this method is standard practice in applied ultrasonic testing so will be used here as a reference value. The associated target frequency is then calculated using Equation (2.29). Thus for a minimum discontinuity diameter of 60 μm, the maximum frequency of interest f_{max} is 24 MHz. In order to resolve high frequency elastic waves, sufficient temporal resolution is required. The maximum time increment for each step of the numerical calculation can be reduced in order to accurately resolve high frequency elastic wave components, but a compromise must be considered so that the model remains efficient. The maximum time increment is thus calculated as [77]:

$$\Delta t \leq \frac{1}{20 f_{max}} \tag{4.13}$$

For a maximum frequency of 24 MHz, the time increment should be no greater than 2.08 ns. For adequate spatial resolution of Rayleigh waves, it is essential to ensure that there are enough nodes per wavelength under consideration so the accurate propagation of energy between adjacent nodes. The general recommended quantity can be expressed as [77]:

$$l_e = \frac{\lambda_{min}}{20} \tag{4.14}$$

where l_e is the length of an element. A length of 10 μm satisfies this requirement and also simplifies the element meshing strategy and geometric partitioning as the use of lengths with multiples of this value result in a consistent mesh. In the creation of a finite element mesh, it is only necessary to apply the recommended spatial resolution within the region of interest. This would include the regions where surface heat flux is applied, where the interaction of waves with sub-discontinuities takes place, and any region within which the received surface waves are expected to propagate. Outside of these regions, it is possible to increase the length of finite elements in order to reduce computational requirements without affecting the accuracy of output information. A gradual decrease in element mesh density eliminates the occurrence of ultrasonic stress wave reflections from boundaries generated by a sudden change in mesh density [78].

4.3.3. Selection of Element Types

Abaqus FEA includes a library of elements; for the 2D and 3D simulations carried out, appropriate element types were chosen for the element mesh depending on geometric and

interaction requirements. In the 2D model, geometry sections with only straight and orthogonal edges were assigned element type CPS4RT, a 4-node linear plane-stress quadrilateral element (Figure 4.3). Geometry sections requiring curved edges were assigned element type CPS3T, a 3-node linear plane stress triangle (Figure 4.3), in order to improve meshing structure and avoid excessive element distortion. The letter T in the element name means that temperature degree-of-freedom is taken into account in numerical solving and allows for the simulation of a thermal-mechanical interaction. The letter R in the element name refers to reduced integration which uses lower-order integration for element stiffness and has fewer integration points per element (Figure 4.3), thus reducing the computational cost to run an analysis. This can lead to hourglassing in some first-order linear elements, whereby strains at the single integration point are calculated to have zero value, leading to distortions in the element mesh. Hourglassing control is an option in Abaqus FEA and it is advised that the effect becomes minimised when using a high density mesh [78], such as that required for the accurate calculation of ultrasonic wave propagation. This option was enabled for all elements when available.

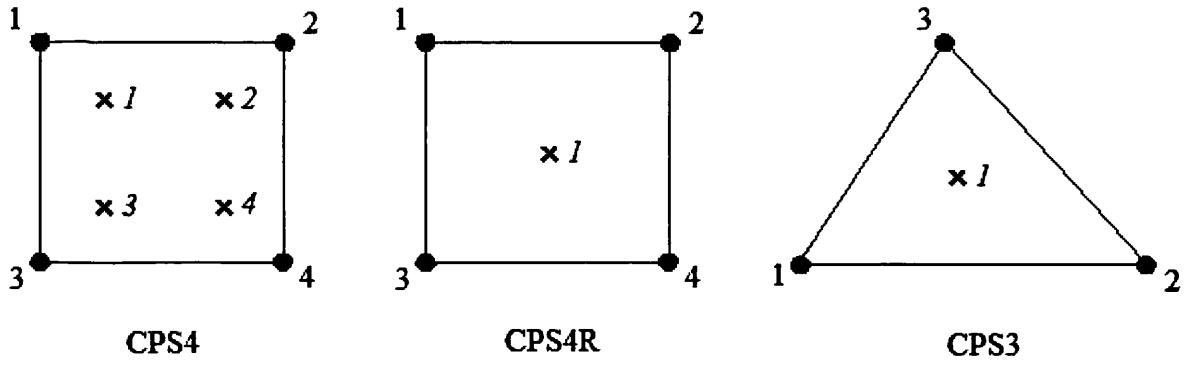

Figure 4.3. Configuration of nodes (black dots) and integration points (crosses) for a selection of 2D linear plane-stress elements.

In the 3D model, element type C3D8RT was used. This is an 8-node linear displacement brick element (Figure 4.4). Reduced integration, temperature dependence, and hourglassing were applied.

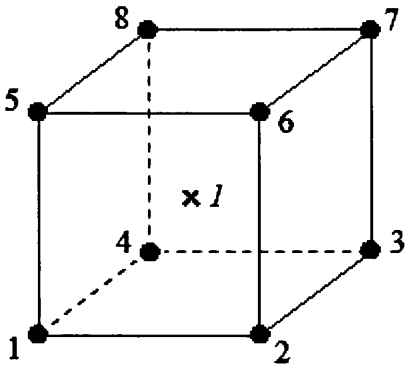

Figure 4.4. Configuration of nodes and integration points for element C3D8R.

To further reduce computational cost, only the region within a few millimetres of the surface of applied heat flux was assigned temperature dependent elements. Beyond this depth, thermal-mechanical interactions are not expected to be of significance to the analysis.

4.3.4. Geometries and Transmission/Reception Configuration

Model geometry was created to simulate that of the thin-walled test pieces to be used in laboratory-based ultrasonic testing, with a depth of 11 mm parallel to the *y*-axis and a length of 20 mm parallel to the *x*-axis (Figure 4.5), ensuring that surface wave reflections from each corner do not return within the time period of interest. Surface heat flux is applied over a line/area of prescribed width by partitioning a thin section at the surface. This is repeated for each desired source position. In the 2D model, discontinuities were included in the form of a circular hole positioned centrally along the length and close to the top surface (Figure 4.6). Diameters of 240 μm, 120 μm, 100 μm, 80 μm and 60 μm were investigated separately to represent a range of sizes corresponding to those reported in literature as summarised in Section 3.3.2. Additionally, the distance between the top of the discontinuity and the surface where transmission and reception takes place was set as 100 μm or 300 μm.

In the 3D model, the same geometry is extended in an additional *z*-axis to simulate thickness of the thin-walled structure; the thickness was set to 0.5 mm. A discontinuity was included in the form of an enclosed spherical volume positioned centrally and near the surface, with a diameter of 150 μm and a depth of 100 μm (Figure 4.7). The geometry in this model has symmetry in the *x*-*y* plane along the length, so it was only necessary to include half of the geometry and apply a symmetry boundary condition along this face, further reducing computational cost. Each area of applied surface heat flux was approximated to a rectangular shape in order to simplify geometry partitioning and improve meshing efficiency.

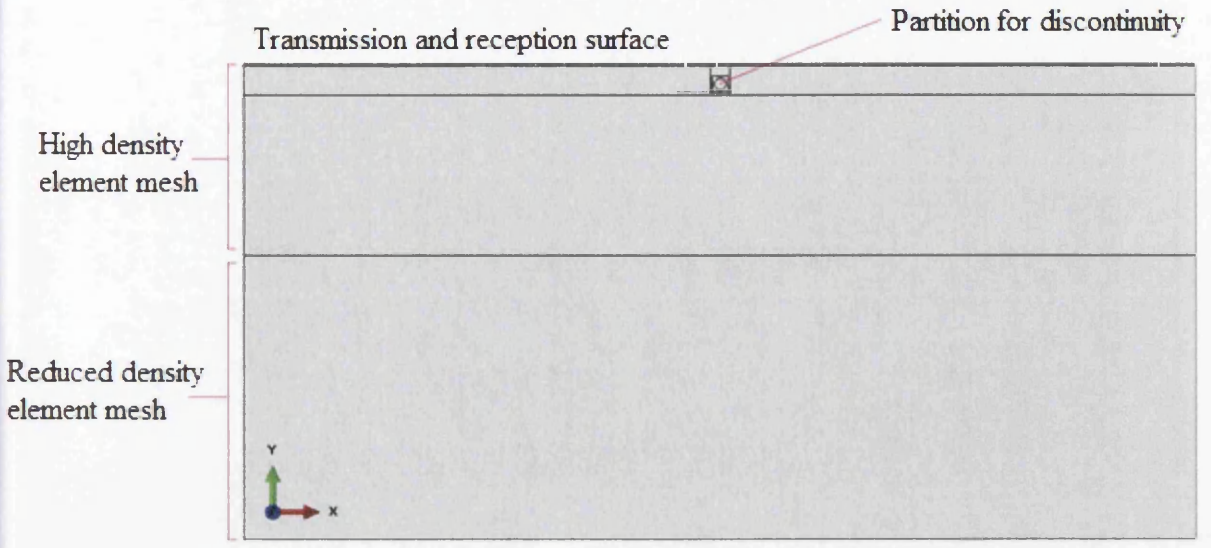

Figure 4.5. Overview of representative geometry and meshing strategy in the 2D and 3D models

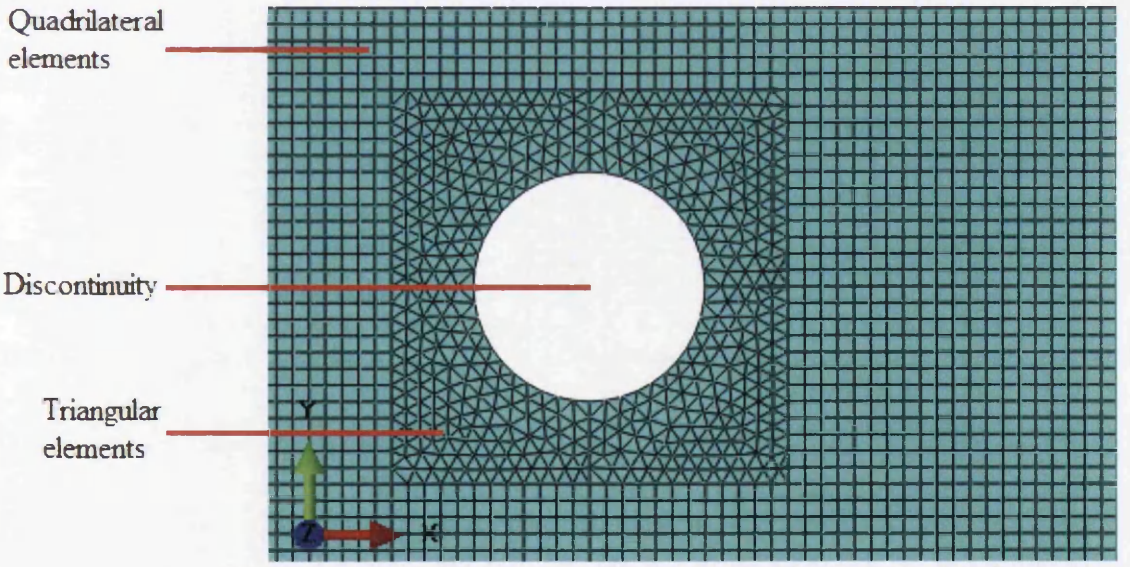

Figure 4.6. Detail of sub-surface discontinuity and meshing strategy in the 2D model.

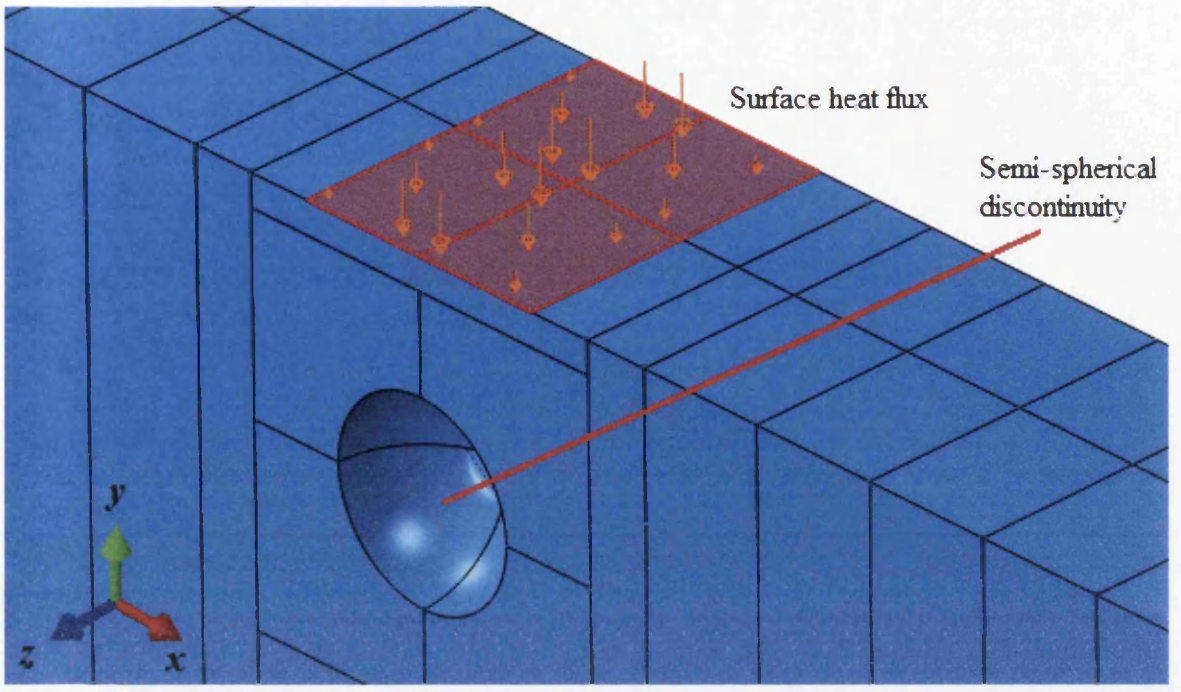

Figure 4.7. Detail of sub-surface discontinuity and area of applied surface heat flux with orange arrows representing Gaussian intensity distribution.

It was necessary to run a separate simulation for every position of the heat flux to simulate its movement across the surface. A sub-routine exists for Abaqus/Implicit analyses to simulate the continuous motion of a surface heat flux as a function of time; however, this sub-routine is not available for use with an Abaqus/Explicit analysis [78]. Similarly, the reception of ultrasonic surface displacements is accomplished by the selection of a vertex on the partitioned surface for each desired position.

From any number of selected positions, a history output can be defined to record relevant variables as a function time and by increments greater than or equal to Δt as given in Equation (4.13). A-scans are recorded in this manner. Two strategies were utilised for the transmission and reception of ultrasonic waves. Scanning laser detection (SLD) has the source stationary whilst the reception position is scanned over a series of positions (Figure 4.8). Constant laser separation (CLS) has the source and reception position separated by a fixed distance and both are scanned in tandem over a series of positions (Figure 4.9). In the models described above, a series of source and/or reception positions follow a linear path on the top surface to form a scan over the position of the sub-surface discontinuity. This surface is assigned as being coincident with the x-axis in 2D or coincident with the x-z plane in 3D. B-scans were generated from successive A-scans using the CLS method in increments of 0.1

mm and with a separation of 1 mm between source and reception. In these outputs, the initial position of the reception point is referred to as $x = 0$.

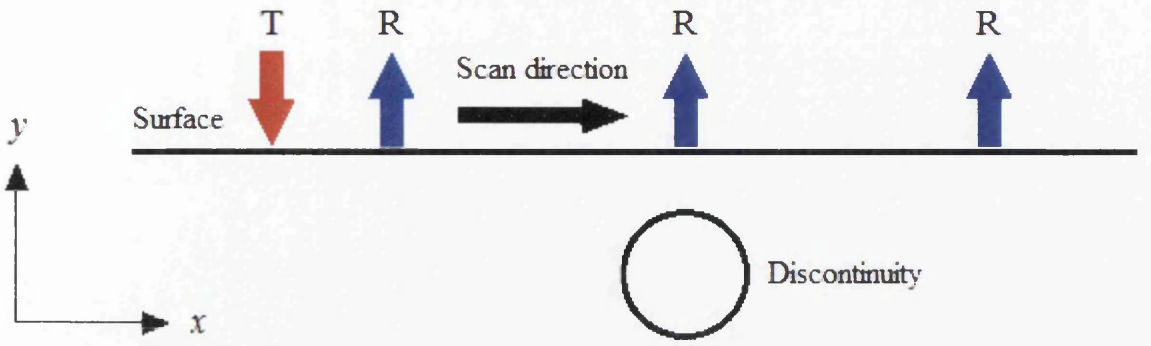

Figure 4.8. Schematic diagram showing the configuration of transmission (T) and reception (R) positions for the SLD method.

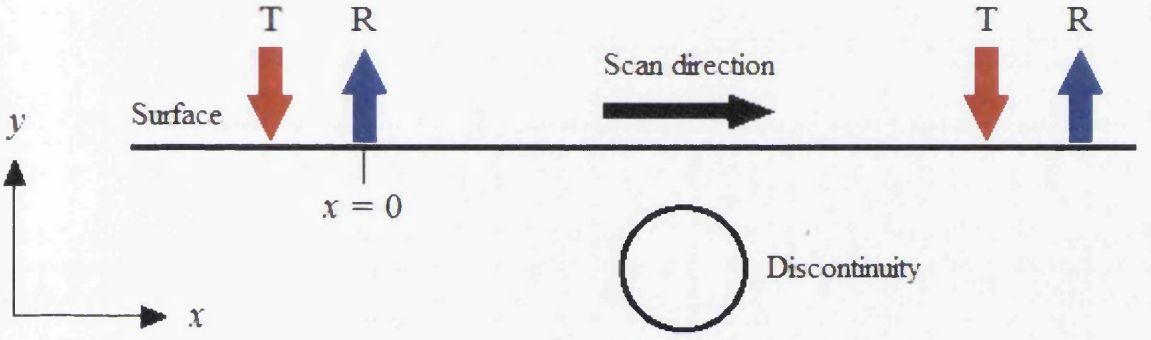

Figure 4.9. Schematic diagram showing the configuration of transmission (T) and reception (R) positions for the CLS method.

An alternative format for recording variables as a function of time is in a field output. This type of output can be specified over regions of model geometry and displays nodal data visually as a field of values, for example in the form of vector arrows or coloured contours.

4.4. Results & Analysis

4.4.1. Thermal and Mechanical Response

In Figure 4.10, the surface temperature rise as a function of time is shown as measured at the node in the centre of the line where surface heat flux was applied. The temperature profile is compared between two cases: with a pulse amplitude-time input representing a square temporal profile (with instantaneous activation and de-activation of peak flux magnitude), and with a pulse amplitude-time input representing a Gaussian temporal profile. In the latter case, there is a delay in the rise of surface temperature as expected due to a gradual increase

to maximum flux magnitude. In both cases, the temperature profile agrees with that predicted by the analytical method of calculation seen in literature.

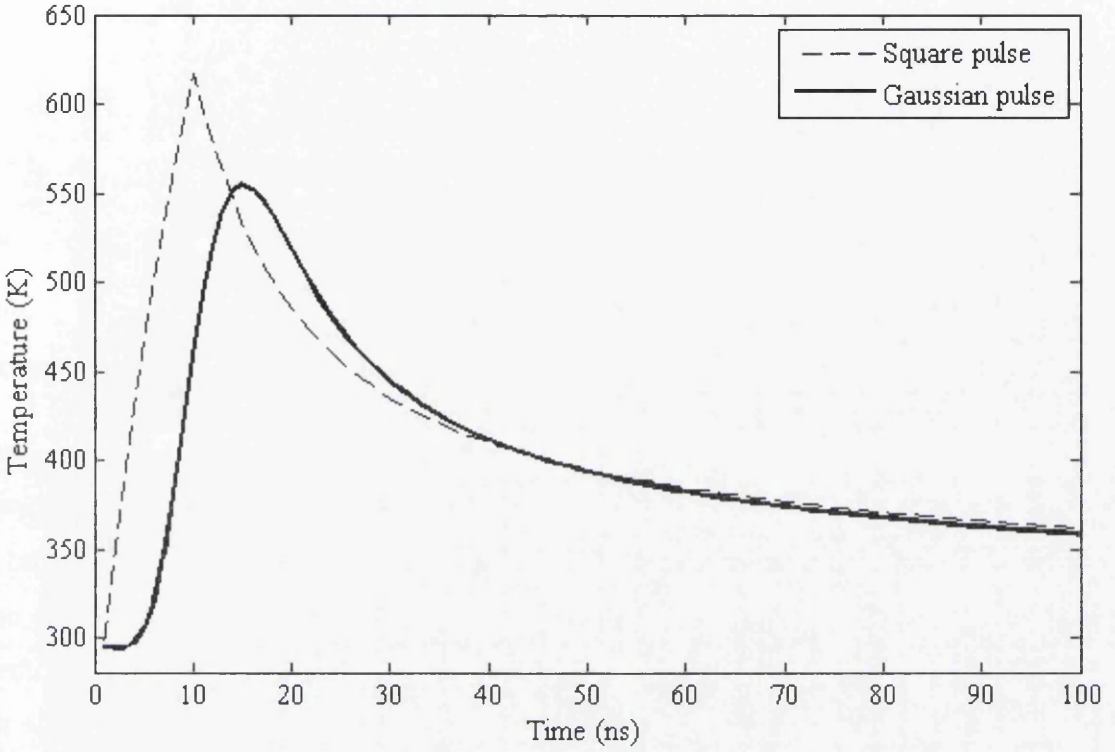

Figure 4.10. Surface temperature as a function of time at the centre of heat flux ($z = 0$).

The temperature field over a larger part of the geometry near the position of surface heat flux can be seen in Figure 4.11 and Figure 4.12; the conduction of heat into the bulk of the material is observed. At any given time, the highest temperature exists at the centre of heat flux and displays a Gaussian distribution over its length equivalent to the spatial distribution of heat flux magnitude, then decreases with distance in all radial directions within the solid.

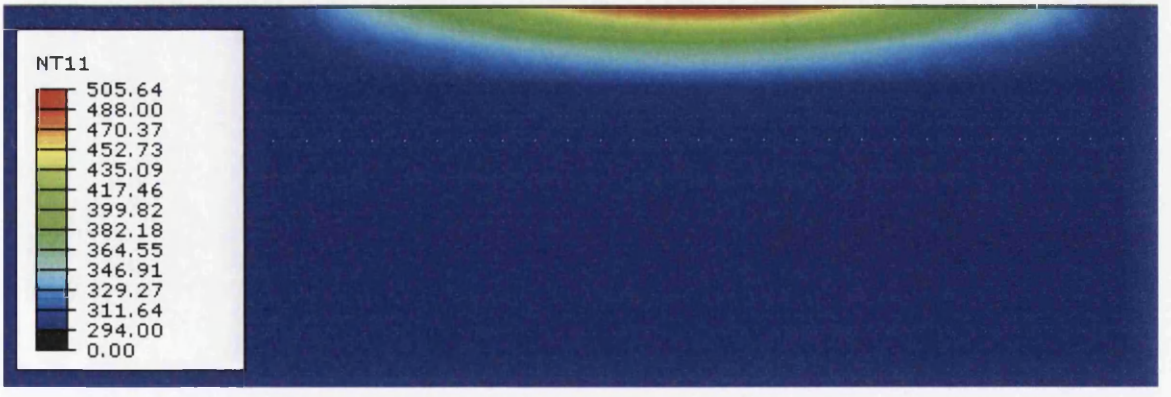

Figure 4.11. Nodal temperature field below the surface heat flux at $t = 20$ ns. The maximum depth shown is 80 μm. Temperatures are in units of Kelvin.

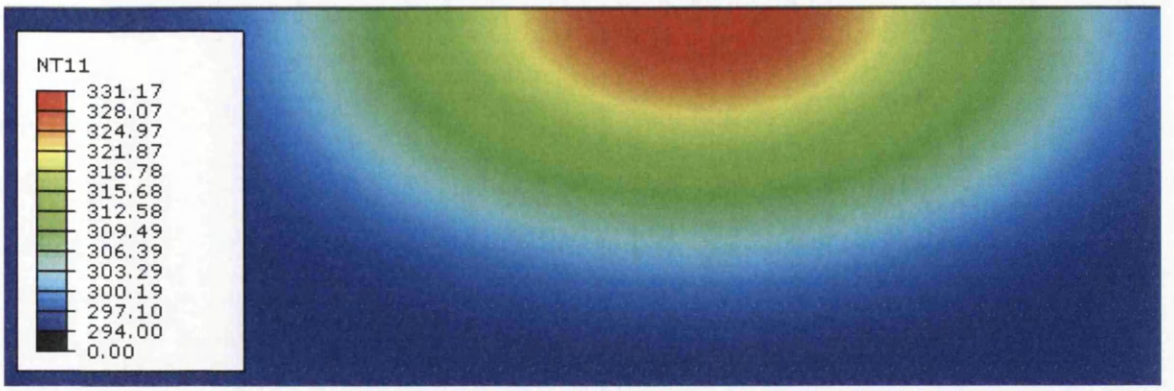

Figure 4.12. Nodal temperature (Kelvin) field below the surface heat flux at t = 200 ns. The maximum depth shown is 80 μm. Temperatures are in units of Kelvin.

Figure 4.13 shows all of the ultrasonic wave types produced by the heat source in the form of a displacement field over a section of geometry. The direction of propagation of each wave can be imagined as a vector originating from the position of surface heat flux to a point on the wave-front. The individual waves become separated after a time due to variation in wave speeds and the distance propagated by each wave-front at any particular time corresponds to their speeds. The directionality of the longitudinal and transverse waves is as expected for a thermo-elastic heat source.

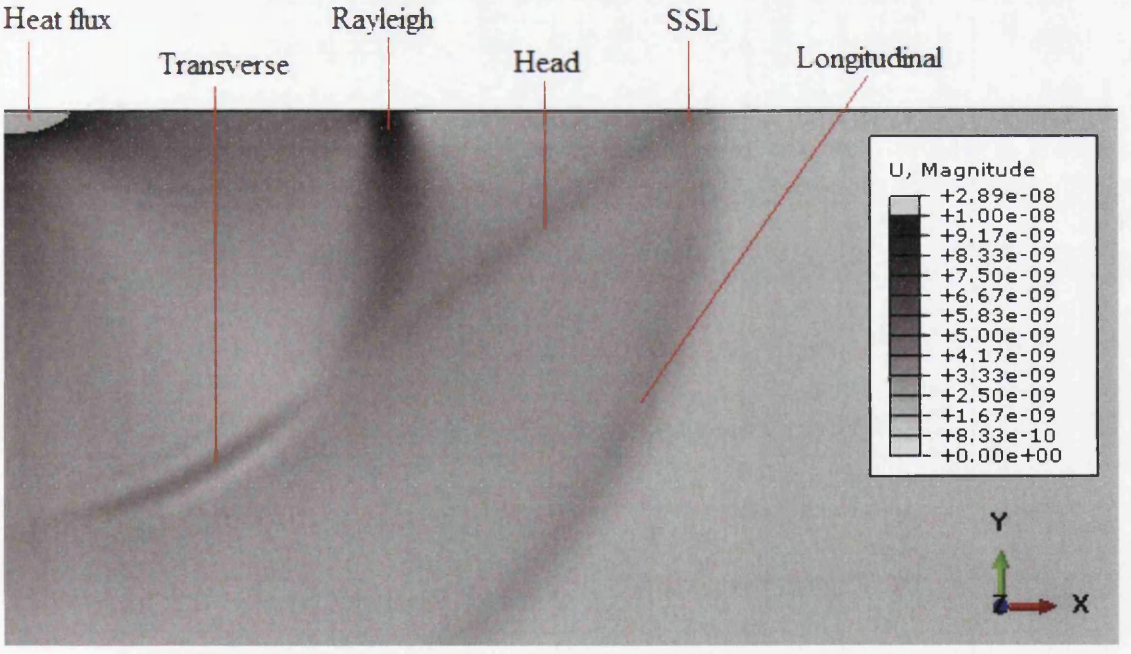

Figure 4.13. Displacement field generated by surface heat flux, at t = 500 ns. Displacements are in units of metres and represent the magnitude of all three axes.

In Figure 4.14, typical out-of-plane surface displacements at some distance from the source are displayed. Wave-forms in the signal correspond to different surface waves with varying arrival time according to their speed of propagation. Displacements measured at the same surface position are also shown for varying temperature field applied to model as an initial condition. The elastic modulus of a solid material is inversely proportional to temperature as a result of changes in inter-atomic bond forces [79]. Due to the dependence of wave speed on elastic modulus given in Equation (2.27) and Equation (2.28), it is expected that the arrival time is delayed at higher temperatures. The amplitude of measured surface displacements decreases with raised material temperature due to a reduction in heat absorption capacity.

Spurious oscillations are an expected feature in finite element modelling of elastic wave propagation. The central-difference solving method assigns a maximum time increment calculated from the propagation of the fastest wave velocity across the smallest element. Thus the most accurate result is produced for longitudinal waves, whilst other wave types display small oscillations due to a mismatch in the time increment stability limit [80].

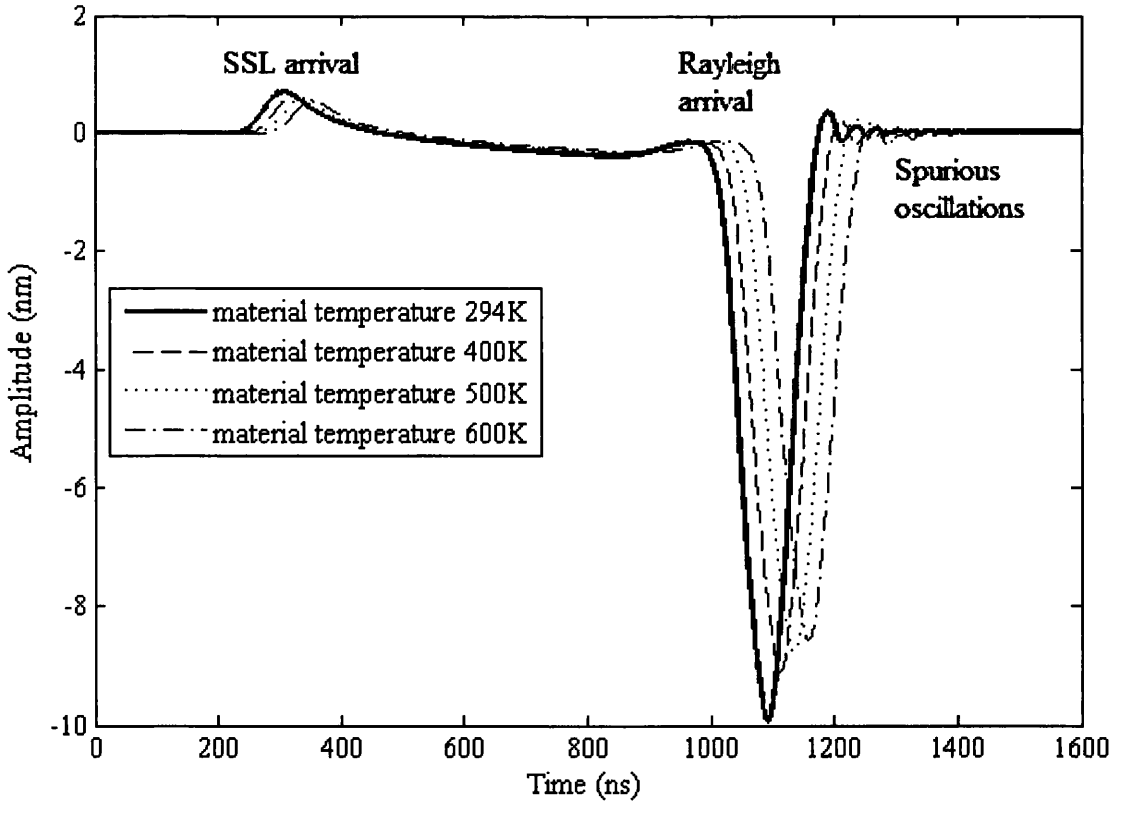

Figure 4.14. Typical surface displacements as a function of time with varying material temperature.

4.4.2. Interaction with Discontinuities in 2D – Static Analysis

This section will look at ultrasonic displacement data at discrete surface positions. A view of the displacement field over a section of the simulated geometry provides visual evidence of the propagation of elastic waves and their interactions with sub-surface discontinuities. In Figure 4.15, this is displayed in a series of frames representing an arbitrary progression in time. The elastic wave source was a surface heat flux with Gaussian spatial and temporal profile and a radius of 250 μm, applied at some distance from a sub-surface discontinuity at a depth of 100 μm with diameter 140 μm. The colour scale represents field magnitude, taking into account both x and y displacements in this case; the scale is constant throughout all frames.

In frame (a), waves which are characteristic of a thermo-elastic source (Figure 4.13) can be seen before reaching the position of the discontinuity. The next frame shows reflection of the longitudinal wave in a radial wave-front, with some of the wave energy being directed towards the surface in the region above the discontinuity. At the same time, some energy from the SSL wave is reflected and reverses in propagation direction along the surface. In frame (c), the Rayleigh wave arrives at the truncated region of geometry above the discontinuity and there is a clear increase in amplitude of the wave which exists within this region. The Rayleigh wave-front also experiences distortion whilst propagating around the discontinuity. The final frame shows that the main Rayleigh wave continues to propagate while some of its energy is reflected back towards the source. This view reveals several possible indications of the presence of a sub-surface discontinuity which can be studied in more detail by measuring out-of-plane surface displacements.

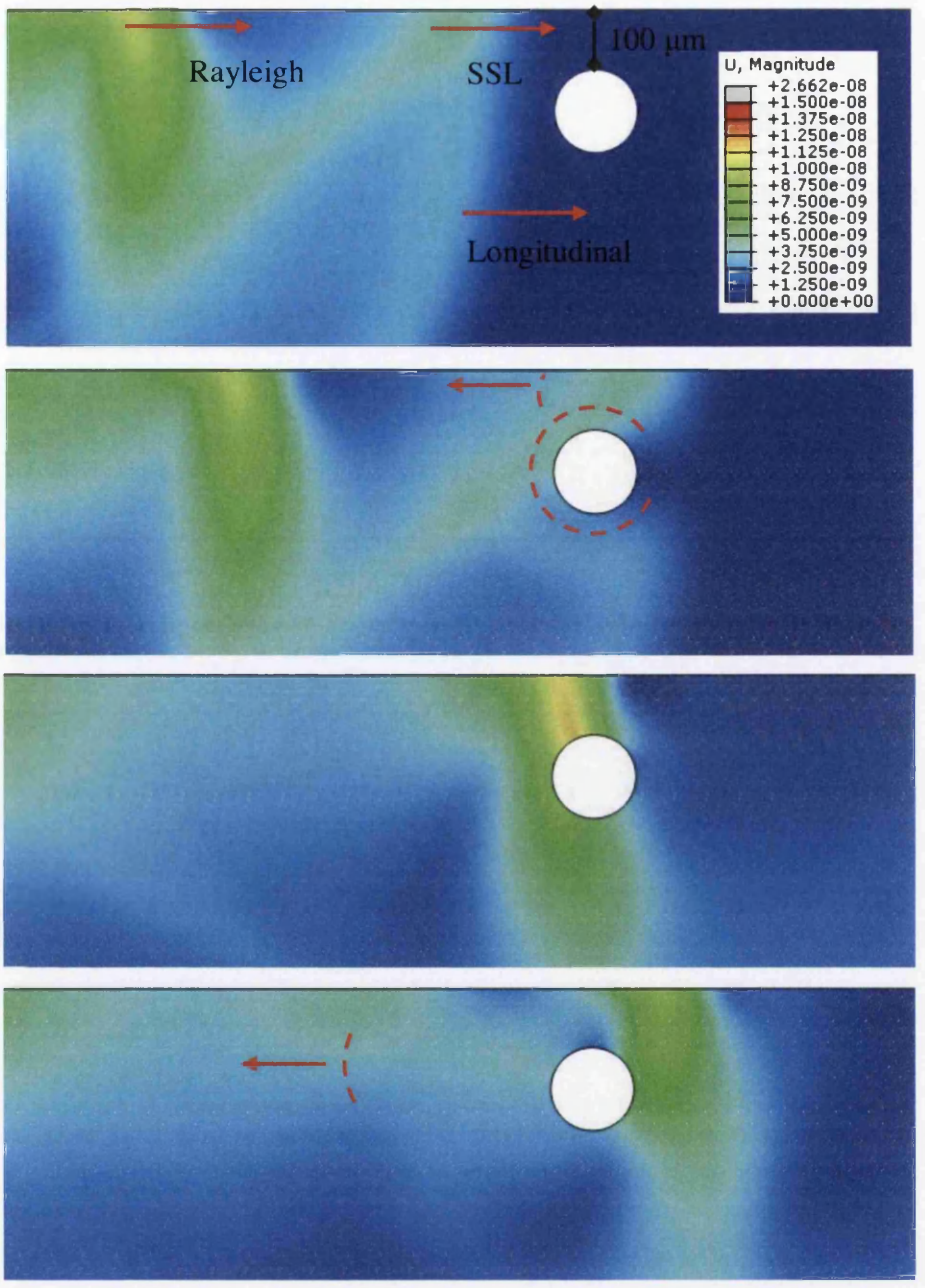

Figure 4.15. Displacement field interactions with a sub-surface discontinuity of depth 100 µm and diameter 140 µm. Reflected waves are labelled in red and displacements are in units of metres.

An alternative view of the displacement field is given in Figure 4.16, where out-of-plane (*y*-axis) displacements are represented in polarity and magnitude by the direction and size, respectively, of vector arrows. In the first frame, two wave types are discernable: the SSL wave has a positive out-of-surface displacement and the Rayleigh wave displays a relatively large negative out-of-plane displacement. This corresponds with characteristic displacements as measured at the surface (Figure 4.14). The next frame shows the resulting configuration after both of these waves have propagated beyond the discontinuity. At least part of the SSL

wave is reflected towards the source, while energy reflected due to the arrival of the Rayleigh wave takes the form of an initially negatively polarised out-of-plane displacement followed by a positive component, from the perspective of its propagation direction. The shape of the signal of such a wave as measured at the surface should match this description if reception takes place sufficiently far from the position of the discontinuity.

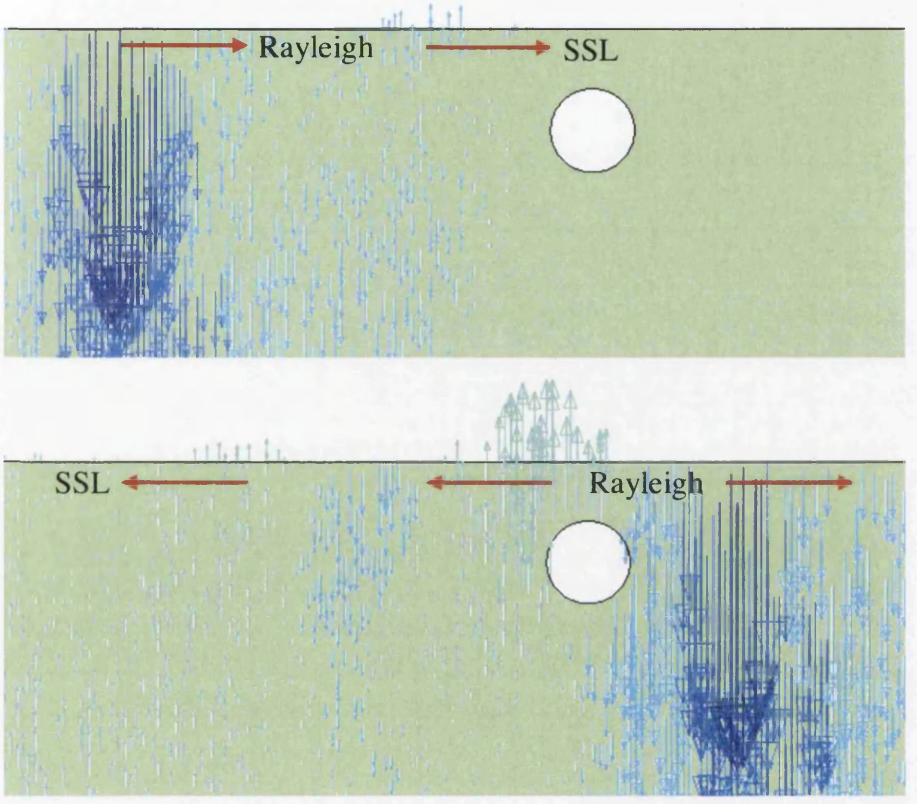

Figure 4.16. Out-of-plane displacement vector field interactions with a sub-surface discontinuity of depth 100 μm and diameter 140 μm. Red arrows represent wave propagation.

There are several cases to consider in searching for indications in measured surface displacements. There may be changes in the main signal when either the source or reception point is located directly above a discontinuity, when both are located either side of a discontinuity, or there may be visible reflection signals measurable at distant positions. Figure 4.17 compares the surface displacement signal as a function of time as received directly above a discontinuity of depth 100 μm and diameter 140 μm to the signal measured at the same position but with continuous geometry with no inner boundaries. There is a significant increase in positive out-of-plane displacement at the tail-end of the Rayleigh wave and for the SSL wave, which also appears to exhibit a delayed arrival time. An increase in peak-to-peak amplitude may provide a useful indication of diameter and/or depth. Figure 4.18 compares the received control signal with that of the case when the heat source is placed

above the discontinuity. There is a relatively slight increase in the magnitude of the Rayleigh displacement and some disturbance in the waveform after this time. Overall, the changes in the signal are less significant.

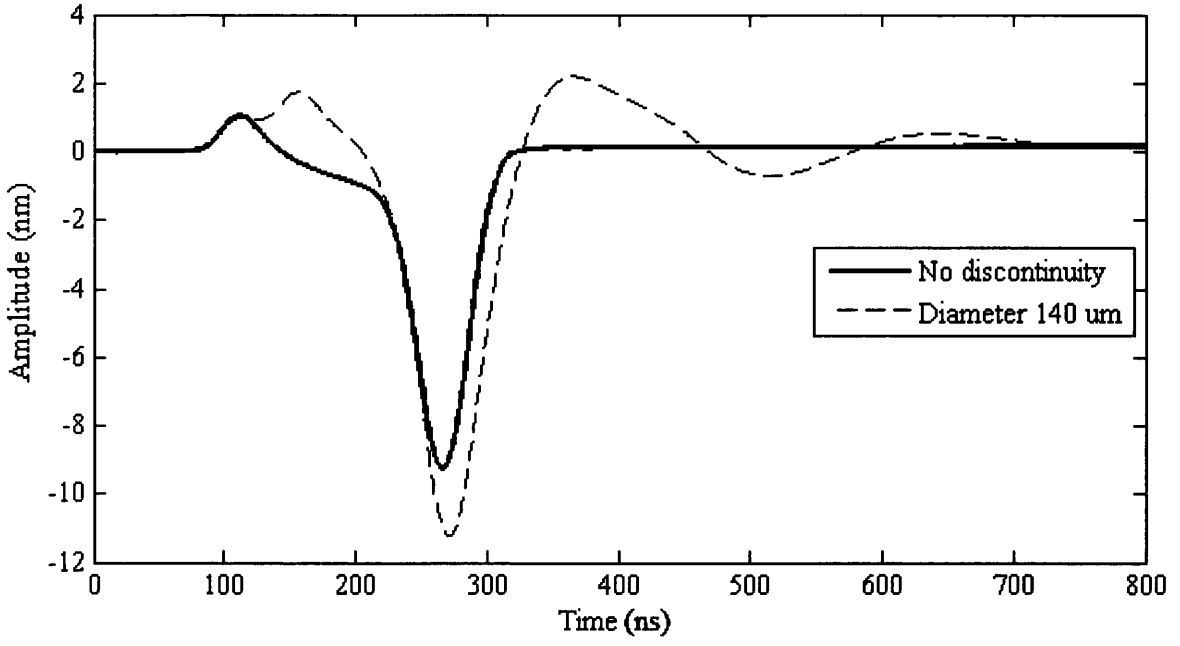

Figure 4.17. Surface displacements as a function of time with the reception position directly above the centre of a sub-surface discontinuity of depth 100 μm and diameter 140 μm.

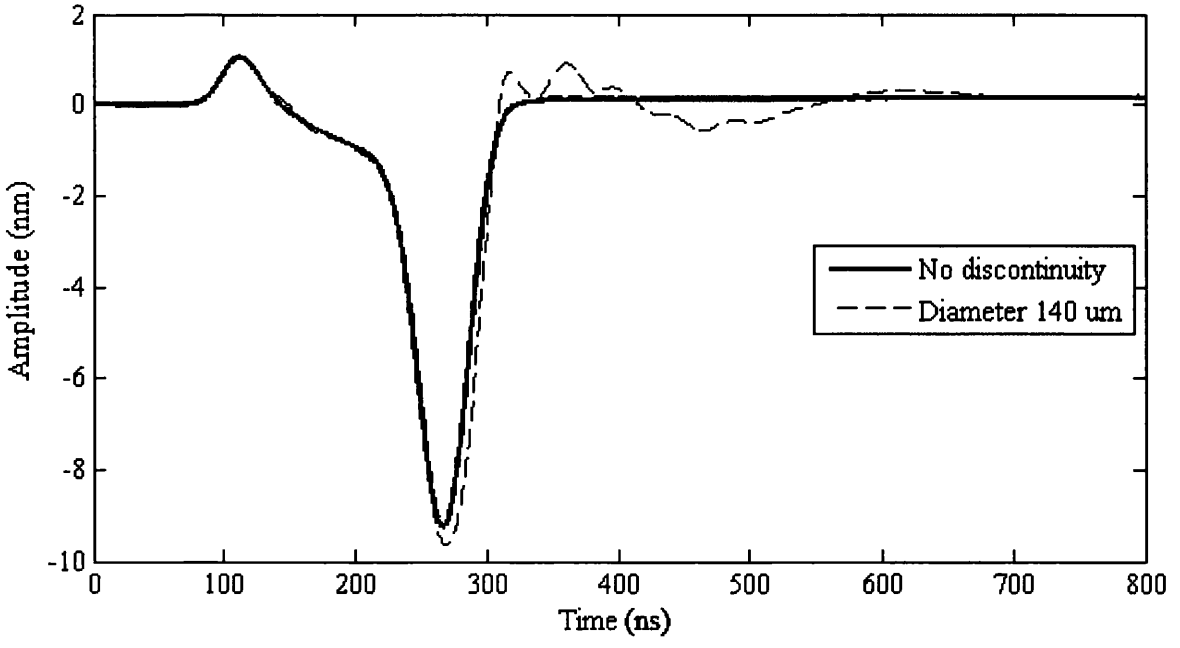

Figure 4.18. Surface displacements as a function of time with the heat source directly above the centre of a sub-surface discontinuity of depth 100 μm and diameter 140 μm.

The following results display surface displacements as received from a position 5 mm from a sub-surface discontinuity, with the heat source also separated by 5 mm from the discontinuity in the opposite direction. Outputs are separated to analyse individually each combination of depth and diameter. In Figure 4.19, it can be seen that the amplitude of the upper and lower peaks of the Rayleigh signal decrease as a discontinuity is introduced, compared to the control signal. As the diameter increases, the Rayleigh signal is damped further. It is suggested that the transmitted Rayleigh wave has reduced energy compared to the incident wave due to reflection at the boundary of the discontinuity. This effect is proportional to the diameter of the circular boundary.

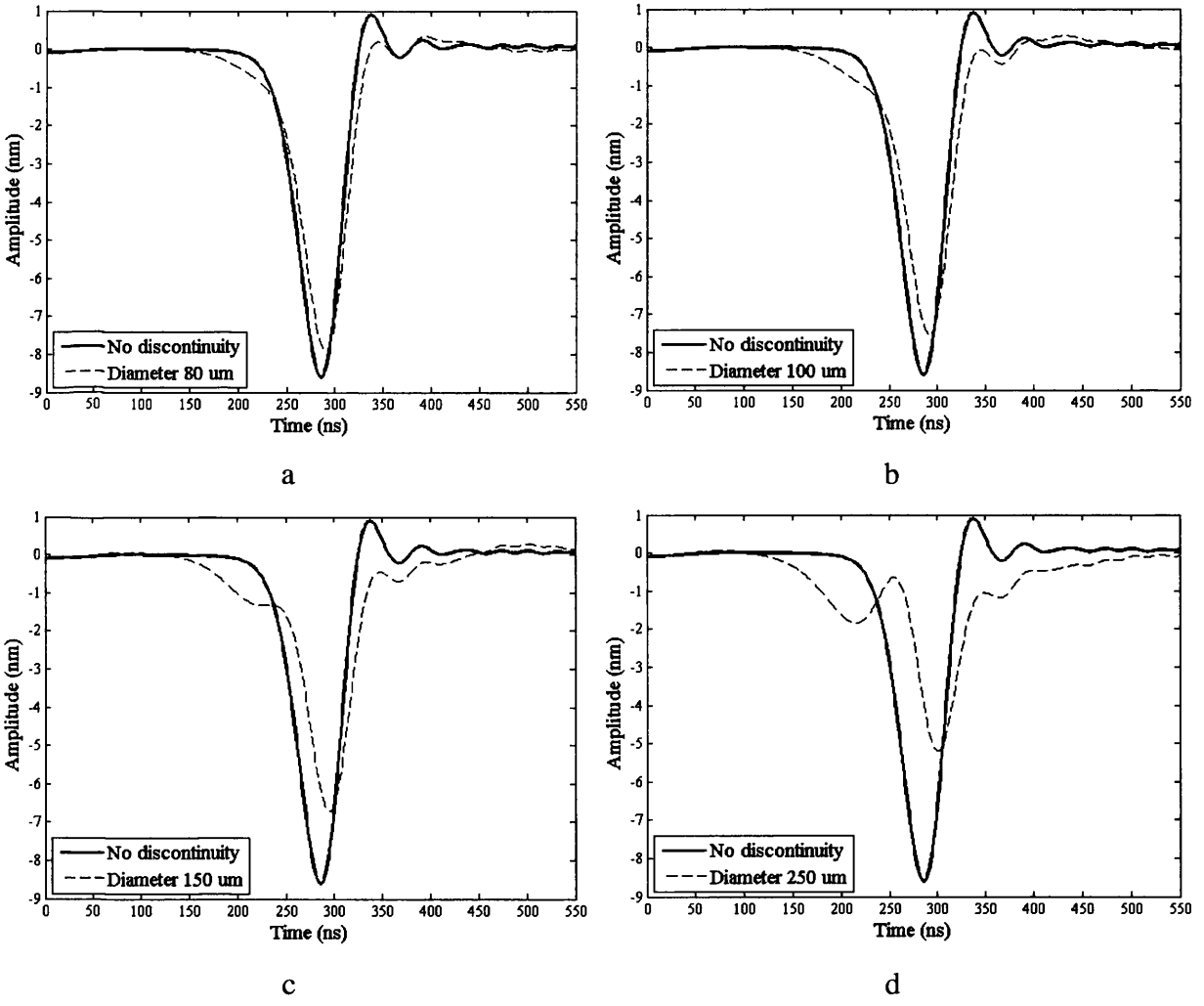

Figure 4.19. Surface displacements as a function of time with a discontinuity of diameter (a) 80 μm, (b) 100 μm, (c) 150 μm, and (d) 250 μm located between the transmission and reception positions at a depth of 100 μm.

A quantitative measure of the reduction in the magnitude of the lower Rayleigh peak is provided in terms of percentage amplitude loss (Figure 4.20). There is a good linear trend of

amplitude reduction with increasing diameter at both depths considered. When the discontinuity is located at twice the depth, a smaller loss in amplitude is seen. This is consistent with the fact that more of the Rayleigh wave's energy lies closer to the surface of propagation, thus energy loss for a transmitted wave should be less when the obscuring boundary exists at a greater depth. For each diameter, the loss is greater with closer proximity of the discontinuity to the surface and this difference diverges with increasing diameter. For the smaller diameters considered the loss in amplitude approaches insignificance and may be difficult to measure in real conditions.

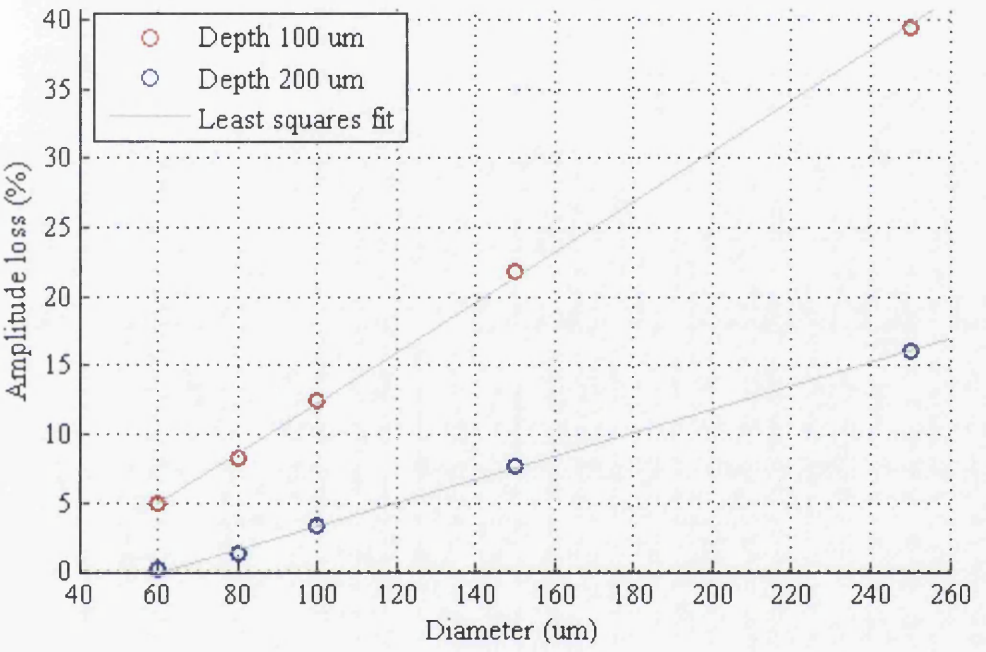

Figure 4.20. Rayleigh wave signal percentage amplitude loss as a function of discontinuity diameter.

4.4.3. Interaction with Discontinuities in 2D – Dynamic Analysis

This section will look at ultrasonic displacement data over multiple position intervals, which is more applicable to in-situ testing as either the ultrasonic equipment or test surface are expected to be in constant motion. The following results represent the application of the CLS method in the 2D model. In each simulation, the separation between source and reception was 1 mm and A-scan signals recorded at intervals of 0.1 mm with a discontinuity located half-way along the scan path. A representative B-scan is displayed in Figure 4.21. The main surface wave arrival signals are static in time due to the fixed separation of transmission and reception. Reflection 'arms' of both the SSL and Rayleigh waves are clearly resolved and each appear with a constant gradient corresponding to the expected wave speeds. From the

beginning of the translation of the reception position over the discontinuity (x = 2.0 mm) until the translation of the source over the same location (x = 3.0 mm), indicated by the red lines on the B-scan, there appears an additional surface displacement signal with positive and significant out-of-surface amplitude. This coincides with a reduction in amplitude of both the SSL and Rayleigh wave signals over the same region. Initially, this signal has an arrival time approximately equal to that of the SSL wave and finally equal to that of the Rayleigh wave. This might be explained by considering the directionality of bulk ultrasonic waves generated by a thermo-elastic heat source and also the reflection of these wave types from the upper edge of the sub-surface discontinuity as the source passes above.

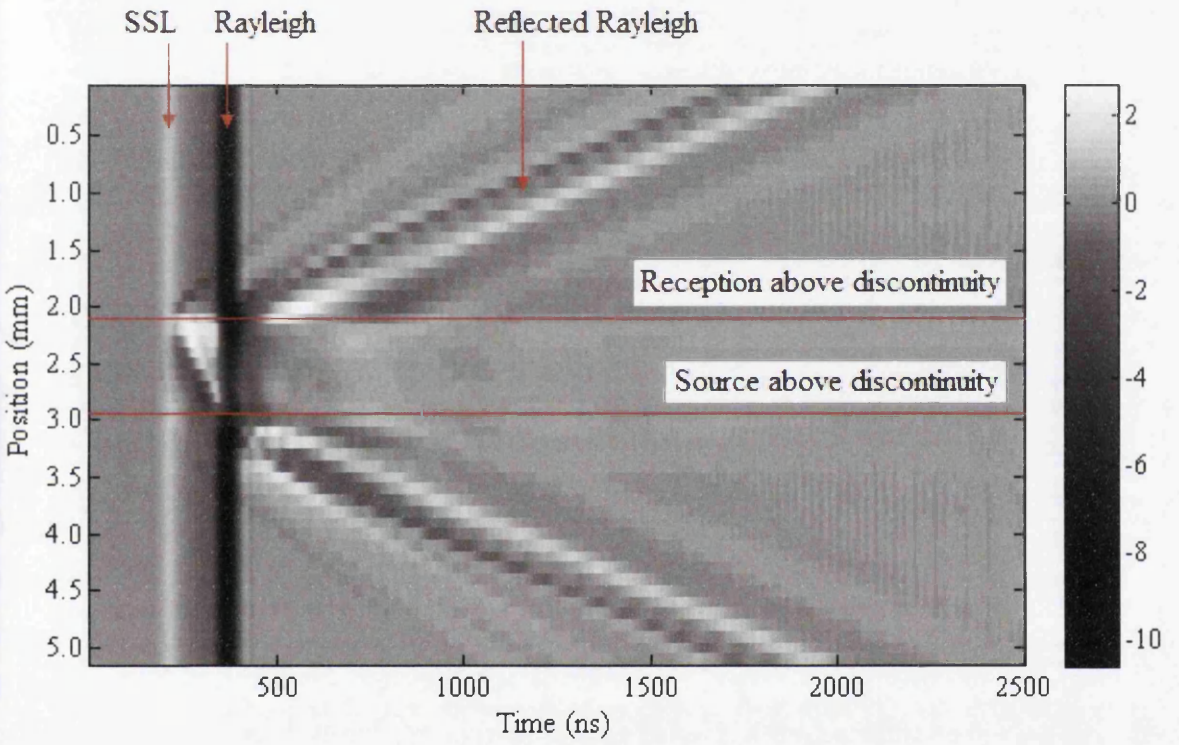

Figure 4.21. Surface displacements as a function of time and reception position with a sub-surface discontinuity of depth 100 μm and diameter 240 μm. Amplitude scale is given in nanometres.

The directionality of longitudinal and transverse waves as produced by a thermoelastic source, previously shown in Figure 2.19, is superimposed onto a sketch of the wave-front paths in Figure 4.22 below. For simplicity, a wave-front path is considered for each of the two wave-types which originate at the heat source and from the centre of the angular range of transmission direction. In configuration (a), part of the faster longitudinal wave reflects from the discontinuity and propagates to the reception position at the surface, arriving after the

SSL wave and before the Rayleigh wave. The transverse wave is directed into the bulk. In configuration (b), part of the slower transverse wave reflects from the discontinuity and propagates to the reception position at the surface, arriving around the same time as the Rayleigh wave. The longitudinal wave is directed into the bulk. In both cases, the arrival signal would appear as a positive out-of-plane signal and in reality there should be a transition between the types of particle motion and thus speed in the reflected energy.

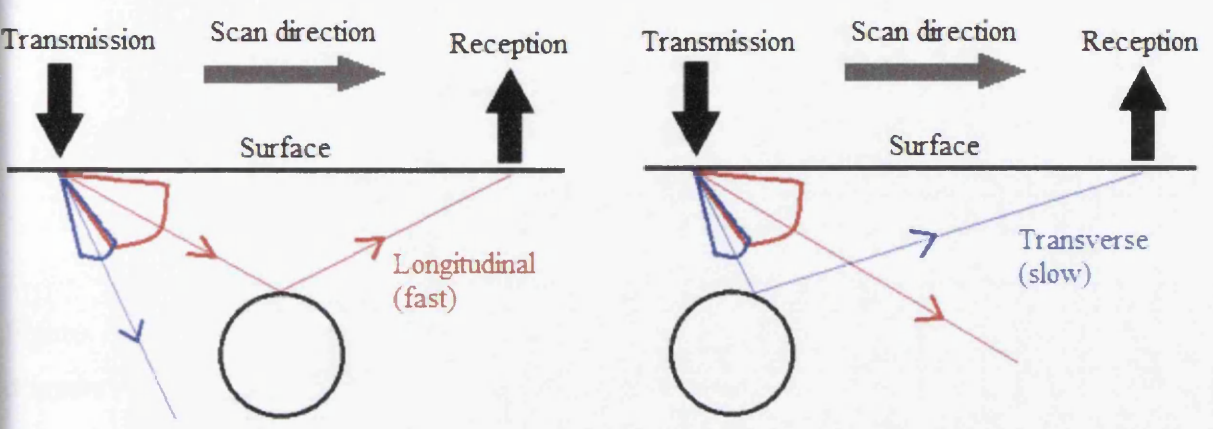

a b

Figure 4.22. Schematic diagram of bulk wave reflections due to the presence of a sub-surface discontinuity at two positions relative to a thermo-elastic wave source.

A method of relating the reflection 'arm' signals to the diameter of a discontinuity is by the measurement of the frequency content of the B-scan data over a range of time immediately after the arrival of the main Rayleigh wave. In the absence of a discontinuity there should be no surface displacements within this range and conversely any surface displacements which do exist in this range will exist uniquely due to interaction of ultrasonic waves with a discontinuity. From the B-scan shown in Figure 4.21, a time-window from 600 μs to 1400 μs was selected in order to analyse the ultrasonic waves reflected from each discontinuity. In Figures 4.23 and 4.24, displacement data in the time and frequency domains is shown for two different sized discontinuities at the same depth as representative examples. The time domain data was transformed using a Fast Fourier Transform (FFT). It was observed that higher frequency components are detected at positions where either the source or detection points 'approach' the sub-surface discontinuity.

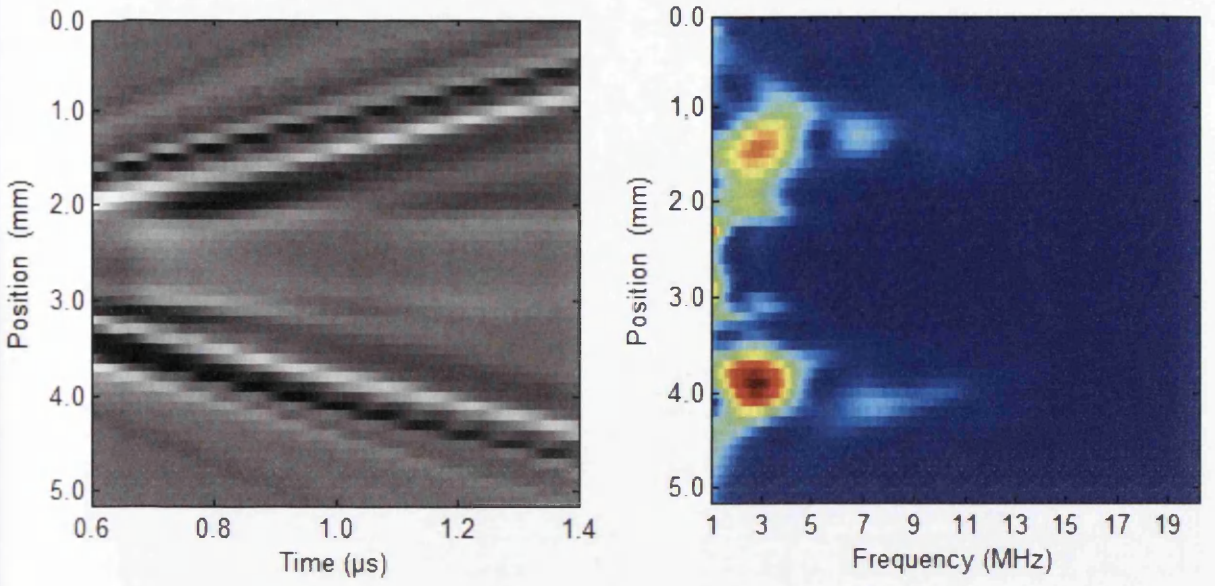

(a) (b)

Figure 4.23. Time-windowed B-scan data in (a) the time domain and (b) the frequency domain with a sub-surface discontinuity of depth 100 μm and diameter 240 μm.

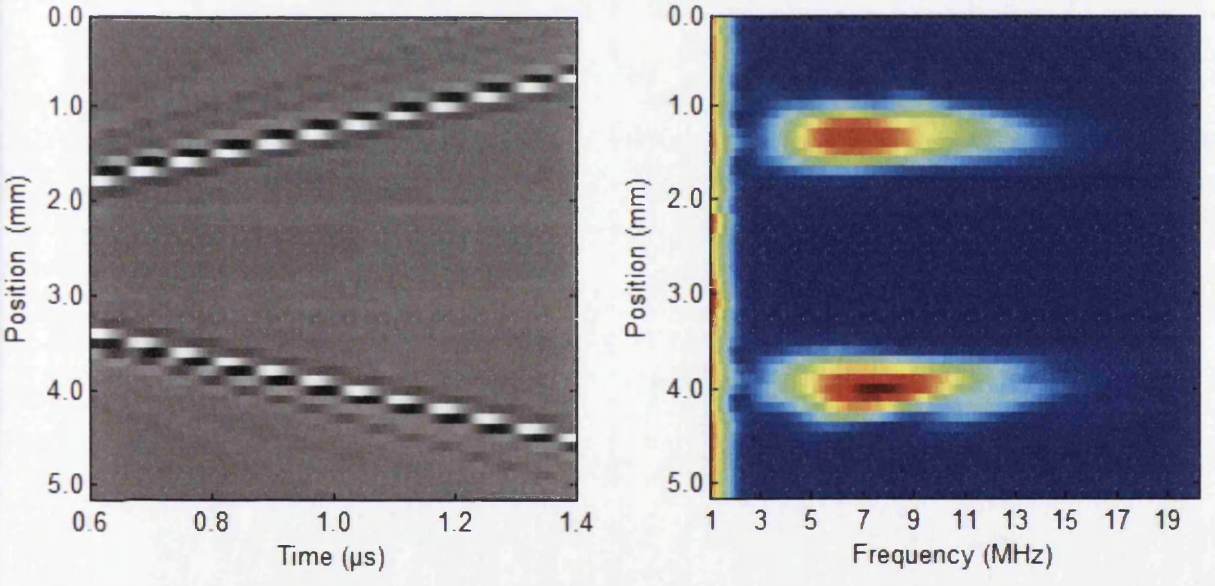

(a) (b)

Figure 4.24. Time-windowed B-scan data in (a) the time domain and (b) the frequency domain with a sub-surface discontinuity of depth 100 μm and diameter 60 μm.

There is a trend of these frequency components increasing in their peak frequency with decreasing discontinuity diameter (Figure 4.25), although the corresponding Rayleigh wavelengths, calculated as the Rayleigh speed divided by the measured peak frequency, do not scale linearly when taken as a ratio of the diameter (Figure 4.26).

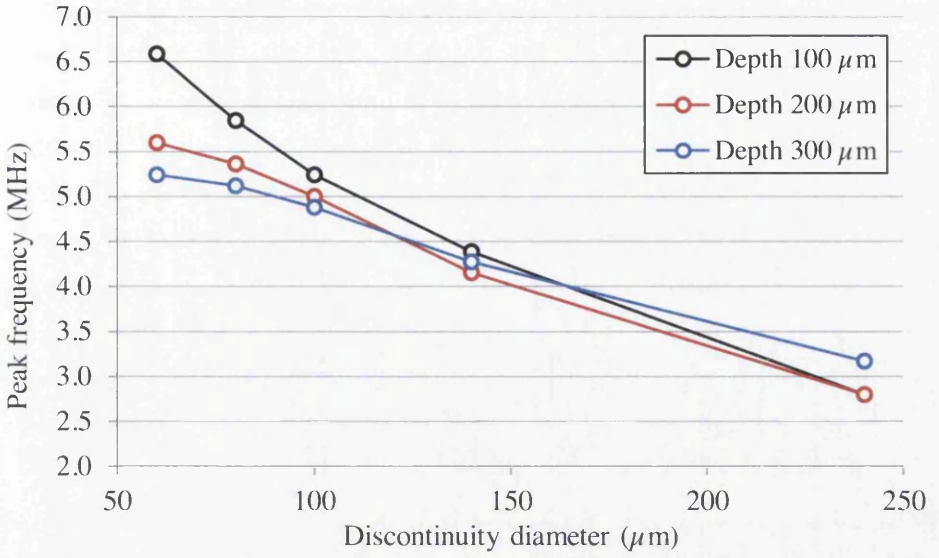

Figure 4.25. Peak frequency as a function of discontinuity diameter as measured from FFT data of surface wave reflection signals.

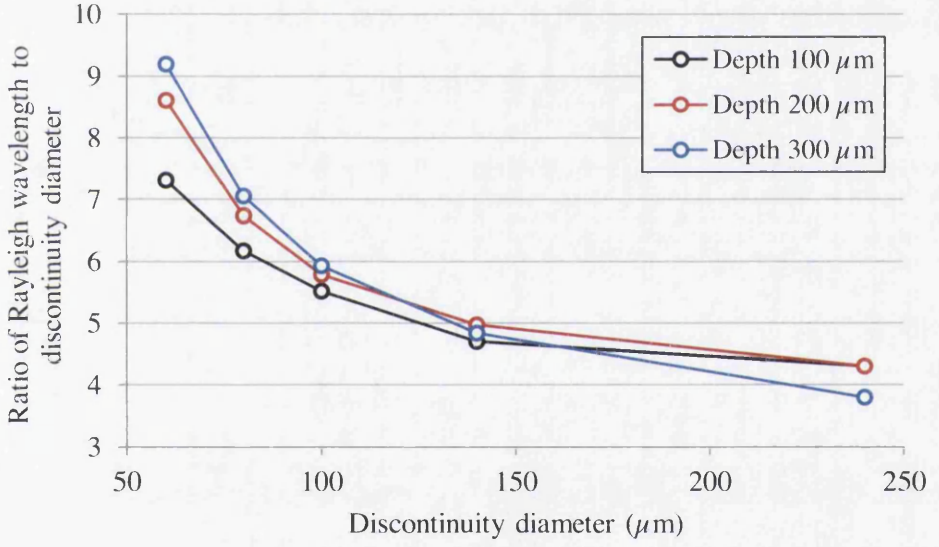

Figure 4.26. Rayleigh wavelength, calculated from measured peak frequencies, as a ratio of discontinuity diameter.

The main Rayleigh wave signal displays variation in its peak-to-peak amplitude near the location of a sub-surface void, as visible in the B-scan shown in Figure 4.21. A quantitative measure takes into account both the maximum and minimum peaks of the received Rayleigh wave-form and their variation as a function of position. The peak-to-peak amplitude is obtained by subtraction of the lower-peak amplitude from the higher-peak amplitude for each individual A-scan signal. One such result is shown in Figure 4.27; the peak-to-peak amplitude is constant as measured far from the centre, and displays significant variation as

the source and reception pass over the discontinuity. The dashed vertical lines, from left to right, mark the locations where the reception position and source position pass over the sub-surface void. For each depth and diameter of discontinuity, the minimum measured peak-to-peak Rayleigh wave difference are summarised in Figure 4.28. The greatest variation from the base-line seen in these results is approximately 40%, representing the decrease in peak-to-peak Rayleigh signal amplitude due to the largest discontinuity closest to the surface. The amplitude difference data is plotted on a log scale to easily distinguish between values for the smaller sized discontinuities.

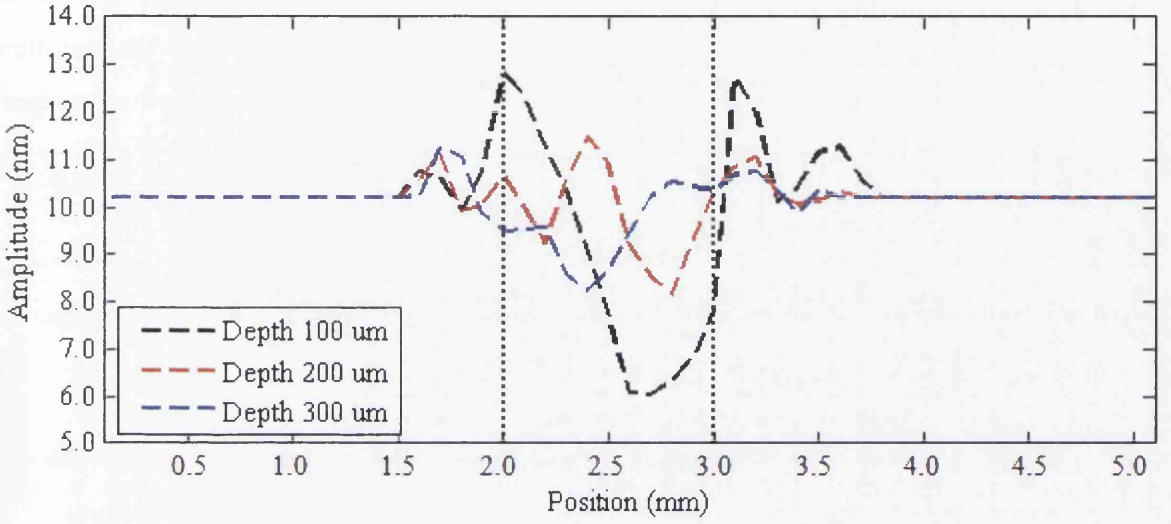

Figure 4.27. Peak-to-peak Rayleigh signal amplitude difference as a function of reception position with a sub-surface discontinuity of diameter 240 μm.

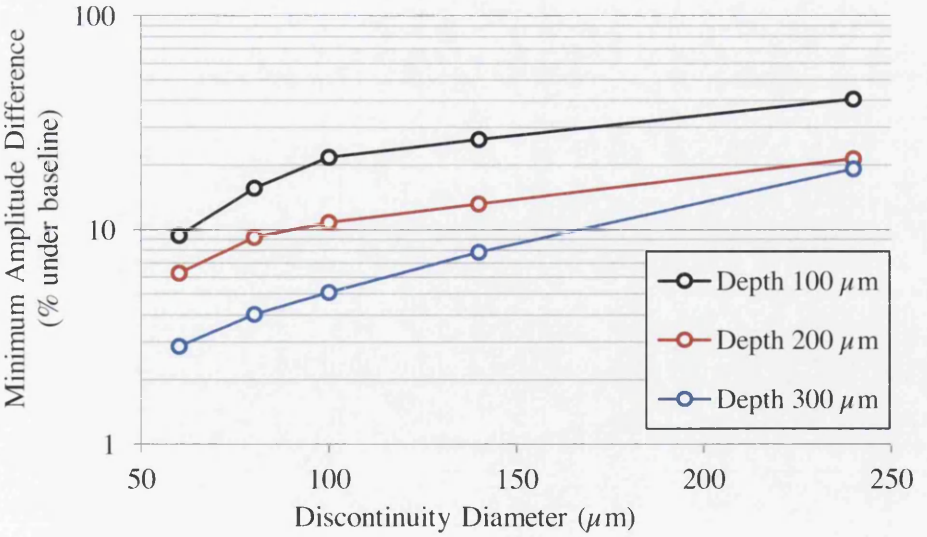

Figure 4.28. Minimum peak-to-peak Rayleigh signal amplitude difference as a function of discontinuity diameter (log scale).

The above method suits the idealised set-up in the finite element model as it can be assumed that the only changes in surface displacements far from the heat source are caused by propagating elastic waves. However, in the case of laser ultrasonic testing on real samples it may also be useful to consider the *ratio* of maximum and minimum displacement amplitude at the time of the Rayleigh wave arrival to mitigate variations in received signal amplitude due to non-uniform surface condition, for example. One such result is shown in Figure 4.29. For each depth and diameter of discontinuity, the maximum measured variation in peak-to-peak amplitude ratio are summarised in Figure 4.30. It can be seen that there is greater variation from the base-line in the peak-to-peak ratio compared with the peak-to-peak amplitude difference for each diameter and depth of discontinuity. The experimental data in Chapter 5 will be analysed similarly to determine if this proves a reliable detection method.

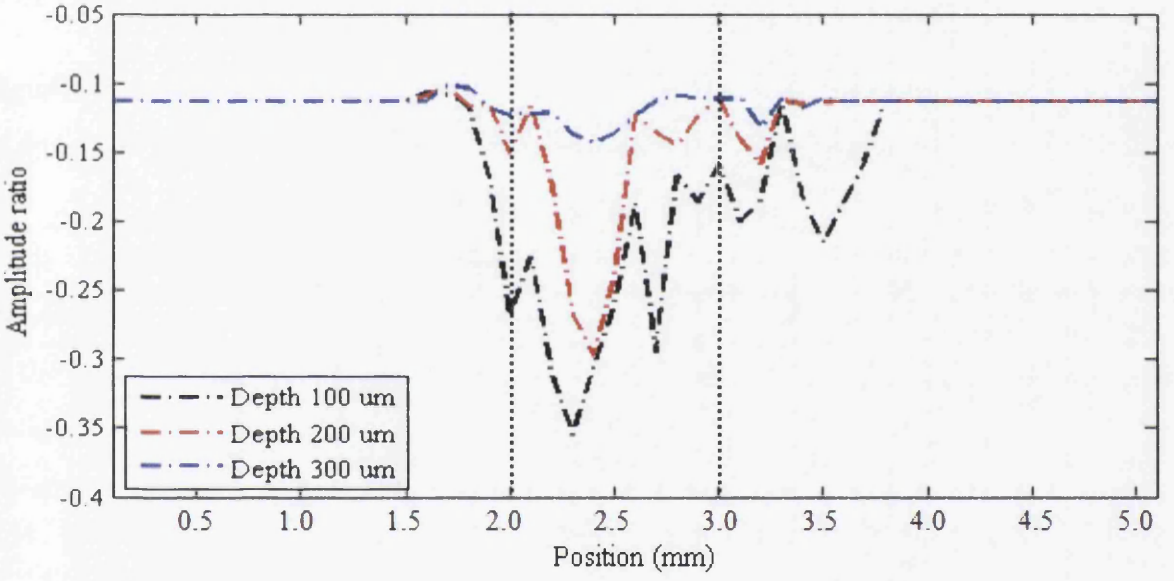

Figure 4.29. Peak-to-peak Rayleigh signal amplitude ratio as a function of reception position with a sub-surface discontinuity of diameter 240 μm.

SWANSEA LIBRARY UNIVERSITY

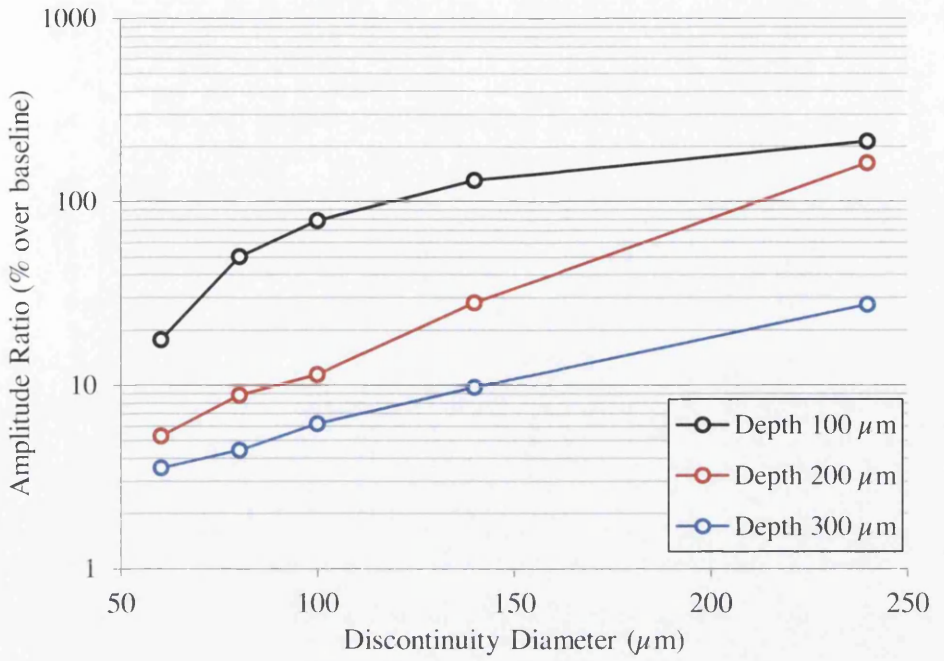

Figure 4.30. Maximum (absolute) peak-to-peak Rayleigh signal amplitude ratio as a function of discontinuity diameter (log scale).

4.4.4. Simulated Ultrasound Interaction with Discontinuities in 3D

In the 3D model, a discontinuity was inserted below the surface in the form of a completely enclosed spherical void. This shape more closely resembles real porosity and produces a signal response more subtle than that seen from the circular voids in the 2D model. In Figure 4.31, the magnitude of a displacement field is represented as it propagates through the 3D geometry comparing the case with and without the presence of a sub-surface discontinuity of depth 100 μm and diameter 150 μm. As in the 2D model, the Rayleigh wave experiences an increase in displacement magnitude upon propagation through the truncated region of geometry and shows disruption in its wave-front.

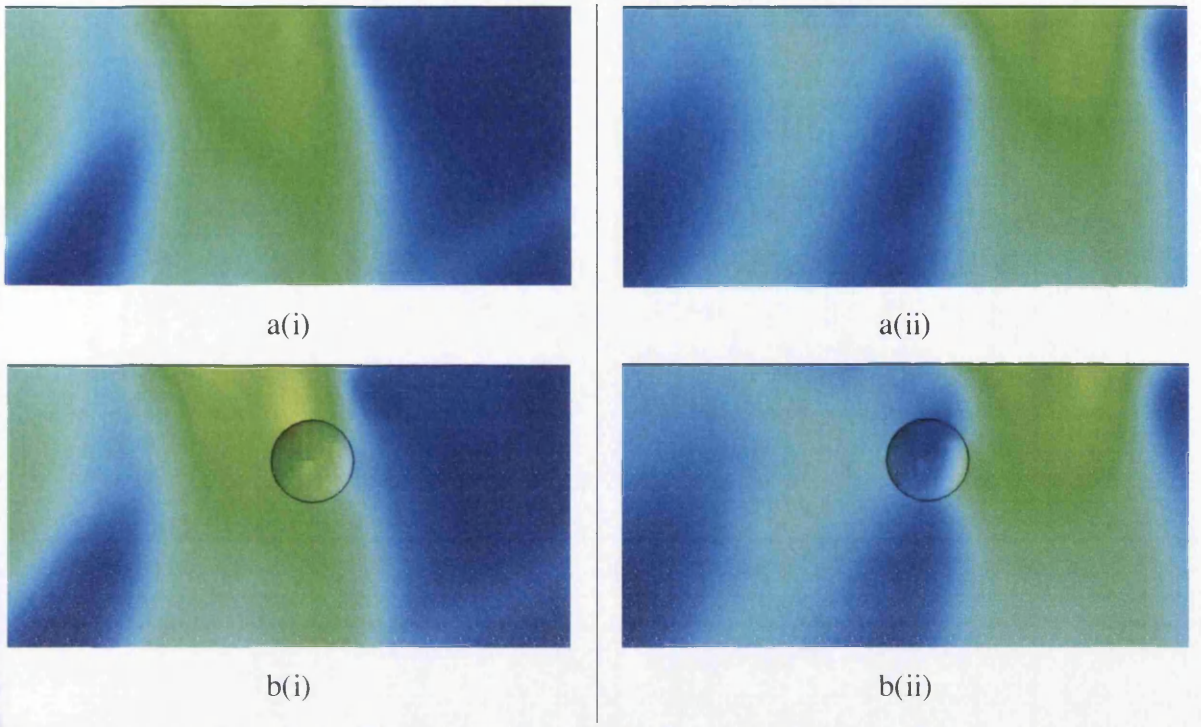

a(i) a(ii)

b(i) b(ii)

Figure 4.31. Displacement field interactions with (a) a continuous volume, and (b) a sub-surface discontinuity of depth 100 μm and diameter 150 μm.

Looking at received surface displacements, the most obvious indication of the presence of a discontinuity occurs as increase in peak-to-peak Rayleigh wave signal amplitude when the reception location is directly above the discontinuity (Figure 4.32). The magnitude of this indication is decreased compared to that measured in the corresponding 2D geometry. This is an expected result as there are continuous regions of geometry either side of the spherical discontinuity through which the Rayleigh wave can more easily propagate; the diameter represents only 30 % of the wall width in this case. Comparing the Rayleigh wave signal transmitted through the discontinuity to that measured at the same location in the fully continuous geometry (Figure 4.33), the change in amplitude is negligible. Furthermore, the spherical shape of the discontinuity is not at all optimal as a reflector as it should be expected that an ultrasonic wave-front would be reflected outwards in many directions.

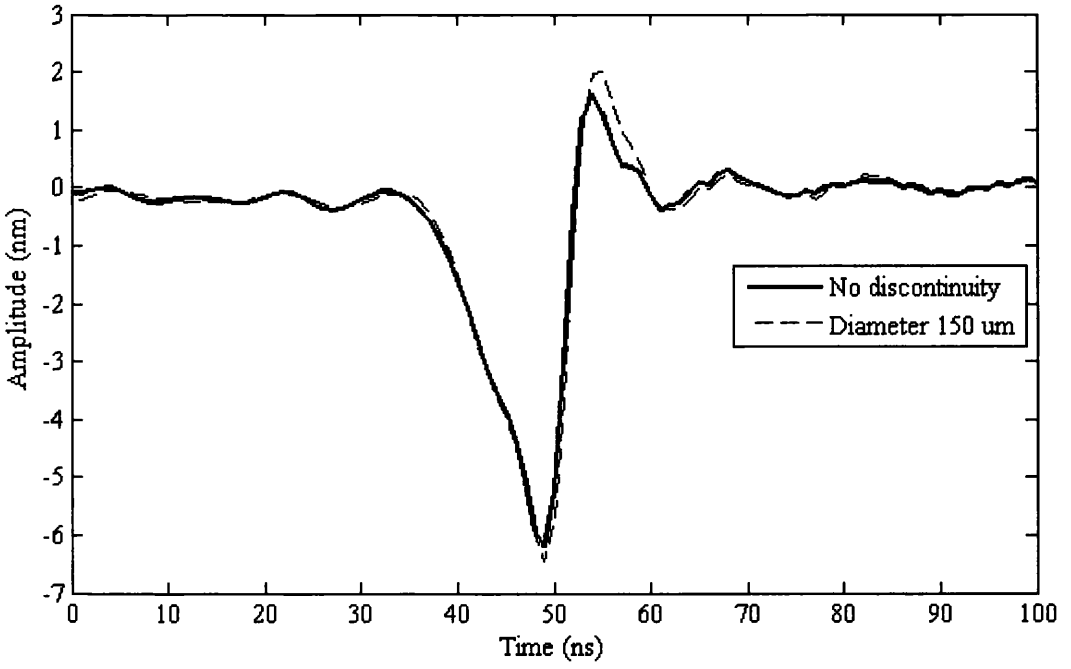

Figure 4.32. Surface displacements as a function of time measured with the reception position directly above the centre of a sub-surface discontinuity of depth 100 μm and diameter 150 μm.

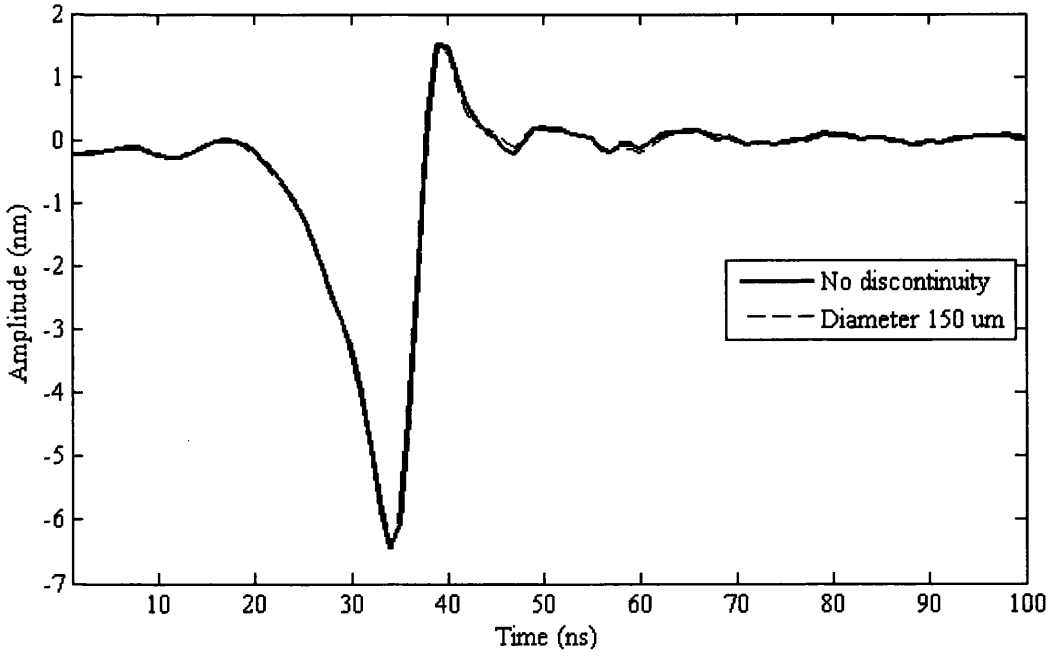

Figure 4.33. Surface displacements as a function of time with a discontinuity of depth 100 μm and diameter 150 μm located between the transmission and reception positions.

4.5. Summary

The simulation of ultrasonic wave propagation in an elastic solid, generated by a surface heat flux with realistic temporal and spatial properties, has provided a unique view on the interaction of waves with sub-surface discontinuities in two-dimensional and three-dimensional geometries. The validity of the model has been demonstrated through analysis of its thermal and mechanical response which has been compared to what is predicted by theory. Starting with a simplified model in 2D, the interactions of elastic waves with circular sub-surface discontinuities was analysed, considering a range of depths and diameters representative of real LMD flaw types as summarised in Chapter 3.

This analysis has considered indications in the received surface displacement signals which can be consistently measured and that may also be applied to laboratory-based testing of real test samples. In particular, measured Rayleigh wave properties have been shown to relate to variations in the depth and diameter of discontinuities. In addition, it has been shown that the Rayleigh wave has a significant amount of its energy reflected from the boundary of a discontinuity – the content of this reflected wave signal have also depend on the size of the discontinuity. The CLS method demonstrated here provides results representative of those which would be produced in laser ultrasonic testing by translating the transmission and detection beams relative to the test surface. Thus the flaw indications identified through analysis of these results in particular can be applied directly to laboratory-based testing and have the potential to also be applied to the detection of real flaw types such as gas porosity. It is important to consider that the FEA results do not include realistic conditions such as surface topology/condition and the resulting effect on the reflection of the detection laser, as well as other dynamic effects, which may introduce noise and unwanted variation in measured surface displacements. Thus it is important to test the reliability of the detection methods presented here on data sets obtained in the laboratory, as will follow in the next chapter.

A 3D model provided the opportunity to simulate the interaction of a surface ultrasonic wave with an enclosed spherical discontinuity. The resulting effect was found to be much less significant compared to the 2D case. The FEA work carried out could be expanded on by simulating the interaction of ultrasound with inter-layer type flaws which are usually elongated and non-uniform in shape. A range of shapes and sizes could be selected by studying 3D X-ray computed tomography images of flaws in LMD structures.

Chapter 5: Laser Ultrasonic Testing & Sensitivity of Flaw Response

5.1. Introduction

The work described in this chapter reports on laboratory-based laser ultrasonic testing of manufactured test pieces for the main purpose of investigating the capabilities of this NDT technique in detecting and sizing sub-surface discontinuities and establishing detection limits. The application of testing techniques is carried out with consideration given to the intention of transferring the same techniques to a manufacturing environment to carry out on-line inspection. Variables apply to laboratory-based testing which are not included in the finite element model, such as the effect of surface roughness and continuous motion on the performance of laser-based reception of ultrasonic surface displacements.

5.2. Laser Ultrasonic Testing Equipment

5.2.1. Equipment for Generating Ultrasound

For non-contact generation of ultrasonic waves, a fibre-coupled Quantel Ultra 50 laser was used. This is a compact Q-switched Nd:YAG laser; the fibre-coupled laser beam output allows for flexibility and remote placement of the laser unit relative to the surface of the test sample under evaluation. The laser unit (Figure 5.1) contains the flash-lamp and resonator cavity and is connected to a control/water-cooling unit via electrical cables and water tubes. Control of the laser is achieved via buttons on the front panel of the control unit (Figure 5.2) or by connection to a PC with hyperlink software via RS-232 cable, through which commands can be entered remotely. The back panel of the control unit includes a BNC output to synchronise the Q-switch timing with data acquisition hardware, and a BNC input to facilitate the use of an external Q-switch trigger.

Another input on the laser control unit is the remote interlock; this allows the laser Q-switch to operate when a low voltage signal is received. The voltage originates from a powered interlock system in the laboratory which is connected to several switches to ensure safe operation of the laser. For example, the opening of a door causes a controlled break in the interlock circuit and prevents the laser from operating with the Q-switch active so that high-power laser radiation does not propagate outside of the permitted area.

The front panel controls include activation of the Q-switch, variation of the pulse repetition frequency, and control over the flash-lamp energy on a unit-less linear scale in 20 discrete increments.

Table 5.1. Specifications of the Quantel Ultra 50 laser.

Maximum energy per pulse	50 mJ / 45 mJ (free-space/fibre-coupled)
Pulse duration	8 ns (FWHM)
Repetition frequency	1-20 Hz
Wavelength	1064 nm
Beam coupling	Fibre cable: diameter = 0.9 mm, NA = 0.22

The duration of the laser pulse τ, a fixed value for this particular laser model, is one property of the laser which determines the maximum central frequency of ultrasound which can be generated. This can be calculated approximately by assuming that the incident pulsed laser beam has the same temporal profile as the resulting ultrasonic pulse in a material, and that the profile of this pulse is Gaussian. The Fourier transform of this pulse reaches half of this maximum value when the frequency is equal to $0.1874/\tau$, the limit above which appreciable ultrasonic energy is produced at the desired frequency [8]. Thus the specified pulse duration of the Ultra 50 laser should result in ultrasound at a theoretical maximum frequency of approximately 23.4 MHz. Another determining factor is the laser beam spot size, or beam diameter at the point of surface irradiance, which will be discussed in Section 5.2.3.

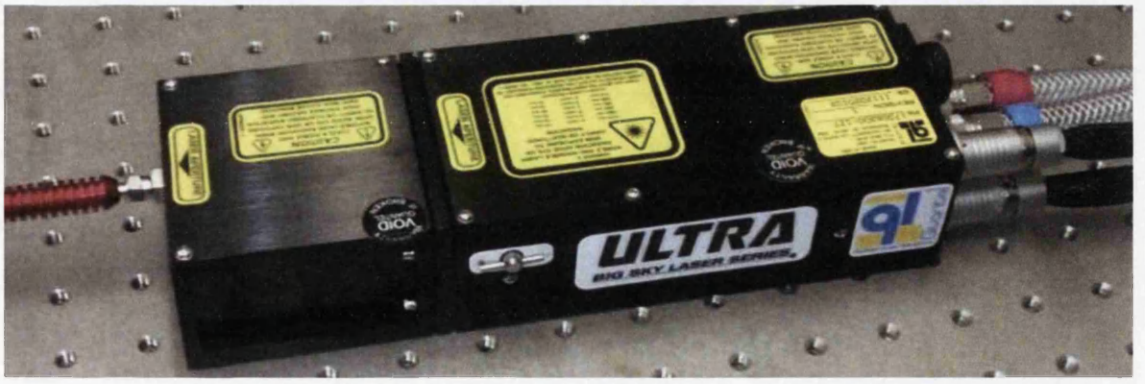

Figure 5.1. Quantel Ultra 50 laser unit with attached fibre-coupling module (left) and electrical and water-cooling connections (right).

a b

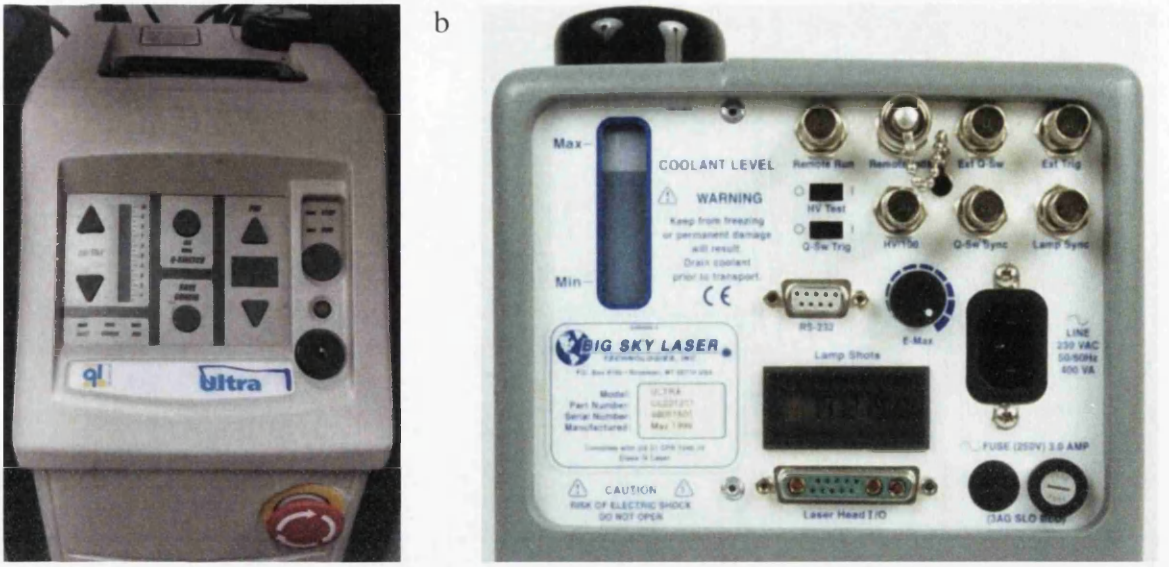

Figure 5.2. Quantel laser control unit with (a) front panel user controls and (b) rear panel inputs and outputs.

5.2.2. Equipment for Receiving Ultrasonic Surface Displacements

For non-contact reception of ultrasonic waves, an IOS AIR-TWM-532 interferometer system was used. This system operates with a Cobolt Samba continuous Nd:YAG laser and the combined specifications are given below.

Table 5.2. Specifications of the IOS AIR-532-TWM interferometer and Cobolt Samba laser.

Detector bandwidth	125 MHz
Surface displacement sensitivity	4×10^{-7} nm rms $(W/Hz)^{1/2}$
Sampling rate (data acquisition card)	125 MS/s
Wavelength	532 nm
Maximum beam power	600 mW
Beam coupling	Split fibre cable: 1x fibre for beam delivery, $d = 50\ \mu m$ 7x fibre for beam collection, $d = 100\ \mu m$

The AIR-532-TWM is a two-wave mixing type interferometer with high detection bandwidth suited to the reception of laser-generated ultrasonic surface displacements, high surface displacement sensitivity, and remote delivery of the detection laser beam for flexibility in set-up. Control of the continuous laser output is achieved via connection to a PC with hyperlink software. The free-space output of the Cobolt laser is directed into a polarising beam-splitter element (Figure 5.3) in order to split into a reference beam and a signal beam, with a half-wave plate for user-controlled variation of the power split ratio.

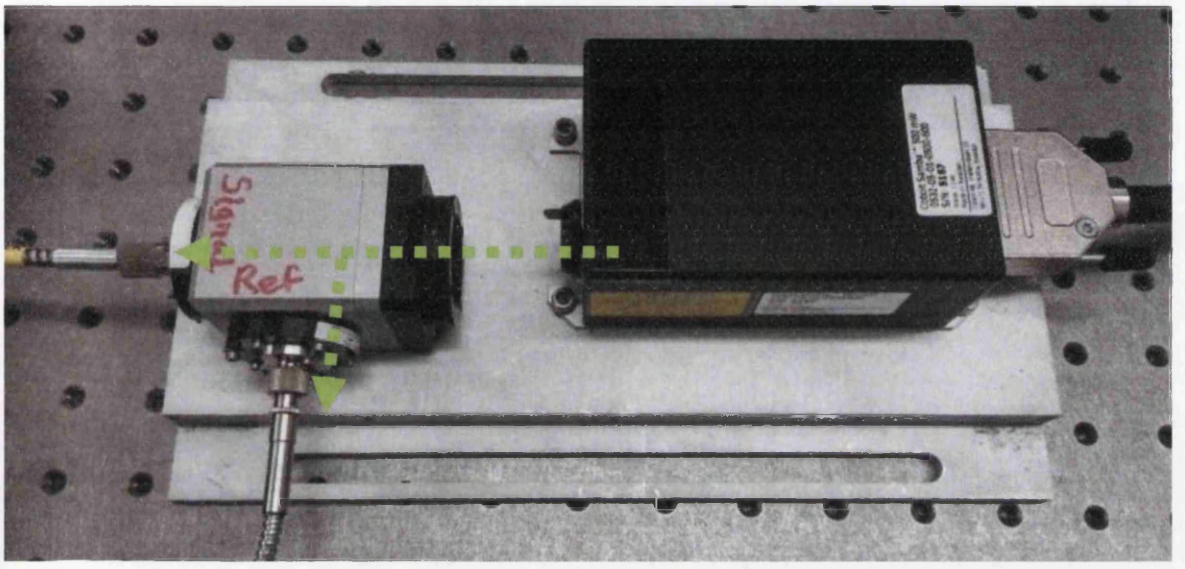

Figure 5.3. Cobolt laser unit (right) and variable beam-splitter module (left) with fibre-coupled outputs for the signal beam and reference beam (labelled). Green lines/arrows represent laser beam propagation path/direction.

The signal beam is delivered via fibre cable to an optical head where it is collimated and focused to a small spot on the surface of a test sample (Figure 5.4). The reflected laser light is collected by the same optical head and returned to the interferometer via a split fibre cable.

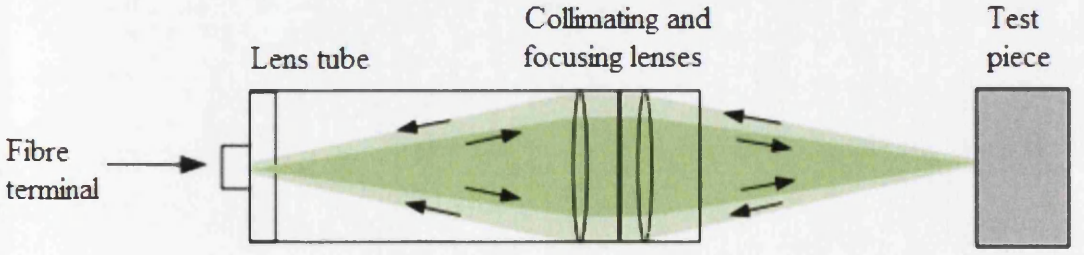

Figure 5.4. Propagation of the signal laser beam through collimating and focusing optics (dark green) and reflection from a test surface (light green) [28].

The proximity of the test surface to the focal point of the laser beam is related to the coupling efficiency (Figure 5.5), an arbitrary measure of received light intensity density which affects the signal-to-noise ratio of received surface displacement signals. Signal quality reduces as the laser beam is moved in either direction away from the point of optimum focus as shown in Figure 5.6 – a clearly resolved surface ultrasonic wave signal measured at the distance of optimum focus becomes diminished compared to the noise signal as the focusing lens is moved closer to or further away from the test surface.

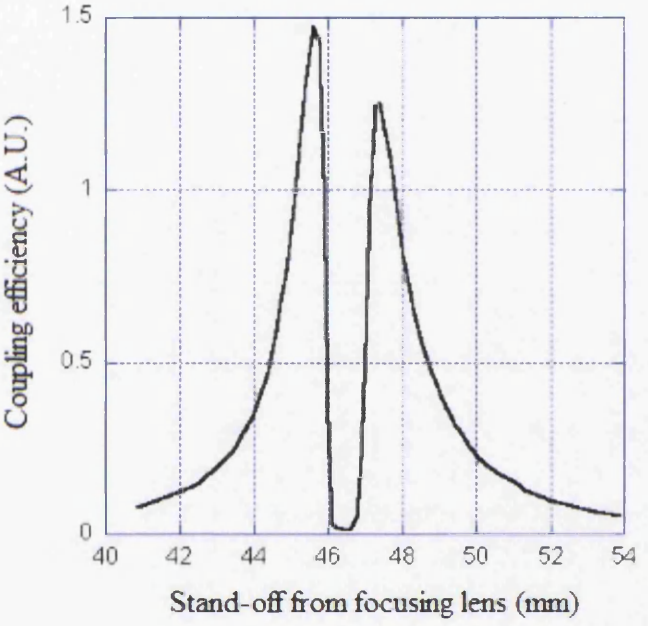

Figure 5.5. Reception laser beam coupling efficiency as a function of stand-off from the test surface [28].

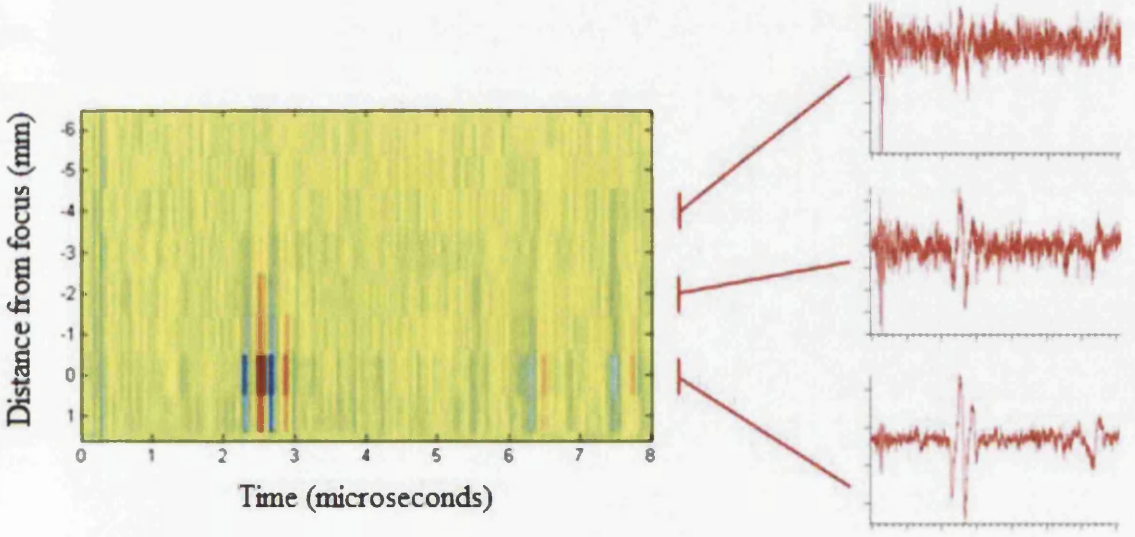

Figure 5.6. Received A-scan signals as a function of time and distance from optimum focus.

Upon delivery to the interferometer, the signal beam is sent through a photo-refractive crystal (Figure 5.7). The reference beam is delivered directly from the laser unit to the interferometer via a separate fibre cable, where it is also sent through the photo-refractive crystal at an angle to the signal beam. Within the crystal, the two beams interfere and a representation of the resulting interference pattern is produced in the form of a hologram. This hologram allows the diffracted reference beam and transmitted signal beam to be combined in a process which converts the phase change in the signal beam to an output AC voltage which is proportional to local surface displacements within the surface area illuminated on the test sample.

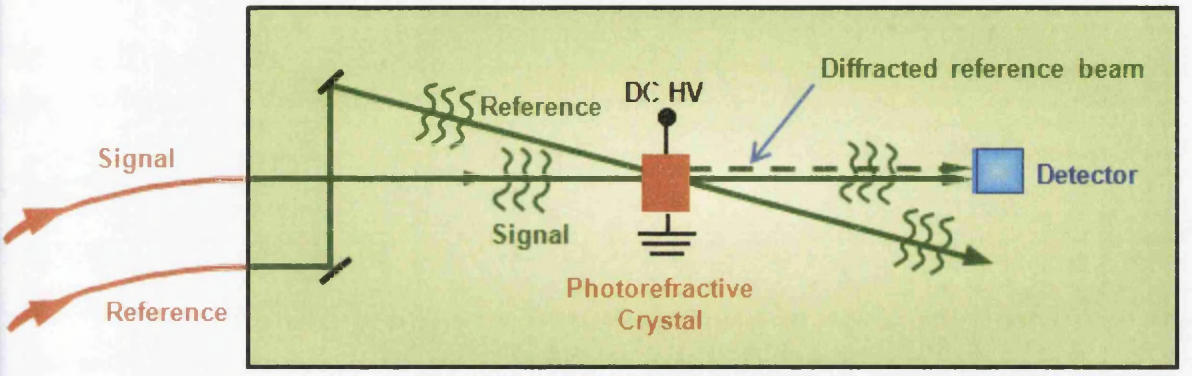

Figure 5.7. Schematic diagram of the AIR-532-TWM. Orange lines represent fibre cable inputs and green lines/arrows represent laser beam propagation path/direction [28].

Increasing power to the signal beam increases the intensity of light reflected from the surface, which is output as a DC voltage. A DC output voltage of 1 V provides optimum surface displacement sensitivity and signal to noise ratio. The best A-scan signal stability is provided when the power to the reference beam is as high as possible. This is especially important when performing laser ultrasonic testing in continuous-scan mode, as more power to the reference beam will allow surface displacements to be resolved accurately when the detection laser beam is translated across the surface of a test sample in a continuous motion. Thus, the optimum split ratio was chosen by setting the laser output power to its maximum value; then, the variable power splitter was set such that the power delivered to the reference beam was maximised while maintaining a DC output of approximately 1 V from the signal beam. The performance of the photo-refractive crystal is improved by the application of a high voltage, controlled by a switch on the front panel of the interferometer.

Figure 5.8. Front panel of the IOS AIR-TWM-532 interferometer. Fibre cable inputs (left to right): reference beam, signal beam. BNC cable outputs (left to right): DC, AC.

5.2.3. Optical Equipment for Laser Beam Manipulation

Both laser beams for ultrasound generation and detection are fibre-coupled. Upon exiting the fibre terminal, the laser beam diverges and must be collimated using a spherical lens. The collimated beam is then focused using another spherical lens at a specified stand-off distance from the target surface. It is important to consider the maximum practicable stand-off distance while ensuring that the spot size was not too large to fit within the edges of the top surface of the thin-walled test-pieces. The interferometer system was supplied with lenses of focal length F = 50 mm and these were supplemented with lenses of focal length F = 60 mm for flexibility in placement of the optical equipment. The resulting spot sizes are listed in Table 5.3, calculated from the respective optical fibre outputs and beam properties for each laser. Also listed are the approximate limits for the central frequency of the Rayleigh ultrasonic waves produced by the corresponding laser spot size. This is calculated by dividing the wave speed by the spot size.

Table 5.3. Approximate spot sizes produced by lenses of different focal lengths, and associated limits of central Rayleigh wave frequency.

	Ultrasound generation beam		Ultrasound detection beam
Focal length	Spot size	Central frequency	Spot size
50 mm	700 μm	4.1 MHz	200 μm
60 mm	840 μm	3.4 MHz	240 μm

5.2.4. Hardware and Software for Data Acquisition

AC and DC signals are output from the interferometer to a National Instruments PCI-5114 digitiser installed in a PC. Software package 'LaserScan' is used for data acquisition, analysis, and output. This software controls the Velmex BiSlide motorised translation platform and accepts a trigger input from the Quantel laser for synchronisation of data acquisition timing with each pulse. Before each scan, acquisition settings were input by the user including sampling rate, duration, and number of averages (Figure 5.9). Averaging of recorded displacement data minimises random electrical and vibrational noise and is only provided as an option in stepped scanning mode where the test sample remains stationary at each scan position, so that multiple pulses can be fired before moving on to the next position. Scan settings were also input including start position, step size, and end position (Figure 5.10). The software includes a setting for continuous mode scanning where the scan speed is a product of the input step size and the pulsed laser repetition rate. In this mode, the laser pulse is triggered externally when the linear translation platform reaches specific positions. A buffer module, connected between the I/O port on the Velmex motor controller and external trigger input on the Quantel control unit, conditions the position signal such that it provides enough current to trigger the laser flash-lamp. Acquired surface displacement data is displayed in real-time in the form of A-scan and B-scan graphs (Figure 5.11). Since the maximum repetition rate of the equipment is fixed, the resolution of a B-scan produced in continuous mode is inversely proportional to the rate of motion. Post-processing of experimental data was done using built-in software functions including FFT, frequency filtering (low-pass and high-pass), and AC/DC normalisation.

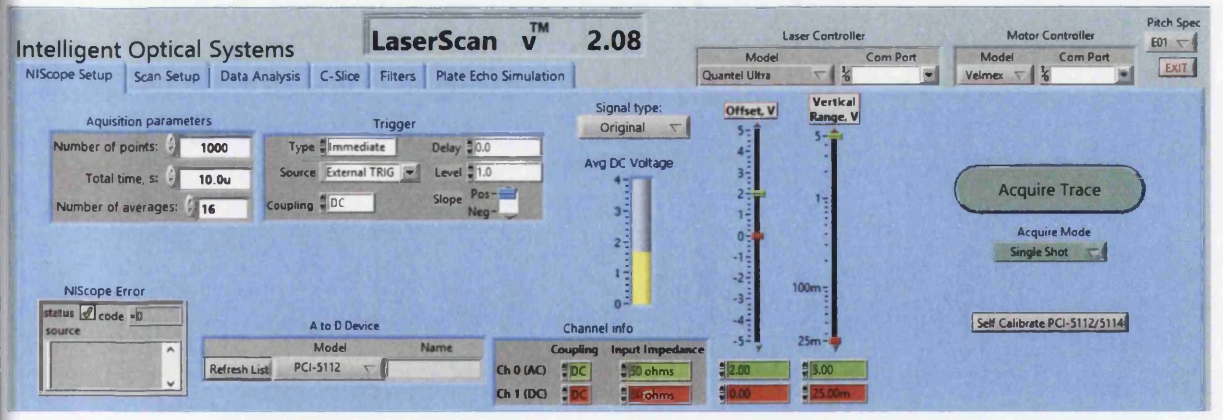

Figure 5.9. Data acquisition settings tab in the LaserScan software. The data acquisition hardware sampling rate limits data points to a maximum of 125 μs^{-1}.

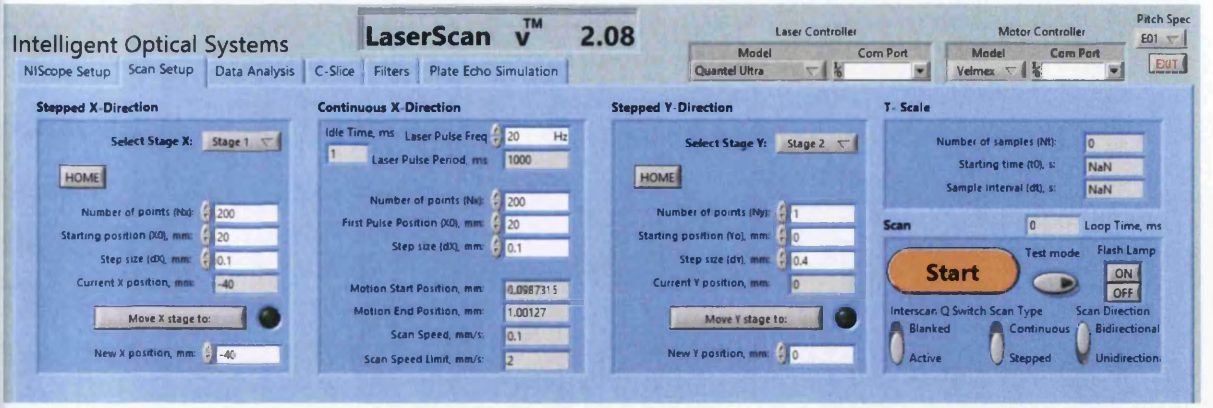

Figure 5.10. Scan settings tab in the LaserScan software, with options for stepped and continuous scanning modes. The additional 'Y-Direction' scan axis was not used.

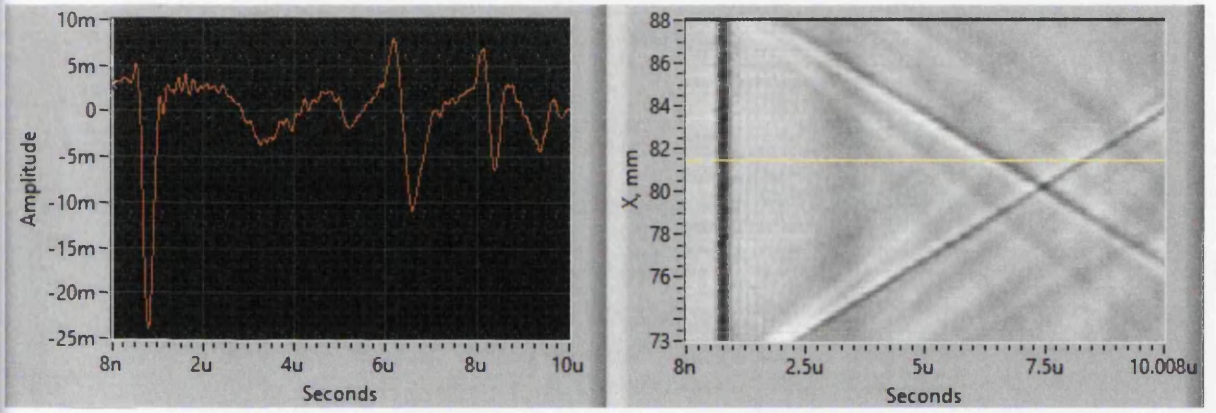

Figure 5.11. A-scan (left) and B-scan (right) data display windows in the LaserScan software. The position of the displayed A-scan is indicated by the (interactive) yellow line in the B-scan window.

5.3. Test Samples & Methods

5.3.1. Test-Pieces & Artificial Defects

Several variations of test samples were manufactured for the purpose of ultrasound propagation and flaw response measurement. The calibration blocks, machined from Inconel 718 material, consist of a thin wall section on top of a thick substrate section (Figure 5.12). This shape is analogous to the thin structures capable of being produced by LMD-powder manufacturing. Wall thicknesses of 0.5 mm and 1 mm were included.

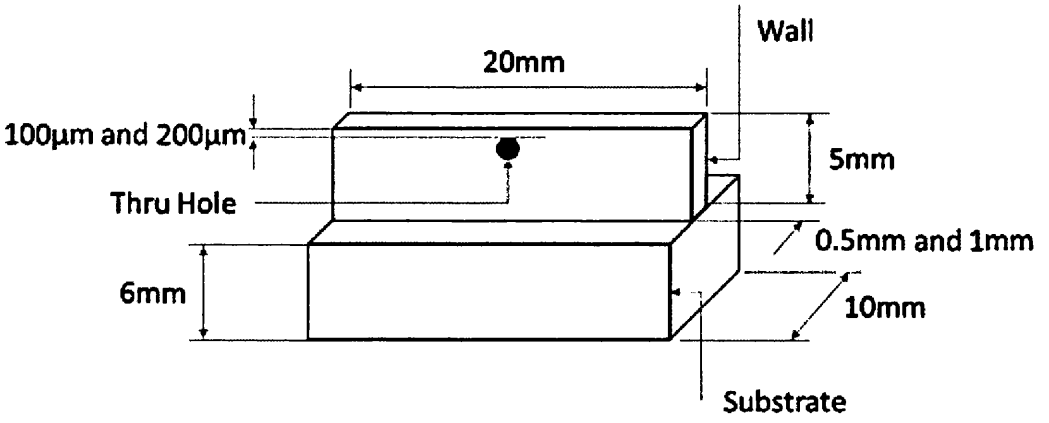

Figure 5.12. Dimensions of the manufactured test-pieces including side-drilled hole.

Sub-surface flaws were simulated by the insertion of side-drilled holes at a central position along the length of each wall (Figure 5.13) using a laser-based drilling method to generate the smallest achievable cavity sizes. Holes with depths of 100 µm and 200 µm, as well as diameters of 250 µm, 150 µm, 100 µm, and 77 µm, were included. In addition, one set of blocks included a single layer of Inconel 718 material deposited on the top surface using the LMD-powder process. These were created in order to investigate the effect of realistic surface roughness and profile – a deposited layer has a rounded top surface rather than the flatness of a machined surface, and thus it should be expected that a smaller portion of the reception laser beam is reflected back into the optical head as some of the light reflected in other directions. A summary of manufactured test-piece geometries and flaw dimensions is given in Table 5.4. For each variation, a 'blank' piece free of artificial flaws was created in order to provide a baseline for comparison of laser ultrasonic testing results.

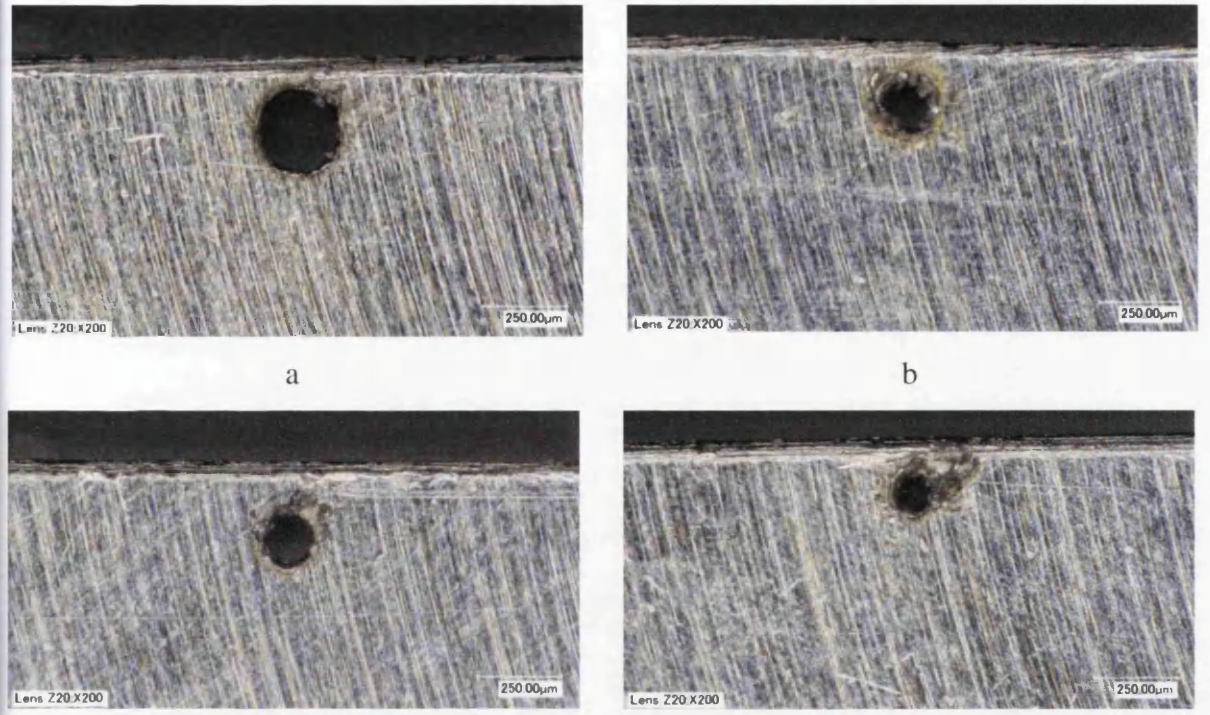

Figure 5.13. Microscopic images of simulated flaws drilled into test-pieces at a depth of 100 µm (distance from surface to top of hole) with diameters of (a) 250 µm, (b) 150 µm, (c) 100 µm, and (d) 77 µm.

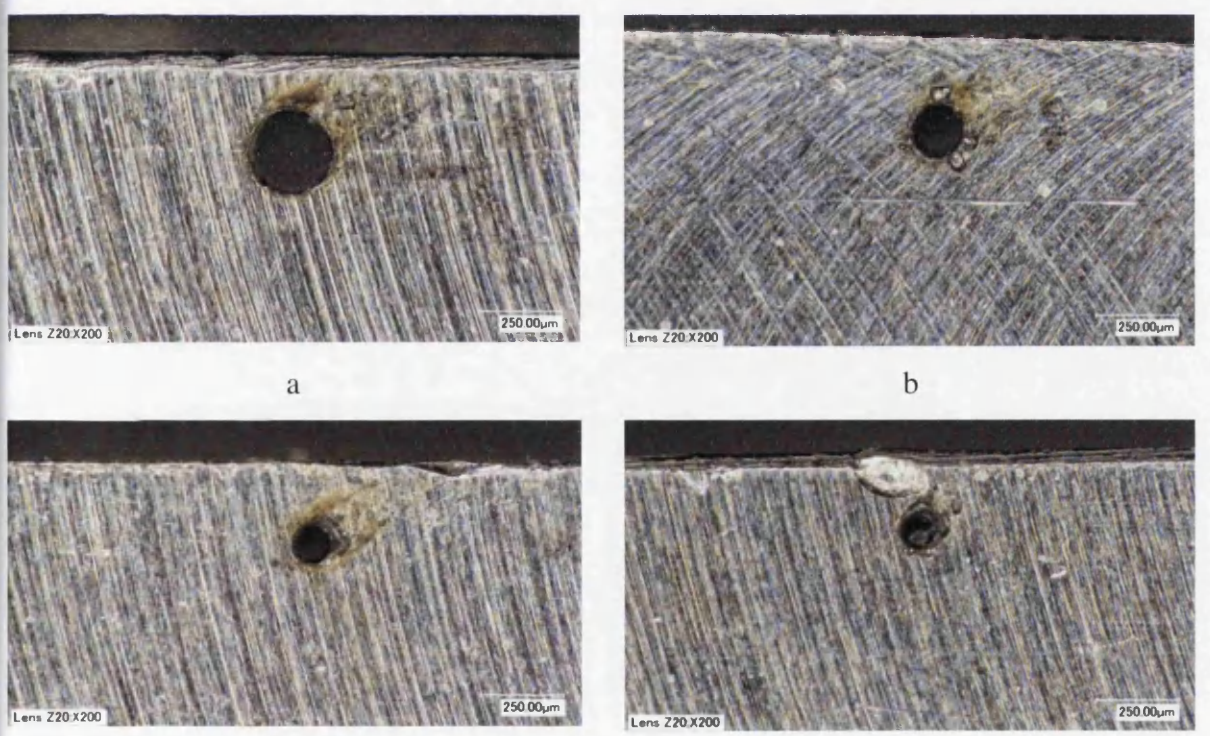

Figure 5.14. Microscopic images of simulated flaws drilled into test-pieces at a depth of 200 µm with diameters of (a) 250 µm, (b) 150 µm, (c) 100 µm, and (d) 77 µm.

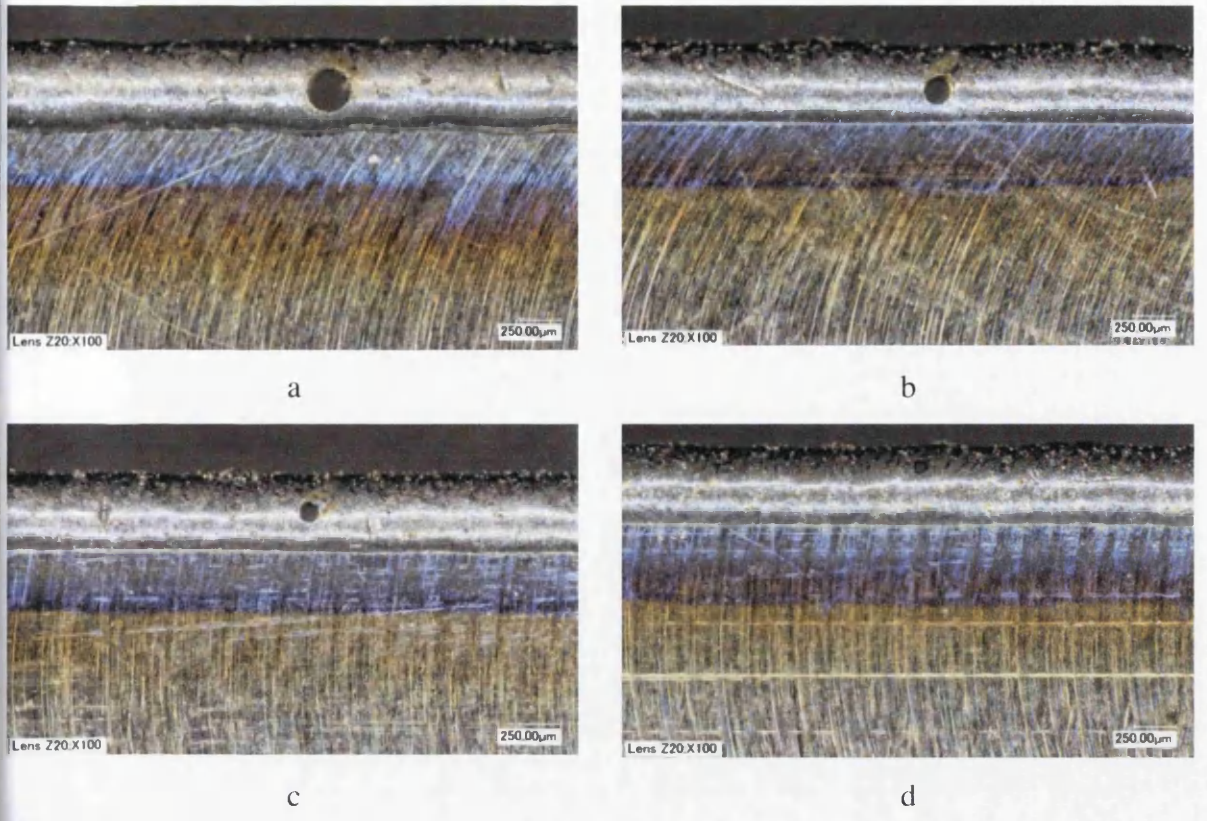

Figure 5.15. Microscopic images of simulated flaws drilled into test-pieces including a laser-deposited layer at a depth of 100 µm with diameters of (a) 250 µm, (b) 150 µm, (c) 100 µm, and (d) 77 µm.

Table 5.4. Summary of test pieces manufactured for laser ultrasonic testing in the laboratory and reference labels (shaded cells).

		Machined surface		Deposited surface
Depth of hole (µm)	Diameter of hole (µm)	Wall thickness 0.5 mm	Wall thickness 1.0 mm	Wall thickness 0.5 mm
None present (blank)		A0	B0	C0
100	250	A100-250	B100-250	C100-250
	150	A100-150	B100-150	C100-150
	100	N/A	B100-100	C100-100
	77	N/A	B100-077	C100-077
200	250	A200-250	B200-250	N/A
	150	A200-150	B200-150	N/A
	100	A200-100	B200-100	N/A
	77	A200-077	B200-077	N/A

It was assumed that the test-pieces made entirely of machined metal would be free of manufacturing defects and that the only void to exist in each structure was the deliberately drilled holes. However, in the case of the test-pieces which included a deposited layer of metal on the top surface, it was decided to verify the quality of the deposited material by the use of X-ray computed tomography – LMD process settings had to be customised in order to achieve a successful deposit and it may have been possible for flaws to occur. Each of the five test pieces was scanned to produce a 3D computed image of the deposited layer which was inspected visually by the machine operator. Only two minor flaws were reported: a void of approximate diameter 26 μm in the 'blank' test-piece C0 (Figure 5.16), and a void of approximate diameter 28 μm in test-piece C100-150 (Figure 5.17). The identified voids may represent gas pores as they appear circular in shape and exist within the volume of the deposited layers. However, they are deemed too small to be of interest to this work; indeed, they fall within the lowest grade of pore size as defined by Rolls-Royce/TWI and described in Table 3.2.

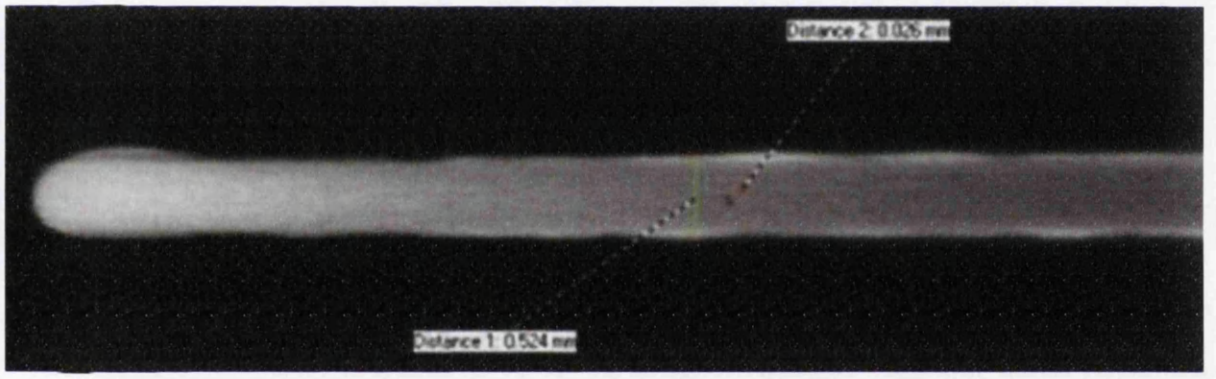

Figure 5.16. Top-down view computed tomography image of test-piece C0 showing the largest detected void within the deposited layer.

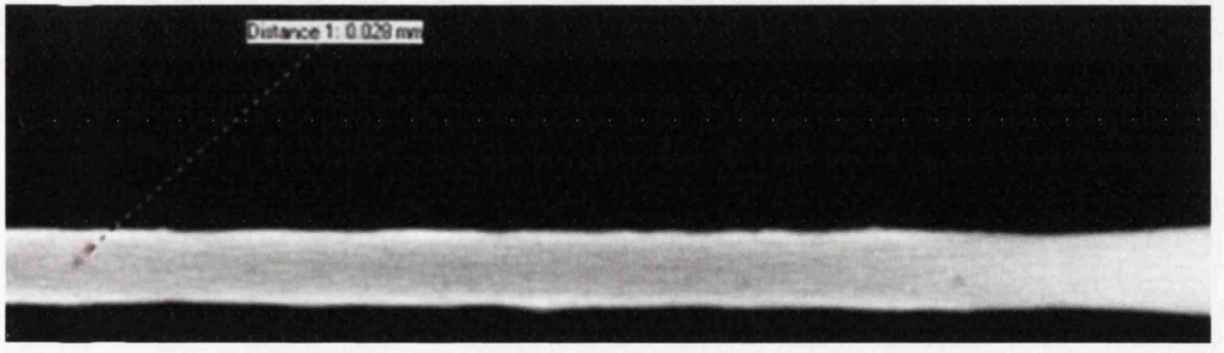

Figure 5.17. Top-down view computed tomography image of test-piece C100-100 showing the largest detected void within the deposited layer.

5.3.2. Laser Ultrasonic Testing Methods

All test samples were scanned in stepped mode with a step size of 0.1 mm and continuous mode with motion rates of 2, 4, 6, 8, and 10 mm/s. In stepped scan mode, surface displacement is measured in between steps in movements when the surface under inspection has zero motion. An A-scan representing surface displacement is recorded at each step up to a time limited to the inverse of the laser pulse repetition frequency. This scan mode is expected to produce the best quality data since the interferometer does not have to compensate for surface motion. Furthermore, it is possible to improve the signal-to-noise ratio of measured data by taking the average of repeat measurements at each step position. This was carried in experiments out using eight averages in order to provide an 'ideal' dataset and to compare to data recorded in continuous scan mode.

In continuous scan mode, the 'virtual' scan step size is determined by the pulse repetition frequency and the scan speed as summarised in Table 5.5. This value is proportional to the spatial resolution of a recorded B-scan image. In order for there to be no physical gaps in the path of surface inspection, the separation between the focal spots of the transmission and reception laser beams must be greater than or equal to this calculated value.

Table 5.5. Distance between successive A-scans recorded in continuous scan mode corresponding to different speeds of motion and a fixed pulse repetition rate of 20 Hz.

Scan speed (mm/s)	A-scan separation (mm)
2	0.1
4	0.2
6	0.3
8	0.4
10	0.5

Flash-lamp/pulse energy was set to maximise ultrasonic wave signal amplitude whilst avoiding excessive surface ablation and an associated high-amplitude, low-frequency airborne acoustic signal which appears in the wave-form. The transition from thermoelastic to ablative ultrasound generation is gradual, and it was found through experience that at a certain level, the flash-lamp energy setting would result in only a negligible level of surface burning which could be removed with a coarse eraser block. Setting the energy higher would

result in visible cratering on the surface due to melting. Since laser energy density depends on beam width and the transmission laser beam was kept at optimum focus, the ideal setting for pulse energy could be determined once per set-up and kept at the same value throughout an experiment. The generation and detection laser beams were scanned relative to the test piece in SLD and CLS configurations as described in Chapter 4 (Figure 4.9). For CLS, the separation distance was fixed at 1 mm.

5.4. Experimental Set-up

A Velmex BiSlide motorised 1D linear scanning platform (Figure 5.18) was utilised for translation of test samples as required in order to automate the process of acquiring B-scans. The motor is controlled via the data acquisition software and is capable of producing stepped and continuous motion with a resolution of 50 μm and maximum travel length of 300 mm.

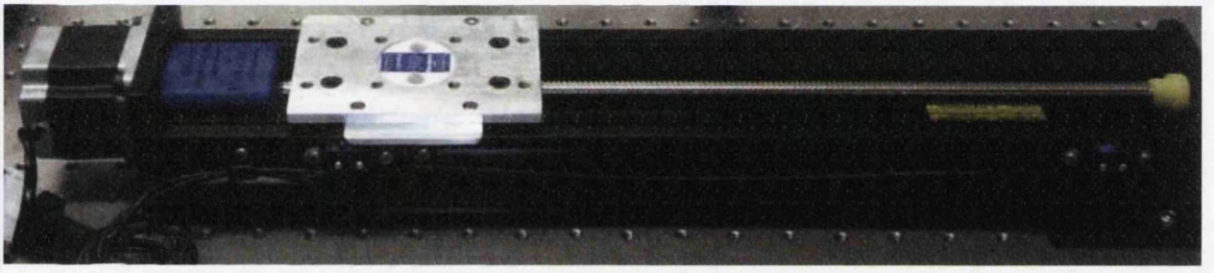

Figure 5.18. Velmex BiSlide motorised 1D linear scanning platform.

The ultrasound detection laser beam must be orientated perpendicular to the target surface in order to receive the reflected light. Efficient generation of ultrasound is achieved by orientating the generation laser beam also perpendicular to the target surface, producing a regular spot shape and energy distribution.

Due to the diameter of the lenses, it was not feasible to position the respective lens tubes parallel to each other as this resulted in too large a distance between the ultrasound generation and detection positions on the target surface. The arrangement of optical elements (Figure 5.19) includes a harmonic beam-splitter mirror orientated at 45 degrees from vertical which reflects light of wavelength λ_{opt} = 532 nm and transmits light of wavelength λ_{opt} = 1064 nm with 99 % efficiency. A diameter of 50 mm provided a large enough aperture to adjust the distance between the focused beams from 0 mm to 15 mm. The beam-splitter could be tilted about the two axes of its plane by the use of thumb-screws built into the mirror mount. Adjustment of laser beam focus and horizontal position was facilitated by screw-driven linear translation stages (Figure 5.20) with travel lengths between 15 mm and 25 mm.

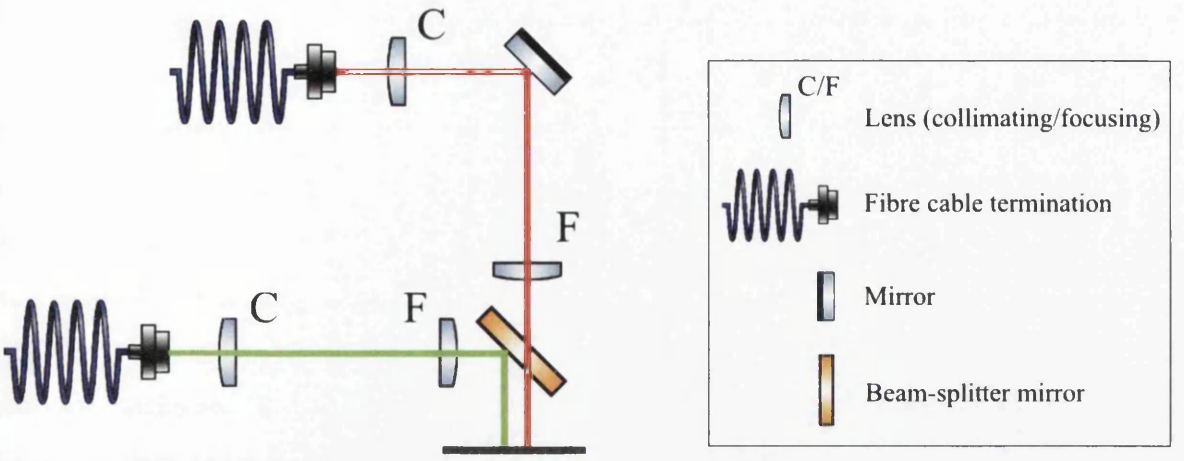

Figure 5.19. Schematic of optical arrangement for off-line laser ultrasonic testing, with the ultrasound generation and detection laser beams represented by red and green lines, respectively.

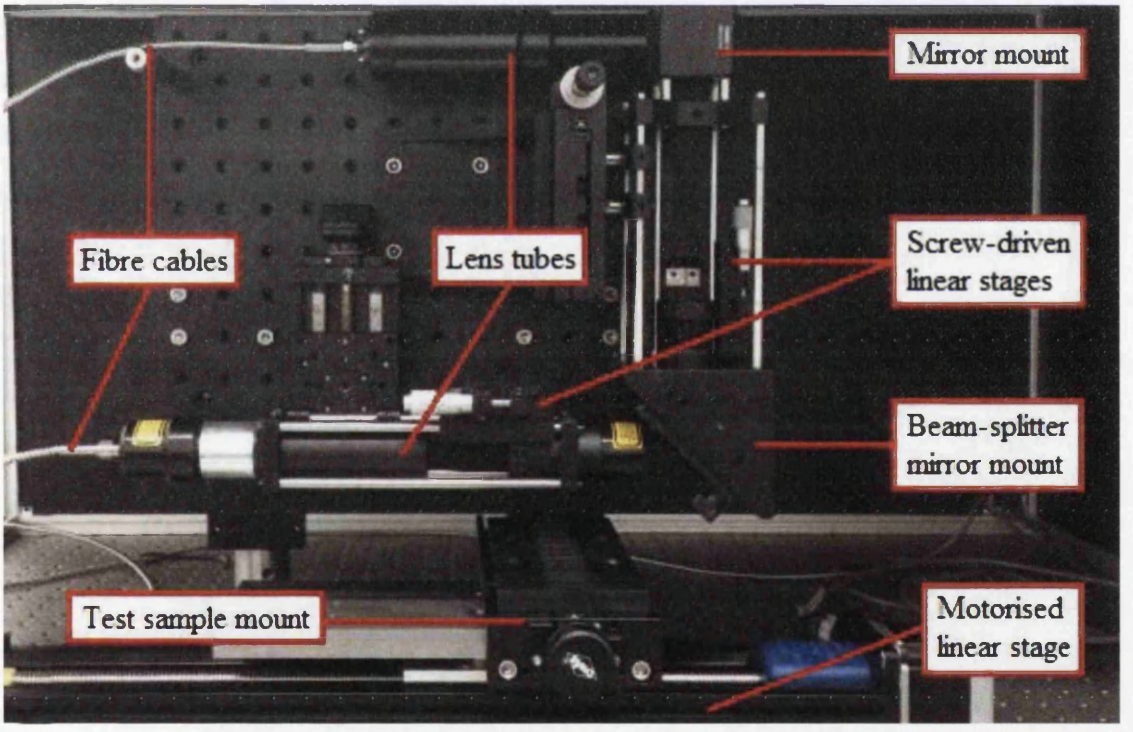

Figure 5.20. Optical arrangement for off-line laser ultrasonic testing.

5.5. Results & Analysis

5.5.1. Ultrasonic Response

According to the theoretical wave velocity equations and typical material properties of Inconel 718 at room temperature, as given in previous chapters, the expected SSL wave velocity is 5685 ms^{-1} and Rayleigh wave velocity 2880 ms^{-1}. These two wave types should be the first to appear in each data acquisition as they propagate directly between the source and reception positions. The appearance of longitudinal and transverse waves should occur later in time as they must propagate through the bulk and return to the top surface after internal reflection. For a source-reception distance of 2 mm and a material depth of 11 mm, the propagation distance before arriving at the reception position is approximately one order of magnitude greater for the bulk waves compared to that of the surface waves. A method of measuring the velocity of recorded wave signals is by taking into account the difference in arrival time of distinct signals while increasing the source-reception distance. Figure 5.21 shows the surface displacements recorded on test-piece B0 using the SLD method in stepped scanning mode. The source-reception distance is extended from 1 mm to a maximum of 12 mm. Measurement of the gradients of the first two visible wave signals gives wave velocities of 5600 ms^{-1} and 2890 ms^{-1}, corresponding to the SSL and Rayleigh ultrasonic waves, respectively. From the amplitude scale, it can be seen that the SSL wave signal exists as a positive peak while the Rayleigh wave signal exists as a deeper negative peak.

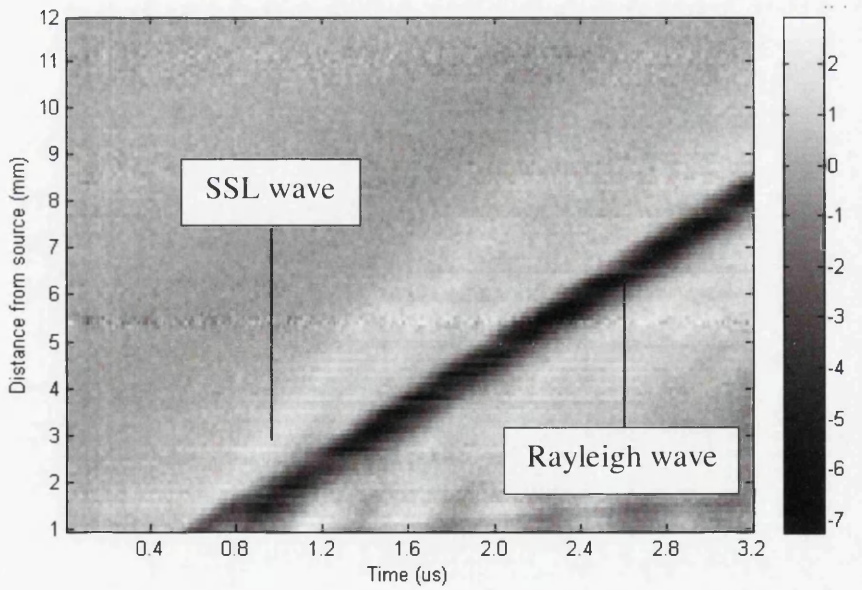

Figure 5.21: B-scan recorded in stepped SLD mode on test piece B0. Amplitude grey-scale is in units of mV.

Figure 5.22 shows the surface displacements recorded on test-piece B0 using the CLS method in stepped scanning mode, i.e. translating both laser beams along the surface at the same rate and at a fixed distance apart. It is compared to the corresponding FEA result and shows strong similarities. The difference in wave arrival times is due to different spacing between the source and detection points (1 mm for the FEA result, 2.6 mm for laboratory result). The first wave-front signal is the SSL wave, followed immediately by the Rayleigh wave signal. These both appear at a constant time because the propagation distance for surface waves is constant. Appearing later in time are the reflection 'arms' of surface waves from the sub-surface discontinuity. The *y*-axis location of the intersection of these reflected signals corresponds to the centre of the length of the test piece and thus also the location of inserted artificial flaws when each laser spot is equidistant.

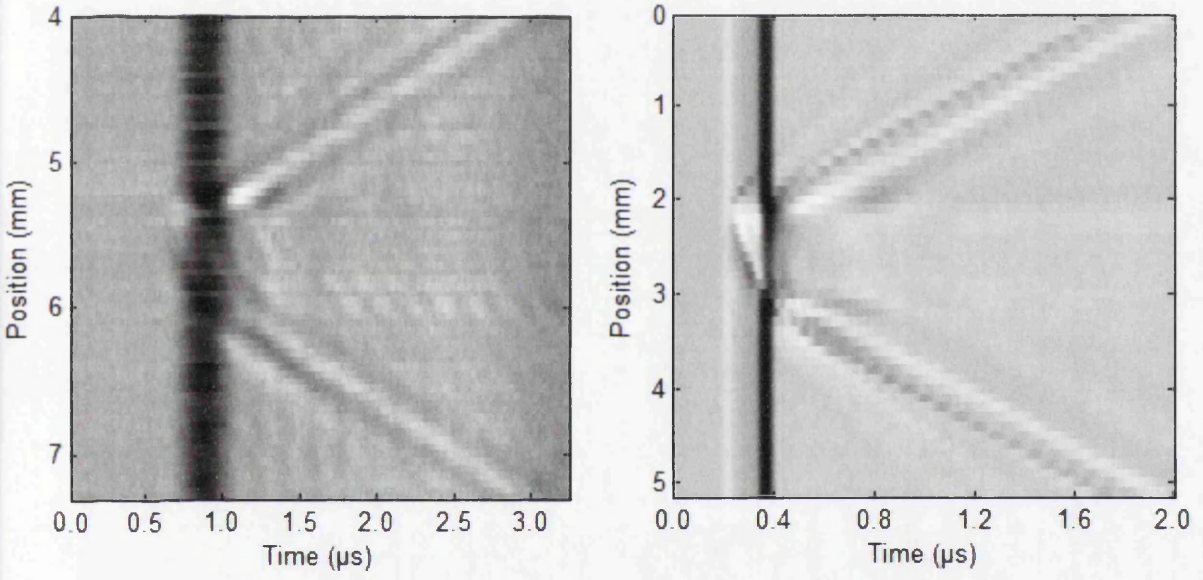

(a) (b)

Figure 5.22: (a) B-scan recorded in stepped CLS mode on test piece B100-250 and (b) the same B-scan performed using FEA with a discontinuity at 100 μm depth and 240 μm diameter.

5.5.2. Stepped Motion Scanning

Figure 5.23 shows the surface displacements recorded on test-piece A100-250 using the CLS method in stepped scanning mode with 1 mm laser beam separation and covering a total linear distance of 15 mm. The left image displays a disruption in the main Rayleigh wave signal and reflections of significant amplitude resulting from the presence of the sub-surface void at the central position. The right image shows the same B-scan rotated to give a side-on view where an increase in the maximum and minimum amplitudes of the surface wave

signals are visible and is greater than the amplitude variations before and after. Figure 5.24 expands the time-window of interest in which surface wave interactions are visible. There are variations in the Rayleigh wave amplitude and additional wave signals further along in time due to reflections from the sub-surface void.

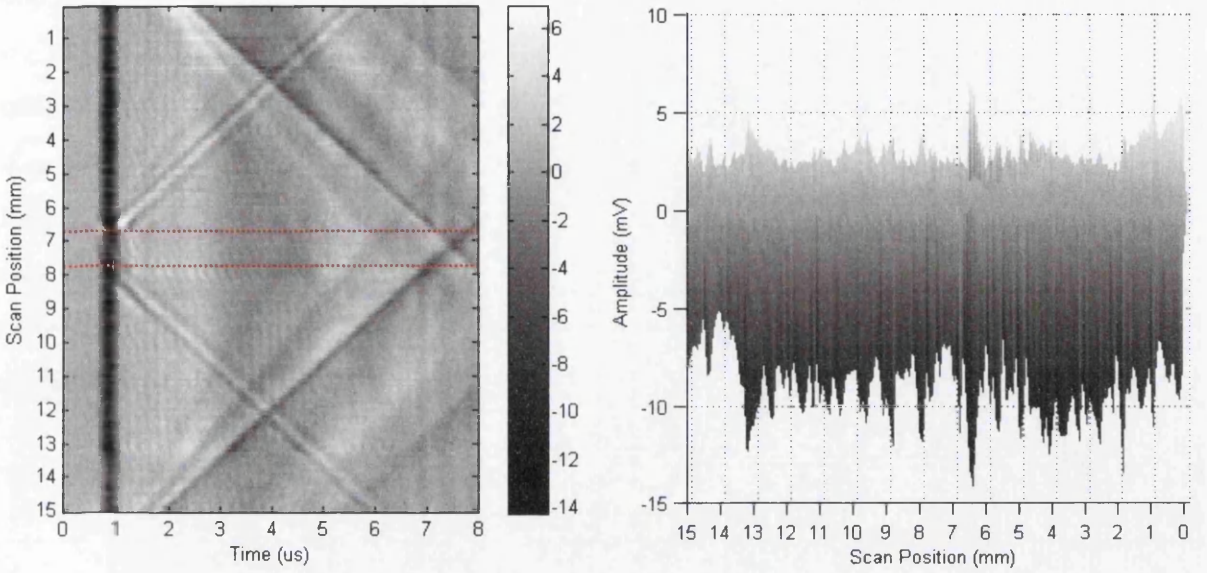

(a) (b)

Figure 5.23. B-scan recorded in stepped SLD mode on test piece A100-250 with (a) scan position as a function of time, amplitude scale in mV and (b) amplitude as a function of scan position.

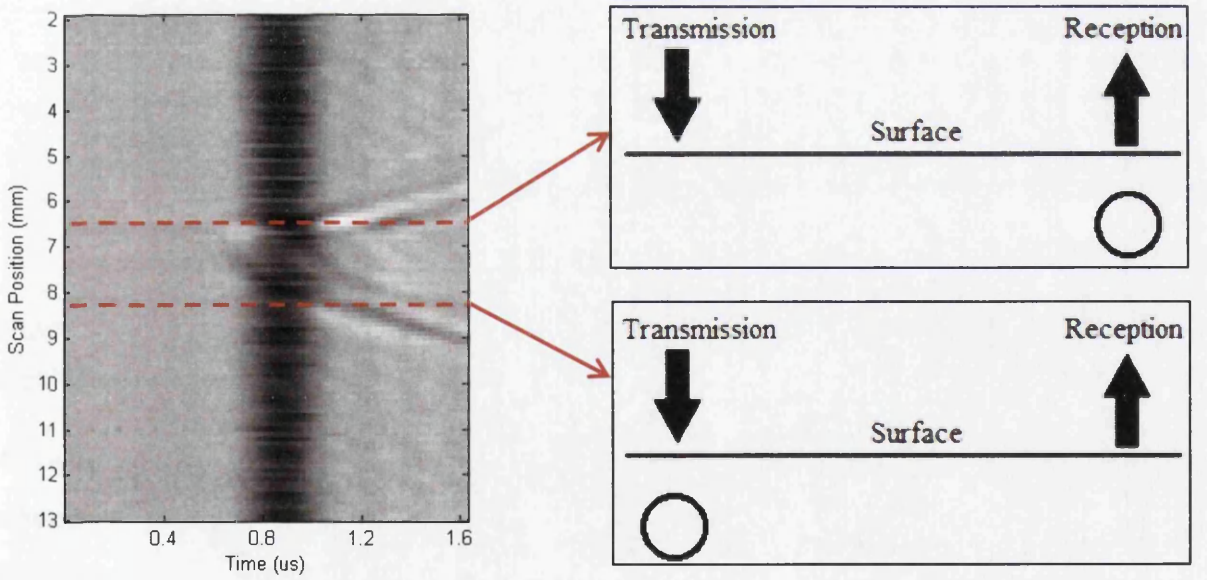

Figure 5.24. B-scan recorded in stepped SLD mode on test piece A100-250 with laser positions, relative to the sub-surface void, illustrated.

5.5.2.1. Time Domain Analysis

In order to perform time domain analysis of variations in the received surface displacements, each data set (B-scan) is divided into time and position windows as illustrated in Figure 5.25. T1 is a time-window from t = 0.5 μs to t = 1.3 μs containing the SSL wave and Rayleigh wave; here both the absolute difference and the ratio between the maximum and minimum amplitudes will be output as a function of scan position. T2 is a time-window from t = 1.0 μs to t = 1.3 μs containing displacements immediately after the Rayleigh wave signal in which there should not be signals above noise, but additional signals do appear due to the presence of a sub-surface void; here the maximum amplitude will be output as a function of scan position. P1 is a position-window from x = 0 mm to x = 5.4 mm and x = 9.6 mm to x = 15 mm, containing positions either side of the location of a sub-surface void in which surface wave signals are unaffected. Conversely, position-window P2 from x = 5.5 mm to x = 9.5 mm contains positions surface wave interactions with the discontinuity should be expected.

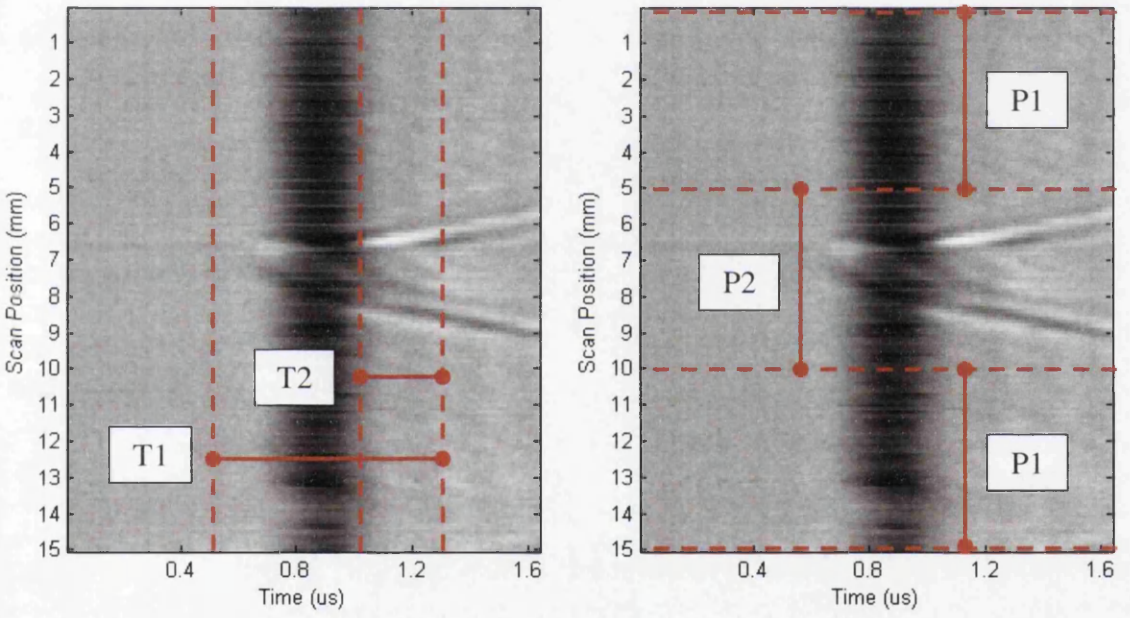

Figure 5.25. B-scan recorded in stepped SLD mode on test piece A100-250 with sections highlighted to represent selected (a) time-windows and (b) position-windows for analysis.

As was performed using the FEA data in Chapter 4, in time-window T1 the ratio of maximum-to-minimum Rayleigh wave amplitude will be measured over all positions. Within time-window T2, there should usually be no ultrasonic wave arrivals and any additional signals should only be due to interaction with the artificial flaw, showing a pronounced increase in surface displacement amplitude, therefore in this case the absolute amplitude can be relied on to provide a measure of signal variation. The result for test-pieces A100-250 and

A200-250 (Figure 5.26) shows a significant increase in both the amplitude ratio of the surface wave signals in time-window T1 (a) and the absolute measured amplitude immediately after in time-window T2 (b). The separation between position-windows P1 and P2 is marked by vertical dashed lines. The amplitude increase occurs when the source laser beam is less than 1 mm from the location of the sub-surface void, and continues until the reception laser beam has passed at least 1.5 mm from the location of the sub-surface void. Amplitude variation diminishes as the diameter of the discontinuity decreases (Figure 5.27).

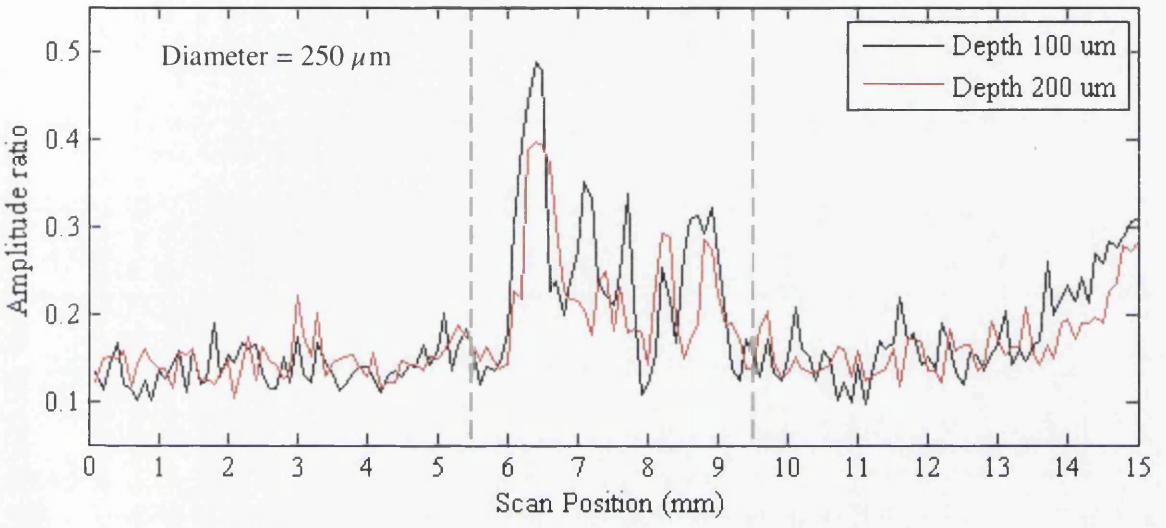

(a)

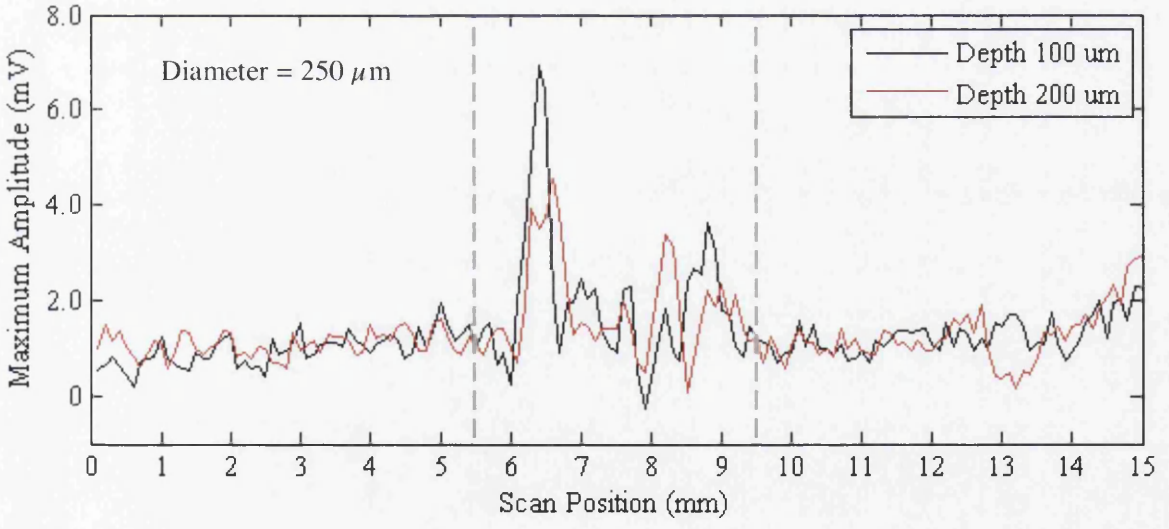

(b)

Figure 5.26. Measured data for test-pieces A100-250 and A200-250, showing (a) amplitude ratio within time-window T1, and (b) actual amplitude within time-window T2.

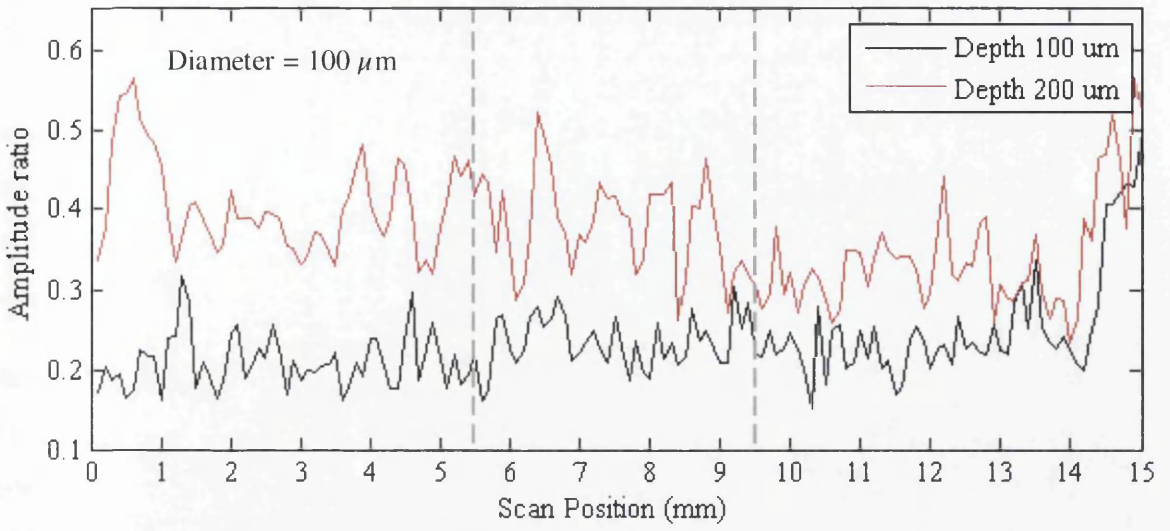

(a)

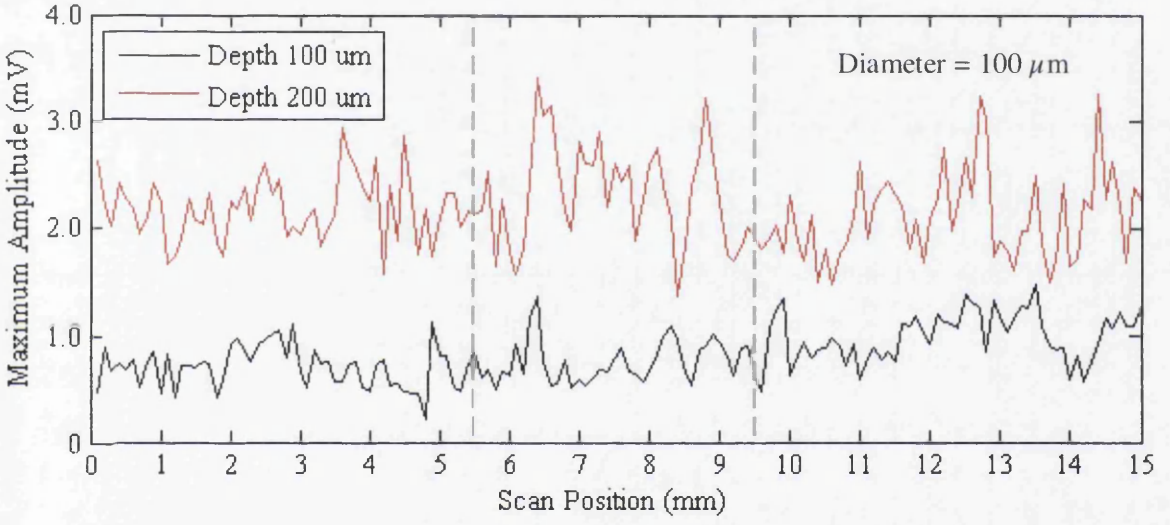

(b)

Figure 5.27. Measured data for test-pieces B100-100 and B200-100, showing (a) amplitude ratio within time-window T1, and (b) actual amplitude within time-window T2.

For all test-pieces, the surface displacement amplitude data was compared between windows P1 and P2 by measuring the maximum amplitude and standard deviation from the mean amplitude within each position-window. It was observed that all B-scans displayed a gradual increase in amplitude towards the end of each scan, after scan position 12 mm. This could be due to misalignment of the lasers with respect to the test surface, or poor tolerances in the dimensions of the manufactured test-pieces. Therefore only data within the scan position range from 0 mm to 5.5 mm were used for window P1.

To compare results between different test-pieces, the percentage increase in output amplitude from window P1 to window P2 is given in terms of maximum and standard deviation from the mean in Figures 5.28 to 5.30 below. The graphs on the left side display the increase in amplitude ratio (labelled 'Ratio') of the Rayleigh wave signal (window T1), while the graphs on the right side display the increase in maximum amplitude (labelled 'Max') within the time-window immediately after the Rayleigh wave signal (window T2).

On each graph, a horizontal green line is placed at $y = 100$ (%), which represents a ratio of 2:1 of the signal of interest to the background signals. In this case, the signal of interest exists in window P2 and the background data in window P1. The ratio of 2:1 commonly represents the minimum threshold above which a flaw indication signal is considered reliably detectable in ultrasonic testing [81], and will be used as such in this work. A result below 100% means that the signal increase above background is not significant enough to be relied upon, and a result below 0% means that the measured signal within window P2 just happens to be less than the measured signal within window P1.

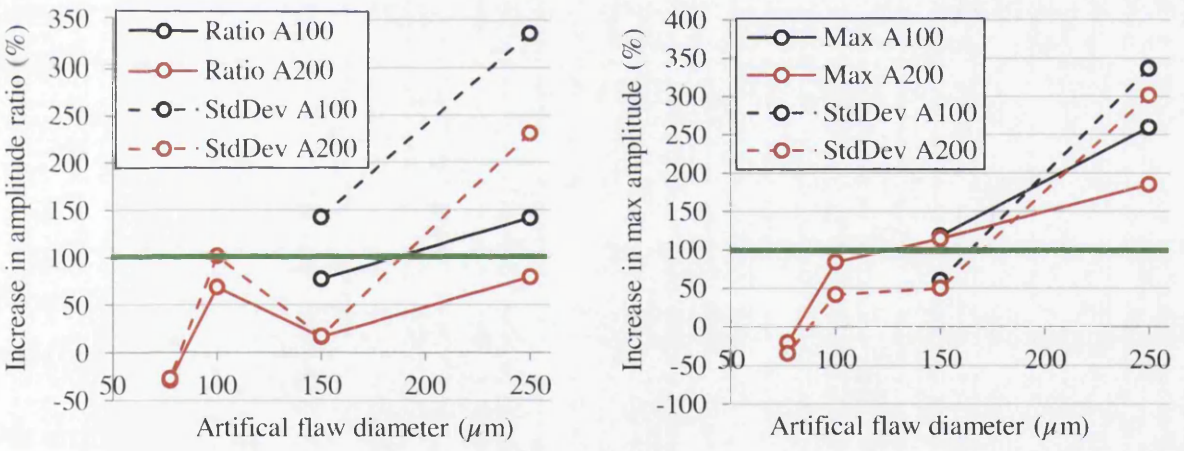

(a) (b)

Figure 5.28. Percentage change in maximum of (a) amplitude ratio within window T1, and (b) actual amplitude in window T2, for test-pieces labelled 'A'.

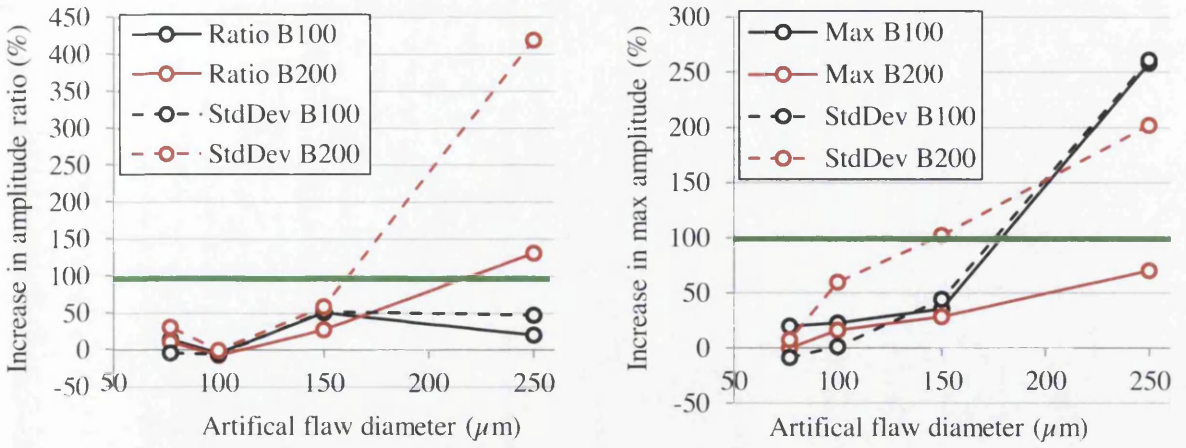

(a) (b)

Figure 5.29. Percentage change in maximum value of (a) amplitude ratio within window T1, and (b) actual amplitude in window T2, for test-pieces labelled 'B'.

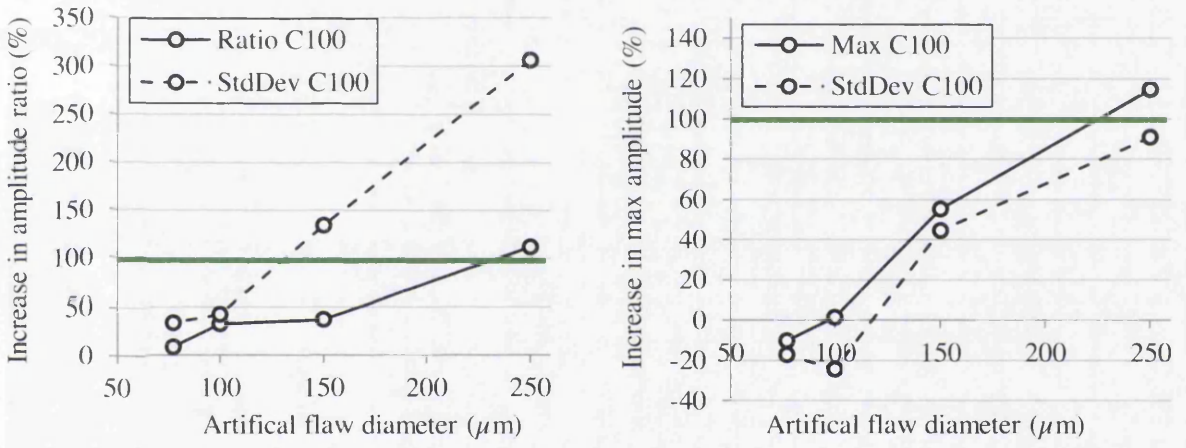

(a) b)

Figure 5.30. Percentage change in maximum value of (a) amplitude ratio within window T1, and (b) actual amplitude in window T2, for test-pieces labelled 'C'.

An artificial flaw diameter of 250 μm proves reliably detectable in the greatest number of cases and in all cases, a diameter of less than 150 μm is not at all reliably detectable. This and other methods, which follow below, will be summarised at the end of this section.

An alternative approach to analysing the acquired B-scan data is to concentrate on the reflection signals which arrive at a time later than the Rayleigh wave signal and diverge from the position of a sub-surface void. These reflection signals are easily distinguishable by eye for the test-pieces with a machined test surface (Figure 5.31), and for all but the smallest artificial flaw diameter for the test-pieces with a deposited surface (Figure 5.32). The reflections consist of a central positive peak flanked either side by a negative peak of slightly

lower amplitude. The peak-to-peak time decreases with flaw diameter, and this will be explored in the 'frequency domain analysis' section.

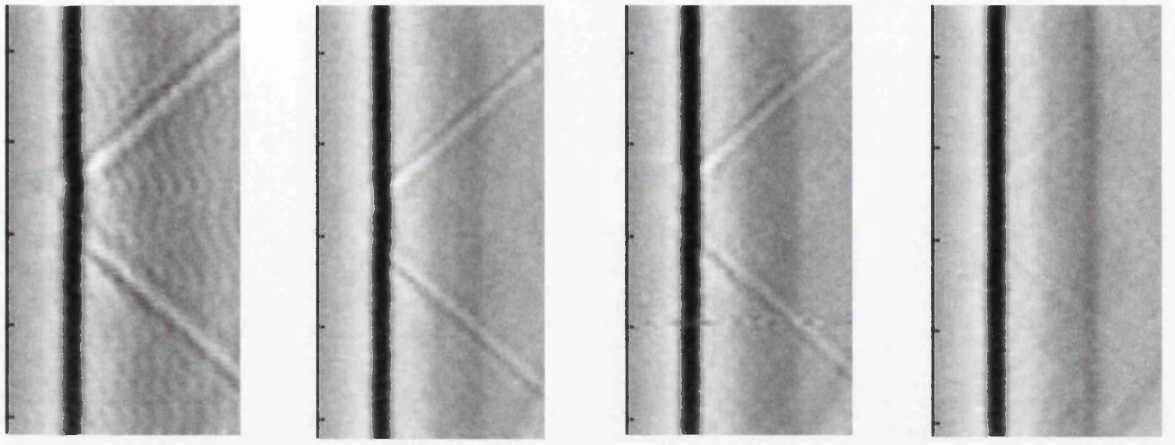

a b c d

Figure 5.31. Surface displacements as a function of time and position for test samples (a) B200-250, (b) B200-150, (c) B200-100, and (d) B200-77.

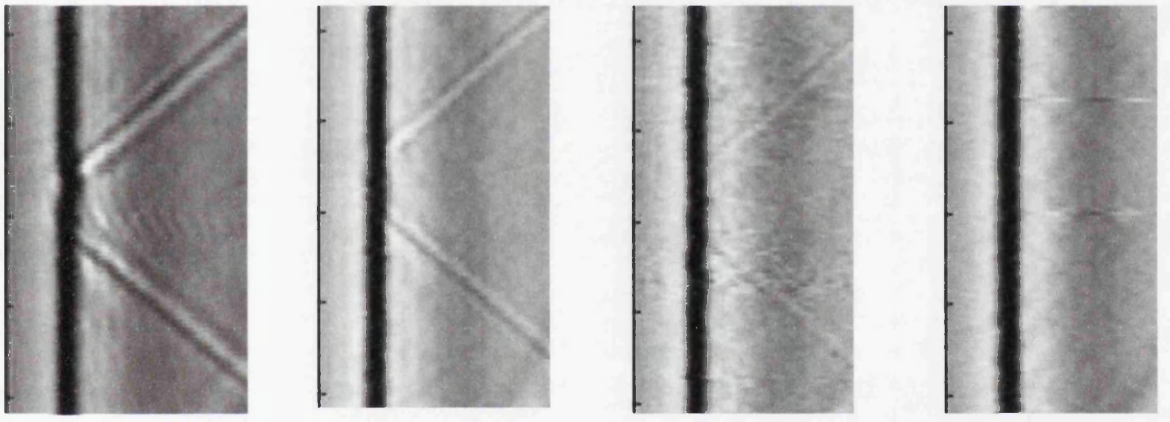

a b c d

Figure 5.32. Surface displacements as a function of time and position for test samples (a) C100-250, (b) C100-150, (c) C100-100, and (d) C100-77.

It is more useful in this case to be able to extract the relevant flaw indications in an automated fashion, as the ultimate aim is to detect near-surface flaws in-situ and with minimal human monitoring. A Matlab script was written to locate the maximum amplitude for each A-scan/position, within a time-window starting after the arrival of the Rayleigh wave signal and thus containing only the reflection signals. Maxima within A-scans not containing the reflection signals (scan positions 4 mm to 7 mm in Figure 5.33.a) were discarded by setting a minimum amplitude threshold. Next, for each A-scan, the local minima either side of the maximum peak were located within a smaller user-defined time-window also selected from

visual inspection. This process was repeated for data from all test-pieces. As can be seen in Figure 5.33.b, the reflection signal displays good symmetry about the central peak, in terms of both time and amplitude.

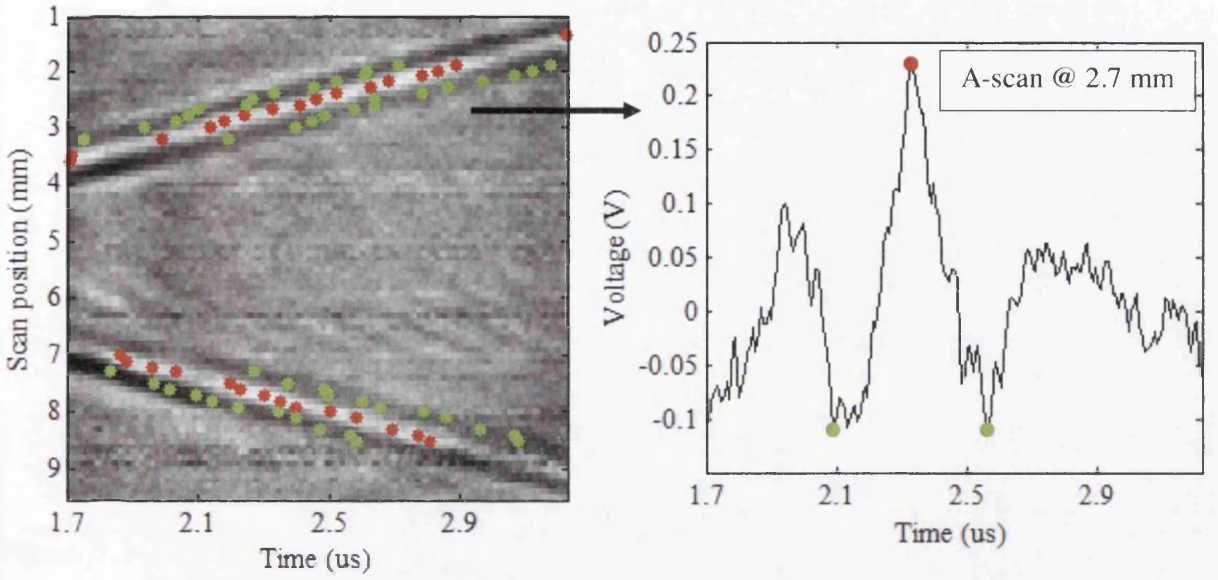

(a) (b)

Figure 5.33. Time-window containing reflected wave signals from test-piece A100-250 (laser scan separation approx. 2.6 mm), displaying maximum amplitudes as red dots and local minimum amplitudes as green dots, for (a) all B-scan positions, and (b) A-scan at scan position 2.7 mm.

For each maxima and local minima, the peak-to-peak amplitude was measured, thus providing two data points per A-scan. In Figure 5.34, these results are displayed as a percentage of the Rayleigh wave signal amplitude and also as a ratio to the noise signals present in each A-scan. The former provides a measure of the proportion of the main Rayleigh wave which is reflected. The latter metric provides a measure of the detectability of the reflection signals. For test-piece sets A, B and C, there is a consistent decrease in these measures values when comparing flaw diameters 250 μm to 150 μm. Only one set of successful measurements was possible for flaw diameter 100 μm (B100-100) and none for flaw diameter 77 μm, due to decreasing signal-to-noise ratio as less of the Rayleigh wave is reflected. The result from the deposited surface scans also consistently falls below that of the machined test-pieces.

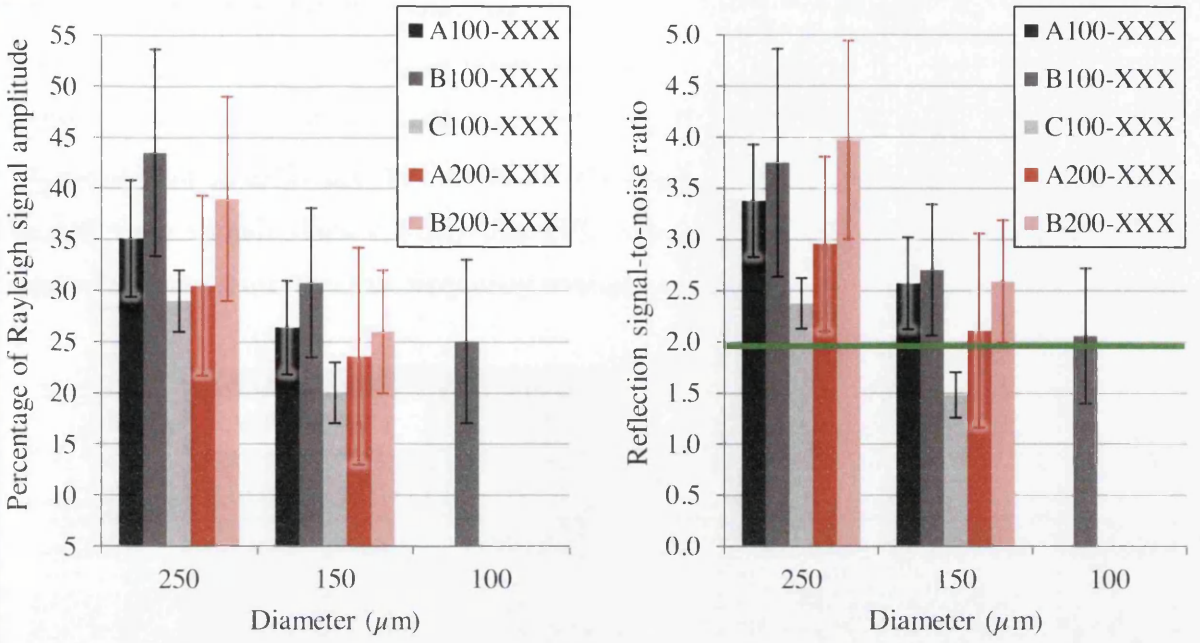

Figure 5.34. Reflection signal peak-to-peak amplitude as (a) a percentage of Rayleigh wave signal amplitude, and (b) a ratio of noise signals, with a horizontal green line at the 2:1 signal ratio threshold. Error bars represent standard deviation.

This detection method might be further automated by searching for successive A-scan maxima which fit to the gradient of the reflection signals as they diverge from the position of the sub-surface void in the B-scans. This gradient can be calculated before scanning by taking into account the known Rayleigh wave speed, the number of A-scans per unit length (determined by the motion rate and pulse repetition frequency), and the acquisition rate of the data collection hardware. Thus the maxima within the A-scans containing only noise signals could be discarded without the need to manually set a minimum amplitude threshold per test-piece.

5.5.2.2. Frequency Domain Analysis

A similar approach was taken in order to analyse the same stepped B-scan data in the frequency domain. First, each data set was separated into two time-windows: the first containing data up to the arrival time of the Rayleigh wave signal, and the second containing the reflection signals (Figure 5.35). An FFT was applied to all A-scans in each of these windowed data sets so that that frequency content could be displayed and changes measured.

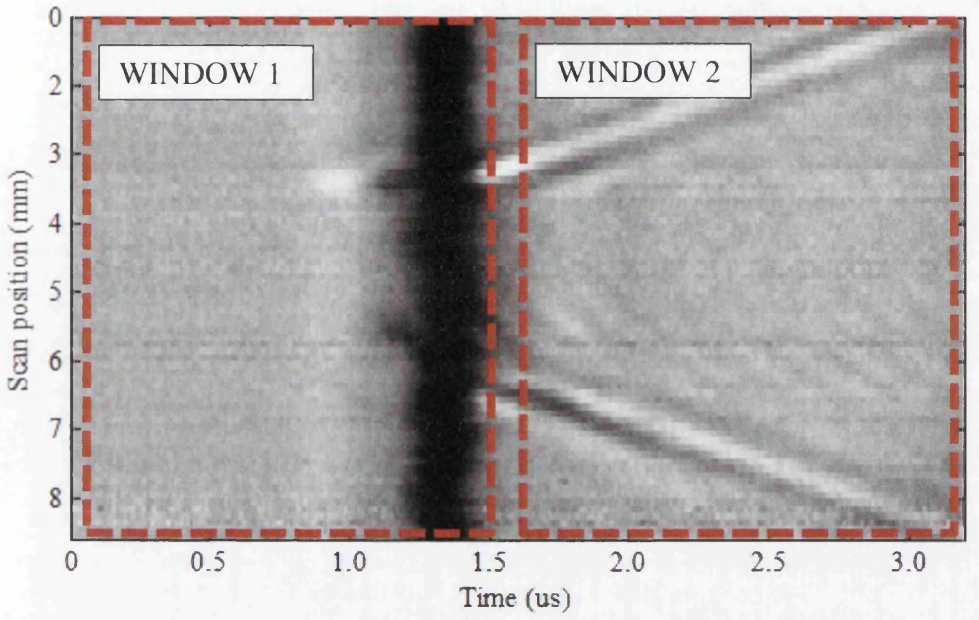

Figure 5.35. Stepped-mode B-scan on test-piece A100-250, highlighting the time-windows selected for frequency-domain analysis (laser separation approx. 2.6 mm).

By plotting recorded B-scans in the frequency domain, it can be observed that there is a reduction in ultrasonic wave energy within the band 2.5 to 4.5 MHz for a large section of the scan where the sub-surface void exists between the two laser beams (Figure 5.36). This begins from the passing of the detection laser and ends approximately 1 mm before the passing of the ultrasonic source. This implies that the artifical flaws act as a sort of frequency filter, blocking parts of the surface wave. The effect is visibly diminished by the increase of depth and decrease of flaw diameter.

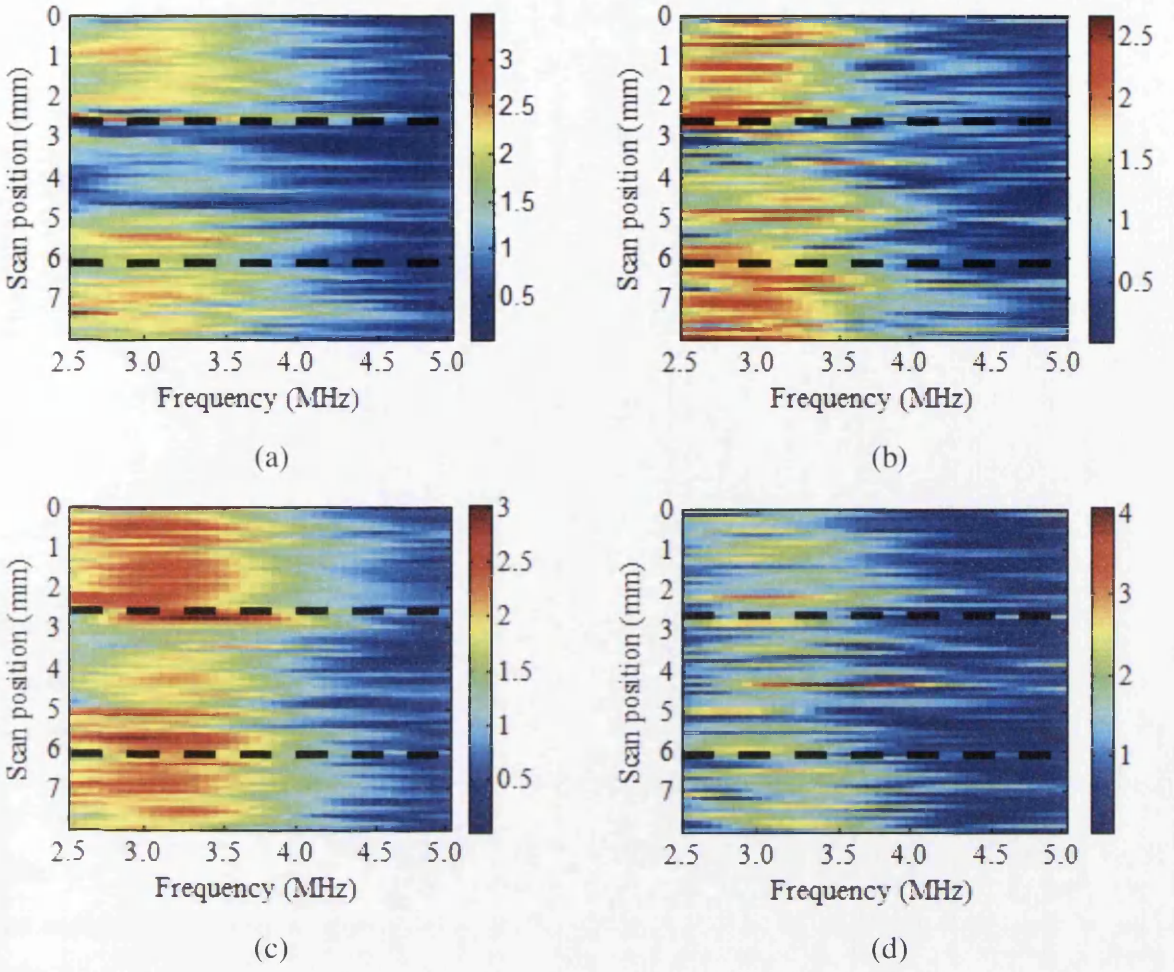

Figure 5.36. FFT applied within 'Window 1' on B-scan data for test-pieces (a) A100-250, (b) A200-250, (c) A100-150, and (d) A200-150. Dashed black lines represent passing of the detection laser (upper) and the generation laser (lower) over the flaw position. Colour scales correspond to FFT amplitude.

The dynamic change in FFT amplitude was measured by selecting an arbitrarily-chosen frequency-window (x-axis) bounded at the point where amplitude drops to 50% of the maximum, taken as an average over all A-scans outside of the central 'filtered' region. For example, this gives a frequency range of interest of 2.5 to 3.9 MHz for test-piece A100-250. Within this bounded data set, the mean FFT amplitude was measured for each position (y-axis) as well as standard deviation from the mean, providing a metric to monitor frequency content per position. Thus plotted in Figure 5.37 is the result for test-piece A100-250, including mean values for FFT amplitude within the affected and unaffected position ranges.

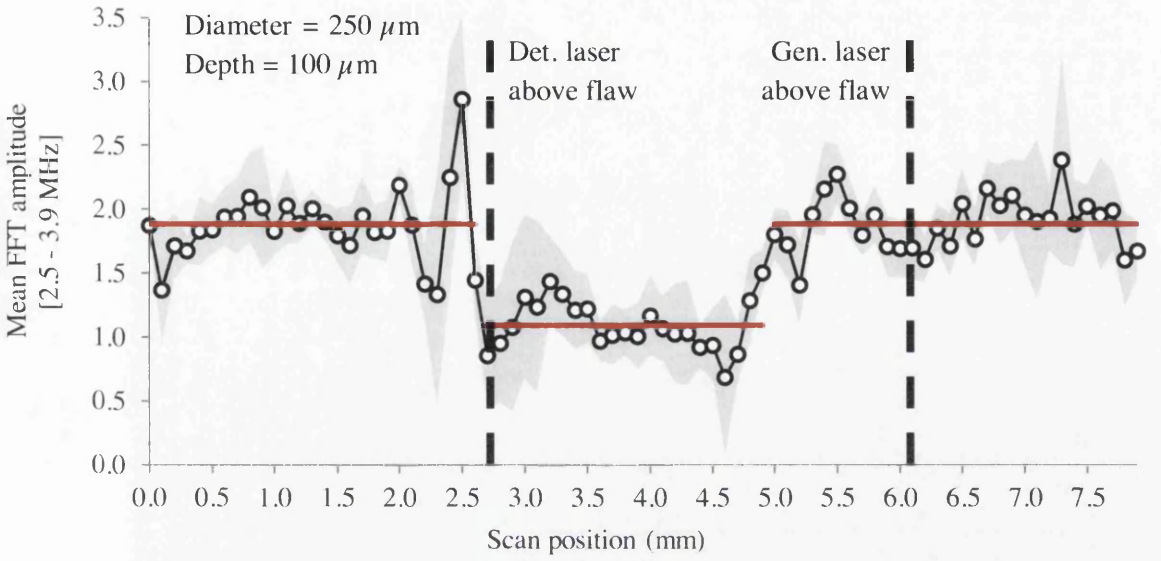

Figure 5.37. Mean FFT amplitude within the frequency band 2.5 – 3.9 MHz, including standard deviation (grey area), as a function of scan position for test-piece A100-250. Red lines represent mean values of the 'filtered' and 'un-filtered' sections.

The mean drop in FFT amplitude, representative of the average area under the amplitude within the selected frequency range and thus wave energy per A-scan, can be considered as a flaw indication signal. The percentage drop in this signal was measured as 42% for test-piece A100-250, and 22% for test-pieces A200-250 and A100-150. This is not equivalent to a 2:1 difference from 'background' signal (i.e. frequency content of the unaffected surface wave) and was not measurable on the remaining test-pieces, so can not be considered a reliable detection method in this case.

The same technique was applied using data within 'Window 2', containing only the reflection signals. Frequency-domain data can be seen in Figure 5.38, showing a significant increase in frequency content in the A-scans where reflection signals are present. This effect also diminishes with increasing flaw depth and decreasing flaw diameter, becoming less discernable from noise signals. Furthermore, the reflection signal content moves up along the frequency scale as flaw diameter decreases, as was observed in the FEA results analysis in Chapter 4. However, the measured frequencies are slightly lower than those seen in the FEA results for the equivalent sized sub-surface voids.

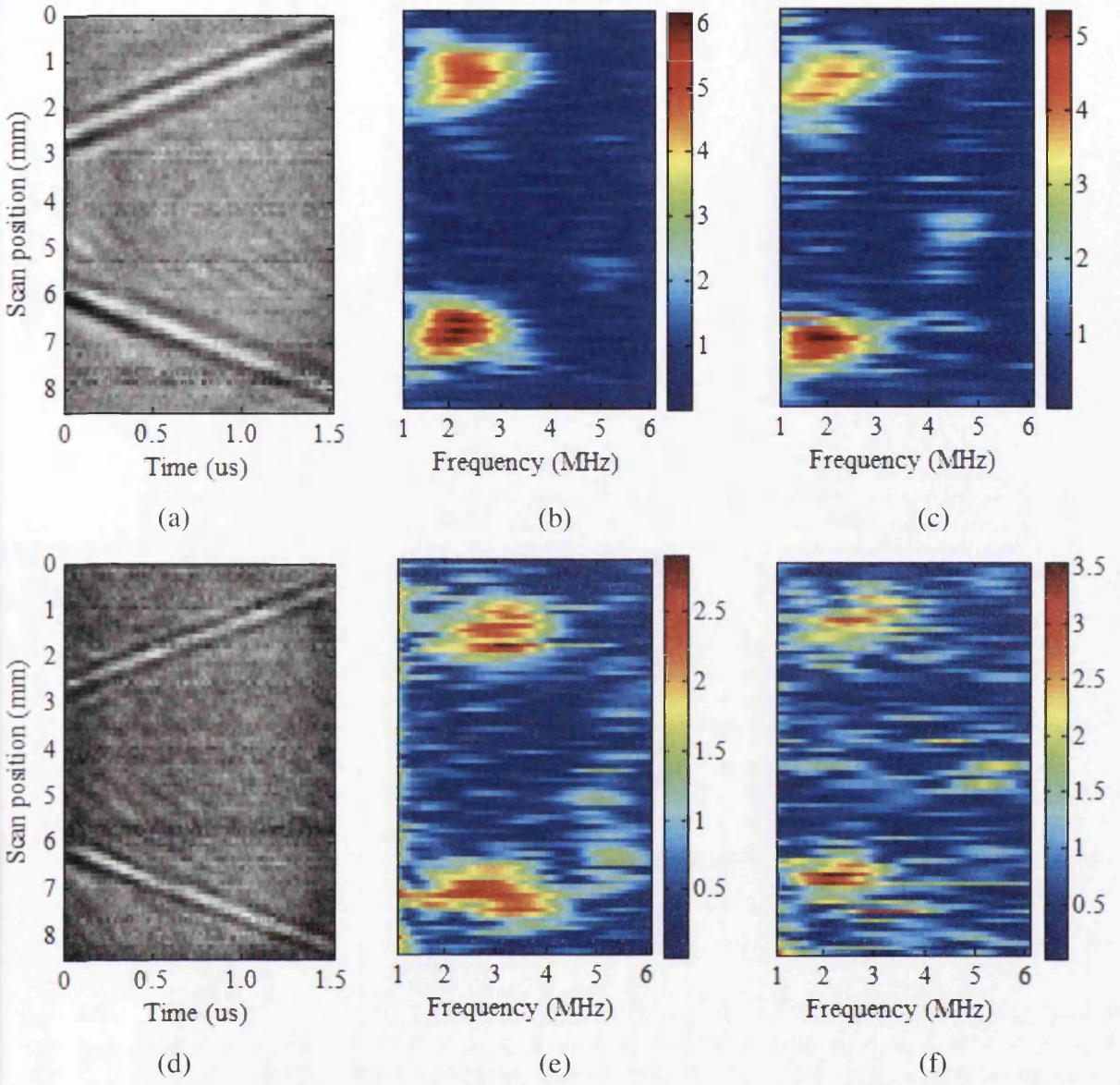

Figure 5.38. Outputs from 'Window 2' in recorded B-scans. Upper row: (a) A100-250, time-domain, (b) A100-250, frequency-domain, (c) A200-250, frequency-domain. Lower row: (d) A100-150, time-domain, (e) A100-150, frequency-domain, (f) A200-150, frequency-domain.

As before, a frequency-window was selected from each data set bounded at the point where FFT amplitude drops to 50% of the maximum, taken as an average over all A-scans containing the reflection signals. Within this bounded data set, the mean FFT amplitude was measured for each position (y-axis) as well as standard deviation from the mean. Thus plotted in Figure 5.39 is the result for test-piece A100-250, including mean values for FFT amplitude within the regions of interest. The increases in mean and maximum FFT amplitude can be used as flaw indication signals in this case, and are plotted for each test-piece in Figure 5.40.

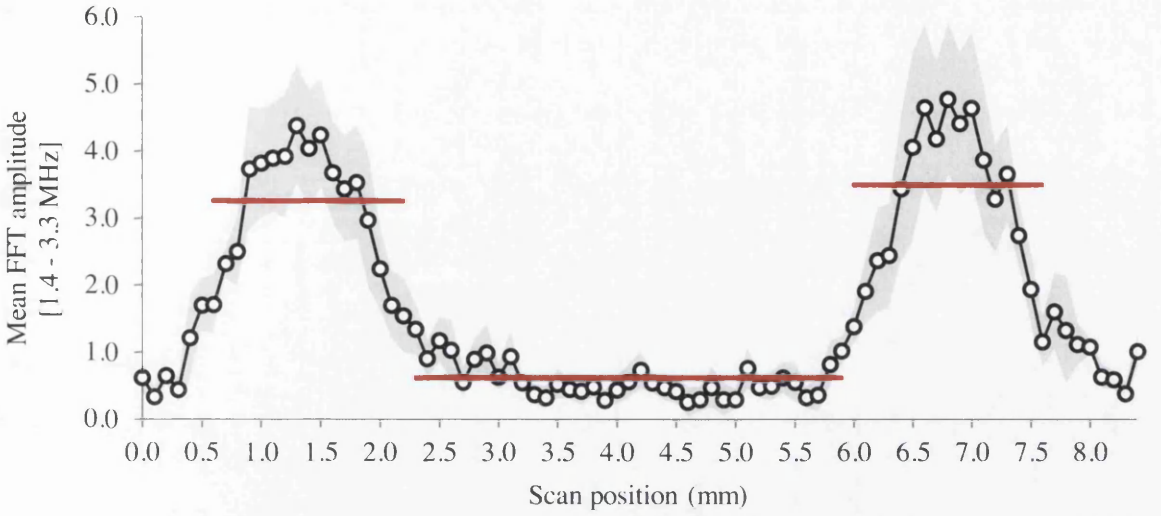

Figure 5.39. Mean FFT amplitude within the frequency band 1.4 – 3.3 MHz, including standard deviation (grey area), as a function of scan position for test-piece A100-250. Red lines represent mean values of the 'background' and 'reflection signal' sections.

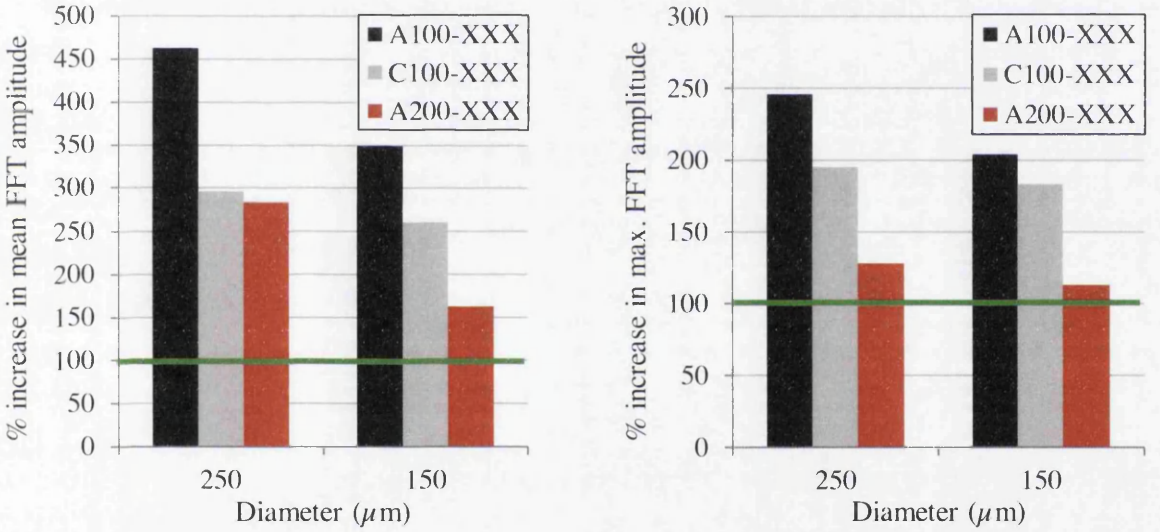

Figure 5.40. Reflection signal percentage increase from noise signals for (a) mean FFT amplitude, and (b) maximum FFT amplitude, within the ranges of positions as described. Horizontal green line represents the 2:1 signal ratio threshold.

This method provides an effective detection technique for both the artificial flaws of diameters 250 μm and 150 μm at depths of 100 μm and 200 μm, including both the machined and deposited surfaces. For all of these test-pieces, the ratio of indication signal (mean or maximum FFT amplitude) to noise signal (FFT amplitude in A-scan positions where no reflection signal exists) is greater than 2:1. This ratio is consistently decreased due to

increasing flaw depth, decreasing flaw diameter, and change in surface finish from machined to powder-deposited.

Finally, the measured frequency range and peak frequency for the reflections signals are summarised for the same test-pieces in Figure 5.41. As previously, the frequency ranges are bounded where FFT amplitude drops to 50% of the maximum, as measured in the A-scans containing the reflection signals. It can be seen that the frequency range and peak frequency is increased in all cases due to decrease in flaw diameter, suggesting that diameter affects the frequency band of the Rayleigh wave which is reflected.

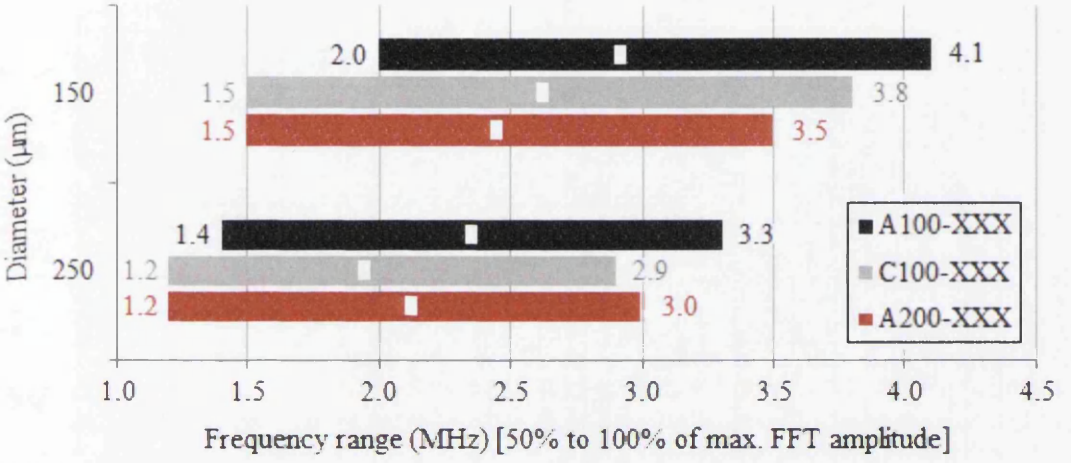

Figure 5.41. Frequency range (horizontal bar) and peak frequency (white marker) of detectable reflection signals.

5.5.2.3. Summary

If an acceptable level of artificial flaw detectability is taken as the measurement of signal data above the threshold set for each of the time-domain and frequency-domain detection methods, then the success of each method as applied to all test-pieces can be summarised as shown in Table 5.6 below. In each case, 'gain' refers to the increase in amplitude of the signal data of interest compared to adjacent signals (either unaffected signals or noise).

Table 5.6. Summary of artificial flaw detectability using the time-domain and frequency-domain analysis methods described. A cross signifies achievable detectability.

	Time-domain			Frequency-domain	
Test-piece reference	Rayleigh wave amplitude ratio gain	Amplitude gain as det. laser passes over flaw	Reflected waves amplitude gain	Reflected waves frequency gain	Total
A100-250	X	X	X	X	4
A100-150	X	X	X	X	4
A200-250	X	X	X	X	4
A200-150		X		X	2
B100-250		X	X		2
B100-150			X		1
B200-250	X	X	X		3
B200-150			X		1
C100-250	X	X	X	X	4
C100-150				X	1
Total	5	7	8	6	

From these combined results it can be concluded that the greatest coverage of detectability over the range of test-pieces is achieved through the analysis of reflected ultrasonic wave signals which appear after main Rayleigh signal and originate from the position of the

artificial flaw. Analysis methods applied to the main Rayleigh signal prove less valuable in detecting the same artificial flaws.

Of the flaw sizes and depths included in the table above, the largest and shallowest tend to be detectable using the greatest number of methods. This reliability drops off when comparing machined test-pieces of width 0.5 mm (labelled 'A') to those of greater width and also those with a deposited surface. Detectability also reduces with depth, where artificial flaws are further away from the main energy concentration of the Rayleigh wave closer to the surface.

Artificial flaws of diameters 100 μm and 77 μm remain undetectable within the thresholds set for each method. The greatest limiting factor in this regard is the maximum generated frequency components of the Rayleigh wave which is used for interrogating each sub-surface void: there is no substantial ultrasonic energy present in the data beyond approximately 5 MHz, as expected from the laser spot size. This translates to a Rayleigh wavelength of approximately four times 150 μm – it should be noted that in training and industrial applications of flaw detection using bulk ultrasonic waves, the generally accepted minimum detectable flaw diameter is half of the wavelength [81]. As the ratio of wavelength to flaw diameter increases, the probability of detection decreases towards insignificance. The generation of ultrasonic waves with higher frequencies, and therefore smaller wavelengths, should increase the likelihood of detectable interactions with flaws of smaller diameters.

5.5.3. Continuous Motion Scanning

Laser scans were carried out on the same test-pieces using continuous motion, at speeds from 2 mm/s to 10 mm/s as described in the set-up section. B-scans performed on test-piece A100-250 are shown in Figure 5.42, where it can be seen that the acquired B-scans appear noisier and less stable than those acquired in stepped scanning with averaging. Additionally, the number of A-scans per unit length reduces proportionally with increasing scan speed due to the fixed maximum repetition frequency of the transmission laser, leading to a reduction in data resolution in the scan position axis. It is also observed that the polarity of the received Rayleigh signal infrequently reverses – this is due to limited motion capability of the interferometer used in the experiments and will be discussed in the final section of this chapter. The ultrasonic wave reflection signals are barely visible against noise signals.

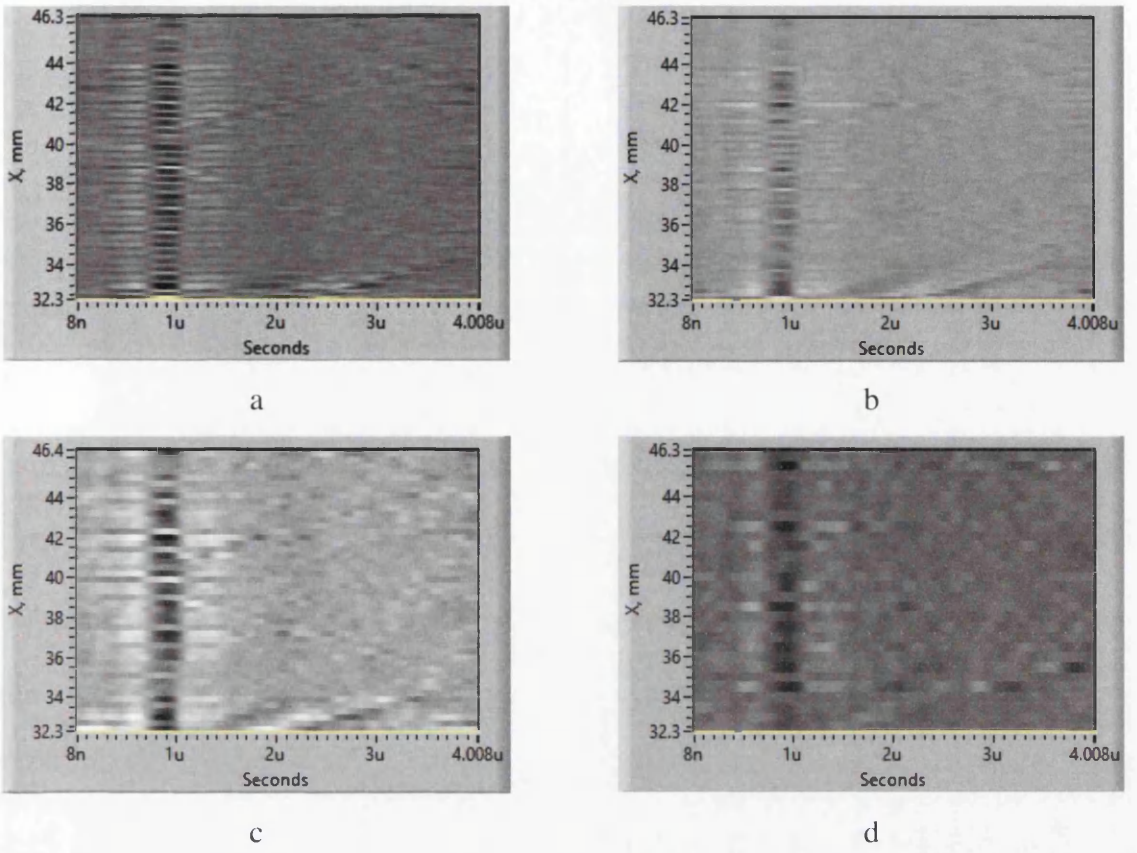

Figure 5.42. B-scans performed on test-piece A100-250 in continuous mode at speeds of (a) 2 mm/s, (b) 4 mm/s, (c) 6 mm/s, and (d) 10 mm/s.

The same time-domain and frequency-domain analyses as described in the previous section were performed on the data acquired in continuous scan mode on the same set of test-pieces. Taking into account to the established detectability thresholds, none of the data sets provided an acceptable level of detectability for any of the artificial flaw diameters or depths. Indication signals were not sufficiently distinguishable from noise signals via data analysis.

It is important then to be able to quantify this loss in signal quality from stepped scan mode to continuous scan mode, and also as a function of increasing scan speed. Figure 5.43 shows a B-scan recorded in continuous mode on a test-piece containing no artificial flaw. In order to compare signal-to-noise ratio (SNR), the Rayleigh wave signal amplitude was measured within 'Window 1' and maximum noise signal amplitude was measured within 'Window 2', repeated over all scan positions to give a mean SNR with standard deviation (Figure 5.44.a). The data within 'Window 1' was measured as absolute values to correct for occasional polarity reversal of the signal. The percentage of A-scans displaying signal polarity reversal was also counted (Figure 5.44.b). These measurements were repeated for all scan speeds and on test-pieces A0 and C0 to allow for variation due to machined or deposited surface finish.

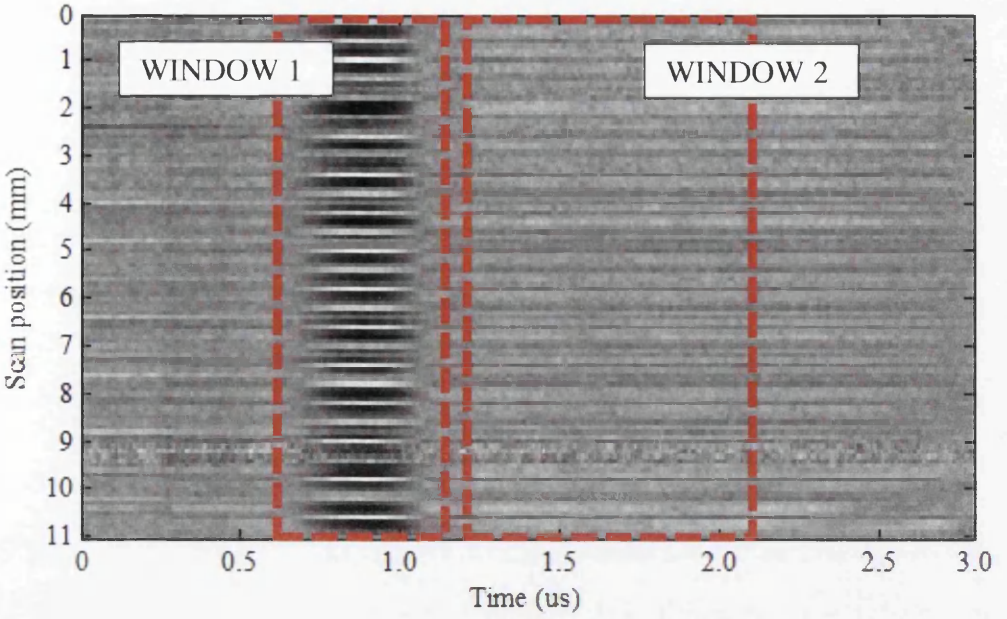

Figure 5.43. B-scan performed on test-piece A0 in continuous mode at a speed of 2 mm/s, highlighting the time-windows selected for SNR analysis.

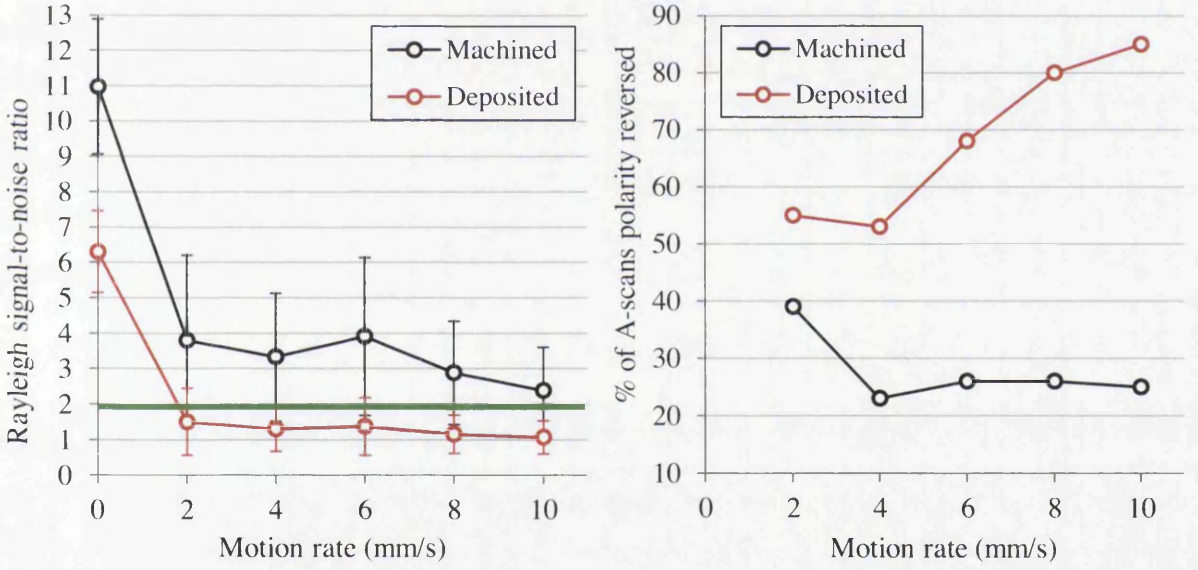

Figure 5.44. (a) Rayleigh wave SNR as a function of scan speed, including result at 0 mm/s for stepped scan, and (b) percentage of A-scans displaying signal polarity reversal as a function of scan speed.

Surface roughness R_a (arithmetic average of surface profile height deviations from the mean) was measured along the surface length of the test-pieces and gave a mean value of 797 nm for test-piece A0 (machined) and 1915 nm for test-piece C0 (deposited). For all scan speeds, mean SNR is lower for the deposited surface - reduced by 45% in stepped scan mode, and

consistently reduced by 60% to 65% in continuous scan mode. This may be attributed to lower reflectivity and increased diffusion of the reflected detection laser beam, reducing the overall amount and consistency of light being received by the interferometer. Standard deviation as a percentage of the mean value of SNR remains fairly consistent over all continuous mode tests so does not appear to depend on surface roughness or scan speed, but is reduced in stepped scan mode probably due to signal averaging.

The level of mean SNR stays above the threshold of 2:1 at all scan speeds with the machined surface, while falling below the threshold in continuous scan mode with the deposited surface. The change from stepped, averaged mode to continuous mode scanning results in a reduction in mean SNR of approximately 65% and 75% respectively, continuing to gradually fall as motion rate is increased.

Signal polarity reveral occurs significantly more often in the deposited surface tests compared to the machined surface tests. This difference becomes more severe with increasing scan speed while the occurrence of polarity reversal remains fairly constant with the machined surface. As a measure of signal stability, this may be a function of both surface roughness and motion rate.

Repeated tests on surfaces with a more varied range of roughness may lead to more robust conslusions. It is important to note that the machined surface might support a better reflection signal due to its flat profile compared to the slightly rounded profile of the deposited surface.

5.6. Discussion

5.6.1. Ultrasonic Frequencies Generated

No significant ultrasonic wave energy was observed beyond approximately 5 MHz in frequency-domain analysis of received signals, as expected due to the limiting factor of the laser spot size as described in Section 5.2.3. This frequency corresponds to a Rayleigh wavelength of approximately four times that of the smallest artificial flaw diameter detectable by the methods employed. Therefore the successful and reliable detection of the smallest artificial flaw considered in this work, at half the size again, may be permissible by the generation of ultrasonic surface waves with frequencies of at least 10 MHz.

The limitation of spot size in this case was due to the use of a generation laser with optical fibre beam output. Instead, a free-space laser could be used whereby the laser beam is emitted already collimated and can be focused down to a smaller spot size.

Pulsed laser irradiation produces a broadband ultrasonic pulse in which the total energy is spread over a wide spectrum of frequencies. There exist methods by which the generated ultrasound can be concentrated within a narrow frequency range using specialised optical elements [82], thus targeting interaction with particular flaw sizes and also leading to a potential increase in SNR within that range. One demonstrated method of producing narrowband, high frequency surface ultrasound uses a laser which outputs an envelope of very short pulses (< 200 ps) to produce an output with a high fundamental frequency of 82 MHz. Additionally, the laser beam was passed through a spatial light modulator, consisting of a 2D array of pixels, to alter the spatial distribution of the beam into a series of linear fringes with spacing matched to the same frequency. Material grain structure and microstructural cracks were successfully resolved.

5.6.2. Performance of Interferometer

Compared to step scanning mode, continuous scanning mode introduces several factors which reduce the ability of the laser ultrasonic testing system to reliably detect sub-surface side-drilled holes:

i. The resolution of a B-scan, i.e. the number of A-scans per unit length, reduces with increasing rate of motion (scanning speed) and limited by the pulse repetition frequency of the generation laser.
ii. Signal amplitude is reduced significantly and variation in amplitude increases with the rate of motion due to inadequate response time of the photo-refractive crystal element within the interferometer.
iii. Signal stability loss results in occasional inversion of the wave-form. This may be mitigated by squaring the signal so that all amplitude data is positive.

All of these factors combined serve to obscure changes in surface displacement signals due to the presence of even the largest and shallowest sub-surface void considered. Data displayed in this chapter highlights the limitations encountered in acquiring data of an adequate quality when performing laser ultrasonic testing on a moving surface, a feature essential for on-line inspection of LMD.

The dynamic performance of the interferometer is affected by two factors:

i. Type of photo-refractive crystal – a silicon crystal is able to better compensate for continuous surface motion and at higher rates of motion due to having a greater compensation bandwidth, which is determined by the response time of the crystal.
ii. Laser beam power – signal stability is increased when more power is available to the reference beam. There is an optimum DC voltage for the reflected signal beam and any remaining laser power can be split to the reference beam; thus a greater overall laser power allows for increased stability.

The IOS AIR-1550-TWM interferometer, an alternative model produced by the same manufacturer, includes a silicon type photo-refractive crystal and is supplied with a 2 W laser, compared to the 0.5 W laser supplied with the AIR-532-TWM interferometer. An experiment was performed in order to quantify the relative dynamic performance of the AIR-532 and AIR-1550 interferometers. In each case, the detection laser was focused on the surface of a work-piece under constant linear motion at speeds of 2, 3, 4, 5, 10, 15, 20, 25, and 30 mm/s. The stability of the output signal measuring instantaneous surface displacements is given as a ratio of AC/DC in arbitrary units, where a value of 1 represents optimum stability and lower values represent decreasing stability. The experiment was repeated on two different surface types: oxidised steel and clean aluminium. For the AIR-532 interferometer, the ratio of AC/DC was recorded with reference beam power measured at 160 mW. For the AIR-1550, the ratio of AC/DC was recorded with reference beam power measured at 80 mW, 160 mW, and 350 mW. The signal amplitude was stabilised by taking several averages of each scan.

The results in Figure 5.45 show that the AIR-532 system and the AIR-1550 system have similar dynamic performance with reference beam power at 160 mW and 80 mW, respectively, whereby the dynamic performance quickly worsens up to 5 mm/s on the tool-marked and oxidised surfaces, and then almost levels off at speeds up to 30 mm/s with only a relatively slight negative trend. For the clean aluminium surface, the decrease in dynamic performance shows a smaller steep drop up to 2 mm/s followed by a similar negative trend. With reference beam power at 160 mW for both systems, there is a clear advantage in the dynamic performance of the AIR-1550 interferometer for all sample speeds. This is improved further with the reference beam power at 350 mW.

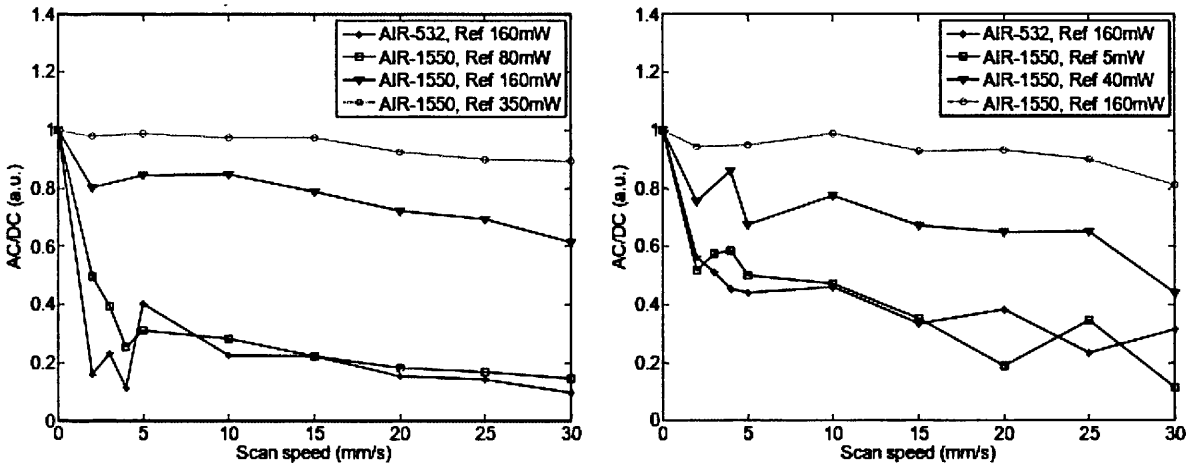

(a) (b)

Figure 5.45. Dynamic performance of the AIR-532 and AIR-1550 interferometers with reflection from (a) an oxidised steel surface, and (b) a smooth aluminium surface. Data provided by the equipment manufacturer on request.

5.6.3. Simulated Flaw Types

The structural flaws simulated in this work consist of cylindrical voids drilled through the width of thin-walled metal structures. This geometry only provides an approximate representation (along two of three axes) of real LMD flaws such as gas porosity, which usually have a spherical or elongated-spherical shape, and can also form more complex voids due to coalescence (see Section 3.3). Most significantly, real flaws are surrounded by solid structure which is the medium for ultrasound propagation. As such, the propagation of ultrasound in the region of a cylindrical, open-ended void is expected to be disrupted to a greater extent than that of ultrasound propagating in the region of a spherical, enclosed void of equivalent diameter. Furthermore, a cylindrical void provides a greater surface area perpendicular to the direction of wave propagation compared to a spherical void, providing a larger boundary from which ultrasound can be reflected and thus greater reflected wave energy which is easier to detect. Similarly in the case of inter-layer lack of fusion flaws which have typically planar faces, the magnitude of ultrasound interaction could be dependent on its angle of incidence relative to the orientation of planar features.

While analysis of laser ultrasonic testing data from the inspection of test samples containing cylindrical voids has provided measurable signals for detection, it would be more ideal to test the same techniques on test samples containing real flaw types. There are two main challenges in producing such test pieces:

i. There is evidence that the LMD manufacturing process has already been successfully refined to the point where the occurrence of flaws above 50 μm in size has been reduced to a level acceptable to aerospace customers (see Section 3.3). Thus the reproduction of larger flaw sizes for the development of detection techniques might require the deliberate use of non-optimal process settings.

ii. The ability to produce real flaws on-demand and in controlled densities may not be possible. It is more likely that a test piece would have to be deposited and then inspected in discrete sections using X-ray computed tomography to non-destructively select volumes containing flaws which meet a set of criteria for testing.

Both of the above points can be addressed providing the availability of sufficient material, time, equipment, and technicians.

Chapter 6: Integration and Performance of Laser Ultrasonic Testing for On-line Inspection of the Laser Metal Deposition Process

6.1. Laser Metal Deposition System

On-line NDT trials were carried out using a Trumpf DMD505 LMD system already in service at TWI Technology Centre in Yorkshire, UK. The system comprises a 2 kW, 1064 nm CO_2 laser with the deposition nozzle on a 5-axis gantry. A rotary platform is installed inside the LMD system (Figure 6.2) with drivers linked to the LMD control interface, facilitating the deposition of structures on a rotating substrate. For the on-line LUT demonstrator, it was decided to deposit a circular wall structure with the LMD nozzle and NDT apparatus separated by one half of a circumference and held stationary, such that each deposited layer could be inspected as it rotated.

Figure 6.1. Trumpf DMD505 LMD system installed at TWI Technology Centre (Yorkshire).

a

b

Figure 6.2. Detail of LMD nozzle and gantry (a) and Nikken rotary platform installed inside the Trumpf DMD505 (b).

6.2. Integration of Laser UT Equipment

Two M10 size screw-holes on the LMD gantry were identified as being the most suitable place to attach a custom-built mounting bracket (Figure 6.3) which provided a 20 cm × 25 cm horizontal platform for mounting the NDT apparatus. A wheel-driven manual X-Y translation stage, with 15 cm travel length in both axes, was attached on the under-side of the mounting platform to provide horizontal position adjustment. Attached to the under-side of the X-Y translation stage was a lab jack with 10 cm travel to provide vertical position adjustment. Finally, two 90 degree brackets were then attached to the under-side of the lab jack so that the NDT apparatus could be mounted such that the laser ultrasonic testing aperture was directed towards the rotary platform.

a b

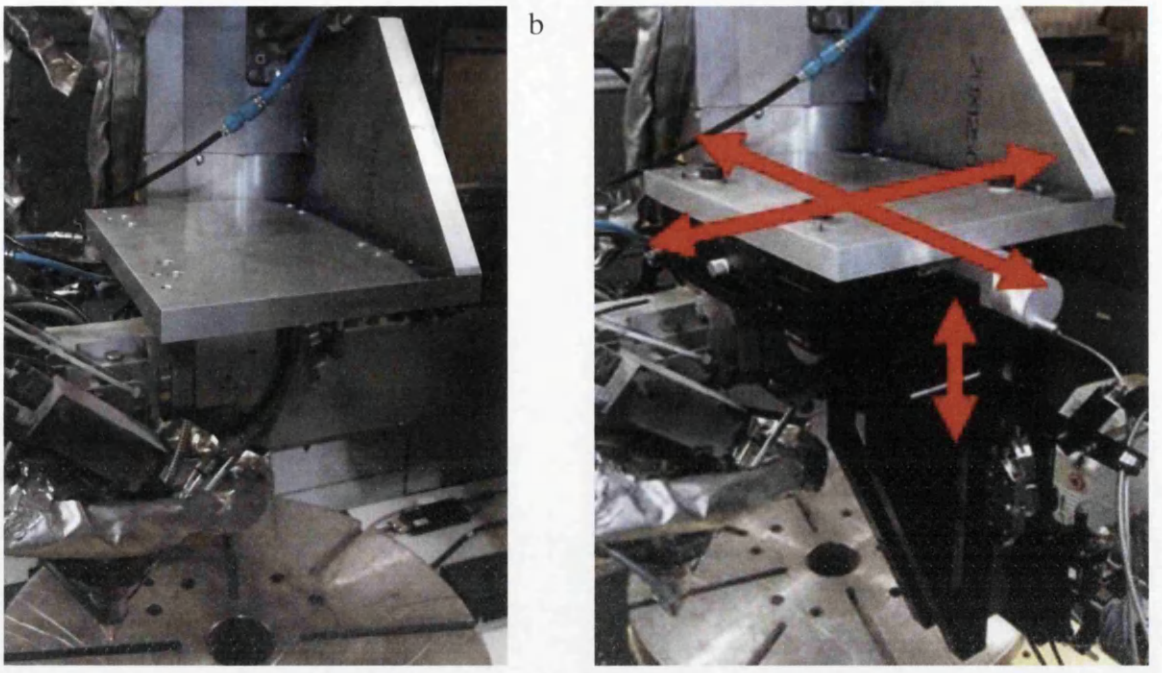

Figure 6.3. Mounting bracket (a) and manual translation stages (b) attached to the LMD gantry.

The LMD system has a large sliding door at the front connected to an integrated interlock which prevents activation of the deposition nozzle when the door is open. Viewing windows provide visibility to the inside of the LMD system during deposition; these windows are made of a thick, tinted plastic material which blocks 1064 nm wavelength light for safety purposes. A foil mask was applied to the windows (Figure 6.4) in order to contain light of wavelength 532 nm used for laser ultrasonic testing.

Figure 6.4. Foil mask placed over the windows on the Trumpf DMD505.

A separate interlock system was constructed to prevent activation of the generation and detection lasers with the door of the LMD system open. Both lasers were connected to the interlock circuit by BNC cables. The interlock circuit is completed by two mechanisms: a key-controlled arming switch and a pair of magnetic proximity switches, one attached to the door and the other attached to the door frame. A large flashing light placed on top of the interlock box illuminates when the interlock is active, signalling to the user that the lasers can be switched on.

Figure 6.5. Assembled interlock system showing external components: warning light, arming switch, arming key, BNC connections, magnetic circuit contacts.

Before mounting the NDT apparatus on the LMD gantry, modifications were made to the optical set-up in order to meet requirements for laser safety. Diode lasers and additional beam-splitter mirrors were added so that an eye-safe laser beam would enter the same propagation path as each of the generation and detection beams to provide a means of positioning the beam paths as required without activating the main lasers. The diode lasers are battery powered and provide a beam output of wavelength 635 nm (visible, red) and power 1 mW (Class 2). It was necessary to place both focusing lenses on motorised linear translation stages with USB connection to the acquisition PC so that focusing of the generation and detection beams could be achieved remotely. With both laser beams already

pointed at their intended positions on the test surface and set manually at approximately the correct stand-off distance, a separate procedure was designed for remotely focusing each laser beam in sequence:

i. The focusing lens for the detection laser beam was translated along the beam axis while monitoring the received DC voltage using a digital oscilloscope. Maximum voltage represented optimum beam focus and therefore maximum coupling efficiency.

ii. The focusing lens for the generation laser beam was translated along the beam axis while monitoring the amplitude of acquired A-scan data in real-time via the LaserScan software. Maximum peak-to-peak Rayleigh wave signal amplitude represented optimum beam focus.

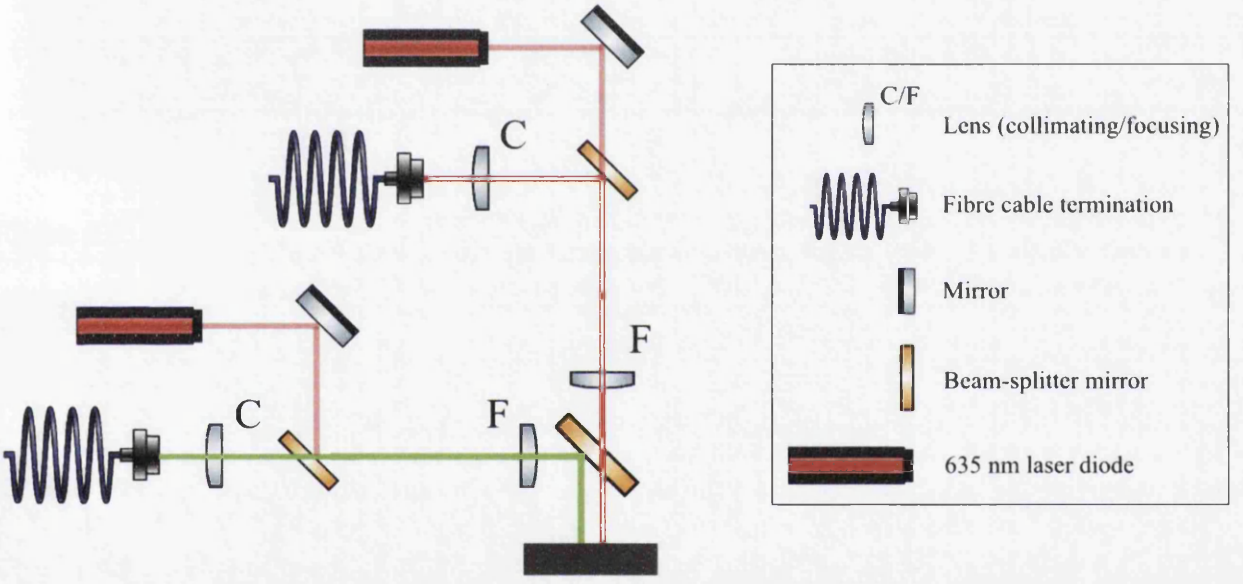

Figure 6.6. Schematic of optical arrangement for on-line laser ultrasonic testing, with the ultrasound generation and detection laser beams represented by red and green lines, respectively. Semi-transparent red lines represent the eye-safe alignment beams.

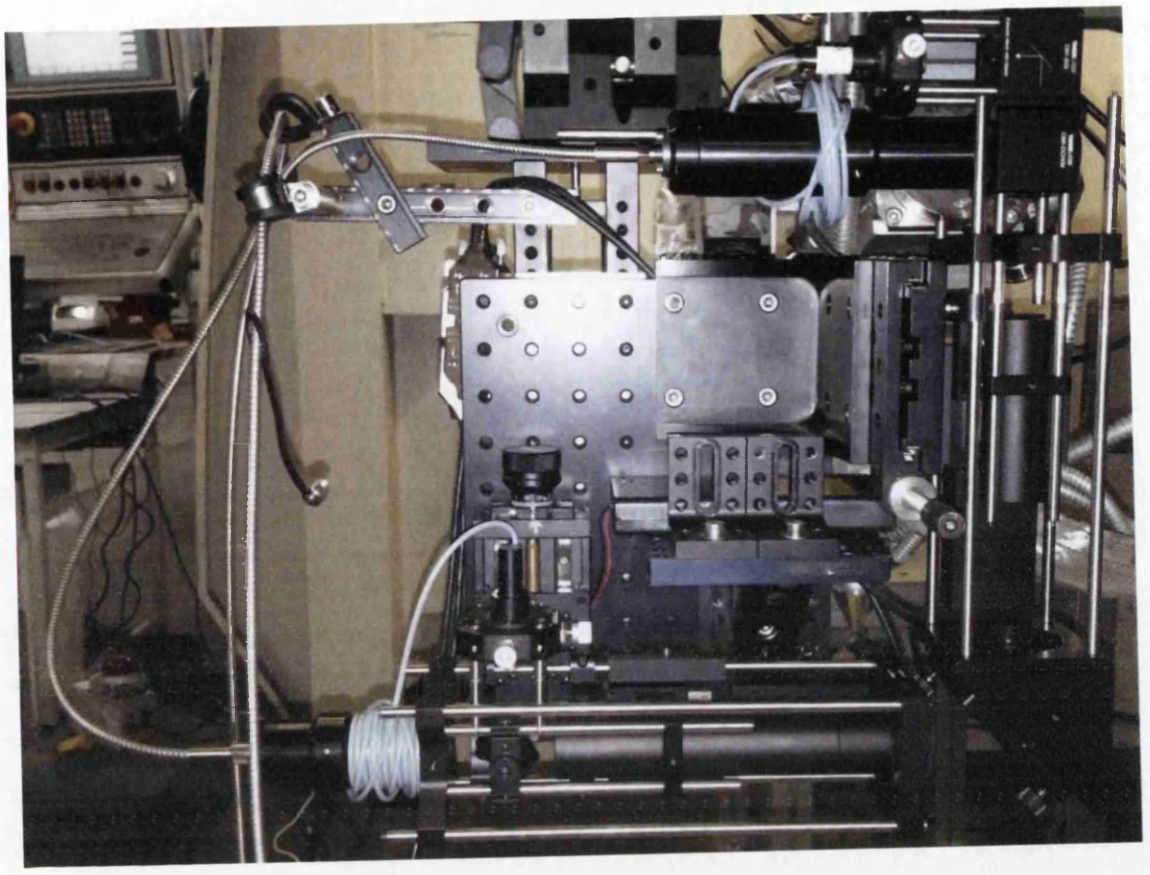

Figure 6.7. Optical arrangement for on-line laser ultrasonic testing.

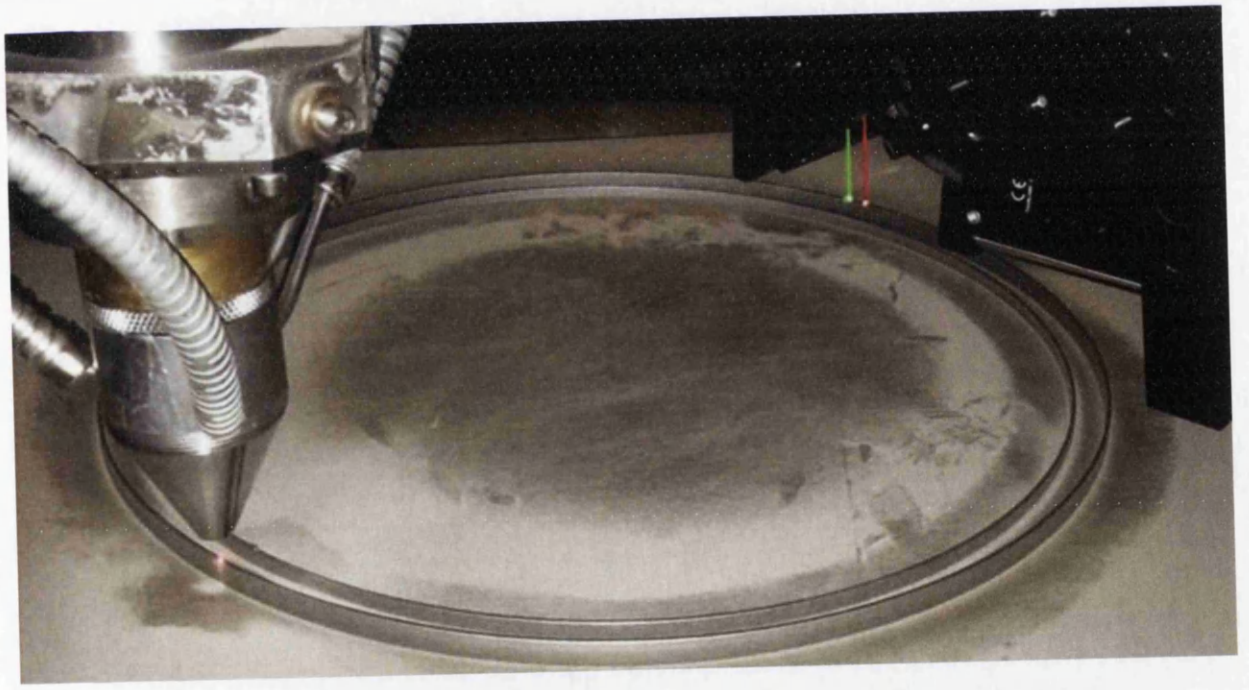

Figure 6.8. Relative positions of the LMD nozzle and laser ultrasonic testing aperture on a circular wall deposit.

For on-line trials, a circular diameter of 280 mm was chosen for the LMD structure. Deposition parameters were selected in order to produce a wall thickness of approximately 1.1 mm. Initially, five layers were deposited to provide a short wall structure onto which the laser beams could be directed and focused. Distortion of the wall structure upon re-starting deposition was found to not be a problem at such a small height. In the first stage of laser ultrasonic, surface displacement data was acquired continuously for a certain length of time while deposition took place. In the LaserScan software, it was necessary to set the scan mode to 'continuous' and input a step size of zero so that data acquisition would occur continuously until stopped by the user.

At a radius of 140 mm from the centre of rotation, the surface under investigation was moving at a rate of ~ 17.6 mm/s during deposition. After halting the deposition process, it was possible to rotate the structure at certain percentages of the full rotation speed. In the second stage of testing, surface displacement data was acquired similarly at a set of reduced rotation speeds given in Table 6.1. From this information, the distance by which the test surface translates between the acquisitions of successive A-scans (based on a pulse repetition rate of 20 Hz) can be calculated. This was considered when setting the generation-detection distance so that B-scan data would include the entire deposited length under investigation with no gaps between A-scans. The generation-detection distance was set at 10 mm.

Table 6.1. Surface translation speeds at percentages of full rpm and calculated surface translations during $1/20^{th}$ of a second.

Percentage of full rotation speed	Surface translation speed at radius of deposition	Surface translation between A-scans
100 %	17.6 mm/s	0.880 mm
50 %	8.8 mm/s	0.440 mm
40 %	7.0 mm/s	0.350 mm
20 %	3.5 mm/s	0.175 mm
10 %	1.8 mm/s	0.088 mm
4 %	0.7 mm/s	0.035 mm

6.3. Results and Analysis

The deposited circular wall structure of diameter 280 mm had an average thickness of 1.15 mm, averaged over ten measurements made using a digital calliper at different positions around the circumference. After depositing approximately 10 mm height, the laser UT system was activated and B-scans recorded at increasing rotational speed settings (Figure 6.9) as allowed by the LMD system controller. It can be seen that Rayleigh wave amplitude decreases relative to the surrounding noise signals as motion rate increases. It was observed that, approximately one minute after activation of the LMD system, there was additional audible noise and vibration due to the operation of attached air and water-cooling units. Tests were repeated with these systems active to investigate the affect.

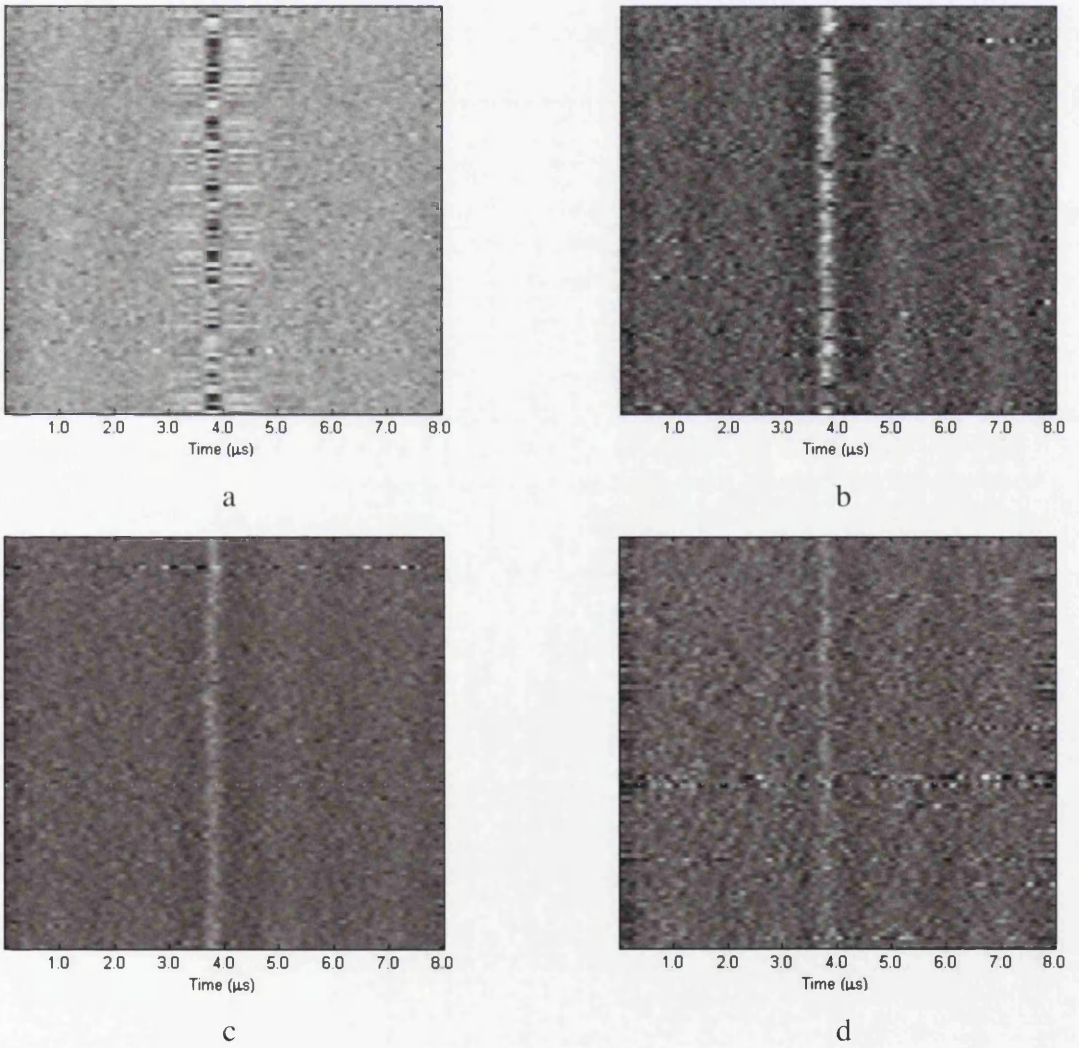

Figure 6.9. B-scans performed on the deposited circular wall at motion rates of (a) 0.7 mm/s, (b) 1.8 mm/s, (c) 8.8 mm/s, and (d) 17.6 mm/s.

As with the laboratory results in Chapter 5, SNR was measured for each separate rate of motion by comparing the Rayleigh wave signal amplitude with the maximum noise signal amplitude per A-scan, repeated over all scan positions to give a mean SNR with standard deviation (Figure 6.10). This was also compared between the results with and without cooling systems active.

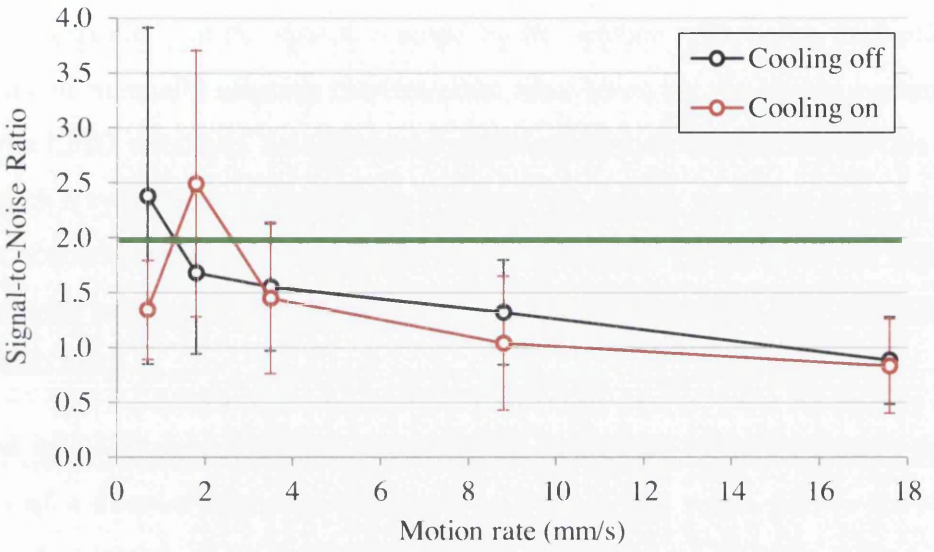

Figure 6.10. Rayleigh wave SNR as a function of surface motion rate. Error bars represent standard deviation from mean SNR.

There is no consistent difference in SNR due to activation of the cooling systems, suggesting that signal quality is unaffected by the additional environmental vibrations. SNR values as a function of motion rate generally agree with those measured in continuous scan mode on test-piece C0 (deposited surface) in laboratory conditions, with almost all results falling below the threshold of 2:1 SNR. At the greatest speeds, SNR drops as low as 1:1 – indications from artificial flaws would be impossible to measure in such cases.

6.4. Discussion

6.4.1. Practicalities of Installation

In a trial integration of the laser ultrasonic system into an LMD environment, there were many difficulties discovered in acquiring a good quality signal. The laser detection equipment is limited in its ability to resolve surface displacements when the test surface is under motion, especially at the speeds reached by the surface undergoing deposition. There was difficulty in manually aligning the detection laser beam on the highly curved and thin surface of the LMD structure. An automated alignment system might mitigate this particular difficulty; such a system could monitor the received DC voltage (reflected light) as measured by the data acquisition card, and adjust the rotation/stand-off of the detection laser head in small increments in order to find the maximum intensity of received light and therefore the optimum beam focus.

The method of LMD manufacturing whereby the deposition substrate rotates around the central axis of a circular deposited structure, as used in this work, allows for the easiest placement and operation of the laser optical heads as they do not have to move to track the inspection surface. A slightly more complex method of deposition makes use of a tilting rotation table which allows for the addition of layers deposited at varying angles with respect to the substrate surface to form over-hanging walls. With the laser optical heads attached directly to the LMD nozzle, this action would cause a collision with the substrate/deposited structure. This limitation might be overcome by the installation of motorised translation and rotation apparatus which would continuously alter the position and direction of the laser optical heads to correspond to the relative position and orientation of the surface under inspection. This would require computer-based control over the motion equipment following a pre-configured path using input from the existing deposition parameters for any given structure. These parameters include the speed, rotation and position of the LMD system parts as a function of time and may be output from the controlling computer. This method would in turn be limited by the available space around the LMD equipment and also the smoothness and accuracy of additional motion equipment as described.

It is common in LMD manufacturing for the deposition nozzle to translate and rotate while the substrate remains stationary. This method of manufacture would also present difficulties for integrated laser ultrasonic testing as the deposition path may be constantly changing in direction. Motion of the laser optical heads might be achieved by their attachment to one

individual or two separate computer-controlled robot arm with the capability of translating and rotating in several axes, providing that there is space available for such an installation. In this case, an important consideration would be the accuracy in movement of the robotic arm, as the successful reflection of the reception laser beam from the inspection surface is highly sensitive to position and angle of incidence. The smallest possible translation or rotation increment in a robotic arm is a limitation of its motion components and sensors and is referred to as the Basic Resolution Unit (BRU). Overall accuracy is also affected by other factors as defined in ISO 9283 including the rate of converting movement commands into physical actions, manufacturing tolerances in component parts, friction in joints, backlash, and thermal expansion [86]. An example of a robotic arm with high movement accuracy is the ABB Robotics IRB2000 which has a linear BRU of 0.125 mm [87].

6.4.2. Deposited Material Properties

Surface reflectivity of metals varies significantly depending on the wavelength of the incident laser light. Reflectivity is measured on a scale from zero to one, which represents 0% reflection of incident light and 100% reflection of incident light, respectively. For example, a smooth, polished surface of Nickel can vary in reflectivity from approximately 0.6 for laser light of wavelength 532 nm and approximately 0.7 for laser light of wavelength 1064 nm [83]. Thus the performance of laser-based detection of ultrasonic waves in LMD can be affected by the type of metal being deposited as the intensity of received light is a factor in the resolving ability of a TWM interferometer.

The absorptivity, that is, the capacity of a material to absorb photon energy at its surface, increases with surface temperature, and thus reflectivity decreases [84]. This means that the performance of an interferometry-based surface displacement detection system could be reduced when utilised on a surface with raised temperature, such as in LMD. However, the dependence of reflectivity on temperature is much less significant than that on wavelength of the light [85]; therefore, this should not be considered an important factor.

6.4.3. Industrial and Commercial Considerations

In addition to all of the aforementioned considerations, the industrial use of in-situ laser ultrasonic testing should be expected to meet the following commercial and practical criteria:

i. Proven to be effective in detecting common flaw types within a size range determined by the quality requirements of the manufacturer/customer.

ii. Include automated, real-time detection algorithms so that a notification can be displayed to the machine operator unskilled in the analysis of ultrasonic testing data.

iii. Development of flaw mitigation/removal procedures (for example by re-melting an already deposited layer) so that the notification of a detected flaw can lead to a useful action either automatically or carried out by the machine operator.

Cost advantage due to potential material or time savings greater than the cost disadvantage of additional equipment, installation, labour, and manufacture time (for example a reduction in process speed or temporary halts to allow for effective laser ultrasonic testing).

Chapter 7: Conclusions

The following sections summarise the achievements of this work corresponding to the objectives set out at the beginning of the thesis. Recommendations for further work in the same areas of research are also considered.

7.1. Finite Element Analysis

A 2D finite element model was produced to simulate the generation and propagation of ultrasonic waves through solid elements with material properties and geometries close to those of the real test-pieces. A range of artificial sub-surface flaws were included in the forms of circular voids, based on sizes reported in literature for real microstructural LMD flaws.

The necessary thermal and mechanical interactions were properly simulated via a surface heat flux input, producing heat conduction and propagation of ultrasonic waves corresponding to theoretical expectations. Ultrasonic wave disturbances due to the presence of sub-surface voids were recorded from positions on the surface of each modelled test-piece, output in sequence to create B-scan images for data analysis. Flaw indication signals were found to be easily measurable due to the absence of noise signals and fully controllable conditions.

Measured surface displacements were analysed in the time and frequency domains using various methods to quantify changes in the received signals corresponding to ultrasonic wave interaction with each sub-surface void. The indications observed were:

i. Loss of Rayleigh wave signal amplitude as the source and detection positions are on either side of the sub-surface void.
ii. The appearance of surface wave signals due to reflection of the Rayleigh wave from either side of the sub-surface void, with an associated shift to higher frequency content at positions where the reflection signals were measured, increasing inversely proportional to void diameter.

The use of FEA also provided an opportunity to simulate ultrasonic wave interaction with a spherical sub-surface void in a 3D model of a thin wall, more closely matching the real examples. It was found that for a void of equivalent depth and diameter, the effect on a propagating surface wave in the 3D model was significantly reduced and signal indications barely measurable compared to the 2D model. The reason for this difference in response was

attributed to a reduction in the portion of the wave-front interacting with the void due to the addition of an extra dimension in the solid geometry.

This particular aspect of the FEA work may be taken further by considering higher frequency and narrowband frequency ultrasonic waves to target small void diameters. Additionally, different microstructural flaw types can be simulated. These can include elongated or coalesced porosity, as well as inter-layer porosity which has one or more planar faces.

7.2. Detection of Artificial Flaws

A set of thin-walled test-pieces were manufactured to include near-surface side-drilled holes of various depths and diameters in order to approximate intra-layer LMD flaws as identified in literature review. The test-pieces were constructed from Inconel 718 alloy and two surface finishes were included: machined and powder-deposited.

Laser ultrasonic testing was performed and several methods of data analysis were employed to measure flaw indication signals in the time and frequency domains. Two parts of the B-scan data sets were considered separately: data including the section of time up to the arrival the Rayleigh wave, and data including the section of time after the arrival of the Rayleigh wave. Taking into account all of the data analysis methods described in Chapter 5, it was found that artificial flaws could be more reliably detected by using the reflection signals which appear in the latter time-window due to the interaction of the Rayleigh wave with the artificial flaws. Dynamic changes in the Rayleigh wave signal were found to be less reliable for detection. Compared to FEA, indication signals were more difficult to resolve due to the presence of signal noise in the real tests. All of the data analysis methods employed were chosen on the basis that they could be conceivably carried out in real-time for use in-situ and depend on continuous monitoring of received A-scans.

The largest artificial flaw diameters of 250 μm and 150 μm were detectable in stepped scan mode, providing measurable indication signals above the thresholds set for each data analysis method. Detectability was reduced for the same flaw diameters at greater depth. The smallest artificial flaw diameters of 100 μm and 77 μm were not detectable at any depth. This is attributed to the limited maximum frequency content of the generated surface ultrasonic waves due to a limitation of the minimum laser spot size imposed by the use of a fibre-coupled laser.

The test-pieces with a powder-deposited surface layer had increased surface roughness and surface roundness. These factors contributed to a decrease in signal-to-noise ratio for both the reflection and Rayleigh wave signals. Detectability was thus reduced in the case of the artificial flaw with diameter 150 μm.

Repeated analysis of test results obtained in continuous scan mode revealed a significant loss in signal-to-noise ratio, becoming slightly worse again with increasing rate of motion. Combined with a decrease in the number of A-scans per unit length due to a limit in the laser pulse repetition frequency, as well as suboptimal motion compensation capability of the interferometer, the result was a complete loss in artificial flaw detectability.

Future work should consider the exploration of methods by which real microstructural LMD flaws can be reliably generated. The side-drilled holes relied upon in this work only approximate the geometry of intra-layer porosity in two dimensions – the volume through the wall thickness in the real case would consist of mostly solid material where a flaw is present. As such, a side-drilled hole provides a greater void volume and wave-front-facing reflector and should be more easily detectable than a real flaw of the same diameter. The creation of real flaws presents difficulties as their frequency and location is unpredictable. The solution might require that large lengths of deposited layers are X-rayed to identify and grade microstructural flaws, involving a non-trivial allocation of materials and labour.

7.3. Hardware Selection

Limitations were met in the attempt to successfully detect the smallest artificial flaw diameters when carrying out laser ultrasonic testing in stepped scan mode, and signal-to-noise ratio was severely worsened when operating in continuous scan mode. Furthermore, the rate of motion required in LMD is even greater than that tested in laboratory conditions. More targeted selection of hardware may improve or resolve these limitations.

Pulse length has the greatest effect on the central frequency and also frequency range of ultrasonic wave energy generated – although the maximum frequency can also be limited by the minimum spot size as I this work. Higher frequency, and therefore shorter wavelength, ultrasonic waves are expected to improve detectability of flaws with smaller diameter. However, this must also be balanced with Rayleigh wave penetration depth which decreases with Rayleigh wavelength.

Pulse repetition rate limits number of A-scans per unit length when operating in continuous scan mode, effectively reducing data resolution at greater rates of motion. Hardware is readily available with faster pulse repetition.

Response time of the TWM interferometer is largely dependent on the type of photo-refractive crystal material and greatly affects stability/quality of the received surface displacement signals when the test surface is in motion. Laser power also improves motion compensation ability, although the maximum power permitted is dependent on the limits of the hardware. Alternative TWM interferometers may improve results on fast moving surfaces, and other types of interferometry suited to surface motion should also be considered, such as Fabry-Pérot.

7.4. Integration into LMD Manufacturing

The laser ultrasonic testing system was installed into a working LMD manufacturing environment. The optical heads of the generation and detection laser beams were attached directly to the LMD nozzle. The following features were included to meet laser safety requirements:

- Remotely controlled, motorised beam platforms to allow manual focusing from outside the LMD unit by monitoring received DC voltage and ultrasonic signal amplitude.
- Foil covering for the viewing window to prevent the escape of laser light with wavelength not filtered by the window material.
- A portable interlock system to prevent laser operation when the door of the LMD unit is open.

The LMD nozzle remained stationary throughout the testing period. A flat deposition platform was used, rotating around the vertical axis in order to form a circular deposit. The NDT laser beams were also held stationary focused on the opposite extremity of the circular deposit surface. Rayleigh wave signal-to-noise ratio was found to be poor and corresponded with laboratory-based testing, although this was not negatively affected by the operation of cooling systems built into the LMD unit.

Aside from the development of reliable flaw detection and sizing methods, a range of practical and commercial requirements can be considered which present obstacles to the deployment of in-situ evaluation of LMD structures:

Practical requirements may include:

- The ability for the ultrasonic source and detection to follow the path of deposition – more complex shapes and a non-stationary substrate will inevitably make this more difficult to achieve and may limit the application to less complex deposits. In this work a flat, rotating deposit was chosen due to space and positioning constraints.

- Ensuring constant coupling of the detection laser beam with the deposit surface – in this work there was difficulty experienced in acquiring a good level of light reflection which is linked to ultrasonic signal amplitude and motion compensation capability. The deposited surface is rough and has a rounded profile. It may be possible to optimise laser beam coupling with motorised positioning of optics to make corrections while monitoring the received reflection signal voltage.

- Established corrective actions to take based on different flaws which can be detected – for example, part of a deposited layer may be re-melted to consolidate the material.

Commercial requirements may include:

- Reliable flaw detection proven capable down to sizes or 'grades' meeting the quality control requirements of the component manufacturer or client – this can determine the number of scenarios where the NDT technique is viable.

- Automated detection and possibly categorisation of flaws via real-time data analysis – ideally the NDT technique should be linked to a user interface which can provide notifications of detected flaws so that an operator not skilled in the NDT technique can take appropriate action. Taking this idea further, corrective action might also be automated based on the nature of the detected flaw signals.

- Procedures for in-situ inspection and corrective actions to not be excessively intrusive – extra cost can be added to the manufacturing process if modification to the LMD system is required or if the rate of manufacturing is reduced. The decision of a manufacturer or client to install and make use of a quality control system may be affected by these costing factors.

Bibliography

[1] L. P. Wang, P.; Felicelli, S.; Kadiri, H.; Wang, P., "Experimental Analysis of Porosity Formation in Laser-assisted Powder Deposition Process," in *TMS 2009 Annual Meeting and Exhibition*, San Fransisco, USA, 2009.

[2] M. N. Ahsan, R. Bradley, and A. J. Pinkerton, "Microcomputed tomography analysis of intralayer porosity generation in laser direct metal deposition and its causes," *Journal of Laser Applications,* vol. 23, p. 022009, 2011.

[3] A. L. Blouin, Daniel; Lord, Martin; Dessendre, Marc; Tretout, Hervé, "Laser Ultrasonics as an Alternative Inspection Method to Detect Microstructural Flaws in Aerospace Structures," presented at the 1st International Symposium on Laser Ultrasonics: Science, Technology and Applications, Montreal, Canada, 2008.

[4] T. H. Maiman, "Stimulated Optical Radiation in Ruby," *Nature,* vol. 187, pp. 493-494, 1960.

[5] M. Choquet, R. Héon, C. Padioleau, P. Bouchard, C. Néron, and J.-P. Monchalin, "Laser-Ultrasonic Inspection of the Composite Structure of an Aircraft in a Maintenance Hangar," pp. 545-552, 1995.

[6] S. D. Kenderian, B. B.; Cerniglia, D.; Garcia, G., "Dynamic railroad inspection using the laser-air hybrid ultrasonic technique," *Insight - Non-Destructive Testing and Condition Monitoring,* vol. 48, p. 5, 2006.

[7] J.-R. Lee, H.-J. Shin, C. C. Chia, D. Dhital, D.-J. Yoon, and Y.-H. Huh, "Long distance laser ultrasonic propagation imaging system for damage visualization," *Optics and Lasers in Engineering,* vol. 49, pp. 1361-1371, 2011.

[8] C. B. Scruby and L. E. Drain, *Laser Ultrasonics Techniques and Applications*: Adam Hilger, 1990.

[9] D. Meschede, *Optics, Light and Lasers: The Practical Approach to Modern Aspects of Photonics and Laser Physics*, 2nd ed.: John Wiley & Sons, 2007.

[10] Y. Kalisky, *The Physics and Engineering of Solid State Lasers* vol. TT71: SPIE Press, 2006.

[11] E. Hecht, *Optics*, 2nd ed.: Addison-Wesley, 1987.

[12] A. E. Siegman, *Lasers*, Revised ed.: University Science Books, 1986.

[13] K. Schulmeister, R. Gilber, F. Edthofer, B. Seiser, and G. Vees, "Comparison of different beam diameter definitions to characterize thermal damage of the eye," 2006, pp. 61011A-61011A-13.

[14] P. W. E. Milonni, Joseph H., *Laser Physics*: John Wiley & Sons, 2010.

[15] "Lasers and laser-related equipment. Test methods for laser beam widths, divergence angles and beam propagation ratios. Stigmatic and simple astigmatic beams," ed: BSI, 2005.

[16] (3rd December 2014). *Polarization and Polarization Control.* Available: https://www.newport.com/images/webDocuments-EN/images/18954.pdf

[17] A. P. French, *Vibrations and Waves*: Taylor & Francis, 1971.

[18] (1st December 2014). *Fiber Optic Basics.* Available: http://www.newport.com/Fiber-Optic-Basics/978863/1033/content.aspx

[19] (2nd December 2014). *Focusing and Collimating.* Available: http://www.newport.com/Focusing-and-Collimating/141191/1033/content.aspx

[20] S. A. Self, "Focusing of spherical Gaussian beams," *Applied Optics,* vol. 22, pp. 658-661, 1983/03/01 1983.

[21] J. D. Achenbach, *Wave Propagation in Elastic Solids*: North-Holland, 1987.

[22] J. K. Krautkrämer, H., *Ultrasonic Testing of Materials*, 4th ed.: Springer, 1990.

[23] J. L. Rose, *Ultrasonic Waves in Solid Media*, Revised ed.: Cambridge University Press, 2004.
[24] H. S. J. Carslaw, J. C., *Conduction of Heat in Solids*, 2nd ed.: Clarendon Press, 1959.
[25] J. F. Ready, *Effects of High-Power Laser Radiation*: Academic Press, 1971.
[26] S. Krishnaswamy, *Theory and Applications of Laser-Ultrasonic Techniques*: CRC Press, 2003.
[27] D. D. Nolte, *Photorefractive Effects and Materials*: Springer US, 1995.
[28] *AIR-532-TWM Operations Manual*: Intelligent Optical Systems, Inc., 2011.
[29] S. Dixon, B. Cann, D. L. Carroll, Y. Fan, and R. S. Edwards, "Non-linear enhancement of laser generated ultrasonic Rayleigh waves by cracks," *Nondestructive Testing and Evaluation,* vol. 23, pp. 25-34, 2008.
[30] J. P. Monchalin, "Optical Detection of Ultrasound," *IEEE Transactions on Ultrasonics, Ferroelectrics and Frequency Control,* vol. 33, pp. 485-499, 1986.
[31] P. Gregorcic, "Ultrasonic Detection with Fabry-Perot Interferometer," in *Seminar*, University of Ljubljana, 2005.
[32] A. M. Aindow, R. J. Dewhurst, S. B. Palmer, and C. B. Scruby, "Laser-based non-destructive testing techniques for the ultrasonic characterization of subsurface flaws," *NDT International,* vol. 17, pp. 329-335, 1984.
[33] J. A. Cooper, R. A. Crosbie, R. J. Dewhurst, A. D. W. McKie, and S. B. Palmer, "Surface Acoustic Wave Interactions with Cracks and Slots: A Noncontacting Study Using Lasers," *IEEE Transactions on Ultrasonics, Ferroelectrics and Frequency Control,* vol. 33, pp. 462-470, 1986.
[34] B. Dutton, A. R. Clough, M. H. Rosli, and R. S. Edwards, "Non-contact ultrasonic detection of angled surface defects," *NDT & E International,* vol. 44, pp. 353-360, 2011.
[35] F. Hernandez-Valle, R. S. Edwards, A. R. Clough, M. H. Rosli, and B. Dutton, "Scanning laser techniques for characterisation of different surface breaking defect geometries," *Proceedings: 18th World Conference on Non-Destructive Testing,* 2012.
[36] S. P. Santospirito, A. Heisterkamp, R. Łopatka, P. R. Herman, M. Meunier, D. Cerniglia, *et al.*, "Defect detection in laser powder deposition components by laser thermography and laser ultrasonic inspections," in *Frontiers in Ultrafast Optics: Biomedical, Scientific, and Industrial Applications XIII*, San Francisco, USA, 2013.
[37] G. K. Jeskey, R.; Damm, E.; Monchalin, J.-P.; Lamouche, G.; Kruger, S. E.; Choquet, M., "Laser Ultrasonic Sensor for On-line Seamless Steel Tubing Process Control," presented at the World Conference on NDT, Montreal, Canada, 2004.
[38] "Final Report Summary - SIGNASTIR (Development of an in-process quality assurance system for friction stir welding)," European Commission 2014.
[39] "Automated Machining of Turbine Blades by Rolls-Royce," *Aircraft Engineering and Aerospace Technology,* vol. 55, pp. 7-9, 1983.
[40] J. Allen, "An Investigation into the Comparative Costs of Additive Manufacture vs Machine from Solid for Aero Engine Parts," presented at the RTO-MP-AVT-139, Neuilly-sur-Seine, France, 2006.
[41] "3D Printing and Additive Manufacturing State of the Industry," ed: Wohlers Associates, 2014.
[42] P. A. P. Carroll, Andrew J.; Allen, J.; Syed, W. U. H.; Sezer, H. K.; Brown, P.; Ng, G.; Scudamore, R.; Li, L. , "The Effect of Powder Recycling in Direct Metal Laser Deposition on Powder and Manufactured Part Characteristics," in *NATO AVT-139 Specialists Meeting - Cost Effective Manufacture via Net Shape Processing*, Amsterdam, The Netherlands, 2006.

[43] N. A. Hoye, E. C.; Cuiuri, Dominic; Li, Hejie, "Characterisation of metal deposition during additive manufacturing of Ti-6Al-4V by arc-wire methods," presented at the Twenty Forth Annual International Solid Freeform Fabrication Symposium, Austin, Texas, 2013.

[44] B. Hubscher. (1st April 2015). *NASA's Space Launch System Using Futuristic Technology to Build the Next Generation of Rockets*. Available: http://www.nasa.gov/exploration/systems/sls/selective_melting.html#.VZRlevlVhBc

[45] TWI, "Laser Powder Metal Deposition Manufacturing of Complex Real Parts," ed: Lortek, 2014.

[46] C. Y. Kong, R. J. Scudamore, and J. Allen, "High-rate laser metal deposition of Inconel 718 component using low heat-input approach," *Physics Procedia,* vol. 5, pp. 379-386, 2010.

[47] (2nd March 2015). *Overview of LMD applications for aerospace components*. Available: http://www.pomgroup.com/index.php?option=com_content&view=article&id=196&Itemid=819

[48] J. M. Wilson, C. Piya, Y. C. Shin, F. Zhao, and K. Ramani, "Remanufacturing of turbine blades by laser direct deposition with its energy and environmental impact analysis," *Journal of Cleaner Production,* vol. 80, pp. 170-178, 2014.

[49] Q. Liu, M. Janardhana, B. Hinton, M. Brandt, and K. Sharp, "Laser Cladding as a Potential Repair Technology for Damaged Aircraft Components," *International Journal of Structural Integrity,* vol. 2, pp. 314-331, 2011.

[50] (5th February 2015). *Inconel Alloy 718*. Available: http://www.specialmetals.com/documents/Inconel%20alloy%20718.pdf

[51] Y. C. Zhang, Xinjin; Wanjara, Priti; Medraj, Mamoun, "Fiber Laser Deposition of Inconel 718 Using Powders," in *Materials Science & Technology 2013*, Montreal, Canada, 2013.

[52] G. K. L. Ng, A. E. W. Jarfors, G. Bi, and H. Y. Zheng, "Porosity formation and gas bubble retention in laser metal deposition," *Applied Physics A,* vol. 97, pp. 641-649, 2009.

[53] D. F. Susan, J. D. Puskar, J. A. Brooks, and C. V. Robino, "Quantitative characterization of porosity in stainless steel LENS powders and deposits," *Materials Characterization,* vol. 57, pp. 36-43, 2006.

[54] P. A. Kobryn, E. H. Moore, and S. L. Semiatin, "The effect of laser power and traverse speed on microstructure, porosity, and build height in laser-deposited Ti-6Al-4V," *Scripta Materialia,* vol. 43, pp. 299-305, 2000.

[55] S. Lasertec. (2013, 15th March 2015). *Giveth and Taketh Away - CNC Milling and Additive Laser Deposition in One Cycle*. Available: http://www.3dprinterworld.com/article/giveth-and-taketh-away-cnc-milling-and-additive-laser-deposition-one-cycle

[56] B. P. Dutta, S.; Choi, J.; Song, L. J.; Mazumder, J., "Additive Manufacturing by Direct Metal Deposition," ed. Advanced Materials & Processes, 2011, pp. 33-36.

[57] R. M. A. Mahamood, Esther T.; Shukla, Mukul; Pityana, Sisa, "Effect of Laser Power on Surface Finish during Laser Metal Deposition Process," presented at the World Congress on Engineering and Computer Science, San Fransisco, USA, 2014.

[58] M. Rombouts, G. Maes, W. Hendrix, E. Delarbre, and F. Motmans, "Surface finish after laser metal deposition," *Physics Procedia,* vol. 41, pp. 810-814, 2013.

[59] "Surface texture: Profile method. Terms, definitions and surface texture parameters," in *BS EN ISO 4287 Geometrical Product Specifications*, ed: BSI, 2000.

[60] R. M. A. Mahamood, Esther T.; Shukla, Mukul; Pityana, Sisa, "Effect of laser power on material efficiency, layer height and width of laser metal deposited Ti-6AL-4V," in *Proceedings of the World Congress on Engineering and Computer Science 2012*, San Fransisco, USA, 2012.

[61] L. P. Thivillon, D.; Bertrand, P.; Smurov, I., "Industrial Technology of Laser Assisted Direct Metal Deposition," in *International Thermal Spray Conference & Exposition*, Maastricht, The Netherlands, 2008, pp. 1171-1177.

[62] A. M. Kamara, S. Marimuthu, and L. Li, "Finite Element Modeling of Microstructure in Laser-Deposited Multiple Layer Inconel 718 Parts," *Materials and Manufacturing Processes,* vol. 29, pp. 1245-1252, 2014.

[63] L. Wang and S. Felicelli, "Process modeling in laser deposition of multilayer SS410 Steel," *Journal of Manufacturing Science and Engineering,* vol. 129, p. 1028, 2007.

[64] F. Wang, H. Mao, D. Zhang, X. Zhao, and Y. Shen, "Online study of cracks during laser cladding process based on acoustic emission technique and finite element analysis," *Applied Surface Science,* vol. 255, pp. 3267-3275, 2008.

[65] "Welding - Electron and laser beam welded joints - Guidance on quality levels for imperfections - Part 1: Steel," ed: British Standards Institution, 1997.

[66] E. Foroozmehr, D. Lin, and R. Kovacevic, "Application of vibration in the laser powder deposition process," *Journal of Manufacturing Processes,* vol. 11, pp. 38-44, 2009.

[67] G. K. Lewis and E. Schlienger, "Practical considerations and capabilities for laser assisted direct metal deposition," *Materials & Design,* vol. 21, pp. 417-423, 2000.

[68] Y. S. Yang, Todd; Ruan, Jianzhong; Ren, Lan; Liou, Frank, "Laser Deposition Cladding On-Line Inspection Using 3-D Scanner," presented at the The Seventeenth Solid Freeform Fabrication Symposium, University of Texas, USA, 2007.

[69] D. Clark, S. D. Sharples, and D. C. Wright, "Development of online inspection for additive manufacturing products," *Insight - Non-Destructive Testing and Condition Monitoring,* vol. 53, pp. 610-613, 2011.

[70] S. D. C. Sharples, Matt; Li, Wenqi; Somekh, Mike G., "Rapid Imaging of Microstructure using Spatially Resolved Acoustic Spectroscopy," presented at the 1st International Symposium on Laser Ultrasonics: Science, Technology and Applications, Montreal, Canada, 2008.

[71] M. Klein, T. Sienicki, J. Eichenbergeer, "Laser-Ultrasonic Detection of Subsurface Defects in Processed Materials," USA Patent, 2007.

[72] S. S. L. Quek, G. R., *Finite Element Method: A Practical Course*: Butterworth-Heinemann, 2003.

[73] A. Pantano and D. Cerniglia, "Simulation of laser generated ultrasound with application to defect detection," *Applied Physics A,* vol. 91, pp. 521-528, 2008.

[74] *User's Manual - ULTRA CFR Nd:YAG Laser System*: Quantel, 2004.

[75] L. Liu, A. Hirose, and K. F. Kobayashi, "A numerical approach for predicting laser surface annealing process of Inconel 718," *Acta Materialia,* vol. 50, pp. 1331-1347, 2002.

[76] (5th February 2015). *Inconel 718 Technical Data.* Available: http://www.hightempmetals.com/techdata/hitempInconel718data.php

[77] F. Moser, L. J. Jacobs, and J. Qu, "Modeling elastic wave propagation in waveguides with the finite element method," *NDT & E International,* vol. 32, pp. 225-234, 1999.

[78] *Abaqus Analysis User's Manual 6.11*: Dassault Systèmes Simulia Corp., 2011.

[79] J. B. Wachtman, W. E. Tefft, D. G. Lam, and C. S. Apstein, "Exponential Temperature Dependence of Young's Modulus for Several Oxides," *Physical Review,* vol. 122, pp. 1754-1759, 1961.

[80] R. C. Kolman, S. S.; Park, K. C., "Accurate Explicit Finite Element Method for Wave Propagation and Dynamic Contact Problems," presented at the 11th World Congress on Computational Mechanics, Barcelona, Spain, 2014.
[81] P. O. Moore, D. Kishoni, and G. L. Workman, *Nondestructive Testing Handbook, Volume 7: Ultrasonic Testing*, 3rd ed.: The American Society for Nondestructive Testing, 2007.
[82] C. E. Duffer and C. P. Burger, "Narrow Band Laser Ultrasonic NDE," in *Review of Progress in Quantitative Nondestructive Evaluation*. vol. 15A, ed: Springer US, 1996.
[83] M. N. Ahsan, "Modelling and Analysis of Laser Direct Metal Deposition of Ti-6Al-4V Alloy," Doctor of Philosophy, School of Mechanical, Aerospace and Civil Engineering, The University of Manchester, 2011.
[84] W. M. Steen, *Laser Material Processing*, 3 ed.: Springer London, 2003.
[85] E. W. Spisz, U. S. N. Aeronautics, S. Administration, and L. R. Center, *Solar Absorptances and Spectral Reflectances of 12 Metals for Temperatures Ranging from 300 to 500 K*: National Aeronautics and Space Administration, 1969.
[86] I. O. f. Standardization, "Manipulating industrial robots -- Performance criteria and related test methods," ed: International Organization for Standardization, 1998.
[87] RobotWorx. (17th April 2016). *ABB IRB 2000 Product Page*. Available: https://www.robots.com/abb/irb-2000